Aero-Thermal Characteristics and Film Cooling of Transonic Turbine Blade Tips



Andrew J. Saul

Pembroke College

University of Oxford

A thesis submitted in partial fulfilment of the requirements for the degree of

Doctor of Philosophy

Hilary Term, 2018

Aero-Thermal Characteristics and Film Cooling of Transonic Turbine Blade Tips

Andrew J. Saul

Pembroke College

A thesis submitted in partial fulfilment of the requirements for the degree of
Doctor of Philosophy
Hilary Term, 2018

Abstract

Film cooling is essential to protect high pressure turbine blade tips from the high speed, high temperature overtip leakage flows, which are forced through the tip clearance gap. Careful design of the blade tip and cooling strategy is necessary to reduce the resulting aerodynamic inefficiencies, high thermal loads and tip degradation. Only with an in-depth knowledge of the overtip leakage flow and its interactions with film coolant can this be achieved, in order to improve the efficiency and prolong the in-service life of unshrouded turbine blade tips.

This thesis presents a combined experimental and computational study of cooled and uncooled tips at engine-representative aerodynamic conditions. A high speed linear cascade was employed for the experimental side, which was overhauled for improved measurement of film cooling effectiveness via implementation of the pressure sensitive paint technique. To the author's knowledge, this is the first time this technique has been used to measure film cooling effectiveness on blade tips in a high speed linear cascade.

The aero-thermal performance of a series of uncooled tips was tested experimentally and the study expanded on computationally. Tip heat transfer coefficient was shown to be determined by the local behaviour of the overtip leakage flow and exhibited a strong dependence on the tip geometry and tip clearance. At increased tip clearance, aerodynamic losses were enhanced, whereas the heat transfer coefficient reduced on the rims but increased in the tip cavity; a common behaviour for all tips tested due to the generalised flow field. Results indicated the relative advantage of using a winglet tip for aerodynamic performance and a suction side cut-back squealer tip for improved thermal performance at the tip trailing edge. The effects of casing motion were also investigated computationally. The casing motion induces a cavity vortex which increased the local heat transfer coefficient, however there was no effect on the pressure side rim.

The impact of film cooling on two transonic squealer tips was examined experimentally, showing a dependence of the film cooling effectiveness and heat transfer coefficient on both the tip clearance and coolant mass flow rate. To the author's knowledge this study is a first of its kind examining these factors. Coolant injection was shown to locally enhance tip heat transfer coefficients, however areas of high film effectiveness on the pressure side squealer rim coincide strongly with a net heat flux reduction and with low heat transfer coefficient due to blockage by the coolant. Comparison of the two squealer designs showed improved cooling performance by a suction side cut-back squealer due to careful placement and angling of the pressure side near-tip film holes. Numerical methods showed strong interactions of film coolant and the overtip leakage flow producing vortical flow structures. Higher film effectiveness levels were gained from the use of larger diameter dust holes due, in part, to the behaviour of the coolant jet.

Acknowledgements

My first thanks go to my supervisor, Professor Peter Ireland, for his support and kind agreement to include me as one of his charges under difficult circumstances. His enthusiasm is infectious and he helped me to be ambitious, achieving more during my DPhil than I thought possible.

Thanks must also go to Dr John Coull, for his guidance and friendship over the last two years. I learned a great many things from him on how to approach and solve problems surrounding experimental rigs. He challenged me on a regular basis and I know that the outcomes of my research are vastly improved because of it.

Further thanks must also go to Professor Li He for his guidance over the first two years of my DPhil. Also, to my examiners, Professor Budimir Rosic and Dr Grant Ingram for their genuine interest in my work and thoughtful discussion during the viva. And, thanks for the nudge Grant!

I am also thankful for the support (both financial and otherwise) of Rolls-Royce plc, in particular Haidong Li and Ed Romero. Without their input and collaboration none of this would have been possible. I am also grateful to the EPSRC for the financial support.

I am eternally grateful for my fellow researchers in the Osney lab for their advice and support. In particular, Andrew D, James T, Brian T, Holt, Rob P, Niharika, Pete F, Joao, Alex M and Nick H. Thank you also to the team of dedicated technicians who helped with rig development and maintenance. Jason, Bill, Hal, Duncan, Dave M, Harry, Gerald, Trevor, Greg and Paul C, your contributions are invaluable.

To the many rowers I have had the pleasure of training and racing alongside at OULRC and PCBC, thank you for making my time here thoroughly enjoyable and rewarding. Many of my unforgettable moments at Oxford come from our time together. It was a unique experience and one I wish I could repeat.

My family also deserve my eternal gratitude for their unwavering love, support and encouragement which has helped me immensely along the way. Mum, Dad, Kathryn, Carole, Michael, Sue, Susan and Brian, despite living far away you are always there to be relied upon and I thank you. I must also thank my future family-in-law for providing support closer to home during my time in Oxford and always reminding me of the bigger picture.

Last but by no means least, to my love, Sarah. I can't put into words how much your love, support and confidence in me over the last 4 and a bit years (and the rest!) has meant to me. You always managed to believe in me, even when I could not. Without you, I could not have done any of this. I only hope that I can provide the same kind of comfort to you throughout our life together.

Dedication

For those about to rock...

Contents

1 Introduction **1**
- 1.1 Background of the Gas Turbine Engine . . . 1
- 1.2 Developments in High Pressure Turbine Blade Tip Technology . . . 4
- 1.3 Motivation for Current Research . . . 7
- 1.4 Aims and Objectives . . . 8
- 1.5 Thesis Structure . . . 9

2 Literature Review **11**
- 2.1 Introduction . . . 11
- 2.2 Axial Turbine Flow . . . 11
  - 2.2.1 Loss Mechanisms in a Rotor Passage . . . 14
  - 2.2.2 Mechanisms for Tip Heat Transfer . . . 16
- 2.3 Tip Leakage and Aerodynamic Loss . . . 18
  - 2.3.1 Low Speed Cascade Studies . . . 18
  - 2.3.2 High Speed Linear Cascade Studies . . . 21
  - 2.3.3 Rotor Studies . . . 22
  - 2.3.4 CFD Studies . . . 24
  - 2.3.5 Aerodynamic Loss Measurement Techniques . . . 26
- 2.4 Tip Heat Transfer . . . 27
  - 2.4.1 Low Speed Cascade Studies . . . 27
  - 2.4.2 High Speed Linear Cascade Studies . . . 29
  - 2.4.3 Rotor Studies . . . 31
  - 2.4.4 CFD Studies . . . 32
  - 2.4.5 Heat Transfer Measurement Techniques . . . 34
- 2.5 Film Cooling . . . 36
  - 2.5.1 Low Speed Cascade Studies . . . 37
  - 2.5.2 High Speed Linear Cascade Studies . . . 39
  - 2.5.3 Rotor Studies . . . 40
  - 2.5.4 CFD Studies . . . 41
  - 2.5.5 Film Effectiveness Measurement Techniques . . . 44
- 2.6 Summary . . . 45

3 High Speed Linear Cascade and Experimental Techniques **47**
- 3.1 Introduction . . . 47
- 3.2 High Speed Linear Cascade Overview . . . 47
- 3.3 Modifications to the Rig . . . 51
  - 3.3.1 Heater Mesh . . . 51

3.3.2 Inlet Turbulence Grid . . . 53
3.3.3 Coolant Feed System . . . 54
3.3.3.1 Blade Root and Base Plate . . . 55
3.3.3.2 Control Systems and Pipework . . . 57
3.4 Heat Transfer Coefficient Measurements . . . 59
3.4.1 Equipment and Methodology . . . 59
3.4.2 Analysis Techniques . . . 64
3.4.3 Uncertainty Analysis . . . 68
3.5 Aerodynamic Loss Measurements . . . 71
3.5.1 Equipment and Methodology . . . 71
3.5.2 Three-Hole Probe Calibration and Analysis Techniques . . . 74
3.5.3 Periodicity in the HSLC . . . 78
3.6 Cooling Effectiveness Measurements . . . 81
3.6.1 Equipment and Methodology . . . 81
3.6.2 Theory and Analysis Techniques . . . 83
3.6.3 Temperature Sensitivity of Pressure Sensitive Paint . . . 87
3.6.4 Photo-degradation of Pressure Sensitive Paint . . . 90
3.6.5 Pressure Sensitive Paint Calibration . . . 92
3.6.6 Uncertainty Analysis . . . 96
3.7 Summary . . . 100

4 Computational Fluid Dynamics Methods 102
4.1 Introduction . . . 102
4.2 CFD Theory . . . 102
4.2.1 The Navier-Stokes Equations . . . 103
4.2.2 Discretisation of the Navier-Stokes Equations . . . 104
4.2.2.1 Finite Volume Method . . . 104
4.2.3 Temporal Solution Schemes . . . 106
4.2.4 Reynolds Averaged Navier-Stokes (RANS) . . . 108
4.2.5 Turbulence Modelling . . . 109
4.3 HYDRA CFD Flow Solver . . . 110
4.4 Computational Domain and Meshing . . . 111
4.4.1 Boundary and Initial Conditions . . . 112
4.5 Mesh Independence Study and Convergence . . . 113
4.6 Film Cooling Methodology . . . 115
4.6.1 HYDRA Source Term Modelling . . . 115
4.6.2 Fully Resolved . . . 116
4.7 CFD Aerothermal and Cooling Performance Parameters . . . 117
4.7.1 Aerothermal Performance . . . 117
4.7.2 Film Cooling Effectiveness . . . 118
4.8 Summary . . . 118

5 Baseline Squealer Tip 120
5.1 Introduction . . . 120
5.2 Accompanying CFD . . . 121
5.3 Blade Tip Geometries . . . 121
5.4 Uncooled Tip . . . 122

5.4.1 Mark I and Mark II Geometry . . . 122
5.4.2 Influence of Tip Clearance . . . 123
5.4.3 Pressure Side Rim Edge Radius and Cavity Depth . . . 127
5.4.4 Casing Motion Consideration . . . 128
5.5 Cooled Tips . . . 129
5.5.1 Comparison of Uncooled and Cooled Tips . . . 129
5.5.2 Influence of Coolant Mass Flow Rate . . . 131
5.5.3 Influence of Tips Clearance . . . 132
5.6 Implications for a Real Engine . . . 134
5.7 Summary . . . 136

6 Experimental Comparison of Uncooled Tip Geometries 138
6.1 Introduction . . . 138
6.2 Uncooled Tip Geometries . . . 139
6.3 Heat Transfer . . . 140
6.3.1 Comparison of Tip Geometries . . . 141
6.3.2 Influence of Tip Clearance . . . 146
6.4 Aerodynamic Loss . . . 148
6.4.1 Comparison of Tip Geometries . . . 149
6.4.2 Influence of Tip Clearance . . . 151
6.5 Summary . . . 153

7 Experimental Comparison of Cooled Tips 156
7.1 Introduction . . . 156
7.2 The Cooled Suction Side Cut-Back Tip . . . 156
7.3 Comparison of the Uncooled and Cooled Tip . . . 157
7.4 Comparison of the Cooled Tip Geometries . . . 159
7.4.1 Influence of Coolant Mass Flow Rate . . . 164
7.4.2 Influence of Tip Clearance . . . 167
7.5 Summary . . . 172

8 Tip Geometry CFD Study 176
8.1 Introduction . . . 176
8.2 Tip Models in Study . . . 176
8.3 Validation of CFD . . . 177
8.3.1 Heat Transfer . . . 178
8.3.2 Aerodynamic Loss . . . 180
8.3.3 Blade Loading . . . 181
8.4 Stationary Casing . . . 182
8.4.1 Heat Transfer . . . 182
8.4.2 Aerodynamic Loss . . . 187
8.4.3 Tip Clearance . . . 191
8.4.3.1 Heat Transfer . . . 191
8.4.3.2 Aerodynamic Loss . . . 193
8.5 Moving Casing . . . 195
8.5.1 Heat Transfer . . . 195
8.5.2 Aerodynamic Loss . . . 199

8.6 Summary and Conclusions 202

9 Influence of Tip Cooling CFD Study 204
9.1 Introduction 204
9.2 The Cooled CFD Tip Geometry 204
9.3 Validation of Cooled CFD 205
9.3.1 Heat Transfer 205
9.3.2 Adiabatic Film Cooling Effectiveness 207
9.4 Coolant Mass Flow 211
9.4.1 Film Cooling Effectiveness 211
9.5 Cooling Hole Size 213
9.5.1 Film Cooling Effectiveness and Coolant-OTL Flow Interactions . 213
9.5.2 Heat Transfer Coefficient 219
9.6 Cooling Hole Location 221
9.6.1 Heat Transfer and Film Cooling Effectiveness 221
9.7 Effect of Alternative Turbulence Models 226
9.7.1 Theory of the $k-\omega$ SST Model 226
9.7.2 Film Cooling Effectiveness 227
9.8 Summary and Conclusions 228

10 Summary, Conclusions and Recommendations 230
10.1 Introduction 230
10.2 Uncooled Tip Heat Transfer 231
10.3 Tip Film Cooling 233
10.4 Aerodynamic Loss 235
10.5 Recommendations for Future Work 236

Bibliography 239

List of Figures

1.1 Cutaway of the Trent XWB high bypass turbofan. (Courtesy of the Rolls-Royce website) . . . 3
1.2 Trends in turbofan design. (Reproduced from Rolls-Royce (2005)) . . . 4
1.3 Examples of shrouded and unshrouded tips (Reproduced from Bunker (2001)) . . . 5
1.4 Common unshrouded tip designs . . . 6

2.1 Tip leakage vortices and secondary flows in a rotor passage with tip clearance. (Reproduced from Yamamoto (1988)) . . . 12
2.2 Tip leakage flow for an unshrouded blade. (Reproduced from Denton (1993)) . . . 13
2.3 Change in tip clearance flow regime. (Reproduced from Moore *et al.* (1989)) 14
2.4 Typical tip leakage secondary and flows in a rotor passage. (Reproduced from Yamamoto (1989)) . . . 15
2.5 Heat transfer coefficient on a flat tip at low speed. (Reproduced from Bunker *et al.* (1999)) . . . 17
2.6 Tip Nusselt number at high speed and low speed flow conditions. (Reproduced from O'Dowd (2010)) . . . 18
2.7 Loss mechanisms downstream of a rotor. (Reproduced from Payne *et al.* (2003)) . . . 23
2.8 Mid tip gap Mach number for a flat tip at high speed flow conditions. (Reproduced from Zhang *et al.* (2011b)) . . . 34
2.9 Schematic of a modern cooled gas turbine blade. (Reproduced from Kwak & Han (2003)) . . . 36

3.1 The Oxford University High Speed Linear Cascade . . . 48
3.2 Schematic of the High Speed Linear Cascade. From Zhang (2007a) . . . 48
3.3 HSLC test section . . . 49
3.4 Data acquisition and calibration hardware . . . 50
3.5 Examples of heater mesh failure . . . 53
3.6 Inlet turbulence grid . . . 54
3.7 Components of the coolant feed system inside the HSLC . . . 56
3.8 HSLC coolant system . . . 58
3.9 IR thermography set-up for heat transfer testing . . . 60
3.10 IR windows used during heat transfer testing . . . 61
3.11 Location of tip surface thermocouple for calibration . . . 62
3.12 Example of IR in-situ calibration . . . 62

3.13 Example of pressure setpoint interpolation and resulting inlet pressure profile for a transient heat transfer test . . . 63
3.14 Example regression plot of heat flux versus tip surface temperature for a single location during transient period . . . 68
3.15 Experimental set-up for aerodynamic loss measurements . . . 72
3.16 Inlet pressure profile during a typical aerodynamic loss conditions test . . 73
3.17 Application matrices for yaw, Mach and total pressure coefficient . . . 75
3.18 Mach number plotted against Mach coefficient from the application matrix (all calibration data) . . . 76
3.19 Full pitchwise traverses at 50% axial chord downstream. Dashed black lines denoted chosen test pitch . . . 79
3.20 Full pitchwise traverses at 50% axial chord downstream. Dashed black lines denoted chosen test pitch . . . 79
3.21 Approximate location of traverse planes, showing paths of blade wakes and overtip leakage flows . . . 80
3.22 Experimental set-up for PSP testing . . . 82
3.23 Flow chart outlining the PSP measurement and analysis procedure . . . 83
3.24 Example calibration plot of image intensity ratio against partial pressure ratio for PSP testing . . . 84
3.25 Heat/mass transfer analogy for measurement of film cooling effectiveness. (Reproduced from Han & Rallabandi (2010)). . . . 85
3.26 Metal tip surface thermocouple locations and cross-section schematic . . 88
3.27 Circumferentially averaged film cooling effectiveness for example cases with and without temperature correction method. (x represents the x-axis of the raw camera image) . . . 88
3.28 Steps through IR temperature correction method . . . 89
3.29 Reference intensity over time showing warm-up of lights and linear reduction in intensity due to photo-degradation and ambient temperature increase . . . 91
3.30 Photos of the calibration rig for pressure sensitive paint calibration . . . 93
3.31 Calibration data plots showing impact of PSP temperature sensitivity . . 94
3.32 Comparison of calibration curves with range of calibrations and typical variance . . . 95
3.33 The effect of the alternative PSP calibration on the film effectiveness . . 96
3.34 Uncertainty in absolute film effectiveness at a range of film effectiveness values . . . 99

4.1 CFD domain and example multi-block mesh structure . . . 111
4.2 Mesh independence analysis for the CFD PS cut-back squealer tip . . . 113
4.3 Mesh independence analysis for the hypothetical tip geometry . . . 114
4.4 Example HYDRA convergence history (note iterations on coarser grid levels at start) . . . 115
4.5 Location of dust hole and coolant direction for source term modelling. (From HYDRA jm52) . . . 116
4.6 Cooling hole CAD and mesh . . . 117

5.1 Squealer tip geometry tested . . . 122

5.2 Experimental uncooled tip HTC $[W/m^2K]$ - as-printed Mark I geometry with slight PS rim edge rounding . . . 124
5.3 Experimental uncooled tip HTC $[W/m^2K]$ - Machined Mark II geometry with sharp PS rim edge (cooled geometry with cooing holes blocked) . . 124
5.4 CFD uncooled tip HTC $[W/m^2K]$ - for comparison to Mark II geometry 124
5.5 CFD predictions of Mach for the uncooled squealer tip at 0.65% and 1.15% g/S: (a),(d) at mid tip gap plane, the blue line denotes $M = 1$ and black lines denote the cut-plane locations; (b),(c),(e),(f) at three cut planes perpendicular to the tip surface. Streamlines shown in grey. 125
5.6 Tip flow mechanisms for a sharp and rounded pressure side rim edge at different tip gaps (high HTC region in red) . . . 127
5.7 CFD uncooled tip HTC $[W/m^2K]$ with casing motion . . . 128
5.8 Experimental cooled tip HTC $[W/m^2K]$ and η contours at 0.65% tip gap and two coolant mass flow rates . . . 131
5.9 Experimental cooled tip HTC $[W/m^2K]$ and η contours at 1.15% tip gap and two coolant mass flow rates . . . 131
5.10 NHFR for the 0.65% g/S tip gap . . . 135

6.1 CAD renderings of the three uncooled tip geometries reported in this chapter . . . 139
6.2 Experimental heat transfer coefficients $[W/m^2K]$ at g/S = 0.65% . . . 143
6.3 Experimental heat transfer coefficients $[W/m^2K]$ at g/S = 1.15% . . . 143
6.4 Circumferentially averaged heat transfer coefficient $[W/m^2K]$ for the uncooled tip geometries at both tip gaps . . . 144
6.5 Experimental total pressure loss coefficient, Y_{P0}, for the baseline squealer tip at 50% C_{ax} downstream . . . 150
6.6 Experimental total pressure loss coefficient, Y_{P0}, for the cavity-winglet tip at 50% C_{ax} downstream . . . 150
6.7 Experimental total pressure loss coefficient, Y_{P0}, for the PS cut-back tip at 50% C_{ax} downstream . . . 150
6.8 Experimental total pressure loss coefficient, Y_{P0}, for the SS cut-back tip at 50% C_{ax} downstream . . . 150
6.9 Experimental mass averaged total pressure loss coefficients at both tip clearances . . . 152

7.1 CAD renderings of the cooled squealer tip geometries . . . 157
7.2 Experimental uncooled heat transfer coefficients $[W/m^2K]$ for the unmodified suction side cut-back tip . . . 158
7.3 Cooled HTC $[W/m^2K]$ (left) and η (right) contours at 0.65% tip gap and two coolant mass flow rates for the suction side cut-back tip . . . 160
7.4 Top view and section view perpendicular to blade pressure surface showing difference in cooling hole angles near tip trailing and suspected coolant flow . . . 162
7.5 Circumferentially averaged HTC and η of the two cooled blade tips at g/s = 0.65% with nominal coolant mas flow rate . . . 163
7.6 Change in cooled HTC $[W/m^2K]$ (left) and η (right) with increased coolant mass flow rate at both tip clearance heights (HTC is normalised by maximum change in HTC) . . . 165

7.7 Circumferentially averaged HTC and FCE comparing relative performance of the two cooled blade tips at two coolant mass flow rates and 0.65% g/S tip gap . . . 166
7.8 Cooled HTC $[W/m^2K]$ (left) and η (right) contours at 1.15% tip gap and two coolant mass flow rates for the suction side cut-back tip . . . 168
7.9 Change in cooled HTC $[W/m^2K]$ (left) and η (right) with increased tip clearance at both coolant mass flow rates (HTC is normalised by maximum change in HTC) . . . 169
7.10 Circumferentially averaged HTC and η for the two cooled blade tips at both tip gaps and the nominal coolant mass flow rate . . . 170
7.11 Circumferentially averaged HTC and η for the two cooled blade tips at both tip gaps and 150% nominal coolant mass flow rate . . . 171

8.1 Tip geometries used in the CFD geometry study . . . 177
8.2 Experimental and computational heat transfer coefficients (W/m^2K) measured on the hypothetical geometry at 0.65% g/S . . . 178
8.3 Circumferentially averaged heat transfer coefficient (W/m^2K) for the hypothetical tip, both experimental and CFD cases . . . 178
8.4 Experimental heat transfer coefficients (W/m^2K) measured on the PS cut-back tip at 0.65% and 1.15% g/S (HSLC) . . . 179
8.5 Computational heat transfer coefficients (W/m^2K) measured on the hypothetical geometry at 0.65% and 1.15% g/S (HYDRA) . . . 179
8.6 Experimental total pressure loss coefficient Y_{P0} measured on a plane 50% C_{ax} downstream for the PS cut-back tip (variation 2) at 0.65% and 1.15% g/S(HSLC) . . . 180
8.7 Computational total pressure loss coefficient Y_{P0} measured on a plane 50% C_{ax} downstream for the PS cut-back tip (variation 2) at 0.65% and 1.15% g/S (HYDRA) . . . 180
8.8 Mass averaged total pressure loss coefficient Y_{P0} at the 50% C_{ax} downstream plane for the PS cut-back tip at 0.65% and 1.15% g/S tip gaps (HSLC and HYDRA) . . . 181
8.9 Blade mid-span isentropic Mach number . . . 182
8.10 Computational tip heat transfer coefficients (W/m^2K) for a range of tip geometries at 1% g/S (HYDRA) . . . 183
8.11 OTL flow field for the closed squealer tip (HYDRA) . . . 184
8.12 Contours of surface static pressure and Mach streamlines . . . 184
8.13 Circumferentially averaged heat transfer coefficients (W/m^2K) for the CFD tip geometries at 1.0% g/S tip gap (HYDRA) . . . 186
8.14 Computational total pressure loss coefficient Y_{P0} measured at 50% and 100% C_{ax} downstream for the closed squealer tip at 1% g/S (HYDRA) . 188
8.15 Computational total pressure loss coefficient Y_{P0} measured at 50% and 100% C_{ax} downstream for the PS cut-back geometry 1 at 1% g/S (HYDRA) 188
8.16 Computational total pressure loss coefficient Y_{P0} measured at 50% and 100% C_{ax} downstream for PS cut-back geometry 2 at 1% g/S (HYDRA) 188
8.17 Computational total pressure loss coefficient Y_{P0} measured at 50% and 100% C_{ax} downstream for PS cut-back geometry 3 at 1% g/S (HYDRA) 188

8.18 Computational total pressure loss coefficient Y_{P0} measured at 50% and 100% C_{ax} downstream for the hypothetical geometry at 1% g/S (HYDRA) 188
8.19 Streamlines of Mach number (range $M = 0 - 1.4$) showing source of loss features at 50% and 100% axial planes. Plane shows total pressure (HYDRA) . . . 189
8.20 Mass averaged total pressure loss coefficient Y_{P0} at 50% and 100% C_{ax} downstream for the CFD tip geometries (HYDRA). In (a) the dotted lines represent 50% C_{ax} and solid lines 100% C_{ax} . . . 190
8.21 Area averaged heat transfer coefficient on the upper surfaces of the squealer rims and cavity for all CFD tip designs (HYDRA) . . . 192
8.22 Computational tip heat transfer coefficients (W/m^2K) for a range of tip geometries at 0.5% g/S (HYDRA) . . . 192
8.23 Circumferentially averaged heat transfer coefficients (W/m^2K) for each tip designs at 0.5% (dotted lines) and 1.0% g/S (solid lines) tip gaps. . . 192
8.24 Computational total pressure loss coefficient Y_{P0} measured at 0.5% g/S tip gap and 100% C_{ax} downstream plane (HYDRA) . . . 194
8.25 Mass averaged total pressure loss coefficient Y_{P0} at 0.5% g/S and 1.0% g/S tip gaps and 100% C_{ax} downstream for the CFD tip geometries (HYDRA). In (a) the dotted lines represent 0.5% g/S and solid lines 1.0% g/S . . . 194
8.26 Computational tip heat transfer coefficients (W/m^2K) for a range of tip geometries at 1.0% g/S with relative casing motion (HYDRA) . . . 196
8.27 Overtip leakage flow for the hypothetical tip with and without casing motion. (a), (b) streamlines of Mach number and contours of static pressure, (c), (d) velocity streamlines and Mach number contours (Note: orientation flipped) (HYDRA) . . . 197
8.28 Overtip leakage flow for the PS cut-back geometry 3 with and without casing motion showing velocity streamlines and Mach number contours (HYDRA) . . . 198
8.29 Averaged heat transfer coefficients (W/m^2K) for all tip designs at 1.0% g/S (HYDRA) . . . 199
8.30 Computational total pressure loss coefficient Y_{P0} measured at 1.0% g/S tip gap and 100% C_{ax} downstream plane with casing motion(HYDRA) . 200
8.31 Mach number streamlines showing source of loss features for the hypothetical tip with a stationary and moving casing (HYDRA) . . . 200
8.32 Mass averaged total pressure loss coefficient Y_{P0} at 1.0% g/S tip gap and 100% C_{ax} downstream for the CFD tip geometries with stationary and moving casing (HYDRA). In (a) the solid lines represent a stationary casing and dot-dash lines a moving casing . . . 201

9.1 Experimental and computational heat transfer coefficients (W/m^2K) measured on the cooled hypothetical tip geometry at 0.65% g/S . . . 206
9.2 Circumferentially averaged heat transfer coefficient (W/m^2K) for the cooled hypothetical tip, both experimental and CFD cases ($T_{cool} = 298K$) 206
9.3 Experimental and computational film cooling effectiveness measured on the cooled hypothetical tip geometry at 0.65% g/S . . . 208

9.4 Predicted coolant-OTL interactions for the hypothetical tip at low coolant temperature (147K) and experimental coolant temperature (298K) (HYDRA) . . . 209
9.5 Predicted η on the cooled hypothetical tip geometry for a range of coolant to mainstream pressure ratios at 0.5% g/S tip gap. Dust hole size = 0.9 mm, CTR = 0.5 (HYDRA) . . . 212
9.6 Streamlines of coolant and OTL flow for 0.9 mm cooling hole diameter and two CPRs. CTR = 0.5 (HYDRA) . . . 212
9.7 Predicted film cooling effectiveness on the cooled hypothetical tip geometry for a range of coolant hole diameters at constant CPR and 0.5% g/S tip gap (HYDRA) . . . 214
9.8 Streamlines of coolant and OTL flow for 1.2mm and 2.5mm cooling hole sizes (HYDRA) . . . 216
9.9 Predicted HTC $[W/m^2K]$ on the cooled hypothetical tip geometry for a range of coolant hole diameters at constant CPR, CTR = 0.5 and 0.5% g/S tip gap (HYDRA) . . . 218
9.10 Streamlines of uncooled and cooled tip with 2.5 mm dust hole diameter, contours of tip surface static pressure (HYDRA) . . . 219
9.11 Net Heat Flux Reduction for cooled cases with a 2.5 mm dust hole and a 1.2 mm dust hole at increased mass flow (HYDRA) . . . 220
9.12 Predicted HTC $[W/m^2K]$, film effectiveness and flow streamlines (coloured by temperature) on the cooled hypothetical tip geometry with various upstream dust hole locations at $\dot{m}_{cool} = 1.46 \times 10^{-3} kg/s$ and CTR = 0.5. Source term cooled (HYDRA) . . . 222
9.13 Predicted HTC $[W/m^2K]$, film effectiveness and flow streamlines (coloured by temperature) on the cooled hypothetical tip geometry with a LE dust hole, source term and fully resolved methods (HYDRA) . . . 224
9.14 Film cooling effectiveness predicted using SA and $k-\omega$ SST turbulence models (HYDRA) . . . 227

List of Tables

3.1 HSLC Geometry 50
3.2 HSLC Nominal Operating Conditions 51
3.3 HSLC coolant system capacity and coolant distribution (all per blade tip) 59
3.4 X5 PID controller settings for transient heat transfer testing 63
3.5 Absolute Uncertainty in calibrated wall temperature, T_w, due to various factors 70
3.6 Uncertainty in heat transfer coefficient, h, for both IR cameras as a percentage of mean original result 71
3.7 X5 PID controller settings for aerodynamic loss testing 73
3.8 Three-hole probe uncertainty values (From O'Dowd (2010)) 78
3.9 Uncertainty contributions to the overall film effectiveness uncertainty (absolute values) 99

5.1 Description of uncooled tip variations and mean tip heat transfer coefficients 122

6.1 Cavity depth of the uncooled tip geometries 139
6.2 Approximate HTC levels in specific regions marked in Figure 6.2. Region of peak HTC on each tip indicated in red. The tip showing the highest HTC levels in each region (and tip gap) shown in **bold**. 143

8.1 Mean tip heat transfer coefficients (W/m^2K) 179

9.1 Cooled tip geometry parameters 205
9.2 Coolant parameters for experimental and CFD validation cases 208
9.3 Coolant parameters for CFD cases at a range of pressure ratios with a 0.9 mm diameter dust hole, measured at hole exit 211
9.4 Coolant parameters for CFD cases at a range of cooling hole diameters, measured at hole exit 214

Nomenclature

Latin

Symbol	Description	Units
C	Concentration	
	or mass fraction	
C_{ax}	Blade axial chord	[m]
C_β	Probe yaw angle calibration coefficient	
C_M	Probe Mach number calibration coefficient	
C_p	Specific heat capacity	[Jkg^{-1} K]
e	Internal fluid energy	
C_T	Probe total pressure calibration coefficient	
D	Mass diffusion coefficient	[m^{2}s$^-$1]
G	Mass Flux	
Ge	Germanium	
g	Tip gap	[m]
h	Heat transfer coefficient	[Wm^{-2}K^{-1}]
$h[n], H(z)$	Discrete impulse response function	
I	Current	[Amps, A]
	or Image intensity	
k	Thermal conductivity	[Wm^{-1}K^{-1}]
	or summation variable	
Le_T	Turbulent Lewis Number	
M	Mach number	
m	Total number of readings	
$\dot{m}$	mass flow rate	[kgs^{-1}]
N	Number of data points	
n	Integration variable	
	or sample number	
N_2	Nitrogen	
O_2	Oxygen	
P	Pressure	[Pa]
	or Power	[W]
$\dot{q}$	Heat flux	[Wm^{-2}]
R	Resistance	[Ohms, Ω]
	or gas constant	[Jkg^{-1}K^{-1}]
	or span-wise radial distance	[m]
S	Blade span	[m]
S_M, S_e, S_ϕ	Source terms for momentum, energy and general property	
T	Temperature	[K] or [^{o}C]
t	Time	[s]
u, v, w	Velocity components in coordinate directions	
$\boldsymbol{V}$	Velocity vector	
V	Voltage	[Volts, V]
x	Axial position	

	or in direction of camera x-axis
Y_{P0}	Total pressure loss coefficient
y	Pitch position
$ZnSe$	Zinc Selenide

Greek

Symbol	Description	Units
α	Thermal diffusivity	$[\mathrm{m^2 s^{-1}}]$
β	Yaw angle	$[^o]$
Γ	Diffusion coefficient	
γ	Ratio of specific heats	
δ	Uncertainty	
$\Delta(z)$, $\delta[n]$	Discrete impulse function	
δ_f	Thickness of film	[m]
η	Adiabatic film cooling effectiveness	
ϵ_T	Turbulent thermal diffusivity	
ϵ_M	Turbulent mass diffusivity	
μ	Dynamic viscosity	$[kgm^{-1}s^{-1}]$
ν	Kinematic viscosity	$[m^2s^{-1}]$
Φ	Dissipation function	
ϕ	General property of fluid	
ρ	Density	$[kgm^{-3}]$
σ	Standard deviation	
τ	Sampling time interval	[s]

Subscripts

Symbol	Description
0	Exit total
01	Inlet total
2	Exit static
∞	Mainstream
A, B, C	Left, right and centre holes of the three-hole probe
ad	Adiabatic
air	Air as coolant
alt	Alternative
avg	Average
aw	Adiabatic wall
b	Dark
$c, cool$	Cooled tip *or* Coolant gas
$calc$	Calculated
$calib$	Calibration
cam	IR Camera

eng	Engine conditions
$exit$	Exit condition
f	Coolant film
fg	Foreign gas
i	Initial time
L	Pixel location of surface thermocouple
$meas$	Measured
min	Minimum
N_2	Nitrogen (Oxygen free) as coolant
O_2	Oxygen
rat	Ratio
rec	Recovery temperature
ref	Reference conditions
rig	Rig conditions
$se, wall$	Reference static
$surf$	Blade surface
tc	Thermocouple
$tempcorr$	Temperature correction used
$timecorr$	Photo-degradation correction used
$uc, uncool$	Uncooled tip
$uncorr$	Raw images
w	Wall

Abbreviations

1D	One-dimensional
2D	Two-dimensional
3D	Three-dimensional
BR	Coolant blowing ratio
CAD	Computer aided design
CCD	Charge-coupled device
CFD	Computational fluid dynamics
CNC	Computer numerical control
CPR	Coolant to mainstream pressure ratio
CTR	Coolant to mainstream temperature ratio
DAQ	Data acquisition
DLC	Diamond-like-carbon
DMLS	Direct metal laser sintering
FIB	Fluoro / Isopropyl / Butyl
HP	High pressure
HSLC	High Speed Linear Cascade
HTC	Heat transfer coefficient
IR	Infrared
LE	Leading Edge
LED	Light emitting diode
LES	Large eddy simulation
MFC	Mass Flow Controller

NHFR	Net Heat Flux Reduction
OFN	Oxygen free nitrogen
OTL	Overtip leakage flow
PID	Proportional-integral-derivative
PIV	Particle image velocimetry
PSP	Pressure sensitive paint
PS	Pressure side
PtTFPP	Platinum Tetra(Pentafluorophenyl)Porphine
RANS	Reynolds-averaged Navier Stokes
RMS	Root-mean-square
RSS	Root-sum-square
SA	Spalart-Allmaras
SFC	Specific fuel consumption
SS	Suction side
SST	Shear stress transport
TE	Trailing edge
TET	Turbine entry temperature
VKI	von Karman Institute

Chapter 1

Introduction

This thesis presents an experimental and computational study of unshrouded high pressure (HP) turbine blade tips at engine-representative aerodynamic conditions, both with and without film cooling. The main tip geometry considered is of the common squealer type, which although well reviewed in literature in low speed flows, lacks studies at engine-representative aerodynamic conditions which are vital to capture the realistic, transonic overtip leakage flows; there are even fewer studies in open literature which consider cooled transonic squealer tips. This thesis addresses these gaps in the literature and aims to improve the understanding of the transonic tip design space and tip film cooling capability. The effect of aspects such as the tip geometry variation, tip clearance and coolant mass flow rate on the aerodynamic, thermal and film cooling performance of the blade tip are evaluated throughout.

This chapter provides a brief history and general background on the gas turbine engine, along with recent trends in HP turbine design. The context and motivations for the current research are then described, followed by the aims and objectives of the present work. The final section lays out the structure of this thesis chapter by chapter.

1.1 Background of the Gas Turbine Engine

The birth of the jet engine can be traced back to three men in three different countries. Sir Frank Whittle is credited with the invention of the turbojet, filing a British patent in 1930 and developing the Power Jets WU design which powered a Gloster E.28/29

to it's maiden flight on 15^{th} May 1941. Several years later than Whittle's patent, in 1936, Hans von Ohain independently filed a patent in Germany for his own design of the turbojet, with the first operational flight of Ohain's design coming in 1939 aboard a Heinkel He 178, two years prior to Whittle. However, the very first patent filed for a turbojet was filed almost a decade before Whittle, in France in 1921, but this design was never made due to the technical capabiliteis of the time. Other turbine engine designs, which were all proposed around the same time as the turbojet include turboprops and turbofans. However, the requirement of fast, agile aircraft during World War II kept the focus on the simpler turbojets for many years, with turbofans being outside the current technological capabilities.

In the years following the end of the war, with the birth of the civil aviation industry, turbojets have been used on many civil aircraft. Arguably the most famous of these passenger aircraft was Concorde which was powered by four Rolls-Royce Olympus 593 engines and capable of sustained Mach 2 flight. However, the retirement of Concorde in 2003 heralded the end of the turbojet in civil aviation, as the primary design consideration for civil engines shifted to a reduction in specific fuel consumption (SFC) and weight. To give an indication of the importance of saving fuel, in a modern airline, an estimated 15 - 25% of operating costs can be attributed to jet fuel (Rolls-Royce (2005)), so any increase in efficiency can bring huge gains in profits for the airline.

Turboprops are usually fitted to small, short-range aircraft due to their high efficiency at lower flight speeds. Turbofans on the other hand, have improved efficiency (over turbojets) and are capable of much higher flight speed than turboprops, making them the engine of choice for larger, long-haul aircraft. The first turbofan engine to enter service was the Rolls-Royce Conway which was used in the 1950's and 60's. The idea behind the turbofan was for some of the air to bypass the main core of the engine, producing thrust from a low velocity jet more similar to that of the aircraft, hence improving efficiency. An additional benefit of this design is reduced noise as the high velocity core jet is surrounded by the low velocity bypass flow.

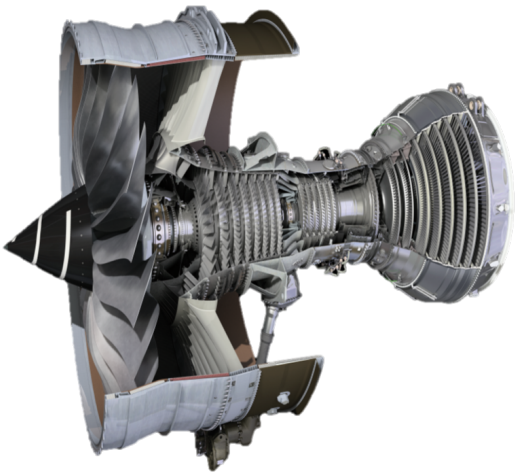
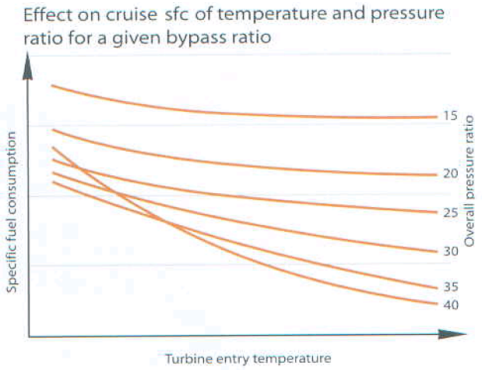


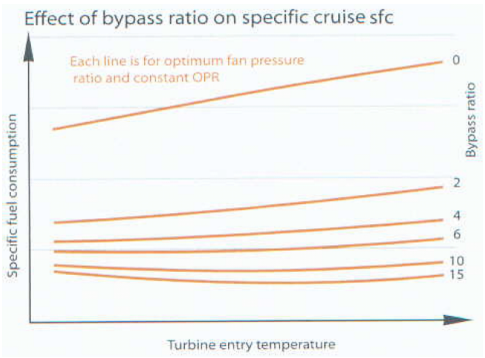
Figure 1.1: Cutaway of the Trent XWB high bypass turbofan. (Courtesy of the Rolls-Royce website)

The development of turbomachinery technology has led to modern high by-pass turbofans with a bypass ratio up to 10:1, such as the Rolls-Royce XWB (shown in Figure 1.1), which produce up to 70% of their thrust through the fan (which is driven by the LP turbine). The large mass flow of air through the large diameter fan is responsible for the proportion of thrust produced. These developments have allowed the scaling back of the engine core, which is now less responsible for producing thrust directly. The resulting compressor, combustion chamber and turbine can be smaller and therefore lighter, with fewer rotating parts. To maximise the performance of the engine core, the pressure ratio and turbine entry temperature (TET) must be increased, which improves the thermal efficiency and specific thrust of the engine respectively. Pressure ratios in modern turbofans reach up to 50:1, with a TET of around $1800 - 1900$ K, several hundred degrees in excess of the blade melting temperature. The impact of this extreme temperature will be discussed in the next section.

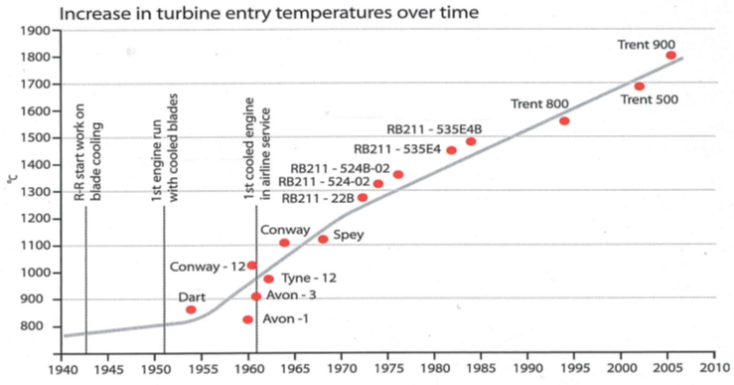
To keep the engine size down, the pressure ratio across each stage can be maximised by increasing the rotational speeds of the turbomachinery, but increased speeds also put extra stress on the rotor disc and blades. Increased pressures result in increased TET, but TET is increased further by the burning of fuel in the combustion chamber. However, there must be a balance between increased fuel use (which raises the TET and power extracted from the turbine) and the specific fuel consumption (SFC). Figure 1.2a



(a) Pressure ratio and TET on SFC



(b) Bypass ratio and TET on SFC



(c) Trend in TET over time

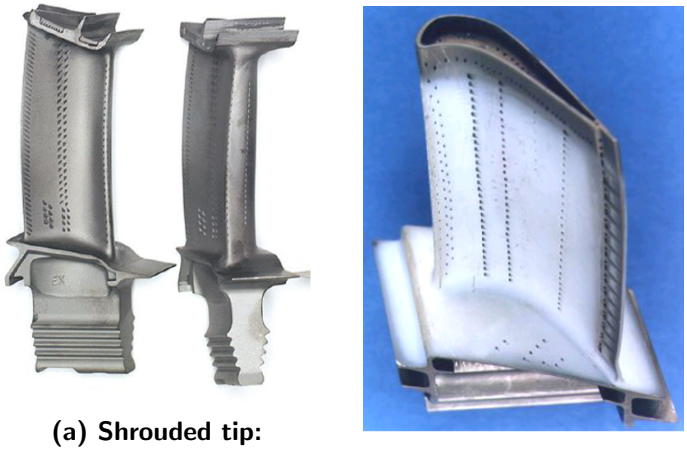
Figure 1.2: Trends in turbofan design. (Reproduced from Rolls-Royce (2005))

shows that at a high pressure ratio, a high TET can also improve SFC.

The trend in turbofan engines is therefore for higher by-pass ratios (see Figure 1.2b), higher rotational speeds and increased TET (see Figure 1.2c), all of which contribute to a reduction in the specific fuel consumption and weight of the engine. These factors not only improve the profits of the airline but in the modern day are helping to reduce the noise and emissions from the engines and drive down the pollution caused by the aviation industry, which is of paramount importance in the public eye.

1.2 Developments in High Pressure Turbine Blade Tip Technology

Civil engine manufacturers have used shrouded high-pressure turbine blades for many years (see Figure 1.3a), as the rotating shroud attached to the blade tip reduces aerody-



(a) Shrouded tip: Rolls-Royce Trent 800 HP turbine blade

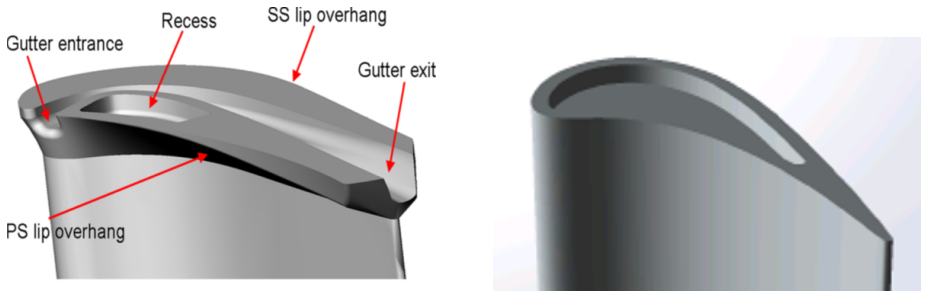
(b) Unshrouded tip: GE HP turbine blade

Figure 1.3: Examples of shrouded and unshrouded tips (Reproduced from Bunker (2001))

namic inefficiencies associated with overtip leakage (OTL) flows. However, as discussed above, the trend in engine development is to increase the TET and the rotational speeds of the rotor disc to produce more powerful and efficient engines. The mass of the rotating shroud limits the blade rotational speed, as it contributes a large portion of the centrifugal stresses on the disc and blades. The solution was to remove the shroud and develop unshrouded blades (see Figure 1.3b) which are lighter, greatly reducing these stresses and permitting higher rotational speeds to be achieved. In addition, the removal of the shroud reduces the overall weight of the engine, which has the potential to improve the efficiency of the engine as a whole. However, these improvements come at a cost of reduced aerothermal efficiency due to the lack of a shroud.

In the unshrouded design, a tip clearance must be maintained between the rotating blade tip and the stationary casing. The pressure difference across the blade tip forces an OTL flow through the tip gap. This OTL flow not only causes a loss of aerodynamic efficiency but also high levels of heat transfer on the tip due to the high temperature and high velocity of the OTL flow, which tends to degrade the tip. This degradation leads to a vicious cycle of larger tip clearances and further tip deterioration.

There have been many advances in the materials used for turbine blades over the past 70 years, now incorporating ceramics, which have allowed engines to operate at a



(a) Winglet tip. (Reproduced from O'Dowd et al. (2012))

(b) Squealer tip. (Reproduced from Virdi (2015))

Figure 1.4: Common unshrouded tip designs

higher TET as required. But these improvements were not enough to keep up with a rapidly expanding civil aviation industry. In the 1960's blade cooling was introduced to allow the turbine to operate at temperatures above the blade material's capability (see Figure 1.2c). It is therefore clear that blade cooling has become exceedingly important, as without it the turbine blades would deteriorate, break apart and cause potentially catastrophic damage downstream in the engine. There are well established methods of cooling the blade pressure and suction surfaces through use of internal cooling passages and external film-cooling. However, the tip region presents a significant challenge and technologies to sufficiently cool the tip are relatively immature.

Even with cooling it is desirable to reduce the OTL flow on a unshrouded tip, thereby increasing the aerodynamic efficiency, reducing tip heat transfer and the cooling requirement for the tip. Such approaches usually focus on variations of common tip designs as shown in Figure 1.4 and include the winglet tip, which acts as a partial shroud, or the squealer tip (also known as a cavity tip) which provides constrictions to the OTL flow path. However, the rims of both of these tip designs are a cause of concern for high heat transfer and difficulty of cooling, as will be discussed further in Chapter 2. Due to the complex nature and high speeds of the OTL flow and lack of accessibility for tip coolant, the blade tip is one of the most vulnerable areas on a turbine blade.

1.3 Motivation for Current Research

A multitude of research assessing the aerothermal and cooling performance of HP turbine tips has already been performed under low speed conditions (see Chapter 2). However, several early studies, for example Moore *et al.* (1989) and Moore & Elward (1993) showed the differences in flow behaviour at higher Mach numbers due to compressible effects. These studies however were overlooked at the time, perhaps due to the difficulties of experimenting at engine-representative Mach and Reynolds numbers.

Engine-representative studies were often done in rotating rigs as these can best capture the tip flow in a real engine. However, these rigs tend to be prohibitively expensive. Recently, authors such as Wheeler *et al.* (2011), Zhang & He (2011) and Zhang *et al.* (2011a) used a combination of a high speed linear cascade and computational fluid dynamics (CFD) to demonstrate that not only were these methods capable of capturing more engine-realistic tip flows but that testing at high speed is a necessity to give a realistic view of tip heat transfer under transonic tip flow. These findings have sparked a new wave of turbine tip research, as an increasing number of authors begin to examine transonic tip flows.

The motivation for the current research is to improve the understanding of the OTL flow and film cooling capability of high pressure turbine blade tips. Only with an in-depth knowledge of the OTL flow and how it interacts with injected coolant under engine-representative aerodynamic conditions can tip designers strive to improve the aerothermal and cooling performance of the blade tip, to improve engine efficiency and prolong the life of an in-service tip.

Currently, as will be explored in Chapter 2, there is still relatively little published research examining turbine tip designs under transonic conditions. The winglet has been more comprehensively studied (e.g. Coull *et al.* (2014a), O'Dowd *et al.* (2010b)) and shows the necessity to consider both the heat transfer and aerodynamic loss simultaneously. The large area of the winglet not only increases the weight of the tip but is susceptible to high heat loads. Transonic squealer tips are less covered in the literature,

with squealer tip cooling studies being even fewer; the only examples found by the author are those by Ma *et al.* (2016), Ma *et al.* (2017) and Arisi *et al.* (2016). This shows a strong motivation for further investigation into transonic squealer tips, alternative squealer variations and especially cooled squealer tips in the current research.

As has already been mentioned, high speed linear cascades are vitally important; they offer a cheaper alternative to rotating rigs and are able to reproduce engine-representative Mach and Reynolds numbers. They furthermore offer improved accessibility to the tip, allowing higher resolution data to be taken. Another motivation of the work presented in this thesis is to improve the capabilities of the existing Oxford University High Speed Linear Cascade, to allow state-of-the-art data capture and an expansion of the available range of experimental techniques. The main drive behind this was to produce high quality combined film cooling effectiveness and heat transfer coefficient data on a transonic squealer tip examining the effects of coolant injection, tip clearance and coolant mass flow rate, in a first-of-a-kind study.

1.4 Aims and Objectives

The design of unshrouded HP turbine blades is a multidisciplinary problem which combines many aspects including heat transfer, aerodynamic loss and cooling; each of the disciplines has a unique optimised solution and finding a design which adequately satisfies all criteria is a complex procedure. The overall aim of this thesis is to improve the understanding of the tip design space and tip cooling capability at engine-representative aerodynamic conditions to aid with the development of designs with improved aerothermal and film cooling performance. This is achieved using a combination of experimental and CFD methods.

The individual objectives for the current research are as follows:

1. Compare the aerothermal performance of a variety of squealer geometry tips and a winglet tip at two tip clearances in the high speed linear cascade.

2. Improve the capabilities of the high speed linear cascade by implementation of the pressure sensitive paint technique to produce state-of-the-art tip film cooling effectiveness measurements.

3. Investigate the impact of cooling injection and the effects of tip clearance and coolant mass flow rate on two of the squealer tip designs by comparison of experimental tip heat transfer coefficients and film effectiveness data.

4. Examine the overall impact of film cooling on the tip heat flux for one of the squealer tips. This shows definitively the success of the cooling design.

5. Consider the affect of varying squealer rim edge radius on the tip heat transfer coefficient.

6. Using the validated Rolls-Royce CFD code, HYDRA, further expand the squealer tip design space, examining the OTL flow, aerodynamic loss and tip heat transfer coefficient of a variety of PS rim cut-back squealer designs at two tip clearances.

7. Using CFD, give an appreciation of the differences in the OTL flow and aerothermal performance that would occur under rotating conditions by application of a moving casing.

8. Examine in detail the interactions of the OTL flow and coolant via CFD, the factors which affect the cooling performance and the influence on the tip heat transfer coefficient.

1.5 Thesis Structure

The structure of this thesis is as follows:

Chapter 2 provides a review of the relevant open literature on unshrouded turbine blade tips, concentrating on the aerodynamics, heat transfer and film cooling.

Chapter 3 describes the high speed linear cascade, modifications made since the previous published work and details of the experimental techniques employed throughout

this thesis to measure the tip aerodynamic loss, heat transfer coefficient and film cooling effectiveness.

Chapter 4 discusses CFD theory and details the HYDRA CFD solver, as well as the implementation and analysis techniques used to examine the tip aerothermal and cooling performance.

Chapter 5 presents a combined experimental study of heat transfer coefficient and film cooling effectiveness on a transonic squealer tip. It compares the heat transfer on an uncooled tip at two tip clearances and with varying squealer rim edge radius. The influence of cooling injection is then examined at the same tip clearances and two different coolant mass flow rates. The success of the cooling scheme is evaluated via the tip heat flux reduction. The research presented in this chapter has been accepted for presentation and publication at the ASME Turbo Expo 2018 in Oslo, Norway and has received journal recommendation.

Chapter 6 provides experimental heat transfer coefficient and aerodynamic loss measurements for a variety of uncooled tip designs at the same two tip clearance heights.

Chapter 7 presents a similar experimental investigation of heat transfer coefficient and film effectiveness on another cooled transonic squealer tip with a suction side rim cut-back. The aerothermal and cooling performance of the two cooled squealer tips is compared.

Chapter 8 presents a CFD study to compare the OTL flow and aerothermal performance for a range of PS cut-back squealer tips. Consideration of tip clearance and casing motion is included.

Chapter 9 uses CFD to investigate coolant-OTL interactions, film cooling effectiveness and the influence of coolant injection on the tip heat transfer coefficient. This study considers the effects of coolant mass flow rate, coolant hole size and hole location.

Chapter 10 provides a summary of the current research, the main conclusions drawn from this thesis and recommendations for future work.

Chapter 2

Literature Review

2.1 Introduction

Turbine blade tip flow is exceedingly complex and decades of research has gone into investigating it. The purpose of this literature review is first to examine the basics of axial turbine flow over a flat tip with a tip clearance and the mechanisms by which tip heat transfer and aerodynamic loss in the passage occur, as determined in literature. Following an establishment of these principles, a thorough examination of the relevant literature will be presented, expanding on the basic ideas and investigating how the tip flow is influenced by multiple factors. This will provide a starting point for the current research.

2.2 Axial Turbine Flow

Early investigations of the flow field in an axial turbine were done under somewhat idealised conditions, meaning essentially incompressible flow. These investigations often utilised simplified two-dimensional models or low speed cascade tests, but were suitable to provide a foundation in turbine passage flow and tip clearance flows.

The fluid flows in an axial turbine with tip clearance are shown in Figure 2.1, as determined in low speed linear cascade tests by Yamamoto (1988). When the inlet

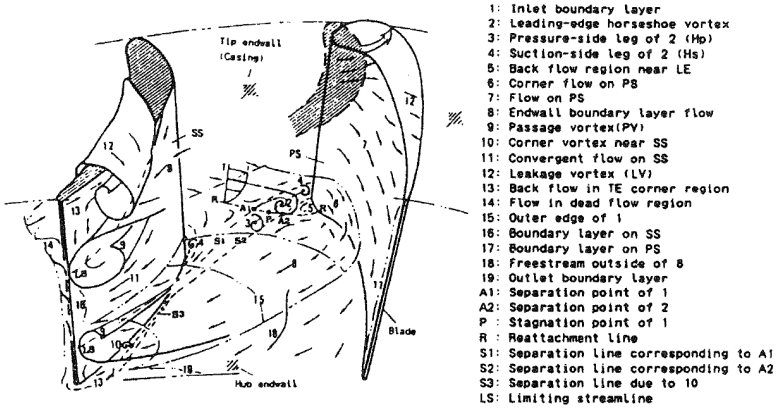


Figure 2.1: Tip leakage vortices and secondary flows in a rotor passage with tip clearance. (Reproduced from Yamamoto (1988))

boundary layer meets the leading edge of the blade, it splits into a horseshoe vortex. With a tip clearance present, the pressure side leg of the horseshoe vortex is scooped into the leakage flow, whereas the suction side leg rolls up into the passage vortex towards the trailing edge of the blade. This passage vortex is counter-rotating to the overtip leakage vortex.

Under low speed conditions, the tip leakage through the tip gap is driven by the natural pressure gradient across the tip chord. In general, these leakages flows are determined by this pressure differential and the size of the tip clearance.

A main feature of the tip gap flow, first postulated by Rains (1954), is the presence of a vena contracta at the entrance to the tip gap. Some years later, evidence of this vena contracta was confirmed during an experimental study in a linear turbine cascade by Moore & Tilton (1988) and also by Graham (1986) using a water flow cascade.

Low speed cascade tests of Yaras *et al.* (1989) and Sjolander & Amrud (1987) noted the formation of separation bubbles from the pressure side tip corner as the flow accelerates into the tip gap (Metzger & Rued (1989)); these separation bubbles took the form of vortices as the separated fluid is driven across the chord of the tip by the blade tip pressure gradient.

Many other early studies confirmed the presence of these separation bubbles, including Moore *et al.* (1989), who examined tip gap flow for a range a Reynolds numbers

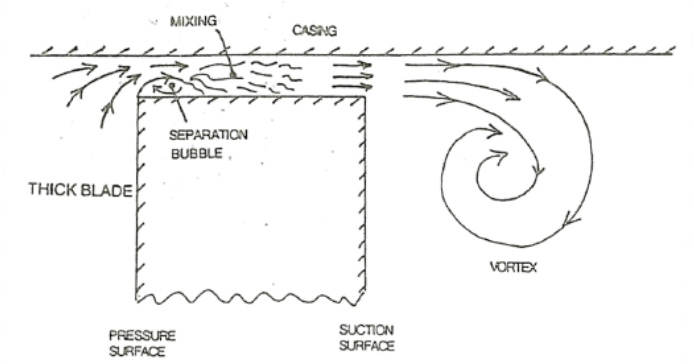


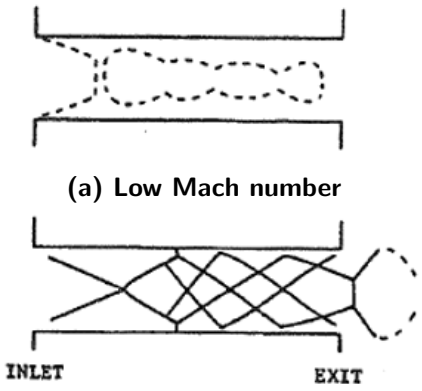
Figure 2.2: Tip leakage flow for an unshrouded blade. (Reproduced from Denton (1993))

using a simplified 2-dimensional model. They found the formation of separation bubbles at higher Reynolds numbers. Furthermore, for a sharp corner (over a chamfered corner) this separation bubble increases in length and the contraction coefficient in the tip gap reduces (peak blockage is higher), as confirmed by McGreehan & Schotsch (1988).

These findings agree with the proposed schematic by Denton (1993), as illustrated in Figure 2.2, which shows the formation of the separation bubble, reattachment and subsequent flow mixing, as well as the tip leakage vortex which forms as the leakage flow exits the tip gap and mixes with the mainstream flow.

At high Mach numbers the picture is quite different, with tip gap flows reaching transonic speeds under engine realistic aerodynamic conditions and peak tip gap Mach numbers in excess of 1; although few authors looked into this in the early days due to the difficulties associated with testing under engine realistic Mach and Reynolds numbers. However, there were two studies which did investigate tip clearance flow at high Mach numbers; these were the water table flow simulations of Moore *et al.* (1989) and Moore & Elward (1993). The studies showed the formation of an oblique shock from the pressure side corner of the tip and a series of shock reflections, should the peak Mach number in the tip gap be high enough. This change in flow regime is shown in Figure 2.3 and is reflected later in Figure 2.8a depicting mid tip gap Mach numbers on a flat tip (Zhang *et al.* (2011a)). It is important to note that real engine effects, such as these shockwave reflections are not present at low speed conditions.

Much later, changes in flow regime have been showed to cause choking of the tip gap



(a) Low Mach number

(b) High Mach number

Figure 2.3: Change in tip clearance flow regime. (Reproduced from Moore et al. (1989))

flow towards the trailing edge (Zhang & He (2011)). This detaches the overtip leakage mass flow rate from the tip pressure differential at the trailing edge, instead making it dependent only on the upstream conditions, specifically the blade pressure side static pressure.

This established picture of tip gap flow can be applied for simplified models or linear cascades. A real engine is much more complex and requires an understanding of the effects of casing motion on the tip flow, which will be discussed later.

2.2.1 Loss Mechanisms in a Rotor Passage

Loss can be defined as a creation of entropy in the flow. Losses in an axial turbine stage can be broken down into three categories: profile loss, which results from entropy generated in the blade boundary layers, away from the endwall; secondary loss, which is generated by the secondary flows when the endwall boundary layer passes through the blade row; and tip leakage loss which is caused by the leakage of flow through the tip gap of unshrouded rotor blades. The term secondary losses is also used to define any source of loss which is neither a profile loss or tip leakage loss. Each type of loss is taken to account for a third of the total losses in an axial turbine stage.

Mechanisms for entropy creation, as defined by Denton (1993), include viscous friction in boundary layers or free shear layers (include mixing processes), heat transfer from

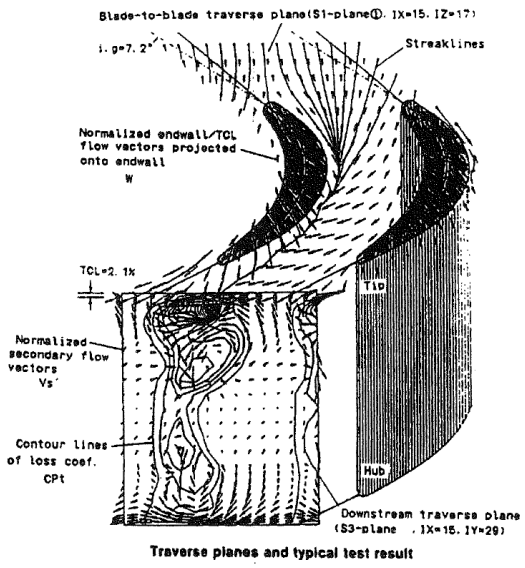


Figure 2.4: Typical tip leakage secondary and flows in a rotor passage. (Reproduced from Yamamoto (1989))

mainstream flow to coolant gas flow, and irreversible processes such as shock waves.

Leakage losses can be further broken down into internal gap shear losses and leakage jet mixing losses (at gap exit). Low speed cascade tests by Bindon (1989), were used to examine loss mechanisms relating to the tip gap clearance. They suggested that the tip gap separation bubble is the cause of the internal gap shear loss, however the cause of the overtip leakage loss core is less obvious. Bindon (1989) thought that the overtip leakage loss was also due to the formation of the separation bubble in the tip gap, but this was disproved by Bindon & Morphis (1992) who determined it was more closely related to the mass flow of the overtip leakage. Furthermore, Dishart & Moore (1990) connected the tip leakage mass flow to the leakage flow kinetic energy.

Bindon (1989) additionally saw that a majority of the flow which forms the overtip loss core (as seen in Figures 2.1 and 2.2) comes from the rear portion of the tip where the near-tip surface pressure differential is greatest; a finding which was corroborated by further linear cascades tests of Yamamoto (1989). Later, Key & Arts (2004) showed that the tip leakage itself is responsible for reducing the (near-tip) suction side (SS) pressure close to the trailing edge (TE) and enhancing this pressure differential and the resultant leakage flow velocities over the TE region.

Yamamoto (1989) also provided a typical loss profile on a traverse plane downstream of the blade trailing edge, due to secondary and tip leakage flows. This can be seen in Figure 2.4 which shows clearly the loss contours and velocity vectors of the tip leakage vortex and upper and lower passage vortices in a rotor passage.

2.2.2 Mechanisms for Tip Heat Transfer

The heat transfer to the tip and near tip regions is directly linked to the tip leakage flow aerodynamics. Two complimentary papers, by Metzger & Rued (1989) and Rued & Metzger (1989) connect the acceleration of flow into the tip gap with a localised increase in heat transfer on the blade pressure side near tip region. A similar increase of heat transfer on the suction side near-tip region was also found due to the leakage of flow from the tip gap, but at the time no clear reason was known.

Linear cascade tests by Bindon (1987) saw a region of low static pressure around the mid-chord on the tip pressure side edge, coupled with a thinning of the boundary layer and flow acceleration at the tip gap entrance, which was related to the area of highest heat transfer and the point where tip burnout usually occurs. It was found that these low pressures are caused by sharp flow curvature over the pressure side (PS) edge and intensified by acceleration of flow over the separation bubble by venturi action. This correlation between flow acceleration and high heat transfer was corroborated by Metzger *et al.* (1989a).

With regards to tip surface heat transfer, it has been found by several authors, for example Moore *et al.* (1989), Vogel & Eaton (1985) and Metzger *et al.* (1989a) that there is an augmentation of heat transfer coefficient (HTC) near to the PS edge of the tip surface, which occurs just upstream of the reattachment of the separated flow; this HTC augmentation can be up to 1.85 times the fully developed value after reattachment.

Liquid crystal measurements in a low speed linear cascade by Bunker *et al.* (1999) were some of the first detailing spatially resolved tip HTC measurements. These noted a 'sweet spot' of low HTC in the thickest portion of the tip, towards the leading edge

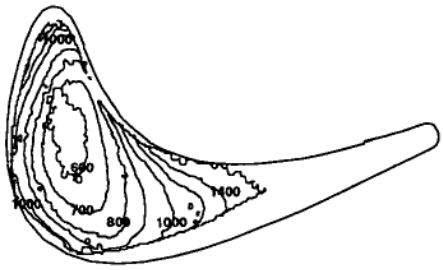
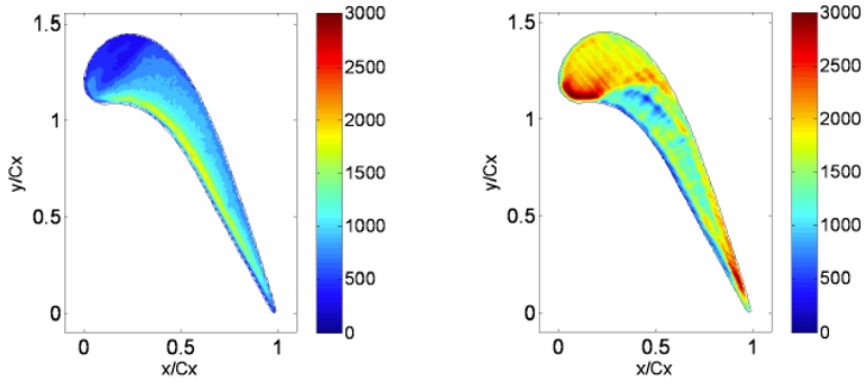


Figure 2.5: Heat transfer coefficient on a flat tip at low speed. (Reproduced from Bunker et al. (1999))

and a region of enhanced HTC between the mid-chord of the tip and trailing edge due to reattachment separated flow over the pressure side edge. This sweet spot is a characteristic feature of low speed flow over a flat tip, which corresponds to the area of lowest velocity over the tip, due to the smallest tip pressure differential. This characteristic heat transfer distribution has been seen by many authors since and is shown in Figure 2.5.

The differences in tip gap flow regime, discussed in Section 2.2, cause large discrepancies in the tip heat transfer between low speed and high speed flow conditions, as examined by Wheeler *et al.* (2011). The heat transfer to the tip is directly linked to the turbulent viscosity in the tip gap, the generation of which is highly dependent on the mechanism of flow reattachment. At low speed, the reattachment is brought about by turbulent mixing, whereas at high speed, supersonic acceleration of the flow over the separation bubble damps the turbulence intensity and is responsible for flow reattachment. As a result of this, tips with a low exit Mach number ($M_{exit} = 0.2$) were found to have a much higher turbulent viscosity over much of the blade tip (apart from the leading edge region) when compared to a similar tip with $M_{exit} = 0.98$, leading to higher heat transfer.

The change in heat transfer on a flat tip from low to high speed flow conditions was looked at by O'Dowd (2010) and can be seen in Figure 2.6. The main differences are that the previously noted 'sweet spot' of low heat transfer becomes the region of highest heat transfer (at high speed), whereas the mid-chord to trailing edge region shows the lowest heat transfer, along with striping due to the shock wave reflections over this



(a) Low speed **(b) High speed**

Figure 2.6: Tip Nusselt number at high speed and low speed flow conditions. (Reproduced from O'Dowd (2010))

portion of the tip.

It is described by Zhang *et al.* (2011a) that these stripes of high and low HTC are the result of rapid supersonic acceleration prior to the shock reflection, which produces low heat transfer, followed by a large adverse pressure gradient across the shock reflection, resulting in increased turbulence production and high heat transfer.

2.3 Tip Leakage and Aerodynamic Loss

Following the establishment of the basic overtip aerodynamics and loss mechanisms, this section aims to cover many of the factors which influence the overtip leakage flow and associated aerodynamic loss; including but not limited to, the tip geometry, tip clearance size and whether or not relative casing motion is applied. A review of the open literature to date is presented, incorporating CFD studies, low speed and high speed cascades, as well as rotor tests. There is also some discussion of aerodynamic loss measurement techniques.

2.3.1 Low Speed Cascade Studies

Tip geometry is well known to influence the overtip leakage flow. Bindon & Morphis (1992) attempted to reduce the losses measured at a downstream exit plane by shaping

of the blade tip. A tip with rounded pressure side edge and one which was also shaped to direct the flow radially were compared to a reference sharp edged flat tip. As expected, the rounded pressure side edge removed the separation bubble, decreasing losses in the tip gap, but at the expense of increased mixing losses of the leakage flow and mainstream. The radial flow tip, although giving higher tip gap losses than the reference tip, also brought about a decrease in the mixing losses, due to decreased mass flow through the tip gap. The overall losses of this tip were slightly lower than the sharp edged flat tip.

Heyes *et al.* (1992) measured the performance of a flat tip against several squealer tip geometries, finding there to be an advantage in loss reduction to be gained from using a suction side squealer tip. They also demonstrated that turbine tip designers should attempt to reduce the mass flow through the tip gap (and hence the mixing losses), by minimising the radius of the rim corner to cause flow separation; this decreases the contraction coefficient in the tip gap, at the expense of increasing the internal shear loss production within the gap itself (Moore *et al.* (1989)). This approach agrees with previous work of Bindon & Morphis (1992) as well as later studies by Zhou *et al.* (2013) and CFD work by Coull *et al.* (2014a) into the effects of tip deterioration.

The main part of the study by Zhou *et al.* (2013) compares a flat tip, squealer (cavity) tip and a winglet tip for loss performance. The purpose of a cavity tip is to reduce the discharge coefficient via contractions over the tip rims. They found that vortices formed in the cavities of the squealer and winglet tips and the discharge coefficient did reduce compared to the flat tip. The main purpose of the winglet tip overhangs is to reduce the driving pressure difference across the tip and hence reduce the tip leakage mass flow. They found that the pressure side winglet did not have the desired effect, however Yaras & Sjolander (1991) has previously reported an enlargement of the separation bubble at gap inlet, resulting in a reduction of tip leakage loss.

Investigation of other winglets geometries by Yaras & Sjolander (1991) revealed that a suction side winglet did reduce the pressure differential near the leading edge, but actually increased it near the trailing edge. The reason for this was due to the fact that

the leakage vortex (an area of low static pressure) is mainly formed towards the rear of the blade. These findings help to explain the result of Dey & Camci (2001), who found a suction side winglet tip to produce higher loss than a flat tip. However, Yaras & Sjolander (1991) found that double-sided, pressure side only and suction side only winglets all reduced the tip leakage losses by up to 10% compared to a flat tip. Overall, Zhou *et al.* (2013) found the winglet tip with a sharp pressure side edge, to produce the lowest losses, compared to a squealer tip and flat tip. This finding was corroborated by Schabowski & Hodson (2013) for a range of alternative winglet-squealer geometries.

Another aspect of geometry known to have an effect on aerodynamic losses is that of squealer cavity depth. Lee & Chae (2008) found that increasing the cavity depth weakens the leakage vortex and reduces it's interaction with the passage vortex, which reduces the mixing losses in the near-tip region. However, the benfits of increased cavity depth show diminishing returns; further increase of the squealer rim height-to-chord ratio above 2.75% was reported to yield no further reduction in losses.

Other loss reducing features were investigated by Park *et al.* (2013) who measured the losses from a variety of multi-cavity squealer tips which used ribs to split the cavity at various locations. Results showed a reduction in leakage flow and losses from the multi-cavity tips compared to the standard squealer and flat tip. The best aerodynamic performance was gained by placing a rib near the LE.

As previously mentioned, one of the drawbacks of cascade testing is the stationary testing environment. To combat this, moving belts have been used, for example by Yaras & Sjolander (1992), to examine the effects of simulated rotation. The casing motion was found to reduce the tip gap flow rate by around 50%, due to a reduction in the driving pressure differential across the tip as the passage vortex is drawn towards the blade suction side and interferes with the gap outflow. They concluded that the tip gap flow is dominated by pressure rather than shear effects.

Studies by Palafox *et al.* (2007) and Palafox *et al.* (2011) used particle image velocimetry (PIV) to investigate the effects of casing motion on a large scale flat tip blade

with a moving belt. They found that the main separation bubble around blade mid-chord is reduced in both height and length with casing motion applied. Palafox *et al.* (2007) also investigated how the secondary and leakage flow are effected by the addition of relative casing motion. They saw a reduction in the OTL vortex but an enhancement of the passage vortex; both vortices were seen to move towards the suction side of the blade. Yaras *et al.* (1992) confirmed these relationships and saw further decrease of the tip leakage vortex with reduced tip clearance and increased wall speed. Additionally, Palafox *et al.* (2007) saw the formation of a scraping vortex, next to the tip leakage vortex, generated by the interactions of tip leakage jet and opposing flow dragged by the moving belt.

2.3.2 High Speed Linear Cascade Studies

Traditionally, any high speed testing had to be done in piston compression facilities or shocktubes, which only have very short duration testing capabilities. An example of this is the von Karman Institute Isentropic Light Piston Compression Tube facility which can maintain a steady flow for approximately 0.4s. Key & Arts (2004) used this facility to compare leakage flow for a flat tip and squealer tip at transonic conditions. Oil flow visualisation revealed the flow patterns to be very similar to those at low speed, with a PS separation bubble on the flat tip and recirculating flow in the squealer cavity. Additionally, they saw that the squealer tip was relatively insensitive to increased Reynolds number and produced lower losses than the flat tip, similarly to low speed testing.

More recently, blowdown rigs have been developed with much longer test times, allowing for enhanced resolution and a wider variety of measurements to be taken. O'Dowd *et al.* (2010b) performed aerodynamic loss measurements on a flat tip in the Oxford High Speed Linear Cascade (HSLC); the rig which was utilised during the current research. Their findings indicate that as the tip gap is increased, the OTL vortex is enhanced and shifts further away from the blade SS. In comparison with numerical

results, the CFD over-predicted the strength of the passage vortex, though in general showed good agreement.

A couple of studies have focussed on transonic squealer tips. Wheeler & Saleh (2013) saw that a squealer tip produced a lower discharge coefficient than a flat tip, agreeing with low speed results. Virdi *et al.* (2013) showed that squealer tips produce similar trends in aerodynamic loss with tip clearance as the flat tip and winglet tip.

2.3.3 Rotor Studies

Rotational rigs allow the most engine realistic measurements to be taken, accounting for rotation effects which are not captured in simple linear cascade tests. However, these rigs are incredibly complicated, often making access for instrumentation difficult, not to mention that they are expensive to build and operate. For these reasons, linear cascades are often preferred, so it is useful to know how well cascades can predict the flow inside rotational rigs and therefore in a real engine.

Rotational rigs can also be run at low or high speed, with the high speed version being the most complex. A low speed, single stage axial rotor was run by Xiao *et al.* (2000) and McCarter *et al.* (2000), showing that many of the same loss inducing features present in the linear cascade tests of Bindon (1989) and Yamamoto (1989) were also found in axial rotor tests. Specific features observed were: the separation of the tip leakage flow from the blade SS to form the tip leakage vortex after 80% chord; the interaction of the tip leakage and passage vortices; and the fact that the highest pressure drop and total pressure loss are found within the tip leakage vortex. Additionally, a scraping vortex is also produced during rotational testing, as similarly predicted by Palafox *et al.* (2007) when relative casing motion was applied to a linear cascade.

Kegalj *et al.* (2012) carried out a combined experimental and CFD study in a 1 1/2 stage turbine rig, measuring the same loss structures as observed by previous authors. They compared a flat tip and squealer tip, reporting a 9.1% reduction in mass flow passing the tip gap and an improvement in the stage isentropic efficiency of 0.24% from

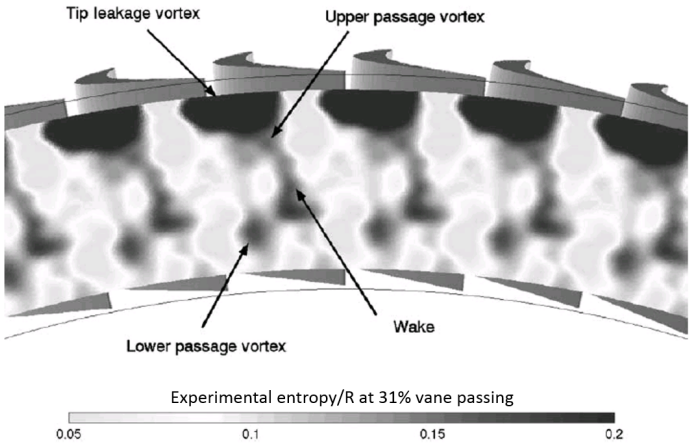


Figure 2.7: Loss mechanisms downstream of a rotor. (Reproduced from Payne et al. (2003))

the use of a squealer tip.

However, there are some differences between cascade and rotor tests; as described by McCarter *et al.* (2000) it is the streamwise turbulence component which is dominant in cascade tests, whereas the radial component is highest in rotor flows, which modifies the structure of the turbulence field.

Payne *et al.* (2003) examined rotor stage efficiency and loss features at engine-representative aerodynamic conditions, using the Oxford Rotor facility. This facility was designed to match the necessary non-dimensional conditions for very short time periods of approximately 15 ms (Ainsworth *et al.* (1988)). Evident were the four main loss producing flow features, as seen in Figure 2.7. These were all noted previously in static low speed cascade testing by Yamamoto (1989), other than the blade wake, which was not obvious in Figure 2.4.

Payne *et al.* (2003) separated the contributions of these flow features to the total loss, concluding that the tip leakage vortex causes a 3.3% drop in efficiency, compared to 1.3% of the secondary losses combined.

Camci *et al.* (2005) investigated the use of partial squealers, focussing on SS only squealers of varying lengths and channel squealer tips with openings at the LE and TE. They found that a SS only squealer running from TE to within 6% axial chord of the LE produced the lowest tip leakage mass flow.

Flow visualisation was first done in a rotating rig by Rao & Camci (2005) on a flat tip at low speed. They reported the same separation and reattachment of flow over the PS edge as that observed in non-rotating rigs; the point of reattachment moved closer to the PS edge at reduced tip clearance, signifying earlier flow reattachment.

2.3.4 CFD Studies

Acharya *et al.* (2003) investigated various leakage reduction strategies at low exit Mach numbers, employing a variety of squealer and winglet tip designs, along with a flat tip with and without ribs. Both they and Kwak *et al.* (2003) found that a suction side squealer produced the lowest leakage flow. The winglet tip did not perform as well as the SS squealer due to the fact that it was a PS only winglet, which was shown by Zhou *et al.* (2013) to do little in the way of reducing the driving pressure difference across the blade tip.

However, the success of full-perimeter cavity winglets have been demonstrated by several authors, for example Harvey & Ramsden (2000), Coull *et al.* (2014b) and Schabowski *et al.* (2014) at low and high speed flows. Harvey & Ramsden (2000) indicated a 31% reduction in tip loss exchange rate and an improvement in turbine stage efficiency of 1.2 - 1.8% compared to a flat tip at low speed. Schabowski *et al.* (2014) reported an optimised winglet-squealer tip design which reduced the losses and tip leakage mass flow further compared to a flat tip and a baseline winglet-squealer at high and low exit Mach numbers.

More recently, Coull *et al.* (2014b) performed an optimisation of flat-tipped winglets, showing improvements in efficiency from a full-perimeter winglet. The winglet overhangs were shown to reduce the mixing Mach numbers, turn the leakage flow in a more streamwise direction and reduce the driving pressure ratio over the tip. Coull *et al.* (2014a) then compared a flat winglet tip to a cavity-winglet, flat tip and cavity squealer tip at high speed. The losses were reduced further by the cavity-winglet due to the inclusion of the cavity; the cavity rims form two contractions, reducing the discharge coefficient

and leakage mass flow. The total loss reduction from the cavity-winglet tip was found to be 24% over the flat winglet, 45% over a flat tip and a 31% improvement gained over the use of a squealer tip.

Focussing on squealer tips, Krishnababu *et al.* (2008b) found a SS squealer to actually increase the leakage flow when compared to a flat tip, due to a decrease in blockage. Conversely, a cavity squealer was seen to reduce the leakage flow, in agreement with Ameri *et al.* (1998). They explained this difference in relative performance to be caused by differences in the ratio of thickness of squealer rim to local blade thickness between studies. So it is seen that the blade tip aerodynamic performance is very geometry specific.

Other squealer tip variations were studied by Lomakin *et al.* (2013), including a full perimeter cavity squealer and cavity squealers with near trailing cut-back rims on PS and SS. They reported the lowest tip clearance loss to come from the SS cut-back squealer tip.

Two papers by El-Ghandour *et al.* (2010) and El-Ghandour *et al.* (2012) examined the effects of squealer cavity depth, rim width and cavity location. They found that a wider, deeper cavity promoted a recirculation of flow which entrained the OTL flow, reducing losses. They further saw that positioning the cavity closer to the PS rim, with a wide SS rim, was beneficial as the wider SS rim allowed reattachment and the mixing process to be completed; this reduced the flow velocity gradient and the leakage flow rate into the passage.

Zhong *et al.* (2016) used CFD to investigate the tip gap Mach numbers and leakage mass flows for a squealer tip and several winglet tips under transonic flow conditions. They found that the winglet tip produces local changes in mid-gap Mach number when compared to the cavity tip, in particular: a decrease in Mach number was observed over the SS winglet near the leading edge caused by increased tip gap exit pressure; an increase in Mach number over the PS winglet due to the formed vena contracta causing flow acceleration. Additionally, they found that the tip leakage mass flow towards the

leading edge was reduced for all the winglet designs tested, with the largest reduction coming from the case with both leading edge SS and mid-chord PS winglets. There was very little difference in leakage mass flow towards the trailing edge because the flow is choked in this region at transonic conditions and the PS geometry is the same in all cases.

Zhong *et al.* (2016) also applied relative casing motion to the same cavity and winglet tips as before. Similarly to Krishnababu *et al.* (2008c), the main effect of the casing motion was to reduce the tip leakage mass flow over the front half of the tip. The leakage flow over the rear of the tips remained similar since the tip gap is still choked in this region.

Zhou & Zhong (2016) attempted a design optimisation for suction side winglet tips with relative casing motion at $M_{exit} = 0.9$, focussed on reducing the mixing between the leakage flow and mainstream towards the leading edge. Their design method (which involved producing iterations of winglets to follow the interface between the leakage flow and mainstream) successfully showed that the driving pressure differential across the tip could be reduced with each iteration, as expected, with a corresponding reduction in leakage mass flow and tip leakage loss. An additional surprising result was that the scraping vortex, formed near to the tip leakage vortex due to relative casing motion, disappears with the largest winglet, further reducing the mixing loss.

The influence of inlet boundary conditions was studied by Coull & Atkins (2015) and showed little change to the tip leakage pattern when introducing either a more realistic inlet condition or relative casing motion individually. However, more significant changes were seen when both the realistic inlet condition and casing motion were applied.

2.3.5 Aerodynamic Loss Measurement Techniques

Aerodynamic measurements can be produced by traversing a pressure probe downstream of the blade row. Five-hole probes have long been used for this purpose, for example Dominy & Hodson (1992), which allow for the measurement of pitch and yaw angles

in addition to total pressure and Mach number. However, Main *et al.* (1996) noted that five-hole probes accumulate redundant information; when capturing these four flow variables, only four holes are needed. Main *et al.* (1996) detailed the design and calibration of a four-hole probe, with a sharp-edged, faceted tip which reduced the Reynolds number sensitivity due to the defined separation points at the sharp probe edges. The probe additionally had 60^o inclined side faces to reduce probe tip shock-waves in transonic flows as per the work of Ainsworth & Batt (1993).

Experimental rigs which have space limitations necessitate the use of probes which are smaller still. Povey *et al.* (2008) describes a three-hole probe, in which the holes are arranged linearly. This probe is unable to measure both flow angles without manual rotation of the probe, however this design was the basis for the probe used by O'Dowd *et al.* (2010b), Virdi *et al.* (2013) and the author as it's design enables measurements to be taken closer to the casing wall than could be achieved by previous symmetrical four-hole probes.

2.4 Tip Heat Transfer

This section presents studies in the open literature which investigate the tip heat transfer, and covers the same areas as Section 2.3, since it is the OTL flow field which determines the heat transfer to the tip, as has already been discussed. Again, there is some discussion of tip heat transfer measurement techniques.

2.4.1 Low Speed Cascade Studies

Various tip sealing methods, aimed at reducing the tip leakage flow, and their effects on the tip heat transfer have been investigated by Saxena *et al.* (2004). These methods involved the placement of ribs and pins on the surface of a flat tip. Results showed that ribs, located orthogonally to the leakage flow direction produced the lowest leakage flow and associated heat transfer coefficient. However, it was noted that the ribs have

a larger effect on the leakage mass flow than on the heat transfer and that none of the solutions tested provide a significant reduction in HTC over the flat tip.

A more robust approach is the use of a winglet tip or squealer tip, although both of these tips are primarily suited to reducing overtip leakage losses, rather than heat transfer. Nonetheless, a reduction in leakage flow can also bring about lower tip HTC and as such these tip geometry designs have become increasingly prevalent; it is therefore important to examine the associated heat transfer coefficient relating to each of these tip designs.

A range of squealer tips have been compared by both Azad *et al.* (2002) and Kwak *et al.* (2003), including a double squealer and various arrangements of single squealers. They found that all the designs tested reduced the tip HTC when compared to a flat tip, with the largest advantage to be gained from using a suction side only squealer. Additionally, it was seen that the rims were particularly vulnerable to high heat transfer coefficients; this was confirmed by Ameri *et al.* (1998) using CFD. It is interesting that a SS squealer was also found by Heyes *et al.* (1992) to produce the largest reduction in tip leakage loss, compared with a flat tip and pressure side only squealer.

Newton *et al.* (2004) also measured the tip HTC of a SS squealer, double squealer and flat tip, noting that the introduction of squealers eliminated the pressure side separation and reattachment mechanism seen on flat tips. Instead the heat transfer is determined by flow impingement, which creates local areas of high HTC on the tip cavity surface.

The thermal side of the study by Park *et al.* (2013) compared the HTC for a flat tip with a series of multi-cavity squealer tips, seeing a general reduction in HTC from all the squealer designs. They showed that the region of high HTC at the LE due to flow impingement was reduced by placement of a rib near to the LE. However, a rib close to the TE promoted reattachment in the downstream cavity and increased HTC compared to the single cavity squealer.

Another factor which is know to effect tip heat transfer coefficient is that of tip clearance height. Kwak *et al.* (2003) and Azad *et al.* (2000) both saw that with increased

tip gap, the HTC on the tip surface also increased due to higher leakage mass flow. They also saw that the blade suction side HTC increased at larger tip gap, however the blade pressure side was found to be insensitive to tip gap clearance. With regards to squealer tips, Newton *et al.* (2004) noted that at increased tip gap, the flow impingements move further from the pressure side edge (or PS rim) and increase in intensity.

Squealer cavity depth also effects the tip HTC, as investigated via cascade testing by Bunker & Bailey (2001). They compared squealer tips of varying cavity depth to a baseline flat tip at high speed, subsonic conditions, finding that the use of a squealer kept similar HTC magnitudes in the flat tip 'sweet spot' but lowered the HTC towards the leading and trailing edges. Furthermore, the deeper squealer cavity produced the lowest HTC over the tip, as it effectively isolates the tip surface. This trend with cavity depth was also observed by Park *et al.* (2014).

Bunker & Bailey (2001) also investigated squealer rim deterioration, using the deepest cavity case. They showed that loss of the pressure side rim in the mid-chord region actually decreased the overall tip heat transfer, but once the SS rim was also lost in the same region, the HTC increased once again.

Few experimental studies into casing motion effects on tip heat transfer coefficient have been performed in linear cascades, due to the lack of optical accessibility to the tip when using a moving belt. However, one such study by Palafox *et al.* (2011) using particle image velocimetry (PIV), revealed that the tip Nusselt numbers can be reduced by up to 13% when relative casing motion is applied. Additionally, the relative performance of a flat tip and squealer tip was found to be maintained once casing motion is added, with the cavity squealer tip resulting in a 32% reduction in tip heat transfer.

2.4.2 High Speed Linear Cascade Studies

It has already been discussed in Section 2.2.2 that for a flat tip, an increase of exit Mach number from 0.2 to 0.98, changes the flow regime over the tip from subsonic to transonic, greatly altering the HTC pattern on the tip. However, it seems that this is

not always the case. High speed cascade tests by Anto *et al.* (2013) showed that an increase in M_{exit} from 0.86 to 1.05 simply caused an increase in HTC on the tip, due to increased leakage mass flow, while the HTC pattern remained the same; that of a typical 'low speed' blade, with no observable shockwave structures. This was contrary to Zhang *et al.* (2011a) and was ascribed to the difference in 2D blade geometry used. However, their study showed a consistent increase in HTC with tip clearance.

Under transonic conditions, the LE portion of a flat tip is subsonic, but the middle portion of the blade, which shows shockwave reflections is supersonic. Zhang *et al.* (2011b) saw that decreasing the tip gap causes reduced heat transfer over the LE and middle of the blade, due to decreased leakage Mach number, which also causes a reduction in the shockwave striping pattern. However, at the very trailing edge of the blade there is a small region which produces the reverse trend and heat transfer increases at smaller tip gaps. A similar behaviour was seen by Virdi *et al.* (2013) for squealer tips with an open trailing edge and highlights the vulnerability of the TE region at reduced tip gap. This experimental study by Virdi *et al.* (2013) is one of the very few in open literature examining transonic squealer tips.

One other example of experimental investigation into the heat transfer of transonic tips was completed by Zhong *et al.* (2016) who examined cavity (squealer) and winglet tips. They found that the main differences between the tips occur on the squealer and winglet rims. The wider pressure side rim of one winglet design allows reattachment to occur where it did not in the other cases (as expected from Figure 2.2) causing higher HTC on that rim. A similar process is seen on the wider suction side winglet case.

The effects of the inlet turbulence level and inlet boundary layer profile on tip heat transfer were examined by Zhang *et al.* (2014) using a combined experimental and computational study. In agreement with the similar aerodynamic study of Coull & Atkins (2015), they reported no apparent change on the tip heat transfer from either the turbulence intensity or boundary layer profile.

2.4.3 Rotor Studies

Heat transfer studies in rotating rigs are the most representative of engine conditions, however obtaining detailed measurements is challenging due to difficulties in accessing and instrumenting the blade tip. Studies usually implement the use of thin-film heat-flux gauges, which provide discrete measurements in the area of interest.

Dunn *et al.* (1984a) and Dunn *et al.* (1984b) performed some of the first heat transfer measurements in a rotating turbine rig, observing high rates of heat transfer on the blade tip and casing. Thorpe *et al.* (2004b) used the Oxford Rotor facility to observe that the heat transfer rate to the casing varies strongly with axial position through the turbine and that the Nusselt number falls by 36% from the rotor inlet to 80% of axial chord, ascribed to changes in flow recovery temperature rather than heat transfer coefficient. Thorpe *et al.* (2004c) and Chana & Jones (2003) both saw a variation in heat transfer rate to the casing associated with the passing of the blade tip, in particular the overtip leakage flow. This was observed as a minimum near the tip SS and increasing to a peak prior to the tip PS, before reducing again once the blade has passed.

Jackson *et al.* (2015) investigated the effects of tip clearance on flat tip heat load, using the Oxford Rotor and CFD, which showed good agreement. They reported that the heat load on a flat tip actually increased with reduced tip clearance, despite a small decrease in the HTC. The enhanced tip heat load at smaller clearance was attributed to the proximity of high relative total temperature fluid near the casing, generated through casing shear, which raised the adiabatic wall temperature at low clearance. The CFD showed that without casing motion, reducing the tip clearance resulted in decreased heat load.

The heat transfer on a squealer tip was measured by Dunn & Haldeman (2000), observing the highest Nusselt numbers on the SS rim and cavity floor near the LE; the cavity floor values decreased with distance along the cavity towards the TE.

Thorpe *et al.* (2005) examined the heat transfer along a tip camber line. Results suggested similarities to previous low speed cascade work of Bunker *et al.* (1999), in

particular the LE 'sweet spot', but differences were also noted which is not surprising giving the low exit Mach number and absence of rotation in the study by Bunker *et al.* (1999). It is hard to read any further into the differences without spatially resolved heat transfer measurements, such as can be achieved in a high speed linear cascade.

A rare example of spatially resolved HTC measurements were taken by Brunner *et al.* (2007) from a rotating, low-pressure turbine stage rig. They used a custom IR pyrometry system to measure the mid-span blade surface temperatures and determine the heat transfer coefficient. The measured area from this method was however quite limited due to the feasible viewing angles and the method was not applied to the blade tip.

2.4.4 CFD Studies

A multitude of CFD has been performed by various authors investigating tip heat transfer. In low speed flow conditions the heat transfer on squealer tips was investigated numerically by Acharya *et al.* (2003); it was found that once again the suction side only squealer tip produced the lowest heat transfer coefficient, in-line with the finding that it also gave the lowest tip leakage flow of the tips tested. This agreed with low speed cascade tests of Azad *et al.* (2002) and Kwak *et al.* (2003) and was in partial agreement with numerical results of Krishnababu *et al.* (2008b), who found that the lower HTC was due to low flow velocities upstream of the SS squealer rim. Krishnababu *et al.* (2008b) also noted that for all geometries, in general, the tip heat transfer increased with increasing tip gap, as a result of increased leakage flow.

The thermal side of the study by Coull *et al.* (2014b) highlighted one of the major drawbacks of the winglet tip. They showed that a full-perimeter flat-tipped winglet produced increased heat load, although this could be reduced by use of an early SS only winglet. Coull *et al.* (2014a) compared the thermal performance of the flat-winglet (full-perimeter) to that of a flat tip, squealer tip and cavity-winglet tip. The highest heat load was found on the cavity-winglet due to the increased surface area. However the

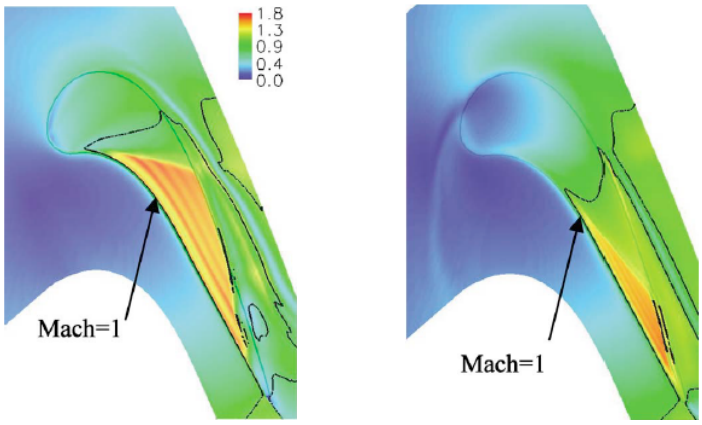
design did reduce the tip peak heat flux and the heat transfer on the winglet-squealer rims. They also commented that, despite the high heat load, this winglet design may be easier to cool and maintain in service.

A flat tip was used by Zhang & He (2013) to show how tip shaping can be used to locally accelerate the flow over the LE to transonic speeds, producing a marked reduction in tip HTC. Another flat tip was used by Virdi *et al.* (2013) for further investigation into the previously described crossover behaviour in HTC, whereby the HTC increases at smaller tip gap towards the trailing edge. They reported that the HTC shows opposite trends with tip gap for the transonic and subsonic regions; a finding which was consistent with the addition of casing motion and the use of a squealer tip. However, the squealer tip was less vulnerable at smaller tip gaps than the flat tip, as the transonic portion of the squealer tip is much smaller and also less effected by casing motion; this is because a majority of the tip surface and cavity flow are further from the casing.

An optimisation of squealer geometry was performed by Mischo *et al.* (2008) who investigated the variation of squealer rim thickness. They found that reduced heat transfer (and tip leakage mass flow) could be gained from an optimised squealer design, with a thicker rim on the SS at the LE, which influenced the generation and interaction of the tip cavity vortices. The reported benefit of a thicker SS rim agrees with the previously discussed aerodynamic studies of El-Ghandour *et al.* (2010) and El-Ghandour *et al.* (2012) into the reduction of the tip leakage flow.

The effects of relative casing motion on the HTC of squealer and winglet tips was investigated numerically by Zhong *et al.* (2016). The main effect of the casing motion was to pull the leakage flow in a tangential direction, causing the impingement of the cavity vortex around the mid-chord of the blade; this resulted in increased HTC in this area in all cases, however the HTC was lowest in the case with both a PS and SS winglet. The formation and impingement of the cavity vortex on a squealer tip with casing motion was confirmed by Virdi *et al.* (2013).

Krishnababu *et al.* (2008c) showed that the addition of casing motion causes a drop



(a) Stationary Casing **(b) Moving Casing**

Figure 2.8: Mid tip gap Mach number for a flat tip at high speed flow conditions. (Reproduced from Zhang et al. (2011b))

in tip leakage mass flow, driving pressure differential and leakage flow velocities in the subsonic flow region towards the LE. They and Zhang *et al.* (2011b) saw that these trends resulted in a reduction in heat transfer close to the LE, akin to the 'sweet spot' seen under low speed conditions and a shift of the LE high HTC impingement region towards the mid-chord of the tip. Towards the trailing edge, where the flow is choked, Zhang *et al.* (2011b) saw a similar reduction in leakage flow Mach number with casing motion, as observed in Figure 2.8b. The stripes of high and low heat transfer (as described by Zhang *et al.* (2011a)) are seen to remain, although they are shifted towards the trailing edge, corresponding to a shift in the $M > 1.5$ flow region (see Figure 2.8b).

2.4.5 Heat Transfer Measurement Techniques

There are various methods of measuring tip heat transfer experimentally. One such technique is the naphthalene sublimation method, as described by Goldstein & Cho (1995) and used on the tip by Papa *et al.* (2003). In this method, the naphthalene sublimation depth is measured locally to calculate the mass transfer coefficient, which is related to the heat transfer coefficient (Nusselt number) by a heat/mass transfer analogy. However, this method is not suitable for high speed flows where recovery temperature effects are significant.

As discussed in Section 2.4.3, heat transfer in rotating rigs is often measured using

thin-film heat-flux gauges, due to lack of optical access to the tip. Examples include, Chana & Jones (2003), Thorpe *et al.* (2005) and Dunn & Haldeman (2000). These gauges work by recording the temperature history of thin film resistive temperature sensors, from which the heat flux can be calculated from the impulse response method of Oldfield (2008), and is averaged over the area of the gauge. Recent developments in Oxford, for example Thorpe *et al.* (2004a) and Collins *et al.* (2015) have allowed for manufacture of miniature thin-film gauges, capable of improved measurement accuracy and resolution. However, the highest spatially resolved measurements are still taken with optical methods where possible.

Cascades allow the optical access to the tip necessary to take high quality spatially resolved measurements of temperature distribution and heat transfer. Liquid crystals have been used extensively to measure surface temperatures and calculate heat transfer, as detailed by Ireland *et al.* (1999) and Ireland & Jones (2000). Liquid crystals used in experiments typically display a full colour change over a narrow band (1^{o}C) or wide band (20^{o}C) of temperatures. In-situ calibration is usually performed using a thin-film gauge and the change in crystal colour recorded by a camera. Application of liquid crystals to the blade tip is quite common in low speed linear cascades, for example by Kwak & Han (2003) and Saxena *et al.* (2004), however liquid crystals are less applicable to the blade tip in high speed flows, when recovery temperature effects are substantial, as the range of tip temperature can exceed the range of the crystals.

High speed linear cascades often use IR thermography, which gives high quality, spatially resolved measurements over a large temperature range. Several methods of obtaining heat transfer coefficients via IR thermography were compared by O'Dowd *et al.* (2010a). This study showed that a transient method using heat flux reconstruction via the impulse method (Oldfield (2008)) was the most accurate, reliable and efficient. These experiments, for example O'Dowd *et al.* (2010b), Virdi *et al.* (2013) and Anto *et al.* (2013) use an IR camera to record a temperature history on the blade tip surface through an IR permeable window. Heat fluxes are reconstructed from the temperature

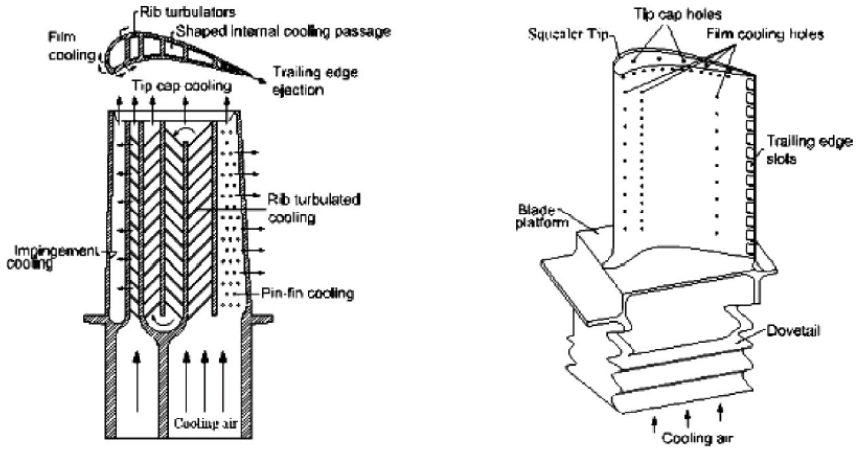


Figure 2.9: Schematic of a modern cooled gas turbine blade. (Reproduced from Kwak & Han (2003))

trace, allowing calculation of the heat transfer coefficient. IR thermography was the method of choice for the current research and is discussed in more detail in Chapter 3.

2.5 Film Cooling

It has already been seen that altering such aspects as tip geometry and tip clearance can influence the OTL flow in such a way as to reduce the aerodynamic losses and heat transfer to the tip. An alternate method to reduce the tip heat flux is to use film cooling. In a real engine this is done by injecting relatively cooler air, bled from the compressor stage, through film cooling holes which are usually located in the blade pressure and suction surface near-tip regions. This cooling air is intended to produce a film around the blade tip and protect it from the hot leakage flows.

A typical blade cooling design can be seen in Figure 2.9, showing internal serpentine cooling passages, near-tip film cooling holes, and a series of 'dust holes' (tip cap holes). These dust holes are usually larger in diameter than the film holes and are necessary for the removal of particulates from the serpentine passages which may otherwise block the cooling holes. Another, very useful, purpose of the dust holes is to inject coolant directly into the tip gap.

This section focuses on film cooling studies and attempt to explain how cooling

injection effects the tip heat transfer and aerodynamic loss. Investigations into film cooling usually focus on aspects such as the cooling hole positioning and injection angle, tip gap size and coolant blowing ratio (BR), all of which can alter the film cooling effectiveness and tip leakage flow. There is also some discussion of commonly used experimental methods for measuring tip cooling.

2.5.1 Low Speed Cascade Studies

Low speed cascade studies generally use simplified internal cooling geometries, rather than the complex serpentine passage systems of real blades. These simplified geometries usually comprise one or more internal plena which are fed by a source of coolant at a known pressure or mass flow rate.

Such a study is that of Newton *et al.* (2008), who compared coolant injection strategies on a flat tip. In the first arrangement, coolant was injected from a row of dust holes located near to the pressure side edge of the tip. Holes were positioned here in order to inject coolant directly into the separation bubble formed over the PS edge. The second arrangement moved the holes towards the tip camberline to inject coolant at the flow reattachment region. Although both strategies were successful, injection into the separation bubble proved more so, successfully removing the high HTC band associated with flow reattachment and providing a larger Net Heat Flux Reduction (NHFR) in areas of high cooling effectiveness as the reattachment of flow is blocked. Observed in both cases was the production of new local areas of high HTC near the dust holes, due to interaction of the coolant and mainstream and local acceleration of the coolant out of the coolant holes. This increase in HTC was also observed by Park *et al.* (2014), who proposed a cooling system to efficiently protect the squealer rims, by locating cooling holes near to the tip PS and additional holes directed at the SS rim.

Narzary *et al.* (2014) studied the effects of tip gap clearance and coolant blowing ratio by examining heat transfer and film effectiveness on a SS squealer tip with $M_{exit} = 0.75$ and film holes located in the PS and LE near-tip regions. They found that with

increasing tip gap, the film cooling effectiveness was reduced, but the HTC increased. Kwak & Han (2003) and Ahn *et al.* (2005) found a similar trend in film effectiveness with tip clearance, although the effects were minimal when compared to those of coolant blowing ratio. With increased BR, Narzary *et al.* (2014) saw enhanced film effectiveness; a trend also observed by Kwak & Han (2003), Mhetras *et al.* (2008) and Ahn *et al.* (2005), although at higher BR some films on the pressure side were seen to lift-off, reducing the film effectiveness. There was no trend observed on the HTC with regards to BR. Overall the injection of film coolant was found to lower the HTC when compared to the uncooled case.

Ahn *et al.* (2005) compared a cooled flat tip and squealer tip with various cooling arrangements. They saw that the addition of a squealer and the location of film cooling holes has a significant impact on the film effectiveness. The addition of a squealer dramatically alters the coolant trajectory from straight across the tip (in the pressure driven leakage flow path) to a trajectory in the direction of the cavity flow, in this case towards the TE. For the flat tip, the highest film effectiveness was seen with PS only injection (except at the highest BR), whereas the squealer tip showed little effectiveness from this strategy. The highest effectiveness case for the squealer tip was seen when combining PS injection with tip injection. Unlike the flat tip, where in general the film effectiveness drops at increased tip gap, the squealer tip shows less of a defined trend due to tip clearance. Compared to a flat tip, Kwak & Han (2003) saw an increase in film effectiveness and a decrease in HTC from the use of a squealer tip.

Focussing on aerodynamics, Ledezma *et al.* (2013) investigated cooled squealer tips in an annular cascade. They noted the equivalent aerodynamic performance of a cooled standard squealer and SS only squealer. Naik *et al.* (2011) also considered a squealer with LE and PS trailing edge cut-backs, finding a similar aerodynamic performance to a standard squealer tip.

It is a common problem that the trailing edge of the tip is hard to cool and often experiences high heat transfer due to the high flow velocities seen in this region. Mhetras

et al. (2008) tried to improve the cooling of the TE by using a squealer tip with PS trailing edge cut-back, allowing accumulated coolant to escape. This strategy showed an improvement in trailing edge film effectiveness over the classic squealer design and was confirmed by Naik *et al.* (2011) using the previously mentioned LE cut-back squealer.

Wang *et al.* (2010) investigated the tip leakage flows over a PS cut-back squealer tip with PS and tip camber-line holes. They reported reduced leakage mass flow when a high coolant blowing ratio is ejected from the camber-line holes, however a lower blowing ratio provided an improved coolant coverage within the tip cavity.

The effects of inlet flow angle on film cooling effectiveness were investigated by Gao *et al.* (2009) using the same PS cut-back squealer as previous authors (GE-E3 tip) with PS holes, tip camber-line and near SS holes. Altering the inlet flow angle was seen to effect the coolant jet direction on both PS and tip region and shift the peak of circumferentially averaged film effectiveness. Additionally, it caused the coolant jet on the cavity floor to spread out and can increase the local cavity floor film effectiveness by up to 25%, although the averaged effectiveness was largely unchanged.

2.5.2 High Speed Linear Cascade Studies

Experimental studies of cooled transonic tips are very rare in open literature. Hofer & Arts (2009) used the VKI Light Piston Compression facility to compare losses of a SS and full squealer tip with PS and camberline cooling. They found that the injection of PS coolant on the full squealer caused additional leakage flow blockage over the PS rim, which did not occur for the SS squealer due to the lack of a PS rim. This led to a lower loss coefficient for the full squealer tip.

O'Dowd *et al.* (2012) performed one of the first studies in a high speed linear cascade on a cooled winglet tip. Aerodynamic loss results showed a reduced loss coefficient with cooling injection, agreeing with Hofer & Arts (2009), ascribed to a sealing effect of the coolant, which reduced the OTL vortex; this blockage effect by the coolant was also backed up by a CFD study of Krishnababu *et al.* (2008a) into cooled squealer tips.

O'Dowd *et al.* (2012) also found an increase in Nusselt number with coolant injection, which disagrees with the low speed study of Narzary *et al.* (2014). However, an increase in tip clearance showed the same trends in HTC and film effectiveness as those observed at low speed i.e. an increase in HTC but a decrease in effectiveness.

To the author's knowledge, the only examples of experimental cooling studies on a transonic squealer tip are those by Ma *et al.* (2016) and Arisi *et al.* (2016). Ma *et al.* (2016) investigated the effects of varying dust hole location, concluding that interactions between coolant and the OTL flow alter the tip HTC distribution compared to the uncooled case. They noted distinctive stripes of HTC associated with each cooling hole and a reduction in heat flux upstream on the tip cavity in an area unreachable by the coolant. The CFD part of their study (Ma *et al.* (2017)) examined the coolant-OTL interactions, noting the creation of counter-rotating vortical flow structures; impingement of these vortical flows increase the HTC downstream of the cooling holes. Upstream, the reduction in heat flux was attributed to upstream propagated impact of the coolant-OTL flow interactions.

Arisi *et al.* (2016) examined the effect of varying exit Mach and Reynolds number on the film effectiveness. They observed an increase in tip HTC at higher exit Mach number, agreeing with Anto *et al.* (2013) but a decrease in film effectiveness due to increased cavity recirculation. Their results further confirmed the blockage effect on the OTL flow by injected coolant, as seen by previous authors. Lastly, the blockage effect of ribs in the squealer cavity resulted in high HTC and low film effectiveness downstream.

2.5.3 Rotor Studies

With established trends from cascade testing, the next step would be to take film effectiveness measurement from a rotating rig. Authors such as Dring *et al.* (1980) and Takeishi *et al.* (1992) evaluated film effectiveness on the blade surfaces, observing similarity to stationary conditions on the suction surface but much lower effectiveness on the pressure surface from the rotating case, attributed to deflection of the coolant jet due

to centrifugal forces. The film effectiveness on the LE region has also been examined by Ahn *et al.* (2007) and Ahn *et al.* (2006) and found to vary with both rotational speed and blowing ratio. However, film cooled measurements on the tip of a rotating blade are still very rare.

To the author's knowledge, the only example of a cooled rotating blade tip study was performed by Rezasoltani *et al.* (2015) to compare a flat tip with a squealer tip, with PS only and tip only coolant injection. The rotor tests showed the same trend of increasing effectiveness with coolant BR seen under stationary conditions in cascade testing. With PS only cooling, a similar relative performance (to stationary conditions) of improved effectiveness from the flat tip was reported (as seen by Ahn *et al.* (2005)). This relationship is maintained for the tip only injection cases, apart from at the lowest BR where the squealer tip shows an advantage due to accumulated coolant in the cavity.

Rezasoltani *et al.* (2015) also investigated the effect of rotational speed, showing that the averaged film cooling effectiveness decreases with increased rotor speed, for all cases except for the flat tip with tip injection only. This outlier was investigated using CFD and explained by the fact that the blade pressure differential drops with increasing rotational speed, meaning that at the highest rotor speed the effect of the casing on the coolant overcomes the natural pressure gradient across the blade for the first two holes near to the LE; this directs the coolant instead towards the tip PS. This effect on coolant trajectory is not seen with the squealer tip and since it is a rotational effect it would not be captured in a stationary linear cascade.

2.5.4 CFD Studies

Acharya *et al.* (2002) studied flat and squealer tips at low speed conditions, with and without coolant injection from a row a dust holes near to the PS of the tip. They found that the coolant flow path is influenced by the tip geometry. For flat tips, the coolant is directed across the chord of the blade, with the leakage flow. The highest levels of cooling effectiveness were in the coolant trajectory direction, and the effectiveness

increased slightly with increasing tip gap. However, for the squealer tip the cavity flow is much more complex and the coolant trajectory is towards the trailing edge at first, before leaking over the SS rim. With increasing tip gap, the cooling effectiveness in most of the cavity (other than the main coolant path) decreases, while the HTC increases, as might be expected. They found that increasing the coolant blowing ratio raised both the local HTC and cooling effectiveness for both tip designs, in agreement with previously discussed experimental studies of other authors.

Compared to the uncooled tips, Acharya *et al.* (2002) saw that the HTC on the flat tip changed dramatically with coolant injection; observed was the removal of the leading edge sweet spot, stripes of low HTC emanating from the cooling holes and a large increase in HTC on the PS edge. The squealer tip showed much less of a change in HTC pattern, suggesting that coolant injection has a smaller effect on the leakage flow.

The rims of a squealer blade are an area of high heat transfer and are also difficult to cool due to inaccessibility for internal cooling. This makes the rims an ideal candidate for film cooling, however there are very few papers in open literature showing the effects of coolant injection on the HTC of the rims.

One example is a low speed CFD study by Acharya *et al.* (2010) which investigated coolant injection to the previously mentioned PS cut-back squealer tip. Coolant injected from the PS near-tip region was found to produce areas of high film effectiveness coinciding with low HTC on the PS rim. On the rest of the tip, a similar trend of increased film effectiveness with coolant BR was seen as long as the films remain attached. At higher coolant BR, detached films produced reduced film effectiveness near the dust holes. These detached films mix with the leakage flow providing enhanced film effectiveness downstream and were observed to influence the OTL flow pattern. The alteration of the leakage flow pattern also changed the cavity HTC.

The impact of coolant injection on the tip leakage loss was investigated by Wheeler & Saleh (2013), Wang *et al.* (2015), Krishnababu *et al.* (2008a) and Zhou & Hodson (2011). They reported the potential for loss reduction with coolant injection, dependent

on both the tip clearance and coolant mass flow rate. A blockage effect was observed at low coolant mass flow or high tip clearance, but the effect of the coolant is diminished by the high leakage mass flow and so the squealer tip provides the best aerodynamic performance, as the tip geometry dominates. However, at a small tip clearance or high coolant mass flow, a substantial blockage effect was observed on the flat tip (but not on the squealer tip), reducing the OTL mass flow. The reduced impact for the cavity tip was ascribed by Wheeler & Saleh (2013) to a loss in the coolant momentum before it can interact with the high speed OTL flow, and due to the fact that the higher Mach number flow seen over the majority of the flat tip is more sensitive to coolant injection. As a result, the cooled flat tip outperformed the squealer tip at low tip clearance or with a high coolant mass flow. Furthermore, Wang *et al.* (2015) discussed how replacing the squealer cavity with a flat tip in the transonic region improved coolability while maintaining the aerodynamic benefit of a squealer.

The effects of casing motion on the same cooled PS cut-back squealer tip (as used by Acharya *et al.* (2010)) were also examined by Acharya & Moreaux (2013). The relative casing motion was seen to have a significant effect on the leakage flow aerodynamics and heat transfer. The coolant trajectory from the PS holes, across the tip chord, is altered by the casing motion which entrains the PS coolant into the squealer cavity and cools the PS region. The dust hole coolant is also altered, being pushed towards the SS rim by the casing motion; this results in reasonable cooling effectiveness on the SS rim where previously the coolant has been directed towards the PS rim under static conditions. Despite the changes the coolant trajectory, the relationship between tip gap size and cooling effectiveness seen with a stationary casing in Acharya *et al.* (2002) was unaffected by casing motion. A final aspect of this study was that rotational effects, such as Coriolis and centrifugal forces, were found to be minimal when compared to the effects of relative casing motion.

A CFD study by Lu *et al.* (2013) simulated the first 1 1/2 turbine stages of the experimental rig of Rezasoltani *et al.* (2015). They examined film effectiveness on the

same cooled flat and cavity tips with tip hole cooling only. Strong interactions of coolant and the OTL flow were observed. Results showed that the squealer tip provides wider film coverage of the tip as a whole, but that the film effectiveness levels are higher for the flat tip, other than at the lowest coolant BR. A similar trend of increasing film effectiveness with blowing ratio was observed as in previous studies.

2.5.5 Film Effectiveness Measurement Techniques

There are several ways to measure film cooling effectiveness which have been applied to blade tips. Temperature based methods, for example Newton *et al.* (2008), Kwak & Han (2003) and O'Dowd *et al.* (2012), use either liquid crystals or IR thermography to measure the surface temperature when a coolant of a lower temperature is injected. The method previously used in the Oxford High Speed Linear cascade (O'Dowd (2010) and Virdi (2015)) required calculation of the recovery temperature of the uncooled blade tip and the adiabatic wall temperature of the cooled tip to find the film effectiveness.

A study by Wright *et al.* (2005) compared the techniques of IR thermography, temperature sensitive paint (another thermal method) and pressure sensitive paint (PSP) for measurement of film cooling effectiveness. They found an advantage from the PSP method, which relies on the mass transfer analogy, making it devoid of conduction related issues which occur in regions of high thermal gradient or around cooling holes, where 2D conduction effects become significant.

Naphthalene sublimation is another mass transfer technique which can be used to measurement film cooling effectiveness. The approach is detailed in Cho & Goldstein (1995) and was employed by Park *et al.* (2014) to measure tip film cooling effectiveness. In simple terms, two experiments are required: one with pure air as the coolant; the second in which the coolant air is saturated by Naphthalene. The adiabatic film effectiveness is calculated as a ratio of the Sherwood[1] numbers, determined by the heat/mass transfer analogy.

[1]The Sherwood number (or mass transfer Nusselt number) represents the ratio of convective mass transfer and diffusive mass transfer

PSP was developed for aerodynamic measurements, for example McLachlan & Bell (1995), but more recently has been used extensively to calculate adiabatic film cooling effectiveness. Examples of such studies include the work of Wong *et al.* (2016) (on the blade TE), as well as Mhetras *et al.* (2008) and Narzary *et al.* (2014) on the blade tip. A stand-out study by Rezasoltani *et al.* (2015) applied PSP to the blade tip of a rotating rig, using a strobe and camera triggered to the rotor shaft speed, with optical access gained by the use of a transparent window in the rotor casing. Although novel, the author questions the safety aspect of this approach were a rotor blade to let go during testing. The PSP technique is the chosen technique for the current research and will be discussed at length in Chapter 3.

2.6 Summary

This chapter provided a detailed, but non-exhaustive, account of the open literature detailing research into unshrouded HP turbine blade tip heat transfer, aerodynamics and film cooling. Much of the current wisdom surrounding the turbine tip has been gained from simplified models and low speed rigs. However, it was recently shown that there are significant differences in the heat transfer coefficient distribution resulting from transonic tip flows under engine-representative aerodynamic conditions. This has sparked a gradual shift in recent years to experiments which match engine Mach numbers as well as Reynolds numbers, as much of the research completed at low speed is repeated under high speed flows.

Tip geometry has been a focus of past research, exploring designs such as the flat tip, and variations of the winglet and squealer tip. Relative benefit has been shown by the winglet and squealer tip designs, however the large area of the winglet is a concern for high heat load and increased weight when considering an operational engine. The squealer tip performs well both aerodynamically and thermally, with a strong dependence on the tip clearance and casing motion, although has been little covered at engine-representative aerodynamic conditions and so forms the basis of the majority of

the current research.

Film cooling is of paramount importance to protect the tip from the high temperatures of the complex, high speed leakage flows, which make tip cooling design a challenge. Research into film cooling has focussed on similar areas as for uncooled tips, incorporating the effects of tip geometry, tip clearance and casing motion as well as cooling hole arrangement and coolant blowing ratio. Improved thermal performance has been seen from cooling strategies which block the reattachment of the OTL flow and several studies observed a change in relative aerodynamic performance of flat and squealer tips due to blockage effects from injected coolant. However, the cooled squealer tip has rarely been covered experimentally at transonic conditions. Addressing this lack in the literature and exploring the complex coolant-OTL interactions is another main focus of the present research. To the author's knowledge, there is currently no published research focussing on the effects of tip clearance and coolant mass flow rate on the heat transfer coefficient and film effectiveness of transonic squealer tips.

Also discussed in this chapter was the development of experimental techniques employed on blade tips in the open literature. Improved experimental methods allow for improved accuracy and resolution of measurement. Improvements in heat transfer coefficient measurement techniques have allowed for high quality, spatially resolved measurements to be taken from the blade tip. An evaluation of techniques for measuring film cooling effectiveness showed an advantage from the use of pressure sensitive paint. The implementation of this technique in the Oxford High Speed Linear Cascade has been a tertiary focus of this research presented in the thesis.

Chapter 3

High Speed Linear Cascade and Experimental Techniques

3.1 Introduction

This chapter gives details of the High Speed Linear Cascade (HSLC) at Oxford University, used for the experimental portion of the current research. Since a detailed description of the HSLC has been documented in O'Dowd (2010) and Virdi (2015), only a brief overview will be given here. The main focus of this chapter will instead be on modifications made to the rig since the work of Virdi (2015), as well as on methodology and analysis techniques employed to measure aerodynamic loss, heat transfer coefficient and adiabatic film cooling effectiveness.

3.2 High Speed Linear Cascade Overview

The HSLC is a high speed, blowdown cascade facility, capable of producing engine realistic Mach and Reynolds numbers in a test section comprising five linearly arranged blades and is shown in Figures 3.1 and 3.2. Air is stored in two 400psi tanks and delivered to the test section at the required inlet pressure using a Spirax-Sarco control valve in tandem with an X5 PID controller, which maintains the desired inlet pressure

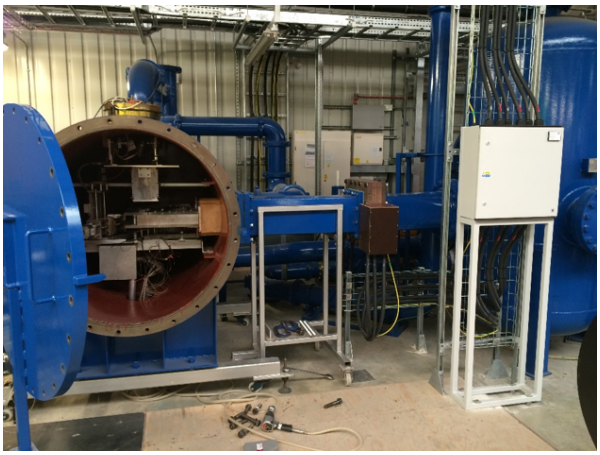


Figure 3.1: The Oxford University High Speed Linear Cascade

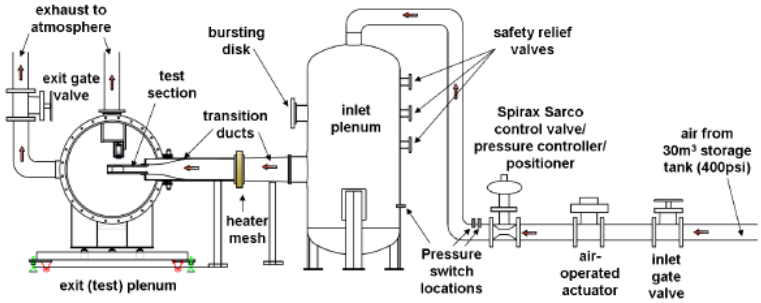
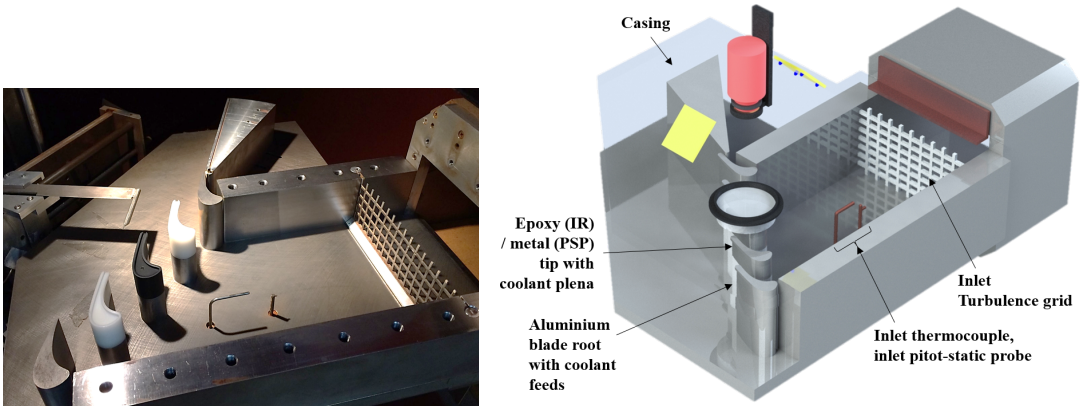


Figure 3.2: Schematic of the High Speed Linear Cascade. From Zhang (2007a)

as the tank pressure drops.

After passing through the control valve, the air enters an inlet plenum or splitting tank. The intended purpose of this tank was to split the flow between two separate exit plena, to enable testing to be performed on two different blade tip geometries simultaneously, for example a commercially sensitive geometry and a publishable geometry. However, this approach was never pursued and in the current set-up, the inlet plenum tank is thought to be redundant.

As already mentioned, the test section comprises five linearly arranged blades or four passages, as shown in Figure 3.3a. The two outer blades are made of stainless steel and span the full height of the test section. The centre three blades have an adjustable tip clearance and consist of two separate parts: a duraluminium blade root; and an interchangeable blade tip which is manufactured either by stereolithography or direct metal laser sintering (DMLS), depending on which experimental technique is



(a) Photo of HSLC test section **(b) CAD of the HSLC test section. (Thanks to Joao Vieira)**

Figure 3.3: HSLC test section

being performed. The centre blade is the test blade from which measurements are taken for all of the experimental techniques used. For all experiments, measurements were taken at tip gap clearances of 0.65 mm and 1.15 mm, as measured by feeler gauges. These tip gaps represent approximately 0.65% and 1.15% of the engine-equivalent blade span (g/S) and will be referred to as such throughout this thesis.

The test section is instrumented with a pitot-static probe and a fast-response K-type 0.0254 mm (0.001 in) diameter thermocouple suitable for transient testing, located one axial chord upstream of the blade row, to enable measurement of the inlet total pressure and inlet total temperature respectively. Figure 3.3 shows the location of this instrumentation in the rig. Included in Figure 3.3 are the inlet turbulence grid, moveable tailboard, to set the passage to passage periodicity and pressure probe installed in a traverse system. Not seen in Figure 3.3 are a series of static pressure tappings on the test section endwall and casing at one axial chord (C_{ax}) downstream of the blade row.

Pressures are measured by a 32-channel pressure measurement unit, developed by O'Dowd (2010). This unit uses an absolute pressure transducer to measure the total pressure at inlet, and all other pressures (32 channels) are measured as differentials to the reference inlet total pressure. Details of the specific pressure transducers can be found in O'Dowd (2010). A GE Druck DPI520 pressure controller is used to calibrate the transducers. Temperatures are measured by K-type thermocouples connected to a 32-

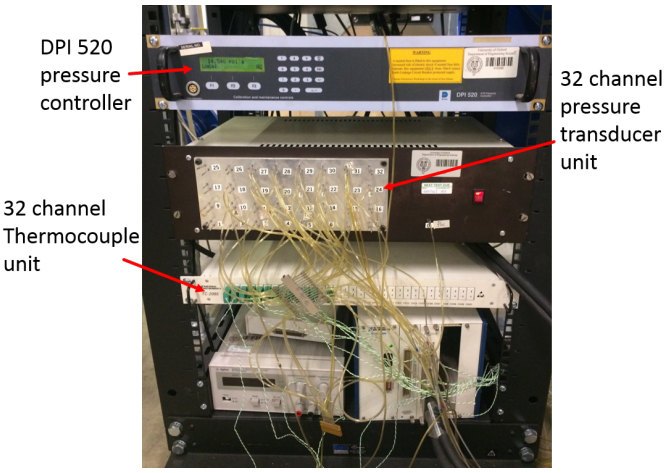


Figure 3.4: Data acquisition and calibration hardware

Test Section Height	71.84 mm
Test Section Inlet Width	201 mm
Axial chord	49.14 mm
Blade pitch	66.46 mm
Inlet flow angle	40.11^o
Exit flow angle	64.23^o
Engine-equivalent blade span	101.78 mm

Table 3.1: HSLC Geometry

channel thermocouple unit. Both the pressure and temperature measurement systems (shown in Figure 3.4) are connected to National Instruments data acquisition (DAQ) cards installed in a PC workstation and measurements are logged via LabVIEW.

For the duration of this research, the HSLC has been using a Rolls-Royce blade geometry with a scaling factor of 1.8 compared to the real blade. Details of the test section geometry are given in Table 3.1. The operating conditions for this blade in the HSLC were determined by Virdi (2015) using a range of inlet total pressures and measuring the exit static pressures. These data were then used for CFD simulations to evaluate the blade loading using the isentropic Mach number at mid-span, which was compared to cascade design data provided by Rolls-Royce. The closest match to the Rolls-Royce data gave the nominal operating conditions used in the HSLC during the current research, which are shown in Table 3.2.

Inlet total Pressure	2.04 $\times 10^5$ Pa
Inlet static pressure	1.92 $\times 10^5$ Pa
Inlet Mach number	0.3
Inlet Reynolds number (based on axial chord)	0.66×10^6
Exit static Pressure	1.0687 $\times 10^5$ Pa
Isentropic exit Mach number	1.01
Exit Reynolds number	1.24×10^6

Table 3.2: HSLC Nominal Operating Conditions

3.3 Modifications to the Rig

Several changes have been made by the author to the HSLC since Virdi (2015), which will be detailed in this section. These include a new specification of heater mesh, turbulence grid with reinforcement mechanism and an upgraded coolant delivery system. There have also been some other alterations to equipment used for specific experimental methods, but these will be covered in the relevant sections.

3.3.1 Heater Mesh

The heater mesh is powered by the lab Drake DC power system (Teager (2015)). The step temperature change produced in the inlet flow (ΔT) by the heater mesh is a function of the power through the mesh ($P = I^2R$), the specific heat capacity of air (C_p) and the mass flow of the inlet air ($\dot{m}$), as defined by Equation 3.1 (see Ireland *et al.* (1999)).

$$P = \dot{m} C_p \Delta T \tag{3.1}$$

The heater mesh used for heat transfer tests at the start of the current research was an SS316, stainless steel, plain weave mesh[1] of dimensions 200 micron aperture, 0.125 mm diameter. This mesh had been used by Virdi (2015) and produced approximately 20^oC of step temperature increase using a set voltage of 90V on the Drake system. However, this specification of mesh was very unreliable. Having worked successfully for a period of time, the mesh failed several times under thermal and mechanical load, with

[1]Manufactured by Plastok (Meshes and Filtration) Ltd.

tears occurring down both sides. A review of other rigs in the lab revealed that this is quite a common occurrence for heater meshes, however this particular specification mesh was remade several times and found to fail after very few cycles. The process of fabricating and replacing the mesh is a lengthy one and multiple mesh failures led to a two month delay in testing.

It was decided to change mesh specification, to that used by Gillespie (1996). The new mesh is of dimensions 40 micron diameter wire, 63 micron aperture, with a resistance of 0.06Ω per square. In the HSLC this specification of mesh produces a 15^oC temperature increase when 80kW of electrical energy is dissipated through it at 1150A and 70V. Note that this corresponds to a set voltage of 90 V on the Drake panel, due to losses inherent in the system.

In the HSLC, the inlet Mach number is calculated to be approximately 0.3 (stated in Table 3.2) using the isentropic relationship between Mach number and total pressure. At this Mach number, the inlet mass flow is estimated to be 3.2 kgs^{-1} at inlet. By Equation 3.1 the 80 kW should have produced a 25^oC step change in inlet temperature. The loss in temperature change can be explained by the positioning of the heater mesh before the boundary layer bleeds. Using Equation 3.1 again, with a delivered power of 80kW, and the recorded ΔT of 15^oC, it is estimated that the actual mass flow through the heater mesh is 5.3 kgs^{-1}, with the difference in mass flow being bled off.

The replacement mesh is significantly thinner than the one used by Virdi (2015) and, at first, there were problems with the mesh failing under mechanical load before the mesh was powered. An example failure is seen in Figure 3.5a. It was discovered that the mesh tabs, top and bottom were coming loose, as the thinner mesh was not being properly held between the layers of insulating tufnol frame. Once loose, the mesh was subject to flutter and was found to rip down the sides soldered to the busbars.

To solve this issue, a thin strip of gasket material was fixed into a groove cut out of the tufnol and additional fixing screws were added in an attempt to hold the frame together more securely; the additional fastenings are shown in Figure 3.5. The combination of



(a) Heater mesh failed under mechanical load

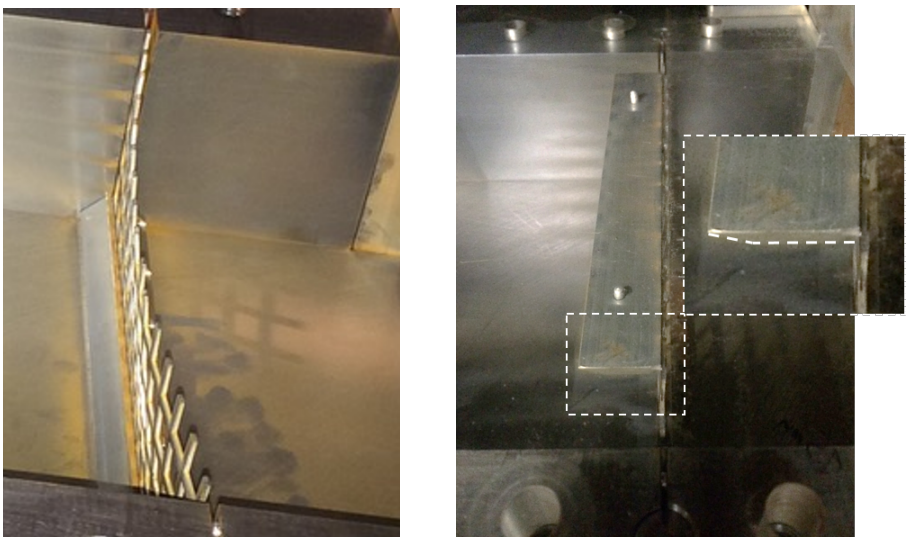
(b) Heater mesh failed under thermal load

Figure 3.5: Examples of heater mesh failure

the latter and the gasket strips were successful at holding the mesh in place. Since the mechanical mesh failure problem was solved, only two meshes have been put in the rig. The first failed under thermal load after 16 runs (Figure 3.5b) and the second is still working, with over 60 runs to date. To further mitigate the impact of a mesh failure, in terms of lost testing times, the author commissioned three spare meshes which are stored in case of future failure.

3.3.2 Inlet Turbulence Grid

The turbulence grid is fixed at the sides of the test section, and supported at the bottom by a compact wedge. Before the start of the test campaign the mesh was unsupported along the top edge, near the wall representing the casing. Inspection showed that the grid had bowed under aerodynamic loading (see Figure 3.6a), leaving a small gap between the top of the grid and casing. To combat this deformation, an additional support was manufactured and fixed to the top of the casing wall. The support was designed to sit flush with the grid profile, so as to restrict the flow as little as possible and the trailing edge of the support was machined to remove any 'backwards facing step', as shown in Figure 3.6b.



(a) Inlet turbulence grid bowed under load

(b) Inlet turbulence grid with support

Figure 3.6: Inlet turbulence grid

It should be noted that this modification was in place for all the experiments performed by the author, however the inlet boundary layer may be different from that measured by O'Dowd *et al.* (2010b). A swan neck pitot probe was designed and manufactured to take inlet boundary layer pressure measurements for the new set-up, however sufficient time was not available to take these measurements.

3.3.3 Coolant Feed System

The most significant change made to the HSLC is a total redesign of the coolant delivery system. The old system, detailed in O'Dowd (2010) and Virdi (2015), was designed to provide film cooling of below ambient temperature, via the use of vortex tubes. This was to enable an experimental film cooling effectiveness to be calculated using the adiabatic wall temperatures of the cooled and uncooled case. To get a sensible result from this method, there must be a sufficient temperature difference between the inlet (mainstream) air and the coolant air, with the cooling provided by vortex tubes. The coolant mass flow rate in the existing system was measured using an orifice plate, which was designed to deliver a specific mass flow rate to the tip to ensure a coolant to mainstream total pressure ratio of 1.08.

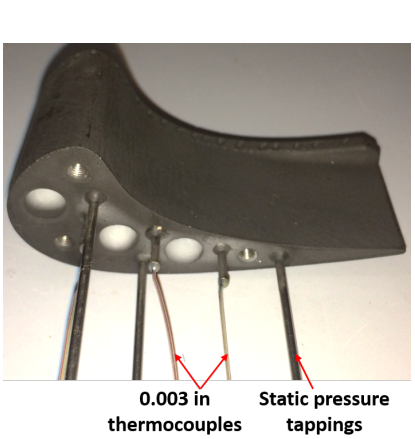
Trials with the facility revealed challenges with the existing method of measuring film cooling effectiveness. The difference between the mainstream (or tip temperature) and the temperature of the coolant causes conduction effects to occur in regions of high thermal gradient or around cooling holes, which can lead to large errors in calculated cooling effectiveness. For this reason, the author initiated the transition of the facility to the use of pressure sensitive paint and foreign gas to measure film effectiveness. The pressure sensitive paint technique has been used extensively in literature to measure film cooling effectiveness, as discussed in Section 2.5.5. This technique will be described in detail, as used in the current research, in Section 3.6.

The design of a new, fully controllable coolant feed system, required for use with this technique, is detailed below. Since the pressure sensitive paint method is based on the mass-transfer analogy (Section 3.6.2), ambient temperature coolant can be used, which minimised problems of thermal conduction and removes the need for vortex tubes in the system.

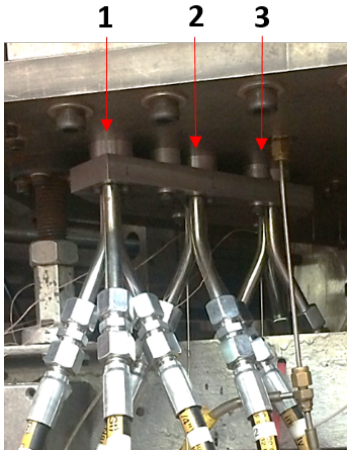
3.3.3.1 Blade Root and Base Plate

In the previous coolant system, each cooled blade had a single plenum, fed by a single coolant hose. The design intent was that the same total pressure would be supplied to the inlet of each cooling hole, so that the mass flow of coolant out of an individual hole would simply be determined from the ratio of coolant total pressure to local static pressure at the hole exit; the local blade surface static pressure varies over the tip, hence determining the coolant distribution.

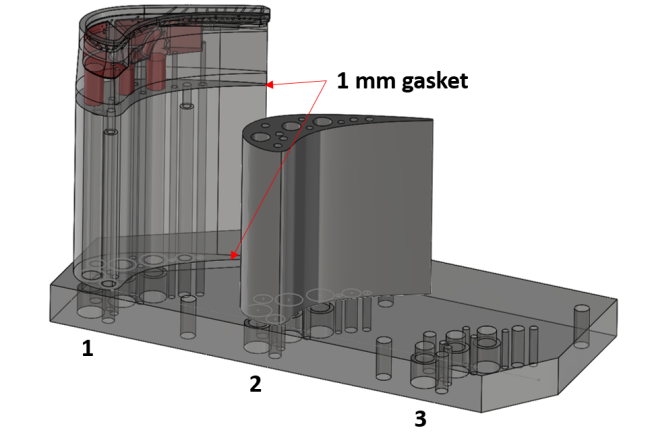
To enable some control over the distribution of coolant, the new system was designed with three plena in each blade; one in the leading edge region of the blade, one in the central portion and one towards the trailing edge, in an arrangement similar to the passages in a serpentine (or multi-pass) turbine blade cooling system. The coolant mass flow is controlled by three Omega mass flow controllers (MFCs). Each MFC feeds either the leading edge, central or trailing edge plena of all three blades, allowing the coolant



(a) Cooled blade tip instrumentation



(b) Coolant feed inside HSLC



(c) CAD assembly of blade root, base plate and blade tip

Figure 3.7: Components of the coolant feed system inside the HSLC

mass flow in each of these tip regions to be controlled individually. The plena of the tips are instrumented with thermocouples and static pressure tappings (see Figure 3.7a) and the split of coolant mass flow between each blade is balanced using three controllable needle valves which were adjusted to equalise the plena static pressure (see Figure 3.8) between each of the three blade tips.

The new blade root and base plate were machined in house via a CNC machine. The blade root was designed to fit the existing test section base. Figure 3.7b shows some details of the coolant feed system inside the HSLC. The black and yellow $1/4in$ hoses can be seen connected to 6 mm internal diameter aluminium pipes, which are fixed directly into the base plate with Loctite sealant rated for the range of pressures to be

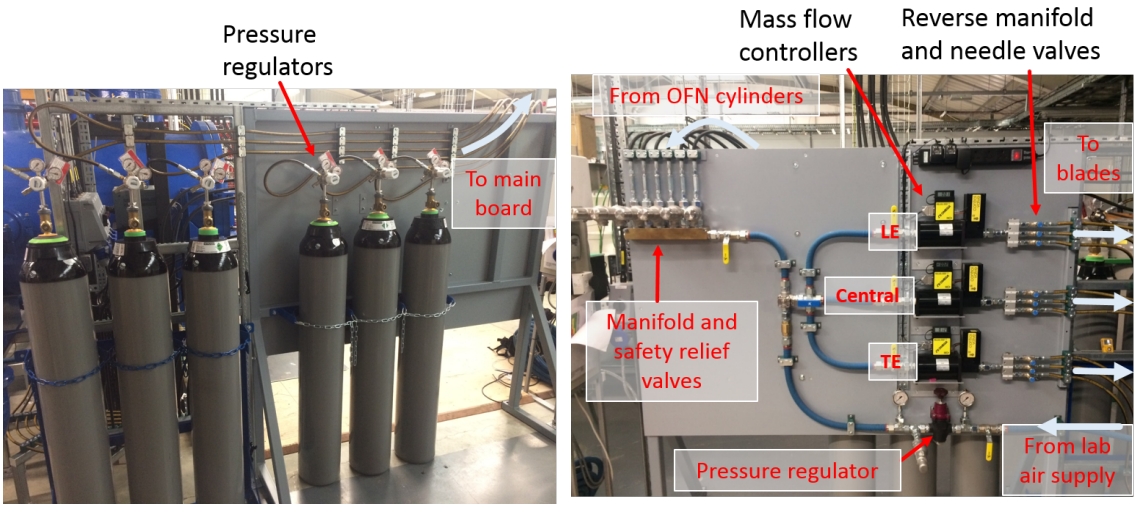
used. To seal between the base plate and blade root, and between the root and blade tip, 1 mm gasket was cut to the shape of the blade root and fixed to either end of the root. The location of the gasket is indicated in Figure 3.7c. Also seen in Figure 3.7c are locations of the plena in the blade tip (highlighted in red), coolant feed holes through the blade root and base plate, as well as other holes drilled for instrumentation and fastening the component parts together. The blades are labelled 1 - 3 for comparison between Figures 3.7b, 3.7c and 3.8c.

3.3.3.2 Control Systems and Pipework

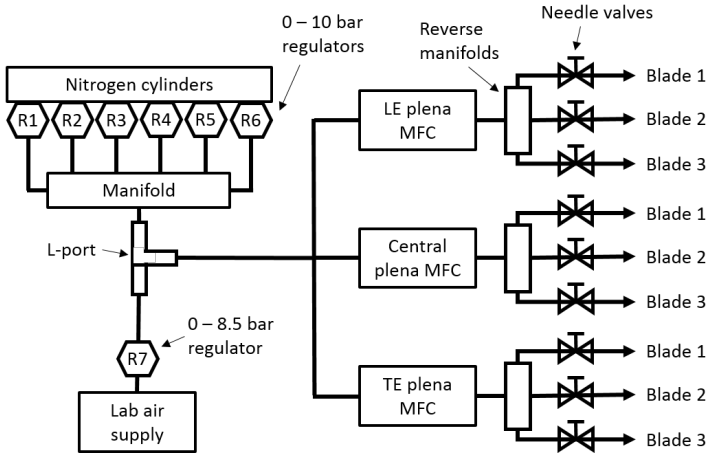
The coolant feed system was designed to satisfy two criteria. Firstly, it was to be able to deliver both Oxygen Free Nitrogen (OFN) gas and air for use as coolant, as required by the pressure sensitive paint method (discussed in section 3.6.1). Secondly, the feed system must be able to deliver a controllable mass flow rate of coolant to three plena inside each of three separate blades (as previously discussed). The coolant feed system can be seen in Figure 3.8. Additionally, the hoses and valves throughout were sized following an analysis based on estimates of the mass flow and pressure that would be present in each portion of the system, with the aim of preventing the coolant from choking over the full range of mass flows the system would be capable to deliver.

The maximum mass flow rate deliverable is limited by the size of the MFCs. The chosen Omega mass flow controllers have a maximum capacity of approximately 20 g/s each, dependant on the density of the coolant fluid.

The system is either fed from six 230 bar OFN cylinders or the lab's 100 psi air supply. Each OFN cylinder is fitted with a 0 - 10 bar pressure regulator (Figure 3.8a) which is used to reduce the pressure in the system to a maximum of approximately 7 bar; this maximum is limited by a series of safety relief valves which are set to exhaust if the system pressure exceeds 7 bar +10%. This value of 7 bar was chosen to match the lab air supply pressure. On the air feed side of the system, a 0 - 8.5 bar regulator was used to set the pressure upstream of the MFCs to a suitable value relative to the



(a) HSLC coolant system N_2 cylinders **(b) HSLC coolant system board**



(c) HSLC coolant system schematic

Figure 3.8: HSLC coolant system

required coolant mass flow. If the upstream pressure is too high, the coolant mass flow rate is observed to continually oscillate with a large amplitude, as small adjustments of the MFC result in a large change in pressure. By regulating the upstream pressure, the MFCs are able to use a larger proportion of their full range and any fine adjustments of the MFC valve do not produce a large variation in output pressure or mass flow.

The total mass flow capacity of the system was seen to be limited on the nitrogen supply side. With the $1/4in$ hoses used between OFN cylinder regulators and manifold, the maximum mass flow of coolant that can be delivered from a single cylinder at 7 bar was found to be approximately 8 g/s. This amounts to a total of 16 g/s per blade, which is 4 g/s per blade less than the maximum allowable by the MFCs. However, this is more

Total coolant mass flow capacity	16 g/s	2% of passage flow
Typical turbine blade tip requirement	8 g/s	1% of passage flow
Leading edge plenum proportion		24% (of total)
Central plenum proportion		18%
Trailing edge plenum proportion		58%

Table 3.3: HSLC coolant system capacity and coolant distribution (all per blade tip)

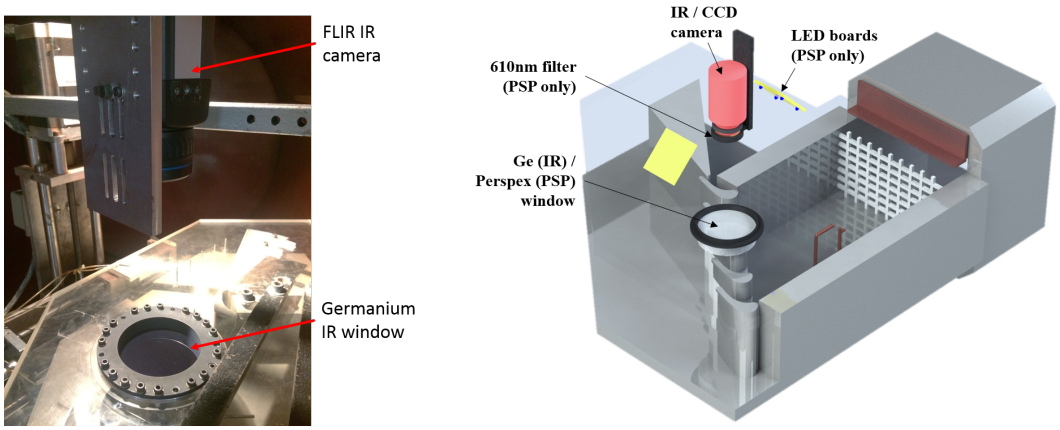
than enough given that the tip coolant mass flow requirement for a typical turbine blade is approximately 1 % of passage flow. The HSLC passage flow is approximately 0.8 kg/s, so a typical tip coolant requirement would be 8 g/s per blade. The coolant mass flow rates tested were a nominal design rate and 150% of nominal. These mass flows were further split into a design intended distribution between the LE, central and TE plena of approximately 24%, 18% and 58% respectively. The capacity of the coolant system and the coolant distribution are summarised in Table 3.3.

3.4 Heat Transfer Coefficient Measurements

This section discusses the experimental set-up, methodology and analysis technique used to measure the heat transfer coefficient on the blade tip.

3.4.1 Equipment and Methodology

The heat transfer coefficients over the tip surface of the central blade were measured via a transient technique that used IR thermography. As discussed in Section 3.3.1, the dissipation of 80kW of electrical energy through the heater mesh produces a 15^{o}C step change in inlet temperature. The temperature response of the blade tip surface during the transient period is recorded using an IR camera. Two different IR cameras were used during the experimental campaign. For a majority of the uncooled testing a FLIR A20M camera was used. This is a 320x240 pixel, 8-bit camera capable of measuring 256 (2^8) discrete temperature levels in greyscale within a manually adjustable range. The FLIR A20M was set up to record a temperature range of 0 - 50^{o}C at 30 fps, so



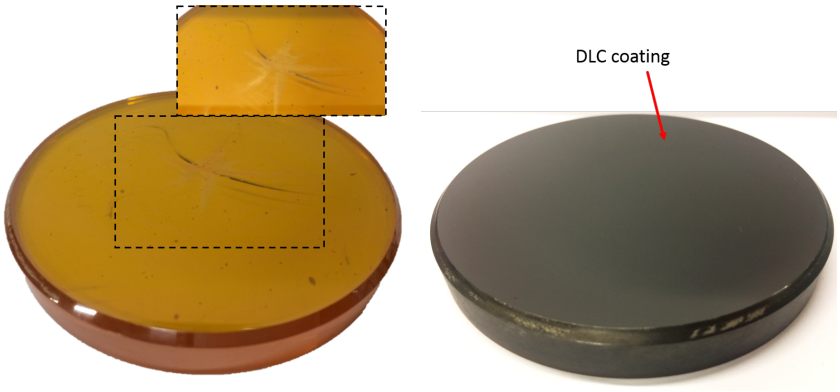
(a) IR thermography equipment in the HSLC **(b) CAD of IR thermography set-up. (Thanks to Joao Vieira)**

Figure 3.9: IR thermography set-up for heat transfer testing

that each greyscale level corresponded to 0.2^{o}C. Later on in the experimental campaign the camera was upgraded to a FLIR A655sc camera, which records images at a higher resolution of 640x480 at 50 fps and has a much higher dynamic range of 16-bit. The FLIR A655sc measures a temperature range of -40 - 150^{o}C, providing a much improved measurement resolution of 0.003^{o}C per level. The outcome of the upgraded camera was a significant improvement in image quality for the cooled heat transfer tests (and final uncooled tests) and reduced uncertainty of measurement, as will be demonstrated in Section 3.4.3.

The experimental set-up for the heat transfer tests is shown in Figure 3.9. An IR window is placed above the central test blade and forms the top of the tip gap. For the early uncooled tests a Zinc Selenide (ZnSe) window was used; the same as in previous testing of O'Dowd (2010) and Virdi (2015). However, degradation of the anti-reflective coating (applied to increase IR transmission) and window surface started to occur towards the end of the uncooled tip testing (see Figure 3.10a). ZnSe has a fairly low Knoop [2] hardness, meaning that it susceptible to indentations in the surface. Particles in the mainstream flow, especially particles which are blown through the test section after a heater mesh failure were responsible for the erosion of the coating and window surface.

[2]The hardness of a material defines its resistance to indentation. Knoop hardness testing is a test for microhardness in which a load is applied to a diamond indenter to make an indention in the material, which is measured and converted to a Knoop hardness value.



(a) Zinc Selenide window showing degradation **(b) Germanium IR window**

Figure 3.10: IR windows used during heat transfer testing

This erosion was assessed to have negligible depth but may have affected the optical properties of the window. It was possible to rotate the window so as to misalign the blade tip and eroded portion, however further testing was worsening the erosion. Before the cooled heat transfer tests were begun, the ZnSe window was therefore replaced with an IR window made from Germanium. Germanium is a much harder material, with the same crystalline structure as diamond and in addition was coated with a diamond-like-carbon (DLC) coating, to further improve the resistance of the window to particulate impact and hence the longevity of the window. Both the ZnSe and Ge windows are shown in Figure 3.10.

The recorded temperature from the IR camera depends on several factors other than simply the surface temperature: the percentage transmission of incident IR light through the window; and the IR emissivity of the surface being measured, which is maximised by spraying the test blade with a matte black paint. To account for both of these factors in the measured temperature (or grayscale value for the FLIR A20M camera), an in-situ calibration is performed using a thermocouple attached to the blade surface. A 0.0762 mm (0.003 in) K-type thermocouple is used for this purpose, as seen in Figure 3.11. The temperature data from the camera pixel corresponding to the thermocouple location is plotted against the recorded camera data just before and after the transient period. A regression analysis of these data (shown in Figure 3.12a) gives a

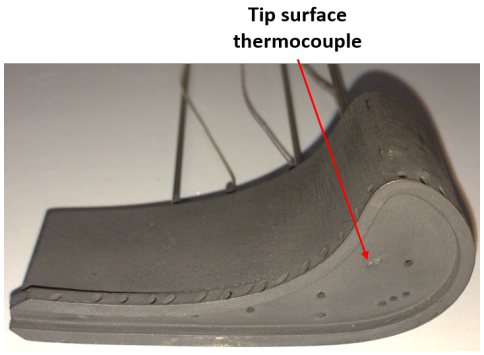
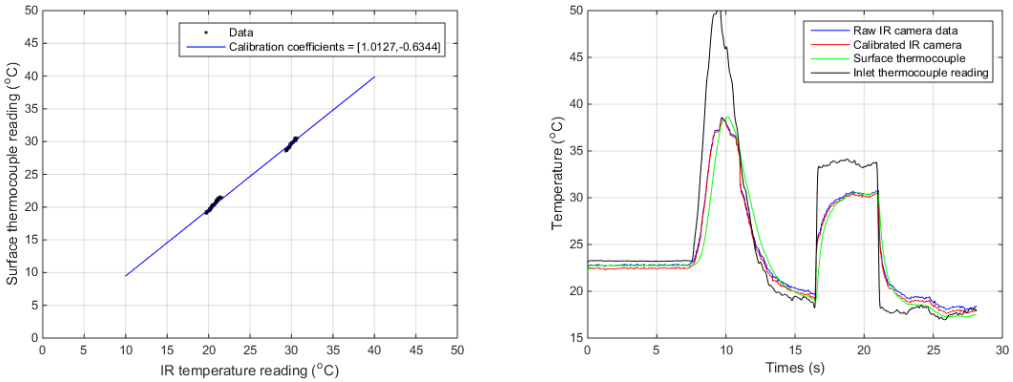


Figure 3.11: Location of tip surface thermocouple for calibration



(a) IR calibration regression

(b) Temperature trace of inlet thermocouple, surface thermocouple and recorded IR data

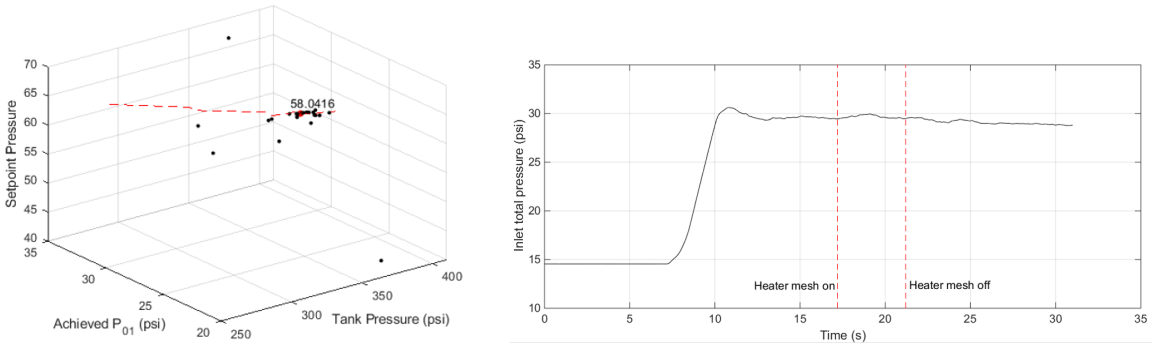
Figure 3.12: Example of IR in-situ calibration

set of calibration coefficients which are applied to the recorded IR data from the camera at every coordinate location on the tip. By this method, a temperature trace for each coordinate on the tip surface can be produced.

An example of the measured temperature profile during a transient test is shown in Figure 3.12b. The sudden opening of the Spirax-Sarco valve causes a compression heating effect to occur, which initially raises the mainstream and tip surface temperature. However, the analysis method used (see Section 3.4.2) removes any errors caused by this pre-heating on the calculated heat transfer coefficients. Following a period of temperature decrease as the high speed flow passes over the tip, the heater mesh is activated for approximately 4 seconds, producing a step increase in the inlet temperature. It was found that the length of the transient period which can be used for calculation of the heat transfer coefficient is approximately 0.8 seconds, before the difference between the

Proportional Band (P_b)	180
Integral Time (T_i)	0
Derivative Time (T_d)	0

Table 3.4: X5 PID controller settings for transient heat transfer testing



(a) Interpolation of pressure setpoint from database at 385 psi tank pressure

(b) Inlet pressure profile during typical transient heat transfer test

Figure 3.13: Example of pressure setpoint interpolation and resulting inlet pressure profile for a transient heat transfer test

tip surface temperature and the adiabatic wall temperature becomes too small which increases errors in the calculated heat transfer coefficient.

The total elapsed time required for a transient heat transfer test is approximately 25 s. During this time the pressure in the 400 psi tank drops by around 35 psi. The PID settings which can be adjusted by the X5 PID controller are the proportional band (P_b), integral time (T_i) and derivative time (T_d). For a transient heat transfer test the values used can be found in Table 3.4.

It was important for the inlet pressure to be as steady as possible during the transient tests, as any oscillation in inlet pressure causes variation in the inlet temperature profile which complicates the calculation of heat transfer coefficient. Any form of integral or derivative control was found to cause large oscillations in the inlet pressure and temperature, so both the integral time and derivative time were set to zero, effectively switching off the derivative and integral terms in the controller. The lack of an integral term results in two other outcomes: firstly there was a large offset between the pressure setpoint input to the controller and the desirable inlet total pressure (29.6 psi); secondly the controller was not able to correct for a drop in the tank inlet pressure during a

blowdown test. To address these issues, a database of tank starting pressure, achieved inlet total pressure and controller setpoint pressure was built up and an interpolation performed in MATLAB based on the current tank pressure before each test, to find the suitable controller setpoint. An example of the interpolation and resulting inlet total pressure during a transient run can be seen in Figure 3.13.

3.4.2 Analysis Techniques

For a one-dimensional, unsteady solid, Fourier's Law of heat conduction can be given written as:

$$k\frac{\partial^2 T}{\partial x^2} = \rho C_p \frac{\partial T}{\partial t} \tag{3.2}$$

Equation 3.2 can be solved using the following initial conditions (Equation 3.3) and boundary conditions relating to the experimental method described in Section 3.4.1. These boundary conditions describe the convective heat transfer due to a transient step change in temperature (Equation 3.5) being applied to the flow over an a thermally insulating blade tip, which can be considered as a semi-infinite solid (Equation 3.4).

$$T(x, t = 0) = T_i \tag{3.3}$$

$$T(x = \infty, t) = T_i \tag{3.4}$$

$$at \;\; x = 0, \;\; -k\frac{\partial T}{\partial x} = h(T_{ad} - T_w) \tag{3.5}$$

The solution of Equation 3.2 subject to the given initial and boundary conditions with a step change in gas temperature is shown in Equation 3.6.

$$\frac{T_w(x,t) - T_i}{T_{ad} - T_i} = 1 - \text{erf}\left(\frac{x}{2\sqrt{\alpha t}}\right) - \left[\exp\left(\frac{hx}{k} + \frac{h^2\alpha t}{k^2}\right)\right]\left[(1 - \text{erf})\left(\frac{x}{2\sqrt{\alpha t}} + \frac{h\sqrt{\alpha t}}{k}\right)\right] \tag{3.6}$$

This particular solution of Fourier's law of heat conduction for a one-dimensional,

transient, semi-infinite solid, with convective boundary conditions has been demonstrated in Schneider (1955).

To determine the heat transfer on the blade tip surface, Equation 3.6 should be evaluated at $y = 0$ as follows:

$$\frac{T_w(t) - T_i}{T_{ad} - T_i} = 1 - \left[\exp\left(\frac{h^2 \alpha t}{k^2}\right)\right]\left[\text{erfc}\left(\frac{h\sqrt{\alpha t}}{k}\right)\right] \tag{3.7}$$

Equation 3.7 can be further simplified to Equation 3.8 using the relationships $\text{erfc}\,(y) = 1 - \text{erf}\,(y)$, $\alpha = k/(\rho C_p)$ and $\sqrt{\alpha}/k = 1/\sqrt{\rho C_p k}$, where $\sqrt{\rho C_p k}$ is the thermal product of the tip material.

$$\frac{T_w(t) - T_i}{T_{ad} - T_i} = 1 - \left[\exp\left(\frac{h^2 t}{\rho C_p k}\right)\right]\left[\text{erfc}\left(\frac{h\sqrt{t}}{\sqrt{\rho C_p k}}\right)\right] \tag{3.8}$$

In Equation 3.8 there are two unknown quantities, h and T_{ad}. There are several methods available to evaluate these two unknowns, which have been discussed in detail in O'Dowd (2010); a brief overview will be given here.

The first method is an idealised approach which solves Equation 3.8 for $T_w(h, T_{ad}, t)$ for an applicable range of h, T_{ad} at a range of times, t, and determines h and T_{ad} by finding the minimum difference between $T_w(h, T_{ad}, t)_{calc}$ and $T_{w,meas}$. However, this technique is less suited for use in the HSLC for several reasons: firstly, the gas temperature change is not a perfect step change; secondly, due to the isentropic compression heating process which occurs at rig start-up (detailed in Section 3.2), which means that the isothermal assumption $T_t = T_w = T_i$ is not satisfied before the heater mesh is turned on.

In order to account for the isentropic compression heating, a method of heat flux reconstruction is used to calculate a time trace of tip heat flux from the measured tip surface temperatures recorded by the IR camera. The first of these heat flux reconstruction methods was developed in Oldfield *et al.* (1978) and uses the finite difference method shown in Equation 3.9. In this equation, τ is the time interval between temperature readings, m is the number of temperature readings taken and n is the integration

variable.

$$\dot{q}(t) = \dot{q}(mt) = \left(\frac{2\sqrt{\rho C_p k}}{\sqrt{\pi \tau}} \right) \sum_{n=0}^{m} \left[(T_{n+1} + T_{n-1} - 2T_n)(m-n)^{1/2} \right] \tag{3.9}$$

The finite difference method of heat flux reconstruction has the added advantage of being computationally more efficient than the idealised approach, and therefore more suitable for high sampling rates of data at high numbers of locations on the tip, as with recorded IR camera data. However, the efficiency can be increased further by use of another heat flux reconstruction method, known as the Impulse Response method, also developed by Oldfield (2008). This is the chosen approach for the current work and will be detailed here.

The Impulse Response method works on the basis of deriving a discrete impulse response function $h[n]$, using a known pair of analytical solutions to the heat conduction equation, and then computing the discrete convolution sum in Equation 3.10 to calculate the heat flux, q, from recorded temperature data, T, on the tip surface. This convolution sum is computed in MATLAB using the built in Fast Fourier Transform function *"fftfilt"*, as shown in Equation 3.11.

$$q[n] = h[n] * T[n] = \sum_{k=0}^{N-1} h[k]T[n-k] = \sum_{k=0}^{N-1} h[n-k]T[k] \tag{3.10}$$

$$q = fftfilt(h, T) \tag{3.11}$$

In Equation 3.10, $h[n]$ is the discrete impulse response function, $T[n]$ is the recorded tip surface temperature data, $q[n]$ is the computed surface heat flux, all in the discrete time domain, n is the sample number, k is the summation variable and N is the number of temperature data points recorded at each location.

Of course, to evaluate this convolution sum, first the specific impulse response function must be derived, relating to current experimental set-up. This is done by a discrete deconvolution of Equation 3.12 for a known pair of analytical solutions, q_1 and T_1. This discrete deconvolution is performed by taking z-transforms, and convoluting with

a discrete impulse function, $\Delta(z)$, to produce Equation 3.13.

$$q_1[n] = h[n] * T_1[n] \tag{3.12}$$

$$H(z) = H(z)\Delta(z) = \frac{Q_1(z)}{T_1(z)}\Delta(z) \tag{3.13}$$

In MATLAB, this deconvolution is carried out by the *"filter"* function, as shown in Equation 3.14, using a discrete impulse function $\delta[n] = 1, 0, 0, 0, ...$ and a unit step in q_1.

$$h = filter(q_1, T_1, \delta) \tag{3.14}$$

Here the function used to generate $h[n]$ is that of the response in $T_1(t)$ to a step in $q_1(t)$. The solution to the heat conduction equation relating to this function, for a semi-infinite model is as follows:

$$T_1(t) = \frac{2}{\sqrt{\rho_1 C_{p1} k_1}}\sqrt{\frac{t}{\pi}} \tag{3.15}$$

Common to both heat flux reconstruction methods, once the heat flux has been reproduced from the recorded temperature trace, a regression analysis of heat flux versus temperature is performed. This is expected to produce a linear relationship as per the convective heat transfer equation (Equation 3.16), as shown in Figure 3.14:

$$\dot{q} = h(T_{ad} - T_w) \tag{3.16}$$

Due to this linear relationship, the heat transfer coefficient for each coordinate point can be determined by the gradient of the slope in Figure 3.14 and the local adiabatic wall temperature can be determined from the intercept with the temperature axis, which represents zero heat flux. It should be noted that the calculated heat transfer coefficient levels presented throughout the current research are at rig conditions and that engine values of heat transfer coefficient would be approximately 7 times higher due to Nusselt number scaling.

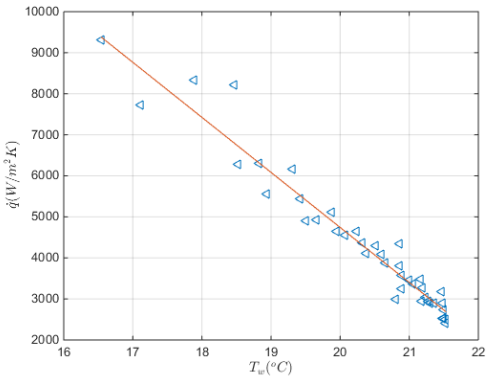


Figure 3.14: Example regression plot of heat flux versus tip surface temperature for a single location during transient period

The beauty of the Impulse Method is that the digital filter designed by Equation 3.14 only has to be computed once, and can then be applied to the temperature data at each coordinate point on the blade tip. This gives it an advantage in computational efficiency over the finite difference method, in which the calculation in Equation 3.9 must be computed at every location, making the method very laborious for high sampling frequency data at a high number of coordinate points. In practice, this makes the Impulse Method far superior for use with modern day IR cameras of high resolution, capable of recording a high number of frames per second.

3.4.3 Uncertainty Analysis

The uncertainty in heat transfer coefficient measurements was determined as a function of the tip material properties (specifically the thermal product) and the measured wall temperature used to evaluate the tip heat flux via the impulse method (see Section 3.4.2). The uncertainty in HTC was calculated using the root-sum-square method (RSS) in Equation 3.17, as described by Kline & McClintock (1953).

$$\delta h = \left[\left(\frac{\partial h}{\partial \sqrt{\rho C_p k}} \delta \sqrt{\rho C_P k} \right)^2 + \left(\frac{\partial h}{\partial T_w} \delta T_w \right)^2 \right]^{\frac{1}{2}} \tag{3.17}$$

where the first term on the right hand side is the individual uncertainty in heat transfer coefficient, h, due to the uncertainty in the thermal product, $\sqrt{\rho C_p k}$, and the second

term is the uncertainty in h due to the uncertainty in measured (calibrated) wall temperature, δT_w.

The tip material was an epoxy resin, DSM Somos GP Plus 14122, which was also used by Virdi (2015). This material has a manufacturer specified thermal product of 644 $Ws^{1/2}m^{-2}K^{-1}$. The manufacturer did not specify an uncertainty level, so this was assumed to be 5.2% ($\pm 33.5 Ws^{1/2}m^{-2}K^{-1}$), as per the experimental calculation of thermal product for an SI40 epoxy resin material performed by Zhang (2007b) (This SI40 material was used by O'Dowd (2010), where the quoted $\sqrt{\rho C_p k}$ was 627 $\pm$ 33 $Ws^{1/2}m^{-2}K^{-1}$). A perturbation analysis, described by Moffat (1988), was used to calculate the change in HTC due to this uncertainty interval in $\sqrt{\rho C_p k}$. First the HTC was calculated with a baseline $\sqrt{\rho C_p k} = 644 Ws^{1/2}m^{-2}K^{-1}$. The perturbed result of HTC was then evaluated using $\sqrt{\rho C_p k} = 676 Ws^{1/2}m^{-2}K^{-1}$. The change in HTC approximates $\partial h / \partial \sqrt{\rho C_p k}$ in Equation 3.17 and was directly proportional to the perturbation in $\sqrt{\rho C_p k}$.

To evaluate the second term in Equation 3.17, knowledge of the uncertainty interval of the measured wall temperature, δT_w, is required. The uncertainty in measured wall temperature is a function of the uncertainty in recorded IR camera reading, the in-situ calibration and the recorded tip surface thermocouple data, and can be described by the root-sum-square shown in Equation 3.18:

$$\delta T_w = \left[\left(\frac{\partial T_{tc}}{\partial T_{cam}} \delta T_{cam} \right)^2 + \left(\frac{\partial T_{tc}}{\partial T_{cam}} \frac{\partial T_{cam}}{\partial L} \delta L \right)^2 + (\delta T_{tc})^2 \right]^{\frac{1}{2}} \tag{3.18}$$

where T_{tc} is the surface thermocouple temperature, T_{cam} is the IR camera reading (either temperature for the FLIR A655 or greyscale for the FLIR A20M), and L is the defined pixel location of the surface thermocouple on the IR camera image.

The first term on the right hand side of Equation 3.18 represents the uncertainty in the calibrated IR camera reading (T_w) due to the bit error and noise on the IR camera, which was determined analytically by multiplying δT_{cam} by the calibration coefficient $\partial T_{tc} / \partial T_{cam}$, which represents the gradient of the calibration line in Figure

Camera Name	Uncertainty Contribution (K)			Overall Uncertainty, δT_w (K)
	Camera	Spatial	Thermocouple	
FLIR A20M	0.241	0.585	0.020	0.632
FLIR A655	0.10	0.28	0.020	0.298

Table 3.5: Absolute Uncertainty in calibrated wall temperature, T_w, due to various factors

3.12a. The second term represents the uncertainty in the calibrated camera reading due to errors in the relative location of the tip surface thermocouple and IR pixel location, L, defined during the calibration process. This uncertainty was evaluated by a perturbation analysis of the defined pixel location, L, within a box surrounding the estimated (original) thermocouple location. The difference between the original calibrated T_w and the average perturbed value was used as the uncertainty interval of T_w due to spatial location of the thermocouple. The third term represents the uncertainty in the recorded thermocouple temperature used in the calibration, which was determined from the twice the standard deviation of the thermocouple reading (filtered) when the tip surface temperature was known to be steady i.e. before the rig is turned on.

The uncertainty calculations were performed identically for both the FLIR A20M (old camera) and the FLIR A655 (new camera), so that a comparison may be drawn about the relative uncertainties of results taken with each camera. The absolute overall uncertainties in T_w are shown in Table 3.5, along with the individual contributions of each term of Equation 3.18. It can be seen that the spatial uncertainty in thermocouple location produces the largest source of error, as this alters the calibration coefficients. The area around which the thermocouple pixel was perturbed represents a significant area on the tip, but this value demonstrates the likely errors which could occur from inaccurate placement L.

Returning to Equation 3.17, the change in h due to the uncertainty in T_w was evaluated by a Monte Carlo analysis, which was previously employed by Brunner *et al.* (2007) to assess errors in HTC on a low pressure turbine blade surface. In the Monte Carlo analysis, T_w is perturbed at every pixel location by random noise with a standard deviation defined as $\sigma = \delta T_w/2$. Since the original values of h vary over the tip, taking

Camera Name	Uncertainty Contribution		Overall Uncertainty, δh
	Thermal Product	Measured wall temperature	
FLIR A20M	5.0	9.5	10.7 %
FLIR A655	5.0	4.7	6.9 %

Table 3.6: Uncertainty in heat transfer coefficient, h, for both IR cameras as a percentage of mean original result

the standard deviation of the perturbed result was not suitable for determining the uncertainty in h. Instead, the original result was compared to the result with added noise and the change in averaged h was used as the uncertainty in h due to δT_w. This process was performed for test results gained with both cameras and the resulting uncertainties in heat transfer coefficient can be found in Table 3.6. It can be seen that the uncertainty in h due to δT_w has reduced for the new camera, with a corresponding effect on the overall uncertainty in h.

3.5 Aerodynamic Loss Measurements

This section describes the experimental procedure for calculation of the total pressure loss coefficient downstream of the blade row. Details of the pressure probes and their calibration are included here, along with discussion of the chosen total pressure loss coefficient. The periodicity in the HSLC will also be examined here as that bares relevance on the downstream plane at which the pressure loss coefficient was evaluated.

3.5.1 Equipment and Methodology

Aerodynamic loss measurements were taken by traversing one of two pressure probes over a uniform grid consisting of 26 pitchwise locations and 7 spanwise locations. The experimental set-up can be seen in Figure 3.15. A dual axis traverse system, driven by stepper motors was used to traverse the probe over a plane 50% of the blade axial chord (C_{ax}) downstream of the blade row. The 50% C_{ax} downstream plane was found to have improved periodicity over a plane 100% C_{ax} downstream, for reasons which will be

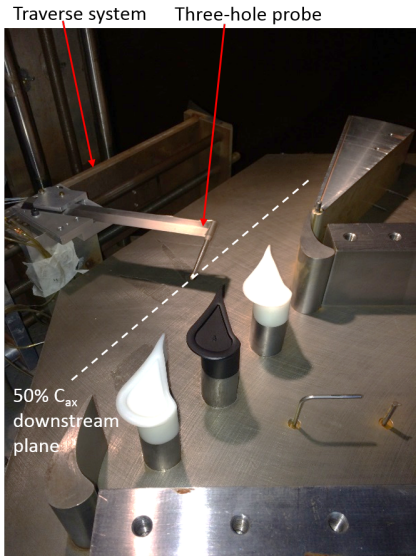


Figure 3.15: Experimental set-up for aerodynamic loss measurements

discussed in Section 3.5.3. In the pitchwise direction, measurements were taken over a full blade pitch which displayed the best periodicity; these locations were kept constant throughout testing.

During each blowdown run the probe was traversed along all 26 pitchwise locations at a particular spanwise height. The probe traverse system was controlled by Labview and was programmed to take a reading (for 0.5 s), move, pause for 0.5 s, take a reading and repeat. This process ensured measurements were not influenced by probe motion or the probe settling time. Following completion of a blowdown test, the probe was then moved to the next spanwise location before the next test. Aerodynamic loss measurements required a longer run time than transient heat transfer tests, to allow for measurements to be taken at all 26 pitchwise locations. A typical test took approximately 90 s, during which time the 400 psi tanks drop by around 110 psi. To keep a steady pressure for this long, some integral control was required on the X5 PID controller. Following an extensive, systematic survey of the tunnel operating conditions at various PID settings, it was found that the PID settings in Table 3.7 were suitable for this purpose. The resulting inlet pressure profile during a typical aerodynamic loss test can be seen in Figure 3.16.

Two pressure probes were used to measure the total pressure downstream of the

Proportional Band (P_b)	100
Integral Time (T_i)	3
Derivative Time (T_d)	0.5

Table 3.7: X5 PID controller settings for aerodynamic loss testing

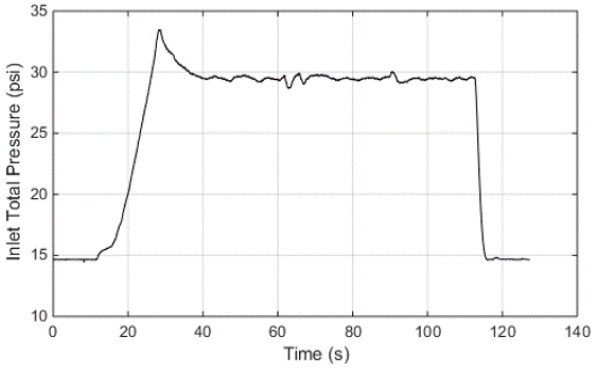


Figure 3.16: Inlet pressure profile during a typical aerodynamic loss conditions test

cascade blade row; a three-hole probe and a single-hole probe. The three-hole probe consists of three stainless steel tubes of 0.4 mm inner diameter and 0.7 mm outer diameter, giving a probe width of 0.7 mm in the spanwise traverse direction. The probe is designed to be insensitive to Reynolds number, with sharp edges and a 60^o angled face machined on the outer two holes. The three-hole probe was used to measure the total pressure between the top 4% and 25% of the engine equivalent blade span, close to the casing (4 mm to 25 mm away from the casing). However, due to the width of the probe sting, the three-hole probe could not measure any closer to the casing than 4 mm. To resolve the top 4% of the blade span the single-hole probe was used. The single-hole probe comprises one tube of 0.7mm outer diameter, which is mounted level with the top of a flat stem. This design allows measurement within 0.5mm of the casing. Further details of the design of both probes can be found in O'Dowd (2010).

Following preliminary testing it was decided to set the probe angle of the three-hole probe to 63^o (to the inlet flow), which is very similar to the design blade exit flow angle of 64.2^o. The reason for this choice in probe angle will be discussed in Section 3.5.2. The single-hole probe was set to an original angle of 63^o and then manually rotated through $+/-10^o$. The total pressure and approximate flow angle from the single-hole probe

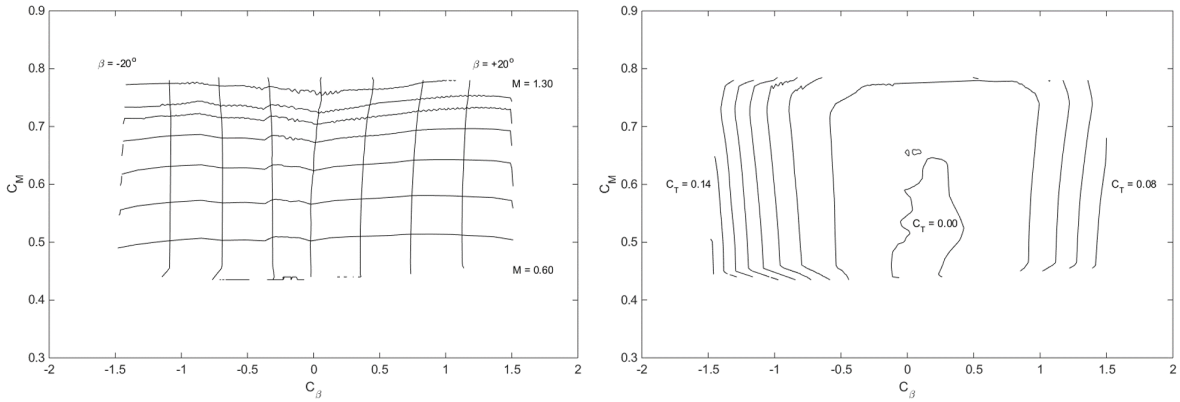
is obtained via interpolation to find the maximum total pressure of the three manually rotated probe angles.

It should be noted that the single-hole probe was only used on the baseline open cavity squealer tip. The number of runs required to resolve the top 4% of data, including set up and manual rotation of the probe was very time consuming. The intention was to design and calibrate a 4-hole probe, capable of measuring within 0.5 mm of the casing, before repeating some of the measurements and resolving close to the casing on the remaining tip geometries. Use of this 4-hole probe would remove all the set-up time associated with the single-hole probe, dramatically reduce the number of runs necessary to complete a full area traverse and allow for calculation of the pitch flow angles.

A four-hole probe was designed by Dr. John Coull and the calibration completed under his supervision at University of Cambridge's Whittle Laboratory, however no time remained for the extra aerodynamic loss measurements to be carried out. Although it is available for future testing in the HSLC, the design and calibration data from the four-hole probe will not be presented in this thesis.

3.5.2 Three-Hole Probe Calibration and Analysis Techniques

The design and calibration of the three-hole probe was based on Povey *et al.* (2008) and was conducted by O'Dowd (2010) in a transonic tunnel at the University of Oxford. The probe was calibrated over a range of known yaw angles ($-20 \leq \beta \leq 20$) and Mach numbers ($0.6 \leq M \leq 1.3$). The yaw, Mach and total pressure coefficients (C_β, C_M, C_T respectively) are defined in Equations 3.19 - 3.21, where P_A, P_B and P_C denote the three pressures measured by the left, right and centre holes of the probe respectively. The calibration data was compiled into a calibration matrix of (β, M, C_β, C_T, C_M), as described by Main (1994). The coefficients C_β and C_M are primary coefficients as they depend only on the measurements taken by the probe. The total pressure coefficient, C_T, is a secondary coefficient, since it depends on other variables not measured by the probe (total pressure, P_0).



(a) The application matrices for yaw angle and Mach number

(b) The application matrix for total pressure coefficient

Figure 3.17: Application matrices for yaw, Mach and total pressure coefficient

$$C_\beta = \frac{P_B - P_A}{P_C - P_{avg}} \tag{3.19}$$

$$C_M = \left(\frac{2}{\gamma - 1} \left[\left(\frac{P_{avg}}{P_C} \right)^{\frac{1-\gamma}{\gamma}} - 1 \right] \right)^{1/2} \tag{3.20}$$

$$C_T = \frac{P_0 - P_C}{P_C - P_{avg}} \tag{3.21}$$

$$P_{avg} = \frac{P_A + P_B}{2} \tag{3.22}$$

During testing in the HSLC, the probe pressures were measured and converted into the primary coefficients C_β and C_M. The method of searching the calibration matrix for the closest values of C_β and C_M and interpolating to find (β, M, C_T) could be computationally expensive. Instead Main (1994) developed an approach whereby the calibration matrix is inverted to create an application matrix containing values of (β, M, C_T) at known steps of (C_β, C_M). The application matrices $\beta(C_\beta, C_M)$ and $M(C_\beta, C_M)$ are shown in Figure 3.17a, while the application matrix for $C_T(C_\beta, C_M)$ can be found in Figure 3.17b. The application matrix was used as a look-up table to rapidly determine the nearest points to the experimental values of C_β and C_M and a simple interpolation performed to calculate the flow variables β, M and C_T.

During the current research, development of the existing processing code (as used by

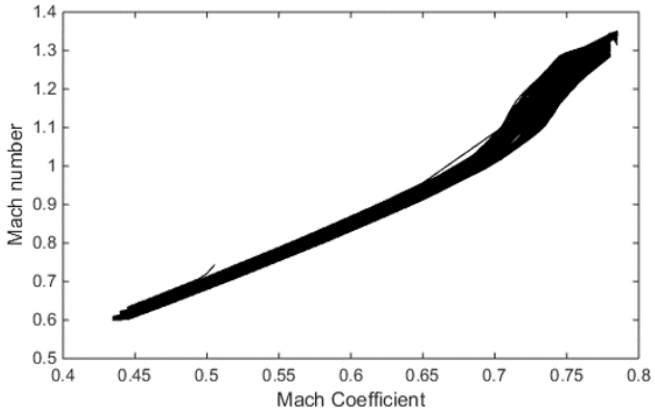


Figure 3.18: Mach number plotted against Mach coefficient from the application matrix (all calibration data)

O'Dowd (2010) and Virdi (2015)) was performed in collaboration with Dr John Coull and will be detailed here.

Near to the tip gap, in the main OTL vortex, there may be some areas of the flow where the Mach number dips below the minimum calibrated range of $M = 0.6$. To account for this, the values of (β, M, C_T) which occur at the lowest calibrated Mach number were repeated at $M = 0$, to extrapolate the application matrices to zero Mach number. This assumption is justified as the form of Equation 3.20 accounts for the relatively small compressibility effects at these Mach numbers. As evident in Figure 3.18, the Mach coefficient forms a linear relationship with the Mach number below $M \approx 0.7$. Under these conditions, the flowfield variables can be considered as dependent only on the yaw angle.

The probe was positioned at an angle such that a majority of the data is within the calibration range; this was found to be 63^o from preliminary tests. A small number of points were found to lie outside the calibration range, necessitating extrapolation from the raw calibration data to determine (β, M, C_T). However, at large angles (typically found close to the tip gap), $P_C \approx P_{avg}$ and the denominator of Equations 3.19 and 3.21 (for C_β and C_T respectively) tends to zero, giving unrepresentative extrapolated values. To prevent this, alternative coefficients for C_β and C_T were developed for the extrapolation routine in which P_{avg} was replaced with $P_{min(A,B)}$ in the denominator, denoting the minimum value of P_A and P_B. These alternative coefficients, $C_{\beta,alt}$ and

$C_{T,alt}$, are given in Equations 3.23 and 3.24 and remain relatively linear even at the extremes of the calibration range. The Mach coefficient does not suffer from this issue, so the original coefficient in Equation 3.20 was used throughout.

$$C_{\beta,alt} = \frac{P_B - P_A}{P_C - P_{min(A,B)}} \tag{3.23}$$

$$C_{T,alt} = \frac{P_0 - P_C}{P_C - P_{min(A,B)}} \tag{3.24}$$

The exit total pressure, P_0, was determined from the relevant total pressure coefficient (C_T or $C_{T,alt}$), depending whether or not the data point was within calibration range. Previous works on the HSLC (for example O'Dowd (2010) and Virdi (2015)) used the calculated P_0 to evaluate a total pressure loss coefficient (C_{P0}) which was non-dimensionalised by a pre-determined mass-averaged reference dynamic head ($0.5\rho V^2$) at the midspan exit plane. However, this approach does not account for any of the unsteadiness in the rig during each area traverse test.

The author used the calculated P_0 to first evaluate a local pressure loss coefficient, $Y_{P0,local}$, which is defined as follows:

$$Y_{P0,local} = \frac{P_{01} - P_0}{P_{01} - P_{se,wall}} \tag{3.25}$$

where, P_{01} is the inlet total pressure measured by the inlet pitot-static probe and $P_{se,wall}$ is the reference static pressure taken from the last static wall tapping in the pitch-wise direction (in direction of probe travel) at the 100% downstream plane, as indicated in Figure 3.21. The static wall tapping is located outside the chosen pitch over which the area traverse was completed and so the probe does not interfere with the readings taken from the wall tapping.

Non-dimensionalising using the instantaneous reference dynamic pressure ($P_{01} - P_{se,wall}$) minimises the effect of any unsteadiness in the mainstream flow during each blowdown test on the calculated $Y_{P0,local}$. The loss coefficient is then referenced to an isentropic dynamic pressure based on the area-averaged static pressure at the traverse

Parameter	β	Mach	P_0
Uncertainty	2.2^o	0.081	0.96%

Table 3.8: Three-hole probe uncertainty values (From O'Dowd (2010))

plane, $\overline{P_2}$, to give the total pressure loss coefficient, Y_{P0}, in Equation 3.26, which is used throughout the current research.

$$Y_{P0} = Y_{P0,local} \times \left(\frac{\overline{P_{01} - P_{se,wall}}}{P_{01} - P_2} \right) = \frac{P_{01} - P_0}{P_{01} - \overline{P_2}} \tag{3.26}$$

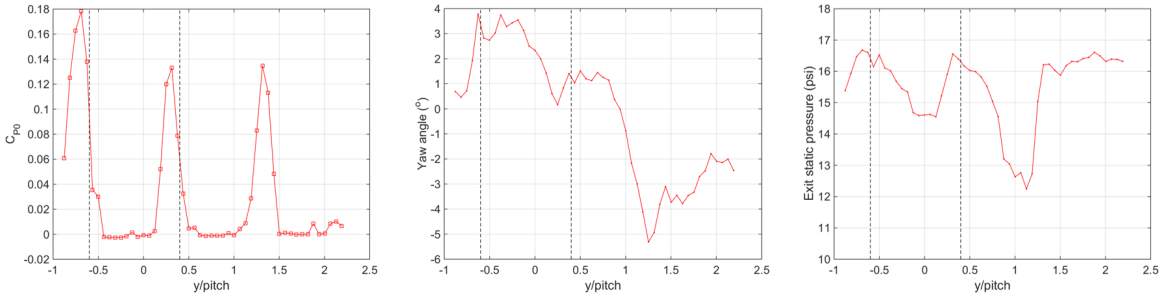
In Equation 3.26, $Y_{P0,local}$ is multiplied by an area-averaged loss coefficient (which is area-averaged over the measurement domain), where P_2 is the exit static pressure from the three-hole probe calculated at each span-wise location from the isentropic relationship between Mach number and total pressure shown in Equation 3.27.

$$P_2 = P_0 \left[1 + \left(\frac{\gamma - 1}{2} \right) M^2 \right]^{\frac{-\gamma}{\gamma - 1}} \tag{3.27}$$

An uncertainty analysis of the three-hole probe measurements was performed by O'Dowd (2010) by substituting the raw calibration data back into the application matrix and calculating (β, M, P_0) at each point. The uncertainties were based on the RMS differences between the raw data and these calculated values and are shown in Table 3.8. It was noted that larger errors occurred within the tip leakage vortex, of up to 2.8 % of the true total pressure measurement at high yaw angles.

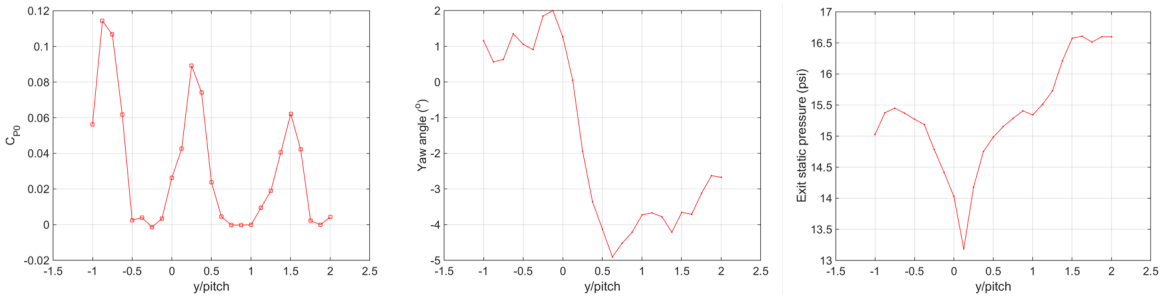
3.5.3 Periodicity in the HSLC

The periodicity in the HSLC was measured to find the optimum starting point for traverses in the pitchwise direction. The three-hole probe was located 27 mm from the casing, as this is the closest to midspan of the blades that can be accessed by the probe. The probe was then traversed over the full range of the traverse system (approximately 3 times the blade pitch), at planes 50% and 100% axial chord downstream of the blade



(a) C_{P0} at 50% C_{ax} downstream **(b) Yaw angle at 50% C_{ax} downstream** **(c) P_2 at 50% C_{ax} downstream**

Figure 3.19: Full pitchwise traverses at 50% axial chord downstream. Dashed black lines denoted chosen test pitch



(a) C_{P0} at 100% C_{ax} downstream **(b) Yaw angle at 100% C_{ax} downstream** **(c) P_2 at 100% C_{ax} downstream**

Figure 3.20: Full pitchwise traverses at 50% axial chord downstream. Dashed black lines denoted chosen test pitch

row. The periodicity was assessed at each plane by evaluation of the yaw angle, C_{P0}[3] and exit static pressure, P_2.

Figures 3.19 and 3.20 show the full pitchwise traverses obtained to assess the periodicity in the HSLC. The zero point on the y/Pitch axis corresponds to a line mid-way between blade 1 and 2 on Figure 3.21, which shows the approximate location of the measured planes in the HSLC. Figure 3.19 shows that there is good periodicity towards the start of the 50% C_{ax} downstream plane traverse. The chosen pitch for test traverses at the 50% C_{ax} plane was between $-0.6 < y/Pitch < 0.4$, as shown by the red dashed lines in Figure 3.19. This chosen pitch shows reasonable periodicity for C_{P0}, yaw and P_2, and captures the 2D blade wake and OTL vortex from blade 2. Shifting the test pitch further towards blade 1 could have improved the periodicity in yaw angle, but then

[3] C_{P0} is a total pressure loss coefficient previously used by O'Dowd (2010) and Virdi (2015) and is defined as follows: $C_{P0} = (P_{01} - P_0)/(0.5\gamma P_2 M^2)$ where the denominator is mass-averaged and evaluated at mid-span.

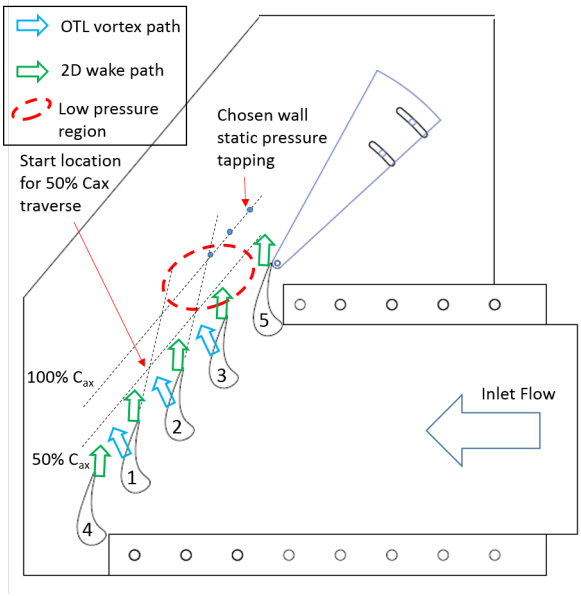


Figure 3.21: Approximate location of traverse planes, showing paths of blade wakes and overtip leakage flows

the 2D wake from blade 1 would have been captured instead of that from blade 2. The C_{p0} at the start of the full traverse also looks to be slightly high (see Figure 3.19a). It is believed that this is caused by the lack of tip gap and similar blade tip design on the outer blade 4 (see Figure 3.21). For this reason, the outer passages should be avoided.

At the 100% axial chord plane there is reasonable periodicity when considering the C_{P0} in Figure 3.20a, however the yaw and P_2 plots show very little periodicity. This lack of periodicity can be explained by use of Figure 3.21, which shows the approximate paths of the OTL vortex and 2D blade wake as they leave the tip. The way in which these two loss mechanisms mix downstream is crucial to the periodicity in the HSLC. At the 100% C_{ax} downstream plane it is believed that any measured pitch will be capturing a 2D wake and OTL vortex which originated at different blades. For example, at the marked test pitch in Figure 3.21 the 2D wake from blade 2 but the OTL vortex from blade 3 will be captured. Furthermore the drop in exit static pressure and large swing in the yaw angle of -6^o (as seen in Figure 3.20c and 3.20b respectively) can be attributed to the lack of a tip gap and OTL vortex from blade 5. The test pitch at 100% C_{ax} which corresponds to the chosen pitch at 50% C_{ax}, is consumed by the region of low pressure, as shown in Figure 3.21. The region of low pressure does also affect the 50% C_{ax} plane,

but it occurs further along the pitchwise direction (at $y/Pitch = 1$ in Figure 3.19b and 3.19c) and can therefore be avoided in the chosen test pitch at the plane closer to the blade row.

Due to the issues described above regarding the periodicity at the 100% downstream plane, it was decided to only take aerodynamic loss measurements at the 50% C_{ax} downstream plane. Only data at the 50% C_{ax} plane is therefore presented in this thesis.

3.6 Cooling Effectiveness Measurements

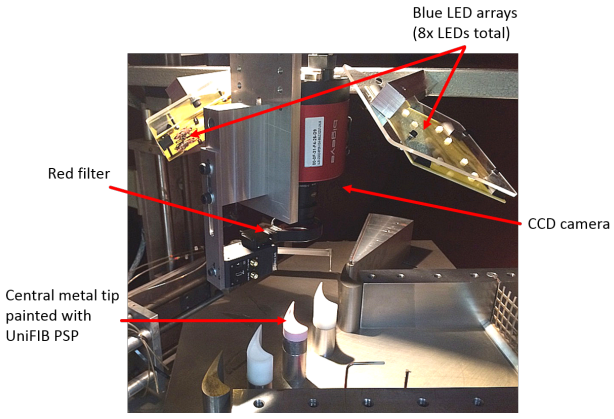
This section describes the experimental set-up and method for the pressure sensitive paint technique, followed by the relevant theory and analysis used to calculate the adiabatic film cooling effectiveness on the blade tip and a detailed uncertainty analysis.

3.6.1 Equipment and Methodology

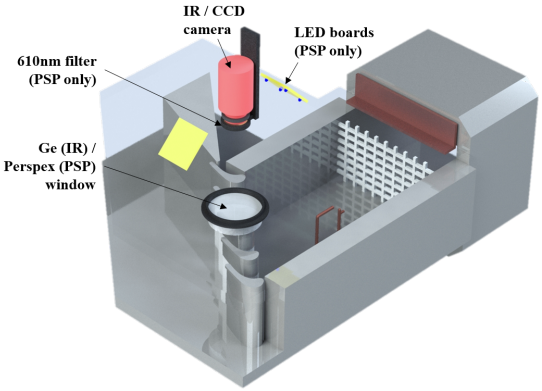
For the first time in the HSLC, the pressure sensitive paint (PSP) technique has been used to calculate the adiabatic film cooling effectiveness. The experimental set-up for pressure sensitive paint tests is shown in Figure 3.22. The central blade was coated with PSP[4] using a modellers spray brush and appears pink in Figure 3.22. The PSP comprises an Oxygen (O_2) sensitive luminophore (Platinum Tetra(Pentafluorophenyl)Porphine, PtTFPP), suspended in an O_2 permeable binder (fluoro/isopropyl/butyl, FIB), which allows Oxygen molecules to diffuse into the binder and interact with the luminophore.

When the PSP is exposed to light in the wavelength range of 380 nm to 520 nm, the luminophore molecules absorb photons and the active component of the luminophore's electrons are excited to a higher electronic state. This excitation light is provided by two arrays of 4 blue LEDs, which are mounted on boards (see Figure 3.22). The excited luminophore molecules can return to ground state via two mechanisms: a radiative process involving the emission of photons in the red region (wavelengths of 620 nm to 750 nm); a non-radiative mechanism in which the luminophore molecules interact

[4]UniFIB from Innovative Solutions



(a) Photo of PSP set-up in the HSLC



(b) CAD of PSP experimental set-up. (Thanks to Joao Vieira)

Figure 3.22: Experimental set-up for PSP testing

with an O_2 molecule, in a process known as Oxygen quenching. The process of Oxygen quenching and the way in which it enables the calculation of film cooling effectiveness will be discussed in Section 3.6.2. The luminescence intensity as a result of these two mechanisms was recorded by a CCD (charge-coupled device) camera[5] with a 610 nm long pass filter (red). The CCD camera is capable of recording in 1928 x 1452 resolution at up to 5 fps and was mounted directly over the central test blade. The IR transmissive Ge window used in heat transfer coefficient testing was replaced by a perspex window of the same dimensions, which formed the top surface of the tip gap.

For a PSP test, the HSLC was operated at the same inlet conditions as for HTC and aerodynamic loss measurements (Table 3.2). The PID settings used on the X5 controller were the same as for an HTC test run (see Table 3.4), as it is desirable to have a very steady inlet pressure, but a long test duration was not required. The coolant supply was switched on and allowed to establish a steady mass flow prior to the start of a test run, with all coolant static pressures and temperatures being recorded throughout. The rig was run for approximately 30 seconds in total and once the inlet pressure had stabilised, 50 images were recorded on the BigEye camera at 5 fps. These 50 images were then averaged to produce a single intensity image for use in post processing.

As will be discussed in Section 3.6.2, the evaluation of film cooling effectiveness

[5]BigEye G-283D Cool monochrome CCD camera by Allied Vision Technologies

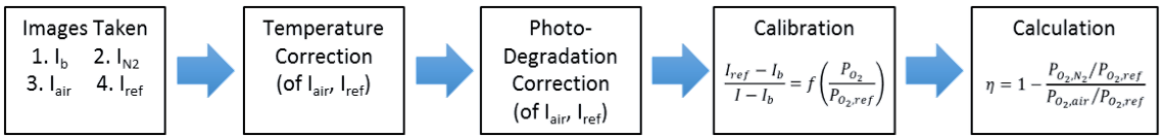


Figure 3.23: Flow chart outlining the PSP measurement and analysis procedure

using the PSP method requires four images to be taken under different conditions. These images are: a dark image, I_b, which is taken in the absence of light with the rig not running to account for any background light intensity; a reference image, I_{ref}, taken at atmospheric pressure (rig off) with the lights on; and two test images taken during a blowdown test, one with N_2 gas as coolant (I_{N_2}) and the other with air as the coolant gas (I_{air}). It was found that the optimum order to take these images was the dark image first, followed by the N_2 test image, the air test image and the reference image last, as will be discussed in Section 3.6.2. A summary of the measurement and analysis procedure described in the following sections is shown in the flow chart in Figure 3.23.

3.6.2 Theory and Analysis Techniques

Due to the Oxygen quenching process (Quinn *et al.* (2013)), the luminescence intensity from the PSP is inversely proportional to the partial pressure of Oxygen (P_{O_2}) at the surface. This relationship can be described by the Stern-Volmer equation (Equation 3.28, Liu *et al.* (2001)):

$$\frac{I_{ref} - I_b}{I - I_b} = f\left(\frac{P_{O_2}}{P_{O_{2,ref}}}\right) \tag{3.28}$$

where $P_{O_{2,ref}}$ is the partial pressure of oxygen at reference conditions given by Equation 3.29. In Equation 3.29, P_{ref} is atmospheric pressure and C_{O_2} is the concentration of Oxygen in air (21%).

$$P_{O_2,ref} = P_{ref} \times C_{O_2} \tag{3.29}$$

The relationship in Equation 3.28 is a function of both pressure and temperature and so a calibration must be performed to quantify the pressure and temperature sensitivity of the PSP over a range of conditions. The calibration is used during post processing

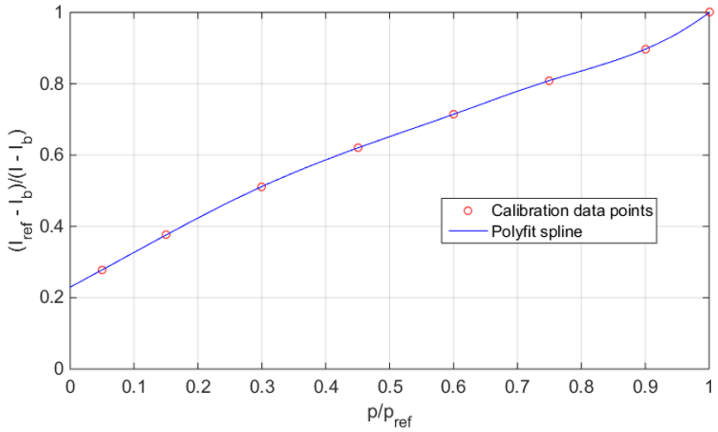
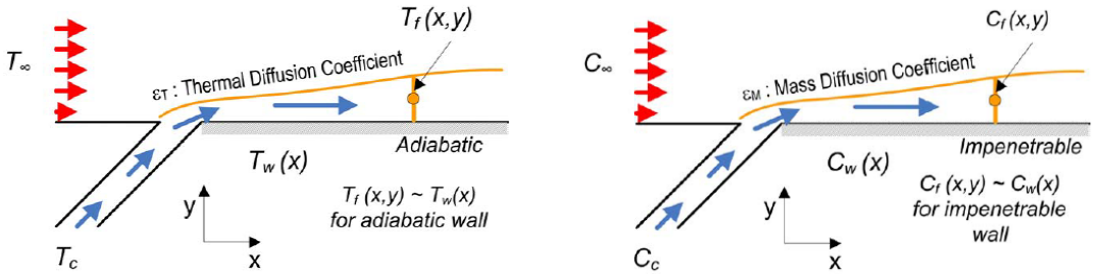


Figure 3.24: Example calibration plot of image intensity ratio against partial pressure ratio for PSP testing

to convert the image intensity ratio into a ratio of the partial pressure of Oxygen on the surface using interpolation of Figure 3.24. The calibration process will be discussed further in Section 3.6.5. Once this partial pressure ratio has been calculated, P_{O_2} can be deduced from Equations 3.28 and 3.29. Furthermore, since the Oxygen concentration in the mainstream under test conditions is known, the static pressure distribution on the blade surface, P_{surf} can be determined by substituting P_{O_2} back into Equation 3.29. The measurement of local static pressure is one other application of PSPs in cascade testing.

The use of PSP to calculate film cooling effectiveness is based on the mass transfer analogy and so is devoid of thermal conduction related issues that lead to errors in thermal measurement techniques, especially in the regions surrounding cooling holes or in thin sections of the tip, where 2D conduction effects become significant. The mass transfer analogy used to calculate adiabatic film cooling effectiveness with PSP is described by Han & Rallabandi (2010) and detailed below for the case where the coolant gases are air and a gas of a similar molecular weight to air (i.e. Nitrogen coolant).

Considering the case in Figure 3.25a, in which a coolant, T_C is injected into the mainstream flow, T_∞, producing a coolant film, T_f, the governing equation for heat transfer in a 2D turbulent boundary layer for a homogeneous fluid (according to Kays *et al.* (2005)) is given in Equation 3.30.



(a) Thermal Boundary Conditions **(b) Mass Transfer Boundary Conditions**

Figure 3.25: Heat/mass transfer analogy for measurement of film cooling effectiveness. (Reproduced from Han & Rallabandi (2010)).

$$G_x \frac{\partial T}{\partial x} + G_y \frac{\partial T}{\partial y} = \rho(\epsilon_T + \alpha) \frac{\partial^2 T}{\partial y^2} \tag{3.30}$$

where G is the mass flux, ϵ_T is the turbulent thermal diffusivity and α is the thermal diffusivity.

For Figure 3.25a, the following boundary conditions apply, describing an adiabatic wall condition (Equation 3.31), where the mainstream temperature beyond the film and the temperature of the injected coolant are given by Equations 3.32 and 3.32 respectively.

$$at \quad y = 0, \ \frac{\partial T}{\partial y} = 0, \ T = T_{aw} \tag{3.31}$$

$$at \quad y > \delta_f, \ T = T_\infty \tag{3.32}$$

$$at \quad x = 0, \ T = T_c \tag{3.33}$$

The analogous case for mass transfer is shown in Figure 3.25b where the mainstream flow and coolant have a tracer gas (here it is O_2) concentration of C_∞ and C_c respectively. The governing equation relating to this case is given as follows:

$$G_x \frac{\partial C}{\partial x} + G_y \frac{\partial C}{\partial y} = \rho(\epsilon_M + D) \frac{\partial^2 C}{\partial y^2} \tag{3.34}$$

where C is the mass fraction of tracer gas, ϵ_M is the turbulent mass diffusivity and D is the mass diffusion coefficient.

The mass transfer case is subject to an impenetrable wall boundary condition (Equation 3.35), with C_∞ and C_c given by Equations 3.36 and 3.37.

$$at \;\; y = 0, \;\; \frac{\partial C}{\partial y} = 0, \;\; C = C_w \tag{3.35}$$

$$at \;\; y > \delta_f, \;\; C = C_\infty \tag{3.36}$$

$$at \;\; x = 0, \;\; C = C_c \tag{3.37}$$

By comparison of Equations 3.30 and 3.34 it is evident that if the turbulent Lewis number is unity ($Le_T = \frac{\epsilon_T + \alpha}{\epsilon_M + D} = 1$) the non-dimensionalised solutions of the governing equations are equal. This is the underlying assumption of the heat/mass transfer analogy which, according to Jones (1999), is valid for turbulent gaseous flow fields such as those found over a turbine blade, due to high Reynolds numbers and turbulence inducing mechanisms (e.g. leakage vortices, film cooling jets).

Therefore, Equation 3.38 relates the adiabatic film cooing effectiveness, η, to the mass fraction of O_2 according to the mass transfer analogy described above.

$$\eta = \frac{T_f - T_\infty}{T_c - T_\infty} \approx \frac{T_{aw} - T_\infty}{T_c - T_\infty} \approx \frac{C_w - C_\infty}{C_c - C_\infty} \tag{3.38}$$

To evaluate η by the PSP and foreign gas method, an expression must be derived based on partial pressures of O_2 (which are related to measured I by Equation 3.28).

For the case with air coolant, $C_\infty = C_{O_2,air}$, which is a known constant. When a foreign gas coolant is used, the mass fraction of O_2 inside the film reduces, therefore increasing the luminescence of the PSP in the local area and $C_w = C_{O_2,fg}$; furthermore, inside the coolant film, the concentration of O_2 is zero ($C_{O_2,c} = 0$). When using N_2 as the coolant gas, as in the present work, the molecular weight of the foreign gas is similar to that of air and so the mass fraction ratio equals the mole fraction ratio, yielding the following relationship for the calculation of η via the PSP method:

$$\eta \approx \frac{C_w - C_\infty}{C_c - C_\infty} = \frac{C_{O_2,fg} - C_{O_2,air}}{C_{O_2,c} - C_{O_2,air}} = 1 - \frac{C_{O_2,fg}}{C_{O_2,air}} = 1 - \frac{P_{O_2,N_2}}{P_{O_2,air}} = 1 - \frac{P_{O_2,N_2}/P_{O_2,ref}}{P_{O_2,air}/P_{O_2,ref}} \tag{3.39}$$

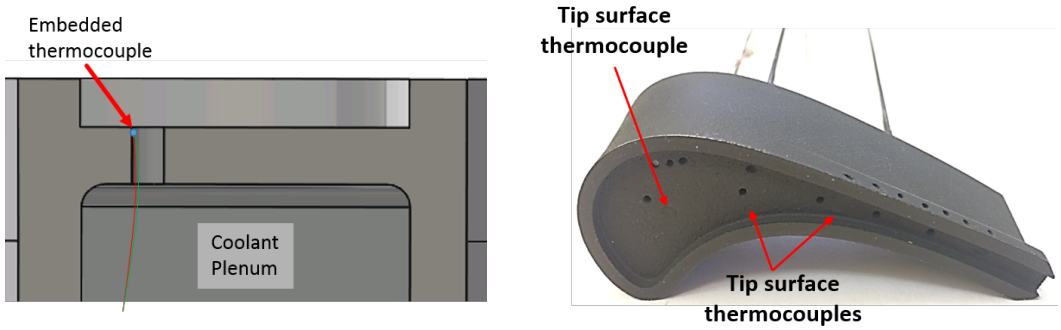
where, $P_{O_2,air}$ and P_{O_2,N_2} are the partial pressures of Oxygen on the tip surface when air or N_2 respectively are used as the coolant gas.

3.6.3 Temperature Sensitivity of Pressure Sensitive Paint

Although thermal conduction effects on the tip do not impact PSP derived film effectiveness results in the same way as they do to temperature based methods, it is essential to limit the temperature differences between the test and reference conditions, as the UniFIB PSP has a temperature sensitivity which causes a decrease in luminescence of $+0.5\%/^{o}$C (as stated by the manufacturer). To ensure that the reference image is taken at the same temperature as the test image, it is common practice (Han & Rallabandi (2010)) to take the reference image immediately following the air test image, once the rig has been shut down but the test material is still at a similar temperature.

However, this approach is not possible in the HSLC, as the closing of the Spirax-Sarco valve causes an expansion cooling effect to occur, which significantly reduces the temperature of the mainstream flow and the tip immediately after the test. Instead, the bulk temperature of the tip was monitored both during and after the test, by use of three embedded surface thermocouples. These thermocouples were fixed to the side of three holes drilled in the tip cavity floor using thermally conductive silver epoxy (see Figure 3.26a), the locations of which can be seen in Figure 3.26b. The reference image was taken at a time, after the air cooled test, when the bulk tip temperature was most similar to the test conditions. Any small differences in temperature were accounted for using the known temperature correction of the PSP, as stated above. By taking this approach and normalising all the images to the same temperature as the N_2 coolant test image, the variance in film effectiveness between successive PSP tests was reduced, as seen in Figure 3.27 which shows circumferentially averaged film effectiveness for repeated tests on a single example test case with and without the application of this temperature correction method. Equations 3.40 and 3.41 show the simple correction calculations used, which act to reduce the intensity of the air or reference image if the temperature of the tip during the air or reference test is lower than that during the Nitrogen test.

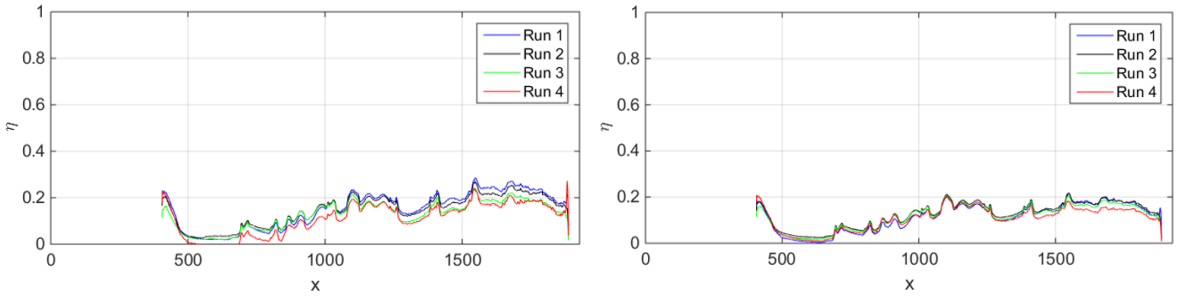
$$I_{air,tempcorr} = I_{air,uncorr}(1 - 0.005(T_{tc,N_2} - T_{tc,air})) \tag{3.40}$$



(a) CAD of surface thermocouple embedded in cooled metal tip (cross-section)

(b) Location of metal tip surface thermocouples

Figure 3.26: Metal tip surface thermocouple locations and cross-section schematic



(a) Without temperature correction method

(b) With temperature correction method

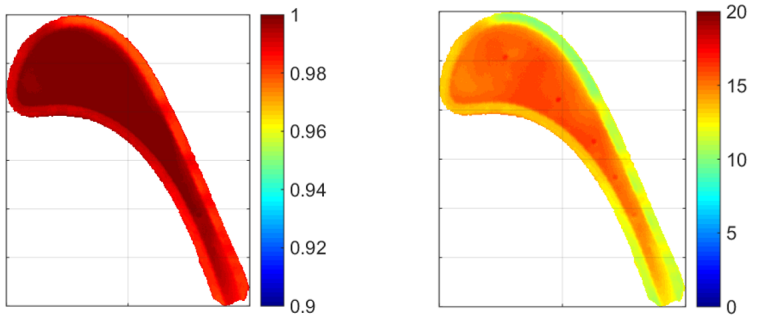
Figure 3.27: Circumferentially averaged film cooling effectiveness for example cases with and without temperature correction method. (x represents the x-axis of the raw camera image)

$$I_{ref,tempcorr} = I_{ref,uncorr}(1 - 0.005(T_{tc,N_2} - T_{tc,ref})) \tag{3.41}$$

where $I_{air,tempcorr}$ and $I_{ref,tempcorr}$ are the temperature corrected image intensity for the air and reference tests respectively, $I_{air,uncorr}$ and $I_{ref,uncorr}$ are the raw image intensity plots from the CCD camera, and T_{tc,N_2}, $T_{tc,air}$ and $T_{tc,ref}$ are the average surface thermocouple temperatures of the Nitrogen, air and reference tests respectively.

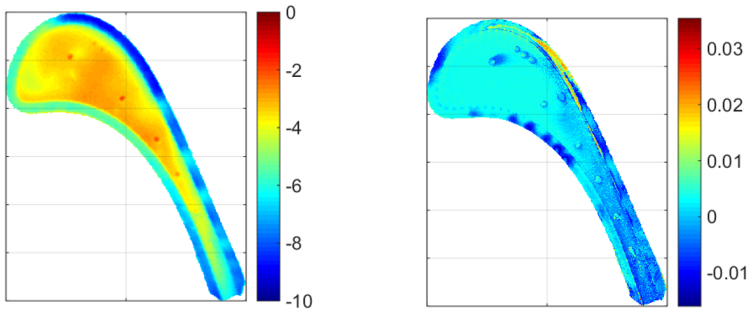
Further to the approach of normalising the temperature between the reference and test images, the Mach number distribution over the blade tip at transonic conditions causes variation in the surface temperature, which can effect the response of the PSP. To reduce this temperature variation, the blade tips for the PSP tests are made from Titanium, which has a much higher conductivity than epoxy resin.

To quantify the remaining tip temperature variation and the effect that it has on the calculated film effectiveness, the metal blades were sprayed black and retested in the



(a) Averaged temperature ratio from IR camera

(b) Reconstructed tip wall temperature (^{o}C) distribution (using T_{rat} and T_{01})



(c) Temperature difference map (^{o}C) from average N_2 test thermocouple data

(d) Change in film effectiveness with IR correction method

Figure 3.28: Steps through IR temperature correction method

HSLC with the IR camera in place. Using the IR camera (and typical calibration coefficients from the in-situ calibration method described in Section 3.4.1) the temperature distribution on the tip surface during a simulated PSP test (with no heater mesh) was determined and the following temperature ratio, T_{rat}, was calculated, where T_w is the measured wall temperature from the IR camera and T_{01} is the inlet temperature. An example of the averaged temperature ratio for all repeats of a particular case is shown in Figure 3.28a.

$$T_{rat} = T_w/T_{01} \tag{3.42}$$

The averaged tip temperature ratio was then applied to each PSP test and tip surface temperatures were reconstructed using the recorded inlet temperature for each run. Figure 3.28b shows an example of reconstructed tip surface temperature, where it is observed that the lowest wall temperatures occur on the rims of the squealer tip, where

the Mach number is highest. From the reconstructed tip surface temperatures, an in-test temperature difference map (Figure 3.28c) was created by calculating the difference between the average N_2 test surface thermocouple temperature to all coordinate points on the tip. It should be noted that the averaged N_2 surface thermocouple temperature was higher than expected from the recorded IR camera data. This can be ascribed to thermal conduction from the plenum coolant to the embedded thermocouple which raised the metal temperature around the thermocouple compared to the external surface temperature. The temperature difference map was applied to the recorded intensity images, I_{N_2} and I_{air}, using the same temperature correction as before (+0.5%/^{o}C), to normalise all points on the tip to a single temperature, which is kept constant for the processing of I_{air} and I_{ref}.

Similar IR correction methodology was applied by Mitsuo *et al.* (2005) on a low speed aerofoil and found to improve accuracy of measured surface pressure. However, when applied to a film cooling effectiveness calculation the author found that the blade tip temperature variation typically accounted for changes in adiabatic film cooling effectiveness of less than 0.02 (Figure 3.28d), when compared with the original temperature correction method presented in the first part of this Section. This limited impact is attributed to the almost identical temperature distribution expected to by seen on the tip in both the air cooled and N_2 cooled tests, which reduces the impact when taking a ratio of partial pressure ratios. The IR correction method is therefore this discounted for the remaining PSP results presented throughout this thesis, however the additional uncertainty from not including this correction is detailed in the uncertainty analysis in Section 3.6.6.

3.6.4 Photo-degradation of Pressure Sensitive Paint

During early PSP testing it was observed that occasionally there were significant differences in image intensity between repeated runs which could not be explained by a difference in the tip temperature. It was found that the difference was caused by the

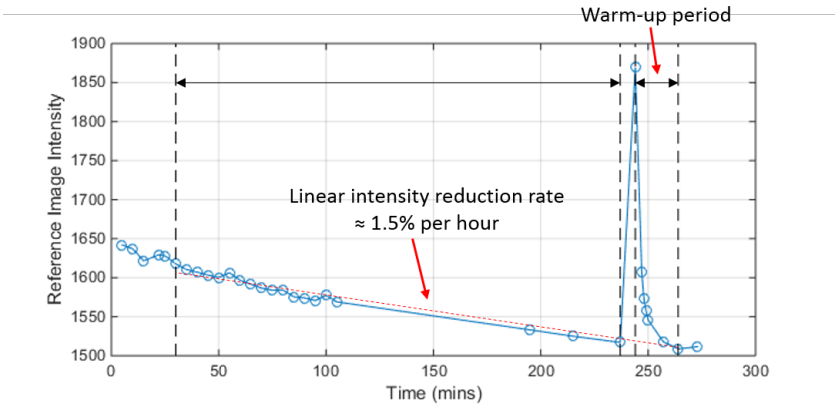


Figure 3.29: Reference intensity over time showing warm-up of lights and linear reduction in intensity due to photo-degradation and ambient temperature increase

LED arrays. The LEDs must be left to warm up for around 30 minutes, to allow the resistance in the lights to increase and the light intensity to drop from the 'start-up' intensity, as characterised by Figure 3.29 which shows the variance in reference luminescence over time as a result of this effect. Marked on Figure 3.29 is the point where the lights are switched off and back on again, causing a large spike in intensity. Also marked is the 'warm-up' time period and the period of linear reduction in luminescence. This linear reduction is due to both the photo-degradation of the PSP and an increase in ambient temperature; once the lights have warmed up, the emitted light intensity assumes this rate of degradation, found to be approximately 1.5% in absolute light intensity per hour (shown by the red dotted line in Figure 3.29). The rate of ambient temperature increase over the 5 hour period was approximately 1^{o}C per hour, which accounts for 0.5% of the total 1.5% decrease in intensity seen. Therefore a reduction rate of approximately 1% per hour can be ascribed to the photo-degradation of the PSP.

In a similar way to the simple temperature correction described in the previous section, the photo-degradation of the PSP is accounted for using the following corrections (Equations 3.43 and 3.44), which act to normalise the light intensity of the air and reference images to the same level as the Nitrogen image based on the time they were taken after the Nitrogen image. Since the Nitrogen image is taken first, it will have a higher base intensity level than both the air and reference images, so I_{air} and I_{ref} must be increased to that same level.

$$I_{air,timecorr} = I_{air,tempcorr}(1 - 0.01(t_{air})) \tag{3.43}$$

$$I_{ref,timecorr} = I_{ref,tempcorr}(1 - 0.01(t_{ref})) \tag{3.44}$$

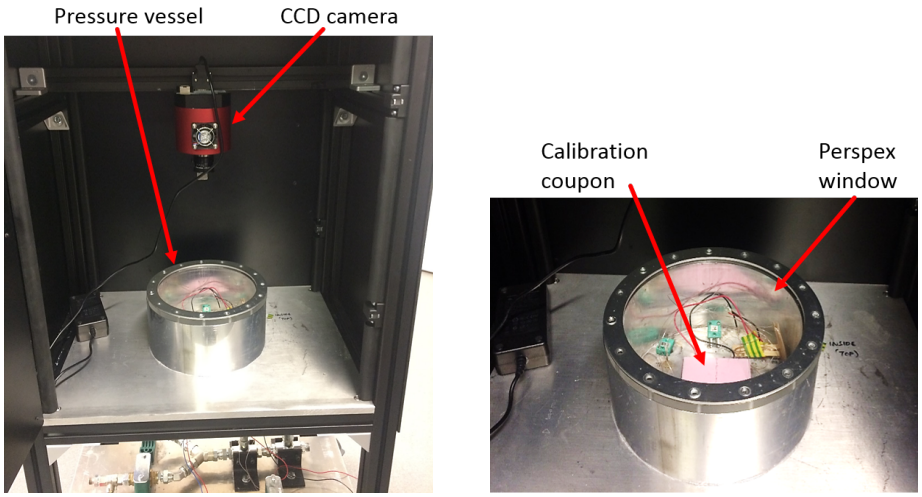
In the above equations, $I_{air,timecorr}$ and $I_{ref,timecorr}$ are the time corrected air and reference images respectively, and t_{air} and t_{ref} are the elapsed time between the Nitrogen image and the air or reference image respectively.

3.6.5 Pressure Sensitive Paint Calibration

A calibration must be performed to characterise the luminescence of the PSP in response to known temperatures and O_2 partial pressures. The calibration curve can change slightly due to factors such as the paint thickness on the surface, batch of paint used and the photo-degradation of the paint, so it is good practice to repeat the calibration regularly. As discussed in Section 3.6.2, the resulting calibration curve is used to interpolate the partial pressure ratio from the emitted light intensity ratio under test conditions.

During the commissioning of the PSP method in the HSLC, a calibration curve was used which was taken by Holt Wong under controlled conditions on a separate low speed test rig. This calibration will be referred to as the *original calibration*; details of the process can be found in Wong *et al.* (2016). Once the main film effectiveness testing campaign began, the intention was to build a mobile calibration rig and use this rig simultaneously to produce more relevant calibration curves for the HSLC results. The calibration rig was built by Holt Wong and Joao Vieira with the author's assistance and was completed part way through the test campaign. However, there were issues with the calibration rig, which are described here along with an outline of the calibration rig design and methodology.

The calibration rig consists of a vacuum sealed pressure vessel, inside a portable dark cabinet, with a large perspex optical window forming the top surface and can be seen

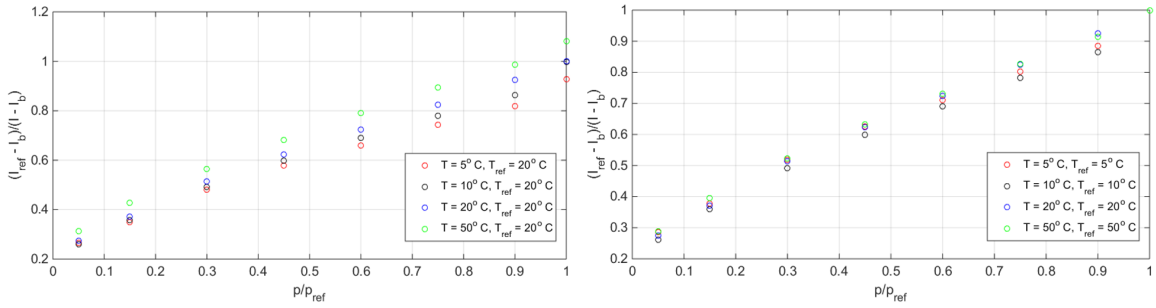


(a) External photo of calibration rig **(b) Internal photo of calibration rig**

Figure 3.30: Photos of the calibration rig for pressure sensitive paint calibration

in Figure 3.30. A coupon of dimensions 70 mm x 70 mm x 2 mm was sprayed with the PSP simultaneously to the test blade tips to ensure consistency of the thickness and batch of PSP between the calibration piece and test tips. The coupon was fixed into the pressure vessel, on top of a Peltier heater, which was powered by a 0-30V, 0-30A DC power supply; the Peltier was used to heat (or cool) the calibration coupon through a range of desired temperatures. The set temperature was obtained via a feedback loop, using an RTD sensor which was fixed to the surface of the coupon, to control the power demanded by the Peltier. The temperature of the calibration coupon was measured by a 0.0762 mm (0.003 in) K-type thermocouple. To control the pressure in the test section, a manual pump was utilised to produce the range of desired absolute vacuum or pressure values in the vessel; the pressures were measured by an absolute pressure transducer. The pressures and temperatures during calibration were recorded using a National Instruments CompactDAQ 9174 system with 9201 voltage input module and 9211 temperature input module. A CCD camera is mounted above the calibration coupon and the excitation light provided by blue LED light arrays.

A preliminary calibration was performed by Joao Vieira, which is referred to as the *alternative calibration*. The calibration procedure was as follows: take a dark image; switch on the LED arrays and allow them to warm up; heat the coupon to a set temper-



(a) Calibration data with a common reference temperature ($T_{ref} = 20^oC$)

(b) Normalised calibration data, $T_{calib} = T_{ref}$

Figure 3.31: Calibration data plots showing impact of PSP temperature sensitivity

ature in the range of 5^{o}C to 50^{o}C; with the coupon temperature held constant, manually vary the absolute pressure in the test section between 95% vacuum and 1 bar absolute pressure; at each pressure level, take 50 images (at 5 fps) and average. This process was repeated for temperatures of 10^{o}C, 20^{o}C and 50^{o}C.

To process the calibration data, the image intensity and pressure ratios were calculated (as defined in Equation 3.28) and a spline was produced for each set temperature. The individual splines for the *alternative calibration* are shown in Figure 3.31a, where the reference conditions are ambient pressure and temperature (1 bar and 20^{o}C). Processing the data with a common reference temperature shows the impact of the temperature sensitivity of PSP. If the calibration curves are normalised so that the reference temperature is equal to the set temperature of the coupon, the calibration curves collapse together, as seen in Figure 3.31b.

The average of these normalised curves should be taken and used to find the partial pressure ratio of Oxygen on the blade tips from the recorded image intensity ratio during HSLC testing, provided that the reference and test temperatures are approximately equal, as discussed in Section 3.6.3.

However, it was discovered that there were significant leaks in the calibration rig which affected the *alternative calibration* and resultant film effectiveness results. A comparison of the original and alternative calibration curves is shown in Figure 3.32. It is observed that the curves are similar when the pressure ratio is between 0.9 - 1.0 but diverge as the percentage vacuum is increased (above $P_{rat} = 1$ the curves are expected

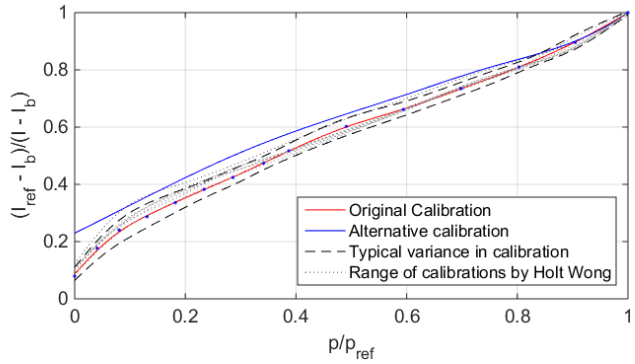
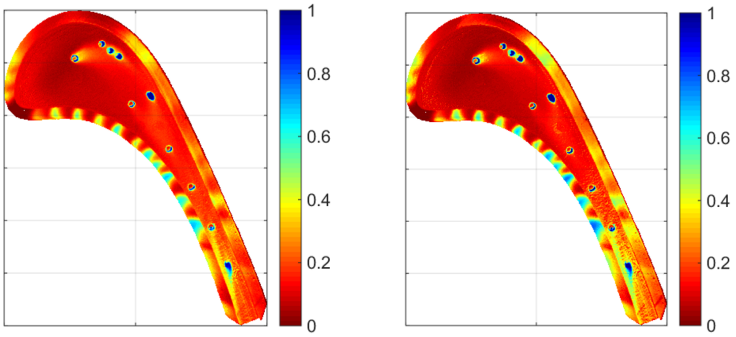


Figure 3.32: Comparison of calibration curves with range of calibrations and typical variance

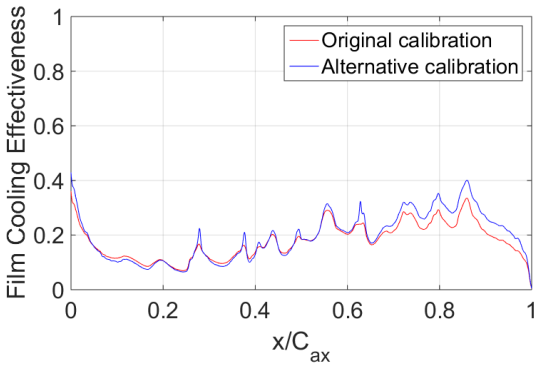
to be linear and are extrapolated). A leak in the calibration rig means that there is no guarantee of uniform pressure throughout the pressure vessel. The observed left shift of the *alternative calibration* curve indicates that for a particular recorded I_{rat} in the calibration rig, the actual P_{rat} on the calibration coupon was higher than the recorded pressure ratio; a difference which increases at higher percentage vacuum, suggesting a more significant leak at a higher vacuum. The increasing leak at higher vacuum will affect regions of higher film effectiveness or those areas of low static pressure on the tip (such as the trailing edge) more significantly, as the interpolation points for such regions sit far to the left on the calibration curve.

A review by the author of numerous PSP calibration curves performed by Holt Wong showed that the *alternative calibration* was outside the normal range of calibration variance (see Figure 3.32). Without time to fix the calibration rig, it was decided to evaluate the film effectiveness results throughout this thesis using the *original calibration*. The difference in film effectiveness which may be seen due to the *alternative calibration* is quantified in Figure 3.33, but this is a comparison of extremes. It is observed that, as expected, the film effectiveness is increased towards the trailing edge and in high effectiveness regions when using the *alternative calibration*, as the curve predicts lower P_{O_2} on the tip for the same image intensity. The expected additional uncertainty in film effectiveness due to the uncertainty in the calibration is included in the uncertainty analysis in Section 3.6.6.



(a) Film effectiveness with original calibration

(b) Film effectiveness with alternative calibration



(c) Circumferentially averaged film cooling effectiveness

Figure 3.33: The effect of the alternative PSP calibration on the film effectiveness

3.6.6 Uncertainty Analysis

The uncertainty in film cooling effectiveness measurements is a function of the uncertainty in recorded image intensity, but in the current research, additional uncertainties are included for the tip temperature distribution and PSP calibration, as described in Sections 3.6.3 and 3.6.5 respectively. The overall uncertainty in film effectiveness can be evaluated by the root-sum-square method (RSS) which combines the contributions of the individual uncertainties of these aspects, as described by Kline & McClintock (1953), as follows:

$$\delta\eta = \left[\left(\frac{\partial\eta}{\partial I_{ref}}\delta I\right)^2 + \left(\frac{\partial\eta}{\partial I_{N_2}}\delta I\right)^2 + \left(\frac{\partial\eta}{\partial I_{air}}\delta I\right)^2 + \left(\frac{\partial\eta}{\partial I_b}\delta I_b\right)^2 \ldots \right.$$
$$\left. \ldots + \left(\frac{\partial\eta}{\partial I}\frac{\partial I}{\partial T_{rat}}\delta T_{rat}\right)^2 + \left(\frac{\partial\eta}{\partial calib}\delta calib\right)^2\right]^{\frac{1}{2}} \quad (3.45)$$

where for example, the term $(\partial\eta/\partial I_{ref})\delta I$ represents the change in calculated effectiveness as a function of I_{ref} due to the uncertainty in image intensity I. The fifth term represents the change in film effectiveness due to a change in image intensity, which is dependent on the temperature ratio, T_{rat}, taken via the IR camera. The last term represents the change in effectiveness due to the uncertainty in the calibration.

To evaluate the uncertainty in film effectiveness due to image intensity (terms 1 - 4 in Equation 3.45), a perturbation analysis was implemented to numerically calculate the partial differentials describing the change in effectiveness result due to each individual image intensity. The uncertainty intervals of I and I_b were found by taking a series of reference and dark images respectively, which are corrected for temperature and photo-degradation, and calculating twice the standard deviation of the mean luminescence of these images ($\delta I = 2\sigma_{I_{ref}}$ and $\delta I_b = 2\sigma_{I_b}$). The perturbation analysis was then carried out by perturbing the variables of I_{ref}, I_{N_2} and I_{air} individually by δI and I_b by δI_b and calculating the resulting perturbed effectiveness. The difference between the perturbed result and original result represents the individual contribution to the overall uncertainty of each image and was used in Equation 3.45 to calculate the overall uncertainty. This process was repeated for a range of original film effectiveness results from different areas of the tip. The uncertainty contribution from image intensity is summarised in terms of absolute effectiveness in Table 3.9.

To calculate the uncertainty in η due to I and T_{rat} (5th term in Equation 3.45), knowledge is required of the uncertainty in temperature ratio, δT_{rat}, which can be summarised as follows:

$$\delta T_{rat} = \left[\left(\frac{\partial T_{rat}}{\partial T_{w,IR}} \delta T_{w,IR} \right)^2 + \left(\frac{\partial T_{rat}}{\partial t} \delta t \right)^2 \right] \tag{3.46}$$

where, the first term represents the change in T_{rat} as a function of the wall temperature, $T_{w,IR}$, measured by the IR camera and the second term represents the change in T_{rat} due the uncertainty in the time at which the temperature distribution is calculated after the compression heating effect (at rig start-up) when simulating the PSP test with the

IR camera in place.

The uncertainty in $T_{w,IR}$ was previously calculated in Section 3.4.3 during the HTC uncertainty analysis and found to be 0.298 K for the FLIR A655 camera used here. The original calculated T_{rat} was perturbed by this uncertainty interval and found to make a very minimal change in the temperature ratio.

The significance of the second term, $(\partial T_{rat}/\partial t)\delta t$, can be explained with reference to Figure 3.12b which shows a temperature trace of blade tip surface. T_{rat} varies with time after the compression heating, as the tip takes time to adjust to the inlet flow temperature. The original T_{rat} was calculated 5 s after the inlet flow achieves steady pressure, similarly to the procedure for PSP testing. The change in T_{rat} was computed when T_{rat} is taken immediately after the acquisition of steady inlet pressure and at the end of the test run. This was also found to make a minimal change the temperature ratio. When combined with the small uncertainty due to IR camera temperature, the overall uncertainty in temperature ratio was calculated to be an absolute value of 0.0028 (or 0.3% of original temperature ratio). This small uncertainty in T_{rat} is attributed the relative small changes in temperature which occur in the rig on the Kelvin scale.

Returning to the 5th term in Equation 3.45, the contribution of this term to the overall uncertainty was calculated via another perturbation analysis. The change in original film effectiveness result (without temperature correction) was calculated when the IR temperature correction method outlined in Section 3.6.3 was used. The IR corrected result was then perturbed by the uncertainty interval of T_{rat}, to calculate two further changes from the original result. The contribution of this term to the overall uncertainty in film effectiveness is summarised in Table 3.9 at the same range of effectiveness levels.

The uncertainty contribution of the final term in Equation 3.45, relating to the calibration uncertainty was again evaluated with a perturbation analysis. The original calibration was perturbed by the upper and lower limits $(+/-2\sigma)$ of the range of calibrations performed by Holt Wong, as shown in Figure 3.32. The perturbed cali-

Original η	Uncertainty Contribution			Overall Uncertainty
	Image Intensity	IR temperature Correction	Calibration	
0.2	0.060	0.015	0.020	0.066
0.35	0.045	0.019	0.030	0.058
0.5	0.037	0.026	0.033	0.056
0.65	0.027	0.030	0.029	0.050

Table 3.9: Uncertainty contributions to the overall film effectiveness uncertainty (absolute values)

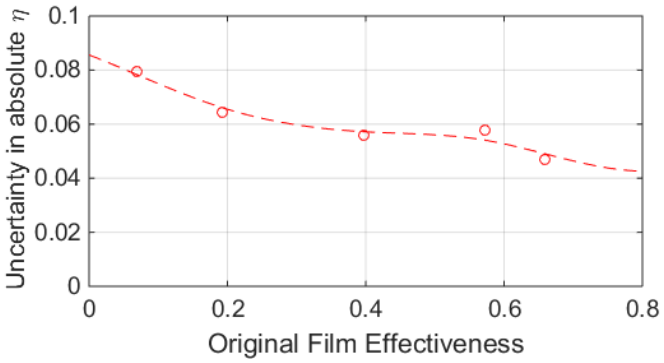


Figure 3.34: Uncertainty in absolute film effectiveness at a range of film effectiveness values

brations were used to calculate the change in film effectiveness for every point on the tip to account for the full range of tip static pressure and original effectiveness values. The contribution to the overall uncertainty was then interpolated for the same discrete effectiveness levels as before and summarised in Table 3.9 .

The overall uncertainties at a range of film effectiveness values are shown in Figure 3.34, presented in terms of absolute effectiveness value. The overall uncertainty is seen to reduce at higher effectiveness, dominated by the contribution of the uncertainty in image intensity. This trend is caused by the difference in intensity between reference and test images, which is smaller when the film effectiveness is low and so the perturbations have a larger difference on the calculated film cooling effectiveness result. It is noted that the absolute uncertainty due to IR temperature correction increases at higher η. This trend is driven by the fact that on the blade tips, the regions of higher effectiveness are located mainly on the squealer rims, where the temperature distribution plays a more significant part. However, as a percentage of the original effectiveness value, the uncertainty is still reducing as the effectiveness increases. Due to the trend of lower

uncertainty at higher effectiveness, conclusions in this thesis were drawn based on either large changes in film effectiveness, or changes in effectiveness which occurred when the base level of effectiveness is high and the uncertainty is lower.

3.7 Summary

This chapter provided an overview of the High Speed Linear Cascade, the modifications made since the previous published work and a detailed description of the experimental techniques and analysis methods employed throughout the current research. The described techniques have been used in the HSLC to capture heat transfer coefficient, aerodynamic loss and film cooling effectiveness data for a variety of blade tips at transonic conditions.

Evaluation of heat transfer coefficient measurements was based on a one-dimensional, semi-infinite conduction analysis with convective boundary conditions. A transient IR thermography technique was employed, which used the Impulse response method to reconstruct heat flux from surface temperature measurements during the transient period. The step change in inlet temperature required for this method was provided by a heater mesh upstream of the test section. A regression analysis of the surface temperatures and reconstructed heat flux was then used to evaluate the convective heat transfer equation and produce maps of tip heat transfer coefficient. A detailed uncertainty analysis was performed for both IR cameras used during the current research, showing an improvement in uncertainty from 10.7% to 6.9% as a result of the new IR camera.

Aerodynamic loss measurements were obtained by traversing a three-hole probe over a plane 50% of axial chord downstream of the blade row. This downstream plane showed improved periodicity over the 100% downstream plane in an area which captured all loss features from the central blade. The calibration of the three-hole probe was described, and the evaluation of the total pressure loss coefficient, Y_{P0}, produced a map of the losses at the particular downstream plane. Uncertainty in total pressure measurements from the three-hole probe were 0.96 %, increasing to 2.8 % at high yaw angles within

the tip leakage vortex.

Film cooling effectiveness measurements were acquired using the pressure sensitive paint technique and employed a newly developed, fully controllable coolant delivery system. The pressure sensitive paint method relies on the mass transfer analogy to evaluate the film effectiveness from separate tests in which Nitrogen and air are used as the coolant gases. The luminescence of the PSP was captured by a CCD camera and related to the partial pressure of Oxygen on the tip surface using a calibration to characterise the PSP. Difficulties with the PSP calibration rig led to an analysis of the influence of the calibration on the resulting film effectiveness. A method of correcting for tip temperature distribution and photo-degradation of the PSP was described with shown improvement in repeatability between tests. An uncertainty analysis was also performed, showing that the uncertainty of the PSP method reduces at increased effectiveness; overall uncertainties are estimated to be 0.066 in absolute effectiveness at $\eta = 0.20$ and 0.050 at $\eta = 0.65$.

Chapter 4

Computational Fluid Dynamics Methods

4.1 Introduction

This chapter will introduce the principles of Computational Fluid Dynamics (CFD) and discuss the procedures used in the present study. As computing power has increased, CFD has become a powerful tool as part of the turbomachinery design process, capable of a providing an in depth understanding of the flow field surrounding increasingly complex problems. In the present study, finite-volume Reynolds-Averaged Navier-Stokes CFD has been performed using the Rolls-Royce in-house CFD solver, HYDRA, to carry out a tip geometry study and a tip cooling study, which complement the experimental work undertaken in the HSLC.

4.2 CFD Theory

This section considers the underlying theory of CFD, covering the governing equations of fluid motion, discretisation methods, solution schemes and turbulence modelling.

4.2.1 The Navier-Stokes Equations

The Navier-Stokes equations are the three fundamental equations of fluid mechanics, which take account of the full three-dimensional, viscous nature of fluid motion. These governing equations are: the continuity equation; the momentum equation (with a vector component for each velocity component u, v, w); and the energy equation. The Navier-Stokes equations individually rely on the principles of conservation of mass, conservation of momentum and the conservation of energy and are given in Equations 4.1 - 4.3:

$$\frac{\partial \rho}{\partial t} + div(\rho \boldsymbol{V}) = 0 \tag{4.1}$$

$$\frac{\partial (\rho u)}{\partial t} + div(\rho u \boldsymbol{V}) = -\frac{\partial p}{\partial x} + div(\mu \ grad \ u) + S_{Mx} \tag{4.2}$$

$$\frac{\partial (\rho e)}{\partial t} + div(\rho e \boldsymbol{V}) = -p \ div \ \boldsymbol{V} + div(k \ grad \ T) + \Phi + S_e \tag{4.3}$$

where, $\boldsymbol{V}$ is the velocity vector, p is pressure, μ is dynamic viscosity, S_M is a momentum source term relating to gravity, S_E is the energy source term, e is internal energy of a fluid, k is thermal conductivity and Φ is a dissipation function. It should also be noted that there are two more momentum equations representing the other velocity components v, w but these are not shown here.

The Navier-Stokes equations can be written in many forms, but the above equations are given in the conservative form for compressible, Newtonian fluids and can easily be generalised into a transport equation (Equation 4.4) which is convenient for computational procedures using the finite volume method, as described by Versteeg & Malalasekera (1995).

$$\rho \frac{D\phi}{Dt} = \frac{\partial (\rho \phi)}{\partial t} + div(\rho \phi \boldsymbol{V}) = div(\Gamma \ grad \ \phi) + S_\phi \tag{4.4}$$

where, ϕ is the property of each Navier-Stokes equation, Γ is the diffusion coefficient for the property, and S_ϕ is the source term for that property.

4.2.2 Discretisation of the Navier-Stokes Equations

The Navier-Stokes equations are a series of non-linear partial differential equations and cannot be solved analytically in all but a few very simple cases. Instead they must be solved numerically. To achieve this, CFD commonly uses either a finite difference or finite volume approach, which both use a grid (or mesh) to discretise the equations. The process of discretisation involves the transformation of continuous differential equations into discrete differential equations.

Two types of grid are used in CFD. A structured grid allows for quicker and simpler calculation of the solution at adjacent grid points via addition and subtraction and often leads to improved solutions. An unstructured grid is often quicker to produce, especially for complex geometries and can more easily be automated for use in optimisation processes. However, unstructured grids are often redundantly large, leading to long convergence times.

Although the finite difference method supplies a simple approach of discretisation to higher order derivatives, it requires a structured grid and is not well suited to complex geometries. For these reasons the finite volume method was developed for use in CFD and is used in the CFD solver throughout the present work.

4.2.2.1 Finite Volume Method

In the finite volume method the volume integral of the governing equations are discretised. The flow field is divided into cells (via meshing) and the discretised flow equations are then solved numerically to determine the property at the nodes of each cell volume. Further details of the following discussion on the finite volume method can be found in Tu *et al.* (2012).

Finite volume schemes are based on the application of the conservation principles over a control volume. Consider the continuity equation in integral form, where the first term on the left hand side represents the change in control volume mass over time and the second term represents the net mass flux over the boundaries of the control volume:

$$\frac{\partial}{\partial t}\left(\iiint_V \rho dV\right) + \iint_S \rho \boldsymbol{V}.dA = 0 \tag{4.5}$$

Since the control volume used in the integral form is the finite volume element (grid element), this reduces to a surface integral of $\boldsymbol{V}$ and ρ:

$$\iint_S \rho \boldsymbol{V}.dA = 0 \tag{4.6}$$

For a 2D finite volume, this can be discretised in the x and y directions to give an approximation for the integral form of the continuity equation, as shown in Equation 4.7. For the conservation of mass, the discretised form of the continuity equation requires that the sum of the mass flow over each edge of the control volume is zero:

$$\iint_S \rho \boldsymbol{V}.dA \approx \sum_{i=1}^{N} (\rho_i u_i A_i^x + \rho_i v_i A_i^y) = 0 \tag{4.7}$$

where, i is the edge of the control volume, and A_i^x and A_i^y are the areas of the edges in the x and y direction respectively, equivalent to the area vector $A_i \bar{n}$.

For a general flow property ϕ and a 3D finite volume, the divergence theorem can be used to relate the volume integral of ϕ, which contains a divergence term, into a surface integral as follows:

$$\iiint_V \nabla.\phi dV = \iint_S \phi.dA \tag{4.8}$$

The left hand side of Equation 4.8 can be expanded to:

$$\iiint_V \nabla.\phi dV = \iiint_V \frac{\partial \phi_x}{\partial x} + \frac{\partial \phi_y}{\partial y} + \frac{\partial \phi_z}{\partial z} dV \tag{4.9}$$

The x component of Equation 4.9 must be equal to the x component of the surface integral in Equation 4.8 and when normalised by the volume (V) results in an approximation for the first order derivative of ϕ in the x-direction, by discretisation of the volume integral of $\partial\phi/\partial x$, in Equation 4.10:

$$\left(\frac{\partial \phi}{\partial x}\right) = \frac{1}{V}\iiint_V \frac{\partial \phi_x}{\partial x} dV = \frac{1}{V}\iint_S \phi_x dA^x \approx \frac{1}{V}\sum_{i=1}^{N} \phi_i A_i^x \tag{4.10}$$

Including all coordinate directions for a 3D mesh, this yields:

$$\nabla.(\phi) = \frac{1}{V}\iiint_V \nabla.(\phi)dV \approx \frac{1}{V}\sum_{i=1}^{N}(\phi_i A_i^x + \phi_i A_i^y + \phi_i A_i^z) \tag{4.11}$$

This principle can also be applied to discretise higher order derivatives, for example Equation 4.12:

$$\nabla^2(\phi) = \frac{1}{V}\iiint_V \nabla^2(\phi)dV \approx \frac{1}{V}\sum_{i=1}^{N}\left(\frac{\partial\phi}{\partial x_i}A_i^x + \frac{\partial\phi}{\partial y_i}A_i^y + \frac{\partial\phi}{\partial z_i}A_i^z\right) \tag{4.12}$$

in which, $\nabla.\phi$ on the RHS can be estimated by developing linear approximations from the values of ϕ in adjacent volumes.

Any source terms in the volume integral form of the governing equations can be approximated as the average value of the source term, $\bar{S_\phi}$ over the control volume:

$$\iiint_V S_\phi dV \approx \bar{S_\phi} \tag{4.13}$$

The finite volume method is advantageous over the finite difference method as the former ensures that the fluid properties are conserved and is not restricted to structured grids. For these reasons, the finite volume method is used by most commercial CFD codes and is employed by the Rolls-Royce CFD solver during the current research.

4.2.3 Temporal Solution Schemes

Not only do the governing equations need to be solved at each mesh point, to give a solution for the whole domain, but the residuals (due to errors in the flow field) must be driven to zero by iterating the calculations. For high-speed compressible flow, this is usually done via a time-marching approach, in which the flow equations are discretised with respect to time and iterated in order to produce a converged, steady-state solution.

There are two possible time-marching schemes: either implicit or explicit. Implicit methods use known information from the current time step and unknowns from the next time step to resolve and therefore require solving of a local system of equations via a complex algorithm. Explicit method are much simpler and a solution for the next time

step can be found from known values at the current time step only.

A time-marching scheme commonly used in CFD is the Explicit 4th order Runge-Kutta method. This method is again based on the Taylor series expansion to find a value of a flow property at time, t_{n+1}. For example, consider the function $(\partial\phi)/(\partial t) = f(t_n, \phi_n)$. The Taylor series for ϕ_{n+1} is given below:

$$\phi_{n+1} = \phi_n + f(t_n, \phi_n)h + \frac{1}{2!}f'(t_n, \phi_n)h^2 + \frac{1}{3!}f''(t_n, \phi_n)h^3 + \frac{1}{4!}f'''(t_n, \phi_n)h^4 + O(h^5) \quad (4.14)$$

where, $h = (t_{n+1} - t_n)$.

This expansion is equated to the Runge-Kutta 4th order method formula, shown in Equation 4.15, which allows the evaluation of ϕ_{n+1} from the value of the function $f(t_n, \phi_n)$ only at certain points in time between t_n and t_{n+1}.

$$\phi_{n+1} = \phi_n + \frac{1}{6}(k_1 + 2k_2 + 2k_3 + k_4)h \quad (4.15)$$

where the coefficients $k_1 - k_4$ are given as follows:

$$k_1 = f(t_n, \phi_n) \quad (4.16)$$

$$k_2 = f(t_n + \frac{1}{2}h, \phi_n + \frac{1}{2}k_1 h) \quad (4.17)$$

$$k_3 = f(t_n + \frac{1}{2}h, \phi_n + \frac{1}{2}k_2 h) \quad (4.18)$$

$$k_4 = f(t_n + h, \phi_n + k_3 h) \quad (4.19)$$

Although simple to implement, explicit schemes have a limit on the maximum time step size, which if exceeded can cause instability of the solution. This limit means that explicit schemes often take longer to reach a converged steady-state solution. Implicit schemes, such as the first order Euler method, shown in Equation 4.20, do not suffer from such instabilities and can therefore be used with much larger time steps.

$$\phi_{n+1} = \phi_n + f(t_{n+1}, \phi_{n+1})h \quad (4.20)$$

4.2.4 Reynolds Averaged Navier-Stokes (RANS)

Turbulence is a chaotic phenomenon for which there is no universal theory. There are several approaches to resolving the turbulence in the flow which are discussed below.

Direct Numerical Simulation (DNS) resolves scales in the flow down to the Kolmogrov length scales, where viscous dissipation dominates. This allows the turbulence to be directly simulated but is exceedingly computationally expensive for most practical applications. Large-Eddy Simulation (LES) is hybrid method which attempts to directly solve the mean flow and large scale turbulent fluctuations, whilst modelling the effects of smaller scale flow structures. LES works on the principle that these large fluctuations contain most of the energy in the system. As the large eddies destabilise, driven by inertial forces, they break up into smaller eddies and the energy contained within them cascades down from the large to small scales. This cascade of energy is assumed to be unidirectional and that by resolving the large structures, most of the energy of the system has been accounted for. It is only at the small scales where viscosity plays a part by dissipating the energy flux. The cut-off between the large and small eddies is determined by a filter, which in most LES codes is set by the grid size. All of the fluctuations below this filter width are represented by a Sub-Grid Scale (SGS) model which mimics the dissipation of energy. This filtering process produces Residual Stresses, which must be modelled by the SGS model.

LES requires significantly less computational resources than DNS, but still several orders of magnitude more than the, much more common, Reynolds-Averaged Navier-Stokes (RANS) method. RANS calculations use a turbulence model to resolve the turbulence and are based on the idea that over a period of time the irregularities of turbulence average out producing a smooth, predictable flow. Taking this fact into account, u_t is decomposed into a statistical mean component and a fluctuating component $(\bar{u}+u')$ and substituted for u_t in the Navier-Stokes equations. Time averaging the Navier-Stokes equations with $u_t = \bar{u} + u'$ produces a series of statistical properties $-\rho\overline{u_i' u_j'}$ (the apparent shear stress) and $-\rho\overline{u'^2}$ (the apparent normal stress) which together are known as

the Reynolds Stresses, akin to the Residual Stresses of LES. Despite the chaotic nature of u_t these statistical properties are somewhat reproducible and are used as standard in RANS CFD codes.

The use of a statistical approach creates more unknowns than equations, giving rise to the closure problem of turbulence. To close the system, a turbulence model must be used to model the Reynolds Stresses.

4.2.5 Turbulence Modelling

Many different turbulence models exist, which are categorised by the number of additional transport equations required to be solved. Examples of such models are the $k-\omega$ SST, $k-\epsilon$ models (2-equation models) and the Spalart-Allmaras (1-equation) model.

The Spalart-Allmaras (SA) turbulence model was used almost exclusively for computations during this work and so is detailed here. The SA model is a 1-equation turbulence model, developed by Spalart & Allmaras (1992), which solves a transport equation (Equation 4.21) for a kinematic turbulent viscosity parameter $\tilde{\nu}$, which is otherwise known as the Spalart-Allmaras variable. This Spalart-Allmaras variable is related to the turbulent viscosity μ_t by equation (4.22).

$$\frac{\partial \tilde{\nu}}{\partial t} + div(\tilde{\nu}\boldsymbol{V}) = \frac{1}{\sigma}\left(div[(\nu+\tilde{\nu})grad(\tilde{\nu})] + c_{b2}(grad(\tilde{\nu}))^2\right) + S \tag{4.21}$$

$$\mu_t = \rho\tilde{\nu}f_{\nu 1} \tag{4.22}$$

where $f_{\nu 1}$ is a wall damping function which is zero near the wall and tends to one at high Reynolds numbers.

The Spalart-Allmaras model was originally developed for aerospace applications, with external aerodynamic flows in mind, but has also been applied extensively for internal aerodynamics such as turbomachinery blade rows. The SA model was chosen on several grounds. Firstly, being a one-equation model, computation times are lower than two-equation models such as $k-\epsilon$. Wheeler *et al.* (2011) compared the two models,

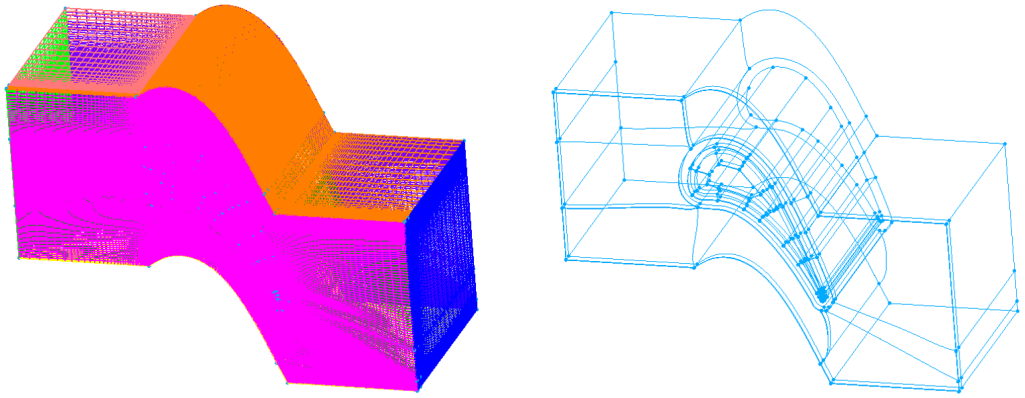
showing that there was very little difference in heat transfer results between the SA and $k-\epsilon$ models at transonic speeds. Secondly, many authors such as Virdi (2015), Zhang *et al.* (2011b) and O'Dowd *et al.* (2010b) have shown that the SA model gives good agreement to experimental cascade data for both tip heat transfer and aerodynamic loss and so is suitable for the current research.

4.3 HYDRA CFD Flow Solver

HYDRA is an in-house CFD solver which was used for all CFD calculations presented in this work. The HYDRA code is a suite of non-linear, linear, unsteady and adjoint CFD solvers, initially developed by Professor Mike Giles at the University of Oxford (Moinier & Giles (1998)) for analysis of turbomachinery flows in partnership with Rolls-Royce.

Hydra uses an edge-based 2nd order finite-volume method to discretise the governing flow equations around median-dual control volumes. The discretised flow equations are marched towards a steady state solution by a five stage Runge-Kutta explicit time-marching scheme with a block Jacobi pre-conditioner to speed up the iteration towards steady state. Convergence is further accelerated in HYDRA by use of an element collapsing multi-grid algorithm which automatically generates sequences of coarser meshes from the input mesh. During each iteration, information is passed from the coarsest mesh to the finest. For the current work it was found that the use of three multi-grid levels struck a balance between the number of iterations required to reach a steady state solution and the clock time taken for completion of one iteration.

RANS calculations are the most commonly used in HYDRA, although LES and detached eddy simulations (DES) are also available. All CFD performed throughout the current research used RANS calculations. There are also several turbulence models available in HYDRA, namely the Spalart-Allmaras (SA) model, $k-\epsilon$ and $k-\omega$ SST models. The SA model is the most mature in HYDRA and as already mentioned was the model of choice in the current research. This required the definition of the initial kinematic turbulent viscosity $\tilde{\nu}$ at inlet of the computational domain.



(a) CFD domain (b) Mesh blocking structure

Figure 4.1: CFD domain and example multi-block mesh structure

4.4 Computational Domain and Meshing

As previously discussed, the spatial discretisation of the flow equations requires the creation of a mesh, on which the finite volume method can be applied. The commercial meshing package Pointwise was used for all meshing done during this research. The meshes produced were structured, multi-block meshes, which can give improved performance over unstructured meshes as discussed in Section 4.2.2. Pointwise gives the user a high degree of control over the mesh and allows for minute adjustments of individual mesh nodes, which can be critical for producing a high quality mesh, with low cell skewness, for a blade tip with a high degree of turning, such as those studied.

The computational domain and multi-block structure can be seen in Figure 4.1, where the full cascade blade span is meshed. The domain inlet and outlet were placed one axial chord upstream and one axial chord downstream of the blade, to represent the positions of the inlet pitot-static probe and thermocouple and the exit wall static pressure tapping respectively in the HSLC.

The mesh quality can have a dramatic impact on the stability, convergence time and accuracy of the solution. The structured meshes produced for this study followed some simple rules: the minimum internal angle of a mesh cell was kept above 30^o, with an average of approximately 65^o; the cell expansion ratio was kept below 1.2. Additionally, the wall-adjacent cell heights were kept as low as practically possible by a fine extrusion

of the boundary layer; this resulted in y^+ values approaching 1, as required to solve the laminar sub-layer.

4.4.1 Boundary and Initial Conditions

Since the Navier-Stokes equations can be used to describe all fluid flows, the specific problem is defined by setting the boundary conditions and initial conditions. It is vitally important to set these correctly, otherwise a converged solution could be achieved but for the wrong flow field.

The boundary and initial conditions used for this CFD study were based on experimental cascade data from the HSLC, determined by Virdi (2015) (and shown in Table 3.2). The inlet and exit boundary conditions were set as a uniform total pressure boundary and a uniform static pressure boundary respectively. The initial conditions at these boundaries were defined to mirror the experimental set-up. The blade, blade tip and casing were set to be viscous walls with no-slip condition. An inviscid wall condition was applied to the hub, which is acceptable since this study focussed solely on the aerothermal performance of the tip region of the blade. Lastly, the upper and lower (mid passage) boundaries were defined as translational periodic.

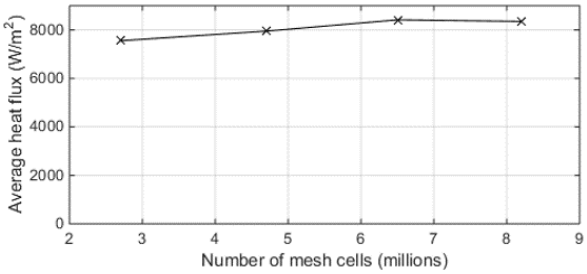
Other initial conditions required were the inlet total temperature, which was also kept similar to experiment, at approximately 290 K. The inlet and exit flow angles were also defined, based on blade design data. Finally, the kinematic turbulent viscosity must be defined at the inlet, as discussed in Section 4.3. An initial estimate for $\tilde{\nu}$ was calculated as follows, based on experimental values of the inlet turbulence intensity, $I \approx 8\%$ and length scale, $l = 15mm$ measured by Zhang *et al.* (2011a):

$$\tilde{\nu} = \sqrt{\frac{3}{2}}\overline{U}Il \tag{4.23}$$

It is noted that these measurements were taken by Zhang *et al.* (2011a) prior to the inlet turbulence grid modification discussed in Section 3.3.2. However, the inlet plane for CFD is located approximately 5 axial chords downstream of the turbulence grid



(a) CAD of the PS cut-back squealer tip geometry



(b) Area averaged tip heat fluxes

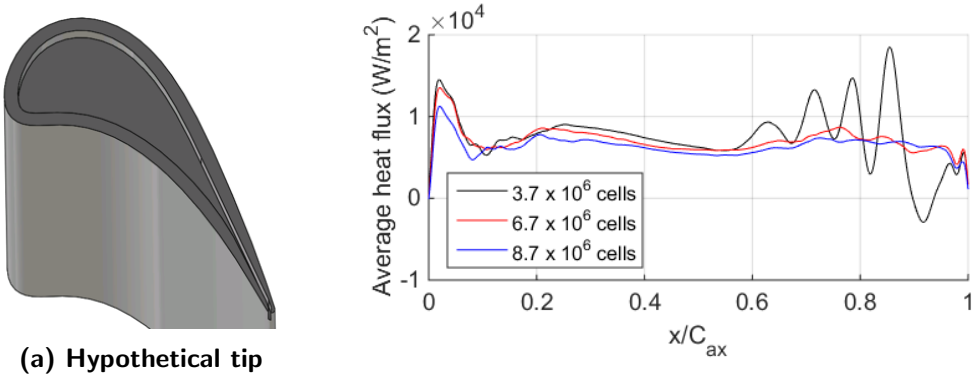
Figure 4.2: Mesh independence analysis for the CFD PS cut-back squealer tip

and it is expected that mixing of flow between the turbulence grid and inlet plane will minimise the effects of the minor grid reinforcement modification.

4.5 Mesh Independence Study and Convergence

It is essential to carry out a mesh independence study, in order to verify that CFD results gained are not influenced by discretisation errors. A mesh independence study was first performed on the PS cut-back squealer geometry shown in Figure 4.2a, which is a closed squealer tip with cut-back pressure side rim towards the trailing edge. Starting with a coarse mesh, four meshes were produced with increasing mesh density until the effects of further increasing the number of mesh cells was seen to be negligible. The number of mesh cells was increased in all dimensions of the model and the wall-adjacent cell height was also decreased. The mesh independence was assessed by examination of the area-averaged tip heat fluxes for each mesh, as shown in Figure 4.2b. The change in solution between the 6.5 million cell mesh and the 8.2 million cell mesh was only 0.7%, therefore the solution was deemed to be mesh independent at 6.5 million cells, where y^+ values were mainly between 1 and 3.

The CFD study in Chapter 8 compared five different geometry variations based around the PS cut-back squealer tip shown above. For a majority of the geometries, meshes were created with similar density and cell spacing parameters as the mesh independent solution shown in Figure 4.2. These were checked by running a single finer



(a) Hypothetical tip geometry

(b) Circumferentially averaged tip heat fluxes

Figure 4.3: Mesh independence analysis for the hypothetical tip geometry

mesh for each case (results not shown).

For the uncooled geometry which formed the basis for the cooled CFD study (the hypothetical tip) in Chapter 9, another full mesh independence study was performed. This geometry is shown in Figure 4.3a, where a narrow channel allows the cavity flow to exit close to the blade trailing edge. The mesh density was increased in the same way as before, starting with a coarse mesh and the circumferentially averaged tip surface heat fluxes were examined and presented in Figure 4.3b. Significant instability is observed towards the tip trailing edge with the coarsest mesh; as the mesh density increases, these instabilities vanish and approximate mesh independence is achieved at 6.7 million cells.

For each CFD simulation it is necessary to monitor the flow residuals, to ensure that the solution has converged. HYDRA allows two root mean square residuals to be monitored: a flow residual which represents the combined flow residuals from all five Navier-Stokes equations; and a turbulence residual, here representing the turbulence equation for the Spalart-Allmaras model. The convergence criteria were that the residuals either drop at least three orders of magnitude or become steady around a constant residual value. An example convergence history is shown in Figure 4.4.

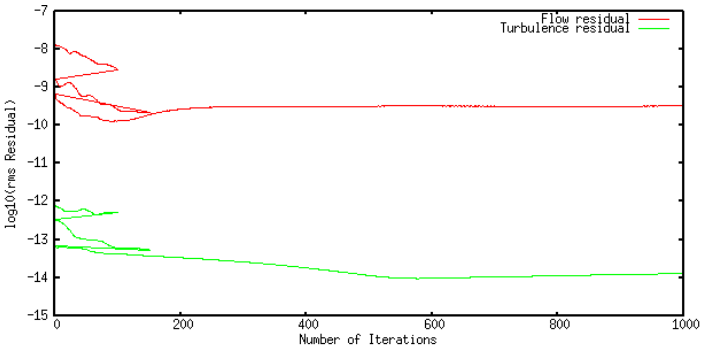


Figure 4.4: Example HYDRA convergence history (note iterations on coarser grid levels at start)

4.6 Film Cooling Methodology

Two methods were used to enable the input of film cooling into the system. A low fidelity approach, utilising HYDRA's source term modelling was used to investigate a large design space, while a high fidelity approach involving the meshing and full resolution of the cooling hole was used as a initial validation of the source term method before experimental results.

4.6.1 HYDRA Source Term Modelling

Film cooling in HYDRA can be defined by source term modelling, where the film coolant is injected uniformly over a specified film cooling strip; this adds a source term to the flow equations, to be resolved. The source terms are declared by use of two files: one which gives the coordinates of the film cooling rows on an existing mesh; the other which gives the film cooling boundary conditions. The source term film cooling functionality in HYDRA was primarily designed for use with blade surface cooling rows, but since the current study examined the influence of a single cooling hole on the OTL flow, the film cooling 'row' was defined by two coordinates a short distance apart, to simulate a single dust hole.

The source term cooling boundary conditions file contains information describing the coolant mass flow, direction of injection and injection angle, hole area, coolant total temperature, coolant density and the maximum penetration distance of the coolant.

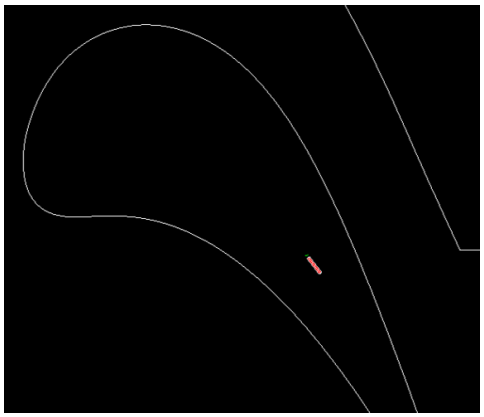


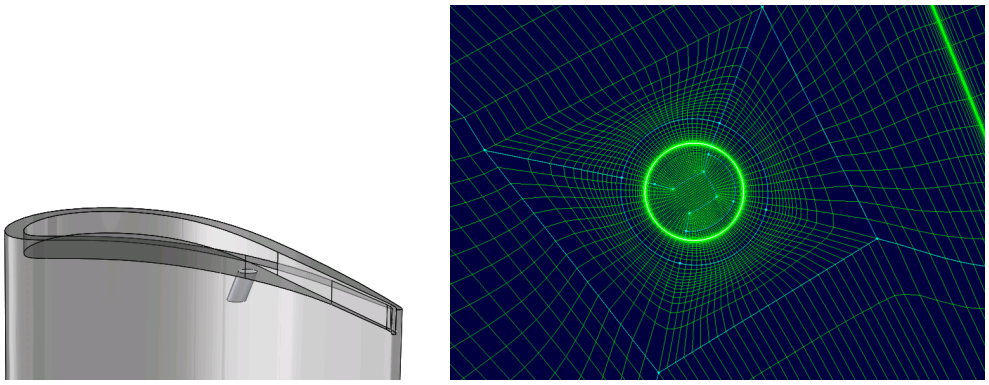
Figure 4.5: Location of dust hole and coolant direction for source term modelling. (From HYDRA jm52)

These were set to suitable values to match the fully resolved cases for the particular tip cooling scenario, as will be discussed in Chapter 9. Following set-up of the cooling source terms, the film cooling data can be checked in HYDRA's jm52, to ensure the basic parameters are correct, as shown in Figure 4.5 for an example case.

4.6.2 Fully Resolved

A higher fidelity approach was used as a first step of validation (before validation to experiment) of the source term modelling. The dust holes were circular in shape and was represented by a 5 mm extrusion in the opposite direction to the coolant flow angle (Figure 4.6a), which was meshed using Pointwise. An example of a cooling hole mesh integrated into the surrounding mesh can be found in Figure 4.6b. The baseline mesh for integration of a 2.5 mm cooling hole was the mesh independent solution for the uncooled tip (6.7 million cells), as shown in Section 4.5. For the cooled mesh, the wall-adjacent cell height within the cooling hole was kept the same as that in the rest of the mesh, with a cell expansion ratio of 1.2. The mesh density in the area downstream of the cooling hole was increased compared to the uncooled case, producing a cooled mesh of 8 million cells. This level of mesh refinement was maintained for the other fully resolved cooling cases presented in Chapter 9.

The cooling hole consists of two boundaries. The cooling hole inlet was set as a



(a) Cooling hole CAD (b) Cooling hole mesh integration

Figure 4.6: Cooling hole CAD and mesh

uniform total pressure boundary, same as the domain inlet, and the internal cooling hole wall was defined as a viscous wall, similar to the blade, blade tip and casing. The initial coolant total pressure and temperature will be discussed in Chapter 9.

4.7 CFD Aerothermal and Cooling Performance Parameters

The uncooled CFD simulations were analysed for aerothermal performance and the cooled simulations also for cooling performance. The methods for determining heat transfer coefficients, aerodynamic loss and cooling effectiveness will be discussed here.

4.7.1 Aerothermal Performance

A two temperature approach was utilised to calculate the tip heat transfer coefficients. Taking the convective heat transfer equation (Equation 3.16), this approach relies on the assumption that h and T_{ad} remain constant for a small change in wall temperature, T_w and therefore depend only on the over-tip aerodynamics for small wall temperature changes. Using two different wall temperatures, T_w, the tip heat transfer was calculated from the following equation:

$$h = \frac{\dot{q}_2 - \dot{q}_1}{T_{w1} - T_{w2}} \tag{4.24}$$

An isothermal wall condition was imposed on the blade tip, blade and casing boundaries and the CFD case ran twice at wall temperatures 5K apart (303K and 308K) to evaluate the heat transfer coefficient.

As discussed in Section 4.4, the outlet boundary of the domain was located one axial chord downstream of the blade row. This was to ensure that the outlet boundary did not interfere with the downstream development of the passage loss mechanisms. Aerodynamic loss was evaluated at the domain exit and the 50% C_{ax} downstream plane by the total pressure loss coefficient, Y_{P0}, as described in Equation 3.26.

4.7.2 Film Cooling Effectiveness

The film cooling effectiveness was evaluated in the CFD using a temperature based method, as it was not possible in HYDRA to perform a mass analogy based method, as used in experiment. This temperature based method required both an uncooled and cooled simulation to be performed and the film cooling effectiveness was calculated by Equation 4.25.

$$\eta = \frac{T_{ad} - T_{rec}}{T_{cool} - T_{rec}} \tag{4.25}$$

where T_{ad} is the adiabatic wall temperature of the cooled case, T_{rec} is the recovery temperature of the uncooled case and T_{cool} is the coolant total temperature at the coolant inlet boundary.

4.8 Summary

This chapter has provided an outline of CFD theory and discussion of the methods used in the current research. The governing equations of fluid mechanics were introduced and the various methods implemented in CFD to numerically solve these partial differential equations were described. The ways employed to resolve turbulence in the flow were introduced, with specifics provided on the Reynolds averaging process and how this

results in the closure problem of turbulence. Discussion of various turbulence models was had, focussing on the Spalart-Allmaras model as used in the present research. The HYDRA flow solver was then introduced.

Specific details of the computational approach employed in the current research were then provided. The computational domain and meshing approach were discussed, using Pointwise to created structured, multi-block grids to discretise the flow field. Details of the baseline tip geometries and mesh independence studies and solution convergence parameters were given; the obtained CFD solutions were shown to have acceptable grid independence and a good level of convergence around a constant residual value.

The chapter then focussed on cooling methodologies employed in the current research. The meshes, boundary conditions and set-up files required for a source term cooling and fully resolved approach were described. A further demonstration of grid independence for the cooled tip mesh was shown.

Finally, the computational aerothermal and cooling performance parameters and analysis methodology was outlined. Included were the calculation of heat transfer coefficient, aerodynamic loss and film cooling effectiveness, as for the experimental methods.

Chapter 5

Baseline Squealer Tip

5.1 Introduction

This chapter introduces a baseline squealer tip geometry and aims to investigate the effect of film cooling on the squealer tip at transonic conditions. Combined experimental data for heat transfer coefficients (HTC) and film cooling effectiveness (η) from the HSLC will be presented for both the uncooled and cooled squealer tip, at a range of tip gaps (0.65% and 1.15% of axial chord) and coolant mass flow rates (nominal and 150% of nominal), allowing the interaction of coolant with the OTL flow and its effects on the tip heat transfer coefficient distribution to be examined. The accompanying CFD presented in this chapter, which helps to explain the phenomenon observed, was performed by Dr. John Coull, who's contribution is greatly appreciated. A brief discussion of the CFD set-up used for this work will be outlined at the start of this chapter.

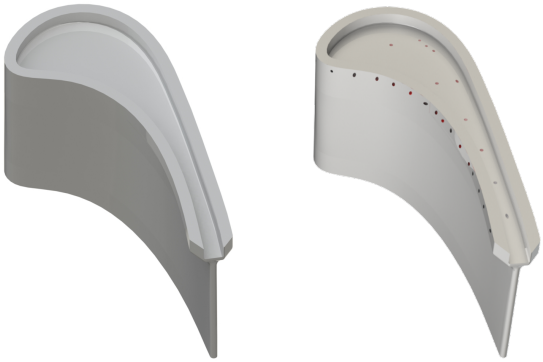
The work contained in this chapter has been accepted for presentation and publication at the ASME 2018 Turbo Expo in Oslo, Norway and has received recommendation for journal publication. To the author's knowledge this is the first time experimental data focussing on the significance of tip gap and coolant mass flow rate has been presented for a cooled transonic squealer tip. It is further believed to be the first time that the pressure sensitive paint technique has been applied for this purpose.

5.2 Accompanying CFD

This section outlines the CFD calculations which were performed by Dr. John Coull for the uncooled cases to compliment the experimental data and help to explain the observations made. Unstructured meshes were generated for a single rotor passage using BoxerMesh v3.6.2. BoxerMesh uses an Octree approach to generate a hex-dominant grid with viscous surface layers. Unstructured meshing has several advantages over structured meshing for the current application, offering improved ease of automation and the ability to concentrate the mesh points in the region of the tip gap. The final mesh contained approximately 40 million grid points with $y^+ < 1$. Steady RANS calculations were performed using the Rolls-Royce in-house solver HYDRA. Details of this code are given by Moinier & Giles (1998). The spatial discretisation is based on an upwind edge-based finite volume scheme and is second-order accurate. Calculations were performed using the one-equation Spalart-Allmaras turbulence model, which was found by Virdi *et al.* (2013) to give good agreement to experiment for tip HTC. Boundary layers were modelled as fully turbulent, since the extent of laminar flow in the tip gap is expected to be small. The applied inlet boundary layer condition was based on the profile obtained experimentally by O'Dowd *et al.* (2010b). The tip gap, flow angle and outlet static pressure boundary conditions were also based on the experimental set-up. Two calculations are performed with adiabatic and isothermal wall conditions to calculate the tip HTCs using Eq. 3.16.

5.3 Blade Tip Geometries

The blade tip geometries studied are of a squealer geometry, with an open trailing edge and a slight overhang on both pressure and suction sides (SS) towards the TE. The uncooled and cooled versions of this tip are shown in Fig. 5.1. Cooling holes are located in the near-tip region on the external surfaces of the squealer rims on both the pressure and suction side (not seen) of the blade tip, as well as a series of dust holes on the cavity



(a) Uncooled tip geometry **(b) Cooled tip geometry**

Figure 5.1: Squealer tip geometry tested

Tip	Squealer rims	Cooling Holes	Cavity Depth (% of S)	Tip Gap (% g/S)	Mean h (W/m^2K)	Camera
Exp Mark I	As-printed (rounded)	No	2.5	0.65 1.15	947.62 1027.73	FLIR A20M (Old)
Exp Mark II	Machined (sharp)	Blocked	2.2	0.65 1.15	1032.18 1042.54	FLIR A655 (New)
CFD	90^o corner	No	2.5	0.65 1.15	1035.9 1098.6	N/A

Table 5.1: Description of uncooled tip variations and mean tip heat transfer coefficients

floor close to the camberline and towards the suction side rim, as seen in Fig. 5.1b.

5.4 Uncooled Tip

This section examines the HTC results for the uncooled tips. Numerical predictions of the tip heat transfer and flow field are used to aide interpretation of the results and to give an appreciation of the changes with relative motion of the blade and casing.

5.4.1 Mark I and Mark II Geometry

Two variations of the uncooled tip were tested which are referred to as the Mark I and Mark II geometry; tip HTC distributions are shown in Figs. 5.2 and 5.3 respectively. The differences between the Mark I and Mark II testing and CFD model are summarised

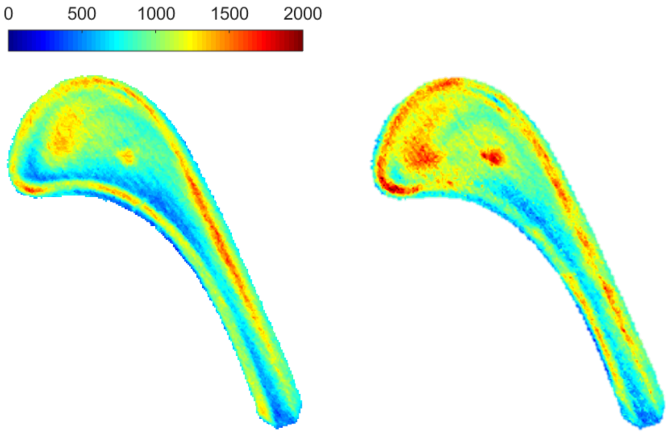
in Table 5.1. The Mark I tip was tested early in the experimental campaign and used the as-printed tip geometry. Subsequent investigation suggests that this case had some rounding on the edges of the tip which affects the results. The Mark II tip is the cooled tip geometry with the cooling holes blocked. Necessary machining done to this Mark II geometry during manufacture left the tip with sharp squealer rim edges and a slightly smaller cavity depth than the Mark I tip. Additionally, testing on the Mark I geometry used a FLIR A20M IR camera, with lower resolution and smaller dynamic range, hence the improved image quality of Fig. 5.3.

The following discussion of the uncooled tip focusses on the Mark II geometry and will examine the influence of changing tip gap, with reference to the flow field from the accompanying CFD (Fig. 5.4). The differences in HTC of the Mark I and Mark II tips observed in Figs. 5.2 and 5.3 will be discussed with respect to the PS rim edge radius and cavity depth differences mentioned above.

5.4.2 Influence of Tip Clearance

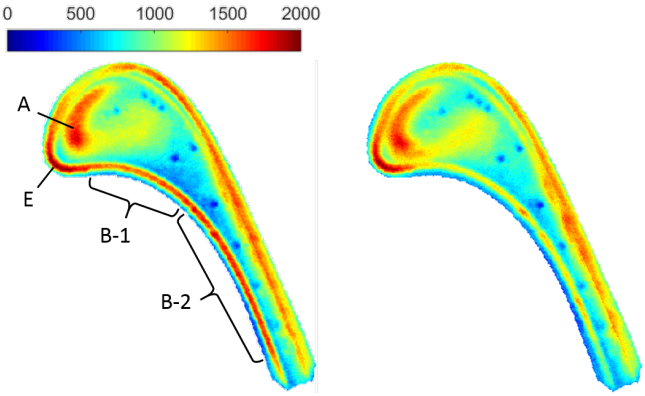
The HTC hotspot marked *A* on the Mark II tip in Fig. 5.3 is caused by the impingement of the overtip leakage (OTL) flow on the cavity floor and is a characteristic feature of flow over a squealer tip. It is observed by comparison of Figs. 5.3a and 5.3b that with an increase in tip gap this impingement hotspot moves closer to the PS rim and is slightly enlarged and enhanced due to higher OTL mass flow at the larger tip gap. These trends have been previously observed by Virdi *et al.* (2013) and are predicted well by the CFD in Fig. 5.4, although the CFD does over-predict the HTC hotspot intensity at both tip gaps.

A region of high HTC is observed on the squealer rim at the leading edge (LE), at *E* in Fig. 5.3. This region is close to the stagnation point and coincides with the main leakage flow path over the rims at the LE. At higher tip gap the HTC intensity is very similar. Although this feature is predicted by the CFD in Fig. 5.4, the exact details and variation with tip gap size is slightly different to experiment.



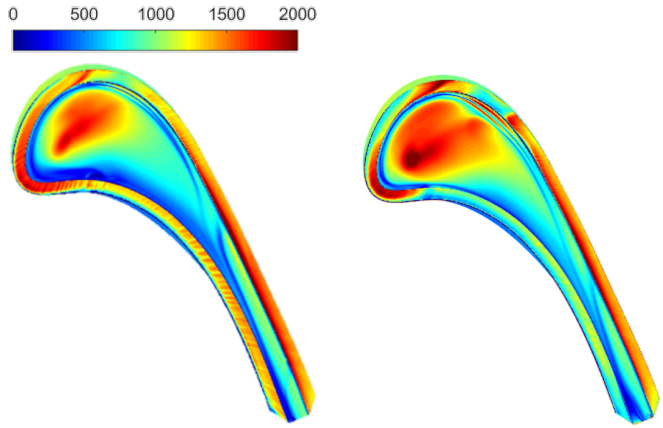
(a) 0.65% Tip Gap (b) 1.15% Tip Gap

Figure 5.2: Experimental uncooled tip HTC [W/m^2K] - as-printed Mark I geometry with slight PS rim edge rounding



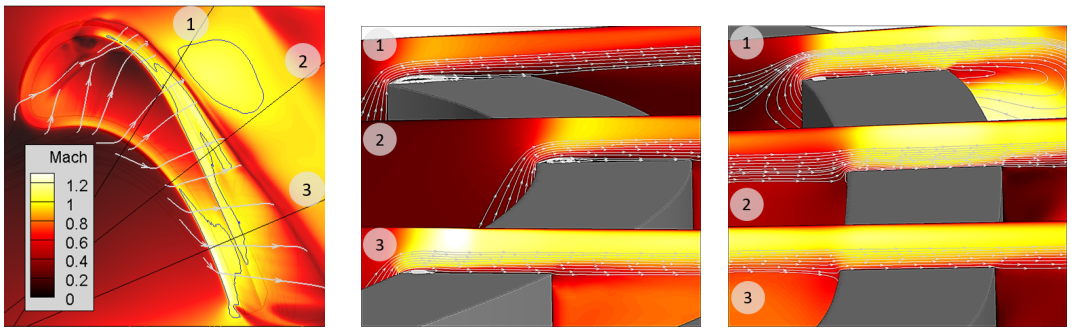
(a) 0.65% Tip Gap (b) 1.15% Tip Gap

Figure 5.3: Experimental uncooled tip HTC [W/m^2K] - Machined Mark II geometry with sharp PS rim edge (cooled geometry with cooing holes blocked)

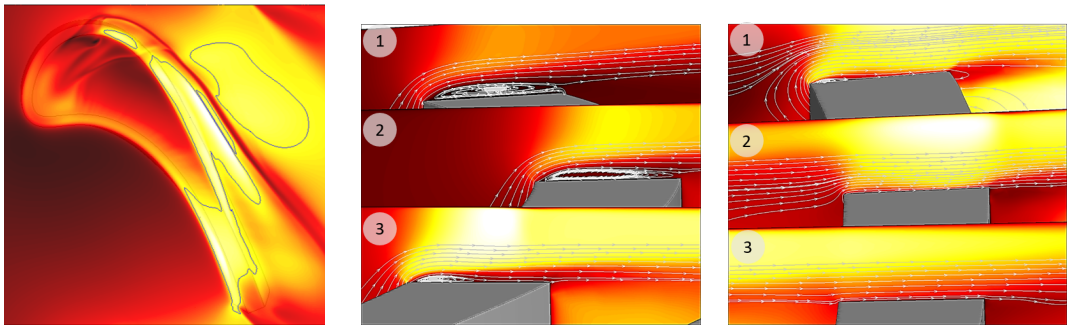


(a) 0.65% Tip Gap (b) 1.15% Tip Gap

Figure 5.4: CFD uncooled tip HTC [W/m^2K] - for comparison to Mark II geometry



(a) 0.65% g/S at mid tip gap **(b) 0.65% g/S PS rim** **(c) 0.65% g/S SS rim**



(d) 1.15% g/S at mid tip gap **(e) 1.15% g/S PS rim** **(f) 1.15% g/S SS rim**

Figure 5.5: CFD predictions of Mach for the uncooled squealer tip at 0.65% and 1.15% g/S: (a),(d) at mid tip gap plane, the blue line denotes $M = 1$ and black lines denote the cut-plane locations; (b),(c),(e),(f) at three cut planes perpendicular to the tip surface. Streamlines shown in grey.

On the PS rim (at *B-1* and *B-2*) in Fig. 5.3, the HTC is higher at the smaller tip gap, which is captured in the CFD predictions in Fig. 5.4 and can be ascribed to earlier reattachment of the over rim flow at the lower clearance. Fig. 5.5b and 5.5e show the predicted Mach numbers and velocity streamlines of the OTL flow passing over the PS squealer rim at three distinct planes. Comparison of these figures shows the earlier reattachment at the smaller tip gap; at 1.15% g/S the flow does not reattach on the PS rim on the two upstream planes.

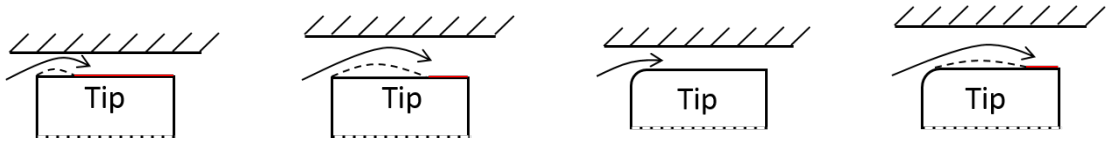
For both clearances it is observed in Fig. 5.3 that the HTC in region *B-2* towards the TE is higher than at *B-1*. This behaviour can be attributed to differences in the Mach number and angle of the OTL flow in these areas, which cause earlier reattachment towards the TE, as observed in Fig. 5.5b. By examination of the mid tip gap Mach numbers in Fig. 5.5a it can be seen that region *B-2* is supersonic, whereas region *B-1*

sees high subsonic flow. As found by Wheeler *et al.* (2011), supersonic reattachment is an accelerating process that damps turbulence intensity and reduces the length of the separation bubble, resulting in an earlier reattachment at *B-2*. Whereas Wheeler *et al.* (2011) saw lower HTC following a transonic reattachment on a flat tip, the current study shows the opposite. In this case the dominant factor is the position of the reattachment on the narrow rim. For example, in the subsonic region of the higher tip gap (*B-1* in Fig. 5.3b and 5.5e-1), the separation bubble covers the width of the rim, reattachment does not occur and the HTC is lower.

The flow angle affects the effective width of the PS rim in the flow direction. At *B-1* the flow over the PS rim is perpendicular to the blade PS, whereas at *B-2* the leakage flow is inclined relative to the rim (Fig. 5.5a-3). Due to the longer flow path, reattachment occurs closer to the PS edge of the rim at *B-2*, causing high HTC over a larger proportion of the rim width.

On the SS rim there is a small increase in HTC observed at lower tip gap in Fig. 5.3, which is also predicted by the CFD in Fig. 5.4. The flow behaviour varies along the length of the blade tip. Towards the LE where the tip is widest, the fluid in the cavity separates over the SS rim before reattachment (e.g. Fig. 5.5c-1). Similarly to the PS rim, this reattachment occurs earlier at the lower tip clearance. However, nearer to the TE the tip is much narrower and the OTL flow passes from the PS rim over the cavity to impinge directly onto the forward edge of the SS rim (e.g. Fig. 5.5c-3). This flow pattern is similar between tip gaps. The modest increase in HTC in this region at lower clearance can be ascribed to the decrease in Mach number observed between Fig. 5.5d and 5.5a; this results in a reduction in acceleration over the SS rim and increased turbulence in the flow in a similar manner to Wheeler *et al.* (2011).

Overall comparison of the Mark II geometry and CFD (Fig. 5.3 and 5.4) shows that the general trends are picked up well by the CFD between tip gaps, with many of the main flow features and trends being captured, despite the small disparity in cavity depth. Table 5.1 shows that the mean tip HTC also agrees well. This gives some confidence in



(a) Sharp edge at small tip gap - early reattachment **(b) Sharp edge at large tip gap - later reattachment** **(c) Rounded edge at small tip gap - attached flow** **(d) Rounded edge at large tip gap - separated flow**

Figure 5.6: Tip flow mechanisms for a sharp and rounded pressure side rim edge at different tip gaps (high HTC region in red)

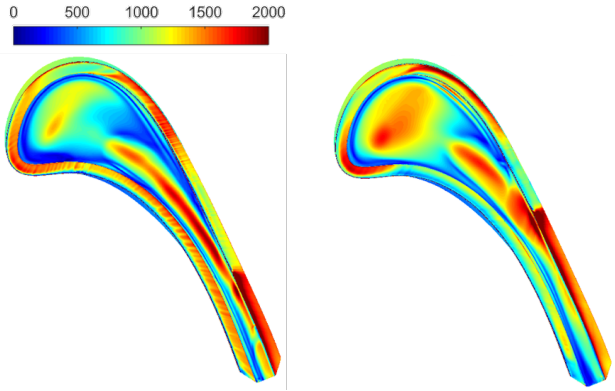
the validity of the CFD and the predictions of casing motion which will be presented later.

5.4.3 Pressure Side Rim Edge Radius and Cavity Depth

The discussion now considers the differences observed between the two experimental geometries, which have different edge radius and cavity depth (Table 5.1).

The HTC distribution at 1.15% g/S is similar for the Mark I (Fig. 5.2b) and Mark II (Fig. 5.3b) tips, suggesting that the over rim flow separates and reattaches in a similar manner for tips with both sharp and rounded PS rim edges when the tip gap is large. The impingement of HTC onto the cavity floor at A is also very similar in magnitude, despite the slight shift in location. This factor indicates that the small disparity in squealer cavity depth is not enough to greatly affect the cavity floor HTC, although the residual uncertainty around the sensitivity to cavity depth should be investigated at a later date.

At 0.65% g/S there is a much larger difference in HTC on the PS rim, SS rim and cavity floor. A study by Ameri & Bunker (1999) showed that the flow over a rounded edge tip remains attached, whereas a sharp edge tip causes separation, resulting in high HTC on the PS rim at reattachment. The lower HTC on the PS rim of the Mark I tip (Fig. 5.2a) indicates that there is little or no separation occurring. The differing flow behaviour for rounded and sharp edged rims are illustrated in Fig. 5.6. At the small tip gap the rounded edge creates an aerodynamically smooth inlet to the tip gap, like a bell-mouth inlet. At increased tip gap the rounded edge is more aerodynamically sharp,



(a) 0.65% Tip Gap **(b) 1.15% Tip Gap**

Figure 5.7: CFD uncooled tip HTC [W/m^2K] with casing motion

causing the flow to separate.

Several studies examined leakage flows over sharp and rounded rims, for example McGreehan & Schotsch (1988) and Heyes *et al.* (1992) described how the rounding of the tip reduced the thickness of the separation bubble. A thinner separation bubble affects the OTL flow in two ways: first, less turbulent mixing would be generated aft of the separation bubble resulting in lower turbulent kinetic energy in the flow; second, the lower blockage increases the Mach number of the leakage flow and may therefore induce a change to a supersonic flow reattachment. These two mechanisms explain the reduction in the impingement HTC on the SS rim and cavity floor, observed for the Mark I tip in Fig. 5.2 compared to the Mark II tip.

In summary, the differences between the Mark I and Mark II tips originate from the PS rim edge radius which must be carefully considered in experiments and simulations. The CFD result is more similar to the Mark II tip because both have a sharp PS rim, however there remain some differences in HTC magnitude as the Mark II tip cannot have a perfectly sharp 90^o rim edge as in the CFD.

5.4.4 Casing Motion Consideration

It is important to appreciate the change in flow field which would occur under more engine-realistic rotating conditions. A step towards this was achieved by applying a tangential velocity to the casing boundary in the CFD. A more in depth look at relative

casing motion on a similar squealer tip was performed byVirdi *et al.* (2013), so only a brief overview will be discussed here. Fig. 5.7 shows the HTC maps for the tips with relative casing motion. By comparison of these to the stationary casing CFD in Fig. 5.4 it is observed that the HTC on the PS rim changes very little, suggesting a similar flow pattern over this rim. However near to the LE, the cavity floor impingement hotspot is reduced in intensity when casing motion is added, due to a reduction in overtip mass flow. The most striking change is in the mid-chord cavity floor region, where the relative casing motion induces the formation of a cavity vortex; this drives the OTL flow downwards to impinge on the cavity floor generating high HTC. A cavity vortex is seen to form over a longer portion of the tip at the smaller tip gap in Fig. 5.7a compared to Fig. 5.7b, as the bulk OTL flow is closer to the casing and therefore more heavily effected by the casing motion when the tip gap is small. The SS rim adjacent to the cavity vortex impingement sees reduced HTC due to a lack of direct impingement onto this rim as the cavity vortex forms, however a peak of HTC is observed where the cavity vortex leaks over the SS rim.

5.5 Cooled Tips

The cooled tip geometry shown in Fig. 5.1b was tested at the same tip gap clearances as the uncooled tip and at two coolant mass flow rates ($\dot{m}_{cool}$), nominal and 150% of nominal; this enabled direct comparison to the Mark II uncooled geometry, to ascertain how the injection of coolant effects the OTL flow and resultant HTC distribution. The uncooled Mark II tip geometry will be referred to simply as 'the uncooled tip' in the following discussion.

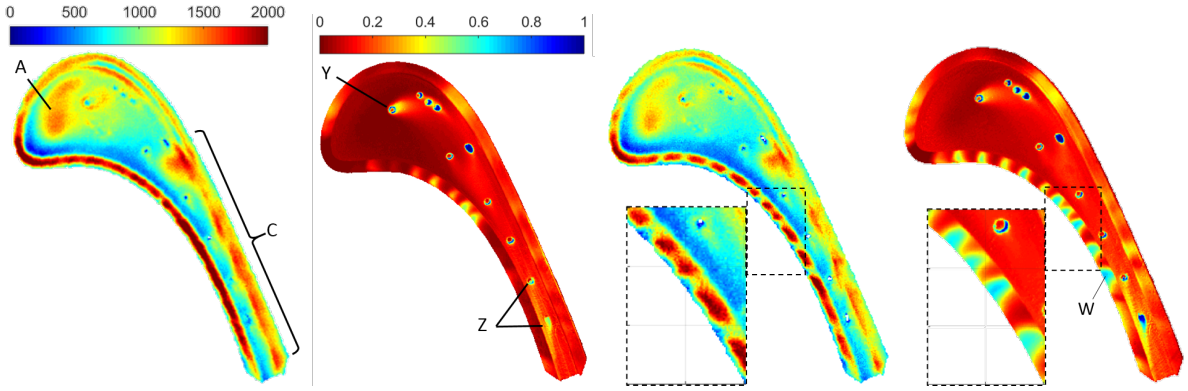
5.5.1 Comparison of Uncooled and Cooled Tips

Figure 5.8a shows the experimental HTC distribution measured for the cooled tip at the 0.65% g/S and nominal coolant mass flow rate. The corresponding adiabatic film

cooling effectiveness is shown in Fig. 5.8b. By comparison of Figs. 5.3a and 5.8a it can be seen that coolant injection increases the HTC in patches of the cavity floor and SS rim downstream of the cooling holes, marked *C*, compared to the uncooled case. Previous subsonic studies, for example Christophel *et al.* (2005), reported seeing increased HTC around the cooling holes, but in this case it is present further from the dust hole. However at transonic conditions, Ma *et al.* (2017) described how the injection of coolant radically alters the OTL flow seen for the uncooled tip by creation of vortical structures emanating from each cooling hole, which entrain the OTL flow and impinge on the tip surface. The pattern of high and low HTC observed on the cavity floor and SS rim in the present study can be ascribed to impingement caused by similar coolant-OTL flow interactions.

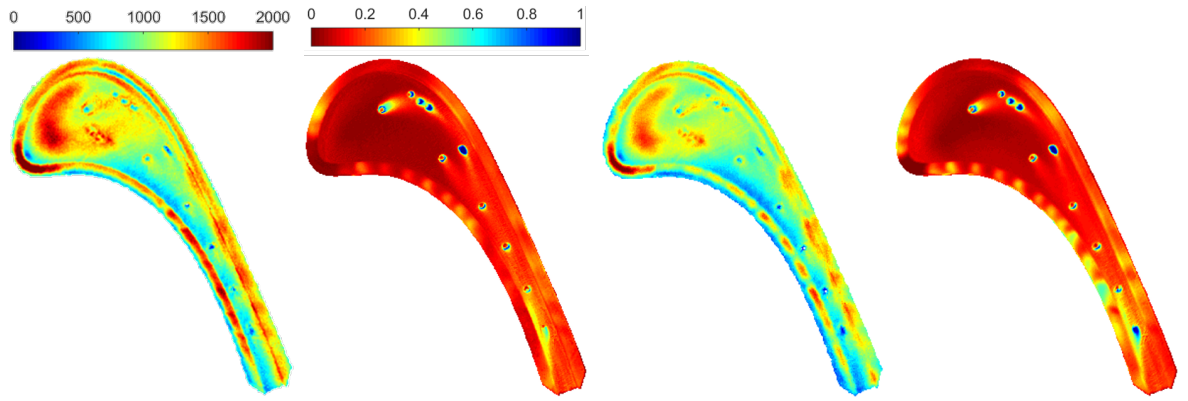
The heat transfer coefficient hotspot at location *A* in Fig. 5.8a reduces in intensity compared to the uncooled tip (Fig. 5.3a), and moves away from the PS rim. This decrease in intensity and movement of the HTC hotspot is in an area without any direct film cooling effect, as seen from contours of η in Fig. 5.8b. This alteration of the impingement can be attributed to a change in flow field caused by downstream coolant injection, for example from dust hole *Y*, which increases the cavity recirculation and blockage to the impinging flow. This upstream reduction in HTC was similarly seen by Ma et al. Ma *et al.* (2017).

It is observed that there is an increase in the HTC on the PS rim for the cooled tip over the uncooled case in Fig. 5.8a and 5.3a respectively. This can be ascribed to an increase in the turbulent kinetic energy of the reattaching flow, as a result of mixing of the coolant and OTL flow. With coolant injection the PS rim exhibits the same increase in HTC towards the TE as seen in the uncooled case, suggesting a similar profile of mid tip gap Mach number and flow angle as described previously (see Fig 5.5a).



(a) HTC, nominal $\dot{m}_{cool}$ **(b) η, nominal $\dot{m}_{cool}$** **(c) HTC, 150% of nominal $\dot{m}_{cool}$** **(d) η, 150% of nominal $\dot{m}_{cool}$**

Figure 5.8: Experimental cooled tip HTC [W/m^2K] and η contours at 0.65% tip gap and two coolant mass flow rates



(a) HTC, nominal $\dot{m}_{cool}$ **(b) η, nominal $\dot{m}_{cool}$** **(c) HTC, 150% of nominal $\dot{m}_{cool}$** **(d) η, 150% of nominal $\dot{m}_{cool}$**

Figure 5.9: Experimental cooled tip HTC [W/m^2K] and η contours at 1.15% tip gap and two coolant mass flow rates

5.5.2 Influence of Coolant Mass Flow Rate

The impact of increasing mass flow of coolant on the HTC can be seen by comparison of Figs. 5.8a and 5.8c. At higher coolant mass flow the LE hotspot decreases due to further upstream influence of the downstream coolant injection and additional enhanced cavity recirculation which blocks impingement.

It can be seen from maps of η in Figs. 5.8b and 5.8d that an increase in coolant mass flow causes a general increase in η over the whole tip. At region C on the SS rim, there is a significant increase in peak η in the coolant flow paths over the rim, denoting improved film coverage in those areas. This improved film blocks impingement of the

previously discussed vortical flow structures onto the SS rim, reducing the HTC at *C* at higher coolant mass flow.

At higher coolant mass flow, a distinctive striping pattern is observed on the PS rim in Fig 5.8c. By examination of the sub-figures in Fig. 5.8c and 5.8d it can be seen that over much of the rim length, the regions of low HTC coincide with regions of high η. High film effectiveness indicates the presence of an attached film from the PS coolant holes; this film blocks reattachment of the separated flow and keeps the heat transfer low in those zones. This behaviour has been seen previously in low Mach number CFD simulations by Acharya *et al.* (2010), but is more obvious in the present study in the subsonic portions of the PS rim. However towards the trailing edge this pattern is not clearly observed. At *W* the coalescence of two cooling jets creates a region of high η which interacts with the OTL flow to produce high HTC. Further towards the TE, the effectiveness is generally low due to several reasons including: differing coolant injection angle; increased Mach number over the TE (to expected transonic flow); a change in streamwise velocity. The overall effect of the film cooling will be discussed below by considering engine-realistic heat flux.

5.5.3 Influence of Tips Clearance

At the higher tip gap, many of the same trends observed with the uncooled tip remain in the cooled case. As for the comparison of Fig. 5.3a and 5.3b, increasing the clearance between Fig. 5.8a and 5.9a shows the following features: the HTC on the SS rim reduces; the PS rim HTC decreases, caused by a later reattachment of the flow; the HTC towards the TE of the PS rim remains higher than area *B-1* due to the tip Mach number distribution and over-rim flow angle.

Moving to lower clearance, the cooled tips in Fig. 5.8a and 5.9a show a larger decrease in the LE impingement hotspot (*A*) than was observed in the uncooled case (Fig. 5.3a and 5.3b). Comparison of the uncooled and cooled tips at the 1.15% g/S tip gap (Fig. 5.3b and 5.9a) shows that the LE hotspot is similar in shape and intensity

in both cases, however the same comparison at 0.65% g/S yields a significant decrease in HTC when coolant is added. These observations indicate that at low tip clearance, when the OTL mass flow and cavity recirculation are lower, the injection of coolant has a larger influence on the upstream OTL flow field; this results in the larger reduction in HTC with reduced tip gap seen for the cooled tips. All of these trends in the HTC distribution with tip clearance described above are consistent at both coolant mass flow rates.

The comparison of Fig. 5.8a and 5.9c shows that at the larger tip gap and higher coolant mass flow rate, the addition of coolant over the PS rim almost completely removes the reattachment onto the rim observed in Fig. 5.8a, greatly decreasing the HTC.

At higher tip gap a reduction in peak film effectiveness occurs on the squealer rims, most evident by comparison of the PS rim in the high coolant mass flow cases of Fig. 5.8d and 5.9d. An increase in tip gap allows greater OTL mass flow to pass over the squealer rims, which dilutes the coolant and disperses it more evenly, producing wider coverage of the films on the PS and SS rims at a lower magnitude of η. Conversely, in the squealer cavity η is seen to increase at higher tip gap. This behaviour can be explained by an increase in the cavity mass flow and velocities, which reduces the local blowing ratio of the dust hole films, keeping them better attached to the cavity floor and increasing the η. The increase in η is most evident by focussing on the LE dust hole (Y) and the two TE dust holes (Z) in Fig. 5.8b and 5.9b. At low tip gap, these films are operating at a high blowing ratio and lift off from the surface.

It should be recognised that a higher coolant mass flow rate does not always produce enhanced η in the local area surrounding the cooling hole. This is highlighted by comparison of the LE film (Y) in Fig. 5.9b and 5.9d, where it is observed that at higher mass flow, lift-off of the film occurs due to an increase in local blowing ratio (similarly to a reduction in cavity mass flow) and the η close to the hole reduces. In such cases, the size of the cooling hole should be increased to keep the coolant velocity low and the

films attached to the surface.

5.6 Implications for a Real Engine

The implications of the results for in-engine heat flux are now considered to assess to overall effect of the film cooling. The Net Heat Flux Reduction (NHFR) has been calculated for an engine realistic case as follows:

$$NHFR = \frac{\dot{q_{uc}} - \dot{q_c}}{\dot{q_{uc}}} \tag{5.1}$$

In the above equation, $\dot{q_{uc}}$ and $\dot{q_c}$ are the uncooled and cooled heat fluxes determined by the convective heat transfer equation (3.16) and evaluated from experimental results:

$$\dot{q}_{uc} = h_{uc}(T_{ad} - T_w) \tag{5.2}$$

$$\dot{q}_c = h_c(T_{aw,c} - T_w) \tag{5.3}$$

Scaling to engine realistic heat flux can be achieved via normalising by engine turbine entry temperature ($T_{01,eng}$) and expressing Equations 5.2 and 5.3 in terms of temperature ratios:

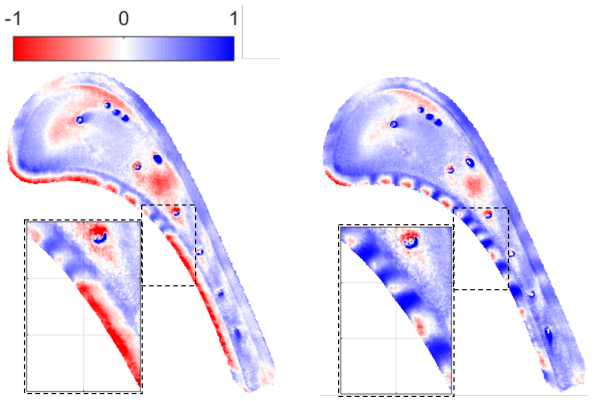
$$\dot{q}_{uc} = h_{rig,uncool}\left(\left[\frac{T_{ad}}{T_{01}}\right]_{rig} - \left[\frac{T_w}{T_{01}}\right]_{eng}\right) \times T_{01,eng} \tag{5.4}$$

$$\dot{q}_c = h_{rig,cool}\left(\left[\frac{T_{aw,c}}{T_{01}}\right]_{eng} - \left[\frac{T_w}{T_{01}}\right]_{eng}\right) \times T_{01,eng} \tag{5.5}$$

where, the ratio of uncooled T_{ad} to rig inlet temperature is scalable to engine conditions, hence $[T_{ad}/T_{01}]_{rig} = [T_{ad}/T_{01}]_{eng}$ in Equation 5.4 and can be evaluated directly from uncooled rig testing as described in Section 3.4.2.

However, due to the disparity between rig and engine coolant to mainstream temperature ratio, $[T_{aw,c}/T_{01}]_{rig} \neq [T_{aw,c}/T_{01}]_{eng}$ in Equation 5.5 and so $[T_{aw,c}/T_{01}]_{eng}$ must be calculated using the measured η_{rig} as follows (again normalised by $T_{01,eng}$):

$$\left[\frac{T_{aw,c}}{T_{01}}\right]_{eng} = \left[\frac{T_{ad}}{T_{01}}\right]_{rig} - \eta_{rig}\left(\left[\frac{T_{ad}}{T_{01}}\right]_{rig} - \left[\frac{T_{cool}}{T_{01}}\right]_{eng}\right) \tag{5.6}$$



(a) Nominal $\dot{m}_{cool}$ **(b) 150% nominal $\dot{m}_{cool}$**

Figure 5.10: NHFR for the 0.65% g/S tip gap

For this analysis, a typical $T_{01,eng}$ of 1800 K was assumed, along with a tip surface temperature to inlet ratio ($[T_w/T_{01}]_{eng}$) of 2/3 and a coolant to inlet ratio $[T_{cool}/T_{01}]_{eng}$ of 0.5.

NHFR for the 0.65% g/S tip clearance and both mass flow rates is shown in Fig. 5.10. It is noted that the heat flux generally reduces with addition of coolant but can locally increase. For the nominal coolant mass flow rate (Fig. 5.10a), the increase in heat flux on the PS rim is driven by the increase in HTC noted on the PS rim in Fig. 5.8a. In the mid-chord of the PS rim the higher cooling effectiveness (Fig. 5.8b) caused a reduction in heat flux in an area where the HTC was not notably reduced. Elsewhere, around the upstream coolant holes increases of heat flux can be observed on the cavity floor, relating to increased HTC, however the high HTC on the SS rim coincides with a reduction in heat flux due to reduced fluid temperature.

Comparison to the higher mass flow case in Fig. 5.10b shows an overall increase in NHFR. The most striking difference occurs on the PS rim, where the areas of high film effectiveness (Fig. 5.8d) are shown to manifest as regions of net heat flux reduction, interspersed by enhanced heat flux where the η is low and HTC is high. The heat flux to the tip on the PS rim is heavily dominated by the presence of the coolant film which blocks the reattaching flow. Closer to the TE in the transonic region there are some areas where high HTC partially coincides with high η (e.g. region W in Fig. 5.8d) but the overall result is still a reduction in heat flux.

Given the observations made in the moving casing CFD, it is expected that the NHFR observed on the PS rim would be similar under rotating conditions. However, in the mid cavity and SS rim the coolant-OTL interactions would become more complex with the creation of the cavity vortex which sits atop the dust holes and likely lead to an increase in heat flux along the cavity floor and some of the SS rim. Further investigations would be required to detail such effects.

5.7 Summary

An open squealer design high pressure turbine blade tip has been experimentally tested, both cooled and uncooled, in the Oxford High Speed Linear Cascade rig. Detailed heat transfer coefficient data was obtained for the uncooled and cooled case at two different tip gaps by an IR thermography technique. Numerical investigation was used to explain some of the features seen on the uncooled blade tip. For the cooled tips, the adiabatic film cooling effectiveness was measured using pressure sensitive paint for two different coolant mass flow rates and tip gaps. These complimentary results allowed examination of the influence of film cooling on the heat transfer to the blade tip. The main conclusions drawn are as follows:

1. Heat transfer to the blade tip is determined by the nature of flow reattachments or impingements onto the tip surface and is therefore dependent on the local behaviour of the OTL flow.

2. The uncooled and cooled tips exhibit similar trends to changing tip gap and can be broken down into three distinct local regions. As tip gap reduces:

   (a) The cavity floor shows a small decrease in HTC resulting from decreased OTL mass flow.

   (b) The PS rim shows increased HTC due to earlier reattachment of the separated flow over the rim edge.

(c) The SS rim shows increased HTC: towards the leading edge due to similar flow behaviour as the PS rim; towards the trailing edge it is due to a reduction in Mach number of the impinging flow.

3. Simulations with casing motion caused little change to the OTL flow over the PS rim, with the main differences occurring in the cavity and on the SS rim. Trends with tip clearance remained similar to those without casing motion.

4. The PS rim edge radius has a significant impact on the behaviour of the OTL flow and the resulting tip HTC distribution at low tip clearance, with implications for consistency between experiments and comparison to CFD.

5. At the nominal cooling rate, the PS cooling jets disrupt the reattachment onto the PS rim tending to increase the HTC compared to the uncooled tip.

6. At increased coolant mass flow, the cooling effectiveness improves over the whole tip, provided that the films do not lift off. In the subsonic region of the PS rim, increased film coverage blocks the reattachment of flow onto the PS rim and reduces the HTC in areas of high film effectiveness. In the transonic regions of the PS rim towards the TE, the film effectiveness is generally low and this pattern is not observed.

7. At increased tip clearance, higher OTL mass flow reduces the film effectiveness on the rims, but increases effectiveness in the cavity. The higher cavity mass flow reduces the local blowing ratio of the films, keeping them better attached to the surface in the vicinity of the dust holes.

8. Scaling to engine temperatures, the injection of coolant alters the OTL flow to cause a reduction in heat flux on the SS rim. Increased heat flux is produced around dust holes and on the PS rim where film effectiveness is low. Areas of high film effectiveness are strongly correlated to reduced heat flux on the PS rim and additionally to low HTC in the subsonic tip region.

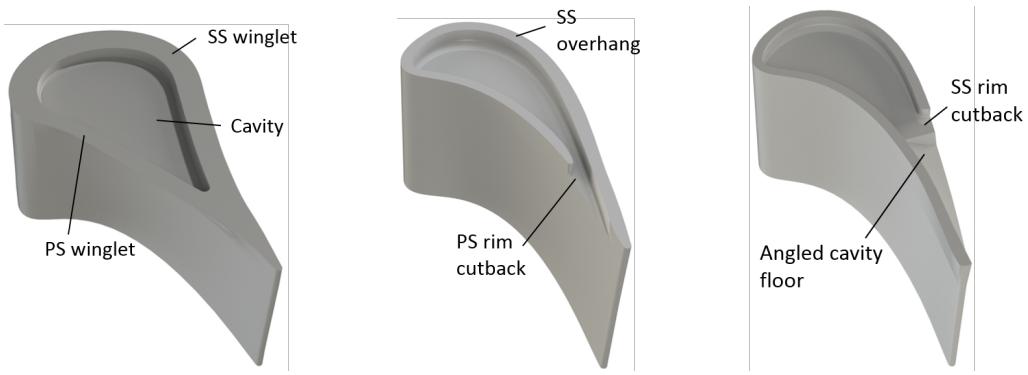
Chapter 6

Experimental Comparison of Uncooled Tip Geometries

6.1 Introduction

This chapter introduces three uncooled tip geometries, for comparison to the baseline squealer tip which was described in Chapter 5. Experimental heat transfer coefficients and aerodynamic loss measurements are presented below for these new tip designs. The same two tip gap heights of 0.65% and 1.15% g/S, as used for the baseline case, were investigated. The first part of this chapter focusses on a detailed comparison of the tip heat transfer coefficients for all four uncooled tip geometries (including the Mark I baseline squealer with PS rim edge rounding) with measurements at the smaller tip gap, before an investigation into the influence of tip gap is presented. A similar comparison is reported for aerodynamic loss measurements.

The interpretation of the flow structures responsible for the performance of the three geometries studied in this chapter build on the knowledge gained from Chapter 5 and are applied to each of the tip geometries in turn, focussing on specific features of the HTC distribution on the PS and SS rim and cavity of each tip separately.



(a) Cavity-winglet tip **(b) Pressure side cut-back squealer tip** **(c) Suction side cut-back squealer tip**

Figure 6.1: CAD renderings of the three uncooled tip geometries reported in this chapter

	Baseline Squealer	Cavity-Winglet	PS Cut-Back	SS Cut-Back
Cavity depth (% of span)	2.5	2.0	2.5	2.0

Table 6.1: Cavity depth of the uncooled tip geometries

6.2 Uncooled Tip Geometries

This section introduces the three new blade tip geometries; a cavity-winglet tip and two squealer tips, one with a pressure side rim cut-back and the other with a suction side rim cut-back. The design philosophy behind each of these blade tip styles has been discussed in the literature review (Chapter 2) and a brief reminder of these design reasons is reviewed below.

The cavity winglet tip can be seen in Figure 6.1a. The main purpose of a winglet tip is to reduce the overtip leakage losses. The winglet overhangs reduce the driving pressure differential across the tip, and thereby reduce the tip leakage mass flow, while the winglet cavity is intended to reduce the tip discharge coefficient by creating two constrictions to the overtip leakage flow similar to the approach used in a labyrinth seal to reduce leakage. However, the extra area of the winglet tip overhangs can be a site for flow reattachments which cause high heat transfer and the winglet tip has been seen to display high heat load due to the large tip area (Coull *et al.* (2014a)). The extra tip area also has the potential to require more cooling flow, which can reduce turbine efficiency and negate the benefit of lower leakage.

The pressure side cut-back tip is shown in Figure 6.1b. The trailing edge region of a squealer tip typically shows high heat transfer and is difficult to cool. The purpose of the opening in the pressure side rim is two fold. This is partly to remove some of the rim material which is difficult to cool and often deteriorates in-service under high thermal load; this approach was found under low speed conditions, by Bunker & Bailey (2001), to reduce the tip heat transfer towards the trailing edge due to decreased local flow reattachment on the flat surface of the tip. In the case of a cooled tip, the opening allows coolant accumulated in the squealer cavity to escape and aid with cooling of the trailing edge. The particular pressure side cut-back tip here also has a small overhang on the suction side towards the leading edge, intended to work in the same way as the overhangs on the winglet tip (see above).

The design philosophy behind the suction side cut-back tip (shown in Figure 6.1c) is similar to that of the pressure side cut-back. The impingement of hot leakage flow onto the suction side rim, causes high thermal load and can result in rim deterioration. The removal of the portion of the suction side rim associated with the leakage flow path pre-empts the inevitable rim deterioration and additionally provides an exit path for the enclosed cavity flow. The tip shown in Figure 6.1c also has an angled cavity floor in the cut-back region to reduce the tendency for reattachment of the leakage flow from the pressure side rim in the local area.

6.3 Heat Transfer

A detailed description of the heat transfer coefficient distribution measurements on the three blade tips considered by the author at the smaller tip gap is presented below. The underlying causes of the main features observed are discussed, with reference to the OTL flow field and relevant reattachment or impingement mechanisms. Comparison is made of the overall heat transfer coefficients for the three tips considered in this chapter and the baseline squealer tip (Mark I geometry with PS rim edge rounding). Changes in the tip heat transfer coefficient distribution with tip clearance are then examined, and

comparisons are made between all four uncooled blade tips.

6.3.1 Comparison of Tip Geometries

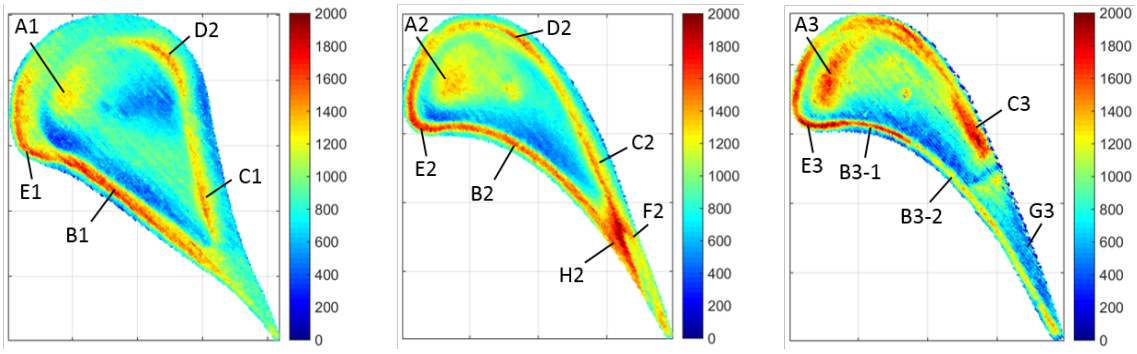
Figure 6.2 shows the tip heat transfer distributions for the three uncooled tip geometries at a tip gap of 0.65% g/S. Table 6.2 gives an indication of the approximate HTC levels in each of the key regions marked in Figure 6.2; the HTC values in this table are used throughout to supplement the qualitative discussion, but are only for indicative purposes. Consideration of the winglet tip HTC data in Figure 6.2a, shows that the highest heat transfer coefficients are located on the pressure side winglet extension, marked *B1*, with HTC levels in the range 1500-1700 W/m^2K (see Table 6.2). This region of high heat transfer is caused by reattachment of the OTL flow onto the pressure side winglet rim. On the cavity floor, towards the leading edge, the impingement zone of high heat transfer (labelled *A1*) can be seen. There is also a band of low heat transfer, inside the PS rim, prior to the region of flow impingement. The final feature of interest is the increased heat transfer on the forward edge of the suction side rim, marked *C1*, which is caused by direct impingement of the leakage flow onto this rim. The main features of the heat transfer distribution for this winglet tip are broadly similar to those observed for the Mark I baseline squealer tip (Figure 5.2a) with the exception of the increased HTC on the pressure side winglet rim (by approximately 33%), as the wider winglet rim allows for reattachment to occur for the cavity-winglet design.

The pressure side cut-back squealer tip (see Figure 6.2b) again shows the impingement high heat transfer zone towards the LE on the cavity floor (marked *A2*), which has a similar level of HTC to that seen for the winglet tip and baseline squealer tip (see Table 6.2). The impingement of flow onto the suction side rim, *C2*, is also present, causing the expected increase in HTC. However it is more evident that for this tip, closer to the LE the fluid in the cavity separates and reattaches onto the SS rim at *D2*, where the aerofoil tip is widest. This behaviour was also observed for the baseline squealer tip in Chapter 5. The main feature of interest for this tip is the area of peak heat transfer located

on the cavity floor in the cut-back region, *H2* (HTC levels approximately 1800-2000 W/m^2K). It will be seen in Chapter 8 that this high heat transfer can be attributed to the scrubbing of an energetic, small diameter vortex, which forms in the cut-back region as the separated flow over the PS edge impinges on the inside vertical face of the SS rim. There is evidence of a small portion of flow leakage over the SS rim in the vicinity of the PS cut-back which manifests itself as increased heat transfer on the rim (marked *F2*), as well as a faint band of increased HTC leading from this leakage point to the trailing edge. This faint band can be attributed to the formation of a leakage vortex from the cut-back region forming atop the suction side rim. The increased HTC in the cut-back region towards the trailing edge is contrary to the findings of Bunker & Bailey (2001) at low speed flows. This phenomenon is considered further in Chapter 8 where the OTL flow field for a very similar pressure side cut-back tip is investigated using CFD.

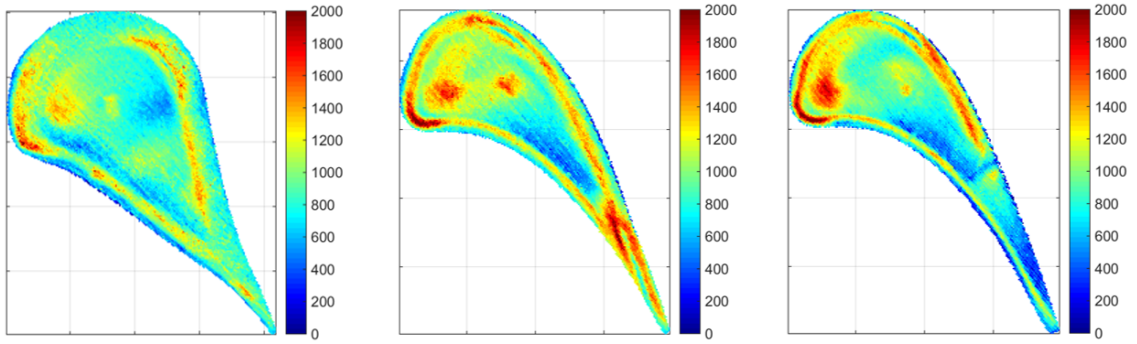
Comparison with the baseline squealer in Figure 5.2a shows that the HTC on the pressure side rim (*B2*) of the PS cut-back squealer tip is also higher (by approximately 25%) than might be expected from the similarity of the geometries. In fact, the heat transfer coefficient magnitude is closer to that measured on the wide winglet rim in Figure 6.2a (see Table 6.2). It is clear that the flow is reattaching onto the pressure side rim of the PS cut-back tip. From the conclusions drawn in Chapter 5 this increase in relative HTC is either caused by a sharper PS rim edge radius on the PS cut-back tip (compared to the baseline squealer Mark I tip), which would cause earlier reattachment or there is some blockage effect caused by the flow in and around the pressure side cut-back region which is influencing the rest of the OTL flow field.

The markedly different geometry of the suction side cut-back squealer tip causes some dramatic changes in the OTL flow field relative to the other designs, resulting in a very different tip HTC distribution, shown in Figure 6.2c, and the highest HTC levels seen in each specific region considered (see Table 6.2). One notable difference is the enhanced LE impingement high HTC zone, *A3*, on the cavity floor compared to the



(a) Cavity-Winglet tip **(b) Pressure Side Cut-Back squealer tip** **(c) Suction Side Cut-Back squealer tip**

Figure 6.2: Experimental heat transfer coefficients [W/m^2K] at g/S = 0.65%

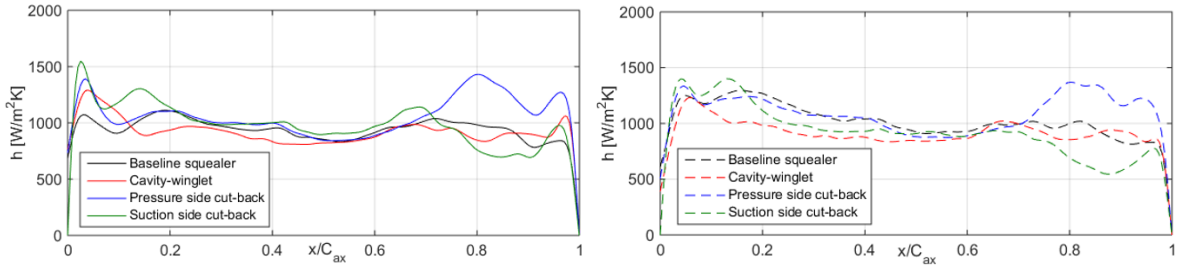


(a) Cavity-Winglet tip **(b) Pressure Side Cut-Back squealer tip** **(c) Suction Side Cut-Back squealer tip**

Figure 6.3: Experimental heat transfer coefficients [W/m^2K] at g/S = 1.15%

Tip Geometry	Tip gap % g/S	HTC in region $[W/m^2K]$ A	B	C	D	E
Baseline	0.65	1250-1350	1100-1300	1400-1600	1200-1400	1600-1700
Squealer	1.15	1500-1650	800-1000	1300-1500	1150-1350	1750-2000
Cavity-	0.65	1200-1300	1500-1700	1300-1500	1300-1500	1450-1650
-Winglet	1.15	1250-1400	1000-1200	1200-1400	1250-1450	1550-1750
PS	0.65	1300-1400	1400-1600	1350-1550	1350-1550	1600-1750
Cut-Back	1.15	1550-1700	1100-1300	1250-1450	**1300-1500**	**1850-2300**
SS	0.65	**1550-1700**	**1550-1750**	**1650-1850**	**1500-1700**	**1750-1950**
Cut-Back	1.15	**1650-1850**	**1150-1350**	**1450-1650**	1150-1350	**1850-2300**

Table 6.2: Approximate HTC levels in specific regions marked in Figure 6.2. Region of peak HTC on each tip indicated in red. The tip showing the highest HTC levels in each region (and tip gap) shown in bold.



(a) g/S = 0.65% **(b) g/S = 1.15%**

Figure 6.4: Circumferentially averaged heat transfer coefficient [W/m^2K] for the uncooled tip geometries at both tip gaps

other tip geometries; an increase of around 25%. The reason for this increased HTC can be ascribed to two factors. Firstly, the SS cut-back tip has a smaller cavity depth (see Table 6.1), which has been shown previously by Bunker & Bailey (2001) and Metzger *et al.* (1989b) to enhance the impinging HTC on the cavity floor. Secondly, the missing portion of the SS rim provides an exit path, or vent, for the cavity flow, reducing the cavity recirculation and therefore diminishing the effective blockage to the impinging flow entering the cavity from over the PS rim. It should be noted here that the cavity-winglet tip also has the same smaller cavity depth as the SS cut-back tip, however the cavity floor impingement demonstrates a lower level of HTC in the impingement region (*A1*), presumably because the cavity-winglet is associated with a lower overall leakage mass flow giving a lower HTC.

Other features of interest on the SS cut-back tip are the high HTC towards the end of the suction side rim (*C3*) caused by flow impingement. The high magnitude of the HTC in this impingement region can be ascribed to increased turbulence intensity around the end of the suction side rim due to mixing between the impinging flow over the PS rim and the path of the cavity flow exiting the cut-back. It is also clear that there is high HTC on the PS rim towards the LE (*B3-1*) in Figure 6.2c, however this stops abruptly in the vicinity of the SS cut-back region (*B3-2*). This behaviour can be attributed to a difference in flow path between the flow arriving at the two regions. Towards the LE, the leakage flow impinges on the cavity floor and is entrained into the cavity flow, which is enclosed by the two squealer rims. However, towards the TE and

close to the cut-back the leakage flow path is inclined towards the trailing edge, where the leakage flow may either impinge directly onto the SS rim (at *C3*) or is free to pass over the PS rim and out into the OTL vortex without reattachment, as the flow path is unhindered by the absence of the SS rim. The angled cavity floor in the cut-back region further prevents any reattachment of the flow over the PS rim which results in low HTC in this portion of the tip surface (*G3*).

A comparative plot of the circumferentially[1] averaged HTC for all four uncooled geometries is shown in Figure 6.4a. This helps highlight trends between the tips. It is observed that the baseline squealer shows the lowest averaged HTC at the LE as little reattachment occurs on the PS rim in this location. The cavity-winglet tip displays the lowest HTC in the mid axial chord portion of the tip due to the large cavity width and low attendant HTC. There is only a small difference (less than 10%) in average HTC between the tip designs until the TE is reached, where the HTC levels for the tip geometries vary significantly. The suction side cut-back tip gives the lowest HTC near the trailing edge, due to lack of reattachment on the rim or cavity floor, whereas the large HTC hotspot in the cut-back region of the PS cut-back tip results in that tip showing the largest averaged HTC.

Consideration of circumferentially averaged HTCs offers a useful means for examining trends between tips, but can often hide local effects, such as peaks in HTC (as indicated in Table 6.2), like the high HTC on the PS rim of the cavity-winglet, which can be offset by the wide expanse of low HTC in the cavity. A peak in HTC can be very significant for the success of a design as local over-heating can limit the life of the blade. Table 6.2 indicates that, at the smaller tip gap, the PS rim at the LE shows the peak in HTC on several of the tips. However, the largest peak HTC of all the tips at this tip clearance was found in the cutback region of the PS cut-back tip; an approximate HTC level of 1800-2000 W/m^2K. These areas are at risk of limiting life and should be protected, for example by the use of cooling films.

[1]Circumferentially in a 2D cascade refers to averaging the HTC at all pitch locations in strips perpendicular to the axial direction (x)

6.3.2 Influence of Tip Clearance

The experimental heat transfer coefficient distributions for the tips (shown in Figure 6.1) at 1.15% g/S tip gap are shown in Figure 6.3. Comparison of the winglet-cavity tip data at the two tip gaps, specifically Figures 6.2a and 6.3a, shows similar trends to those expected from the baseline squealer tip as discussed here. With increasing tip clearance the following trends are observed: there is a clear reduction in the heat transfer on the PS rim (*B1*), of approximately 31% (see Table 6.2), due to delayed flow reattachment; a small increase in HTC level for the LE cavity impingement region (*A1*), although this increase (with increasing clearance) is not as large as that seen for the Mark I baseline squealer (6% compared to 21% respectively). This behaviour can be attributed to the addition of the winglet geometry which limits the increase in leakage mass flow at higher tip gap for the cavity-winglet tip. The final trend observed is the slight reduction in the HTC level on the SS rim at the higher tip clearance (of approximately 7%), due to delayed reattachment close to the LE and an expected expansion of the region of flow above $M = 1$ nearer to the TE, causing increased flow acceleration and reduced turbulence in the impinging flow, as discussed in Chapter 5. Table 6.2 shows that the location of the peak HTC on the winglet tip has shifted from the part way along the PS rim (region *B1*) to the LE area of the PS rim (region *E1*) with a corresponding increase in HTC level. This high HTC area is close to the stagnation point at the LE and corresponds to the main leakage flow path over the PS rim at the LE.

Comparison of the PS cut-back tip data in Figures 6.2b and 6.3b again shows many of the same trends that follow from increased tip clearance as were observed for the baseline squealer and winglet tip. At the higher tip gap, the following trends can be observed: the LE impingement hotspot on the cavity floor is enhanced (by 20%) and moves closer to the PS rim as the impinging mass flow increases; the HTC on much of the PS rim shows a similarly large reduction of approximately 20%, most likely due to delayed reattachment; on the SS rim, the impingement region seems less well defined and shows a slight decrease in the HTC level (of approximately 7%).

The flow in the cut-back region of the PS cut-back tip (region *H2*) reattaches slightly later at the higher tip gap, closer to the SS rim. For this reason the HTC hotspot in that area has shrunk, although the HTC levels appear similar. The band of high HTC on the SS rim at the trailing edge, attributed to a leakage vortex originating from the cut-back region, has increased at the higher tip gap due to increased leakage flow. Similarly, the region of peak HTC on this tip has shifted to the LE area of the PS rim due to increased mass flow of the main leakage path at the larger tip gap. This LE area was seen to be the location of the peak HTC for all four tip geometries at the higher tip gap (see Table 6.2), with a significant increase in peak level for most cases at g/S = 1.15%, of up to 14% (for the baseline squealer tip).

A comparison of the suction side cut-back tip (Figures 6.2c and 6.3c) reveals that the above trends with increasing tip clearance are fairly ubiquitous for all the tip geometries studied. The expected reduction in HTC on the PS and SS rims (of around 24% and 11% respectively) can be observed at higher tip gap, suggesting later reattachment (on the PS rim) and reduced turbulence for the high Mach number impingement flow on the SS rim. The peak HTC on the PS rim at the LE has increased due to the increased leakage mass flow. The LE cavity impingement region of high HTC is also observed to increase (by approximately 8%) and move towards the PS rim at higher tip clearance. The level of HTC in the impingement region (*A3*) of this tip at the higher tip gap is the highest of all the geometries (see Table 6.2), as a result of the reduced cavity recirculation and smaller cavity depth present in this tip, which was discussed in Section 6.3.1 when considering the small tip gap.

Figure 6.4b shows the circumferentially averaged HTCs for the 1.15% g/S tip gap. A comparison of this plot with Figure 6.4a reveals that the features that differentiate between the tip geometries are largely maintained at the higher tip gap, apart from the relative performance of the SS cut-back tip which appears slightly improved compared to the other tip designs, despite the local peaks in HTC seen on this tip in several areas.

The differentiating features are maintained because the influence of an increased tip

gap has a similar effect on the OTL flow field and the resultant HTC distribution for each tip. All of the tips studied, which broadly consist of a cavity enclosed by two rims, can be divided into common sections, specifically the PS rim, SS rim and cavity floor, as discussed in the summary of Chapter 5. The PS and SS rims show a similar reduction in the HTC levels at increased tip clearance across all the tips studied, of approximately 20-30% and 7-11% respectively. The increase in HTC in the cavity (region A) at higher tip gap is more dependent on tip geometry, showing approximately 20% increase for the baseline squealer and PS cut-back tips, but only an increase of around 7% for the cavity-winglet and SS cut-back tips, due to the reasons discussed above. The data for the tip geometries considered in this chapter have highlighted the fact that an additional section must be included; for cases where the tips differ radically in geometry and the OTL flow field is significantly altered, e.g. in the cut-back regions, the flow field and HTC distribution both change markedly and the influence of increased tip clearance on such regions (cut-backs) must be considered separately. However, the present data indicate that the same overarching trends still govern the flow in these areas and so the relative thermal performance of the tips studied has remain fairly consistent at the higher tip gap.

6.4 Aerodynamic Loss

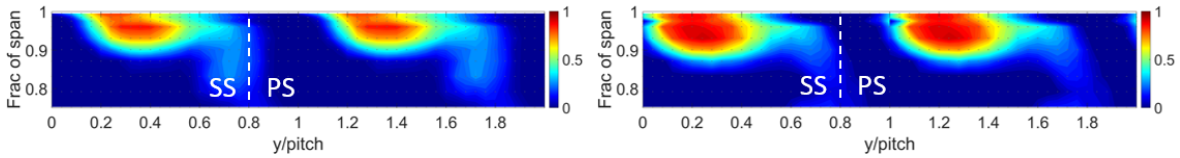
This section reports the experimentally measured aerodynamic losses for all four uncooled tip geometries, specifically the baseline squealer tip, cavity-winglet tip, PS cut-back tip and SS cut-back tip. The losses were evaluated at a plane 50% C_{ax} downstream of the blade row using the total pressure loss coefficient, Y_P, defined in Chapter 3. The single-hole probe was used to complete the top 4% of measurements only in the baseline squealer case. The discussion of the experimental results for loss will focus first on a comparison of all the uncooled tip geometries at 0.65% g/S tip gap. The discussion is then broadened to include the influence of tip clearance on the aerodynamic loss coefficient.

6.4.1 Comparison of Tip Geometries

The total pressure loss coefficient, Y_{P0}, for the baseline squealer tip at 0.65% g/S tip gap is shown in Figure 6.5a. Measurements were taken over one full blade pitch and the data is translated to create the plot seen (i.e. between $1 < y/Pitch <= 2$). The approximate positions of the blade suction and pressure sides, viewed upstream in a direction parallel to the exit flow direction, are marked on the figure, along with the measurement locations (denoted by grey dots). Several of the main loss generating flow features can be observed in Figure 6.5a. The overtip leakage vortex is the largest loss feature, which is responsible for a majority of the loss in this system, and can be observed between $0.1 < y/Pitch < 0.6$. Evidence of the upper passage vortex can also be seen adjacent to the OTL vortex, at a position corresponding to approximately $y/Pitch = 0.7$, although much of the latter loss feature is overwhelmed by the larger OTL vortex. The final loss feature, which contributes the least to the overall system losses, is the 2D blade wake, which can be observed at $y/Pitch \approx 0.8$.

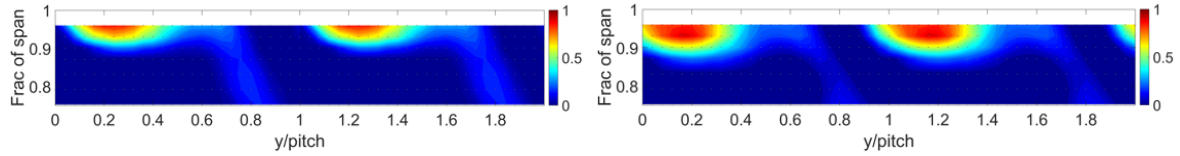
Figures 6.6a, 6.7a and 6.8a show the loss coefficients for the winglet, PS cut-back and SS cut-back tips respectively. It can be observed that there is good periodicity in the HSLC at the 50% C_{ax} downstream plane. Comparison of the relative positions of the OTL vortices shows that the different tip geometries shift the vortex either away from or towards the suction side of the blade. Compared to the baseline squealer in Figure 6.5a, the OTL vortex is pushed away from the SS by the winglet overhangs (Figure 6.6a). The small overhang on the PS cut-back geometry also has a similar effect on the OTL vortex, however the removal of a portion of suction side rim in the SS cut-back tip causes the OTL vortex to form closer to the blade SS. There is no notable difference in the relative position of the 2D blade wake observed, as this feature is less influenced by the tip geometry.

From the contour plots, it is difficult to discern any real difference between the relative strength of the loss vortices. However, the winglet tip appears to have the smallest OTL vortex, suggesting that the winglet has successfully reduced the losses



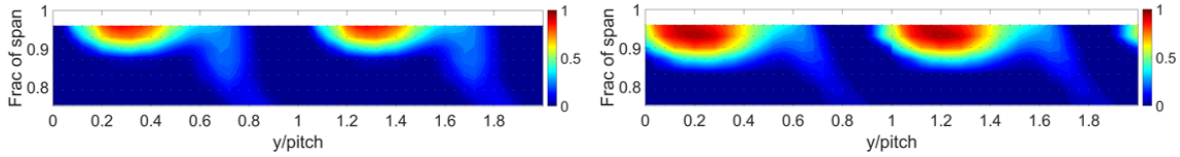
(a) 0.65% g/S **(b) 1.15% g/S**

Figure 6.5: Experimental total pressure loss coefficient, Y_{P0}, for the baseline squealer tip at 50% C_{ax} downstream



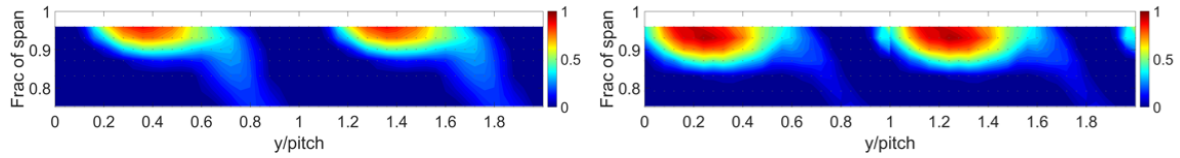
(a) 0.65% g/S **(b) 1.15% g/S**

Figure 6.6: Experimental total pressure loss coefficient, Y_{P0}, for the cavity-winglet tip at 50% C_{ax} downstream



(a) 0.65% g/S **(b) 1.15% g/S**

Figure 6.7: Experimental total pressure loss coefficient, Y_{P0}, for the PS cut-back tip at 50% C_{ax} downstream



(a) 0.65% g/S **(b) 1.15% g/S**

Figure 6.8: Experimental total pressure loss coefficient, Y_{P0}, for the SS cut-back tip at 50% C_{ax} downstream

over the tip, as intended. The winglet tip (Figure 6.6a) also shows very little evidence of an upper passage vortex over the measured plane; the only tip to do so. The baseline squealer tip shows the most developed upper passage vortex as flow out of the open trailing edge enhances this secondary loss feature.

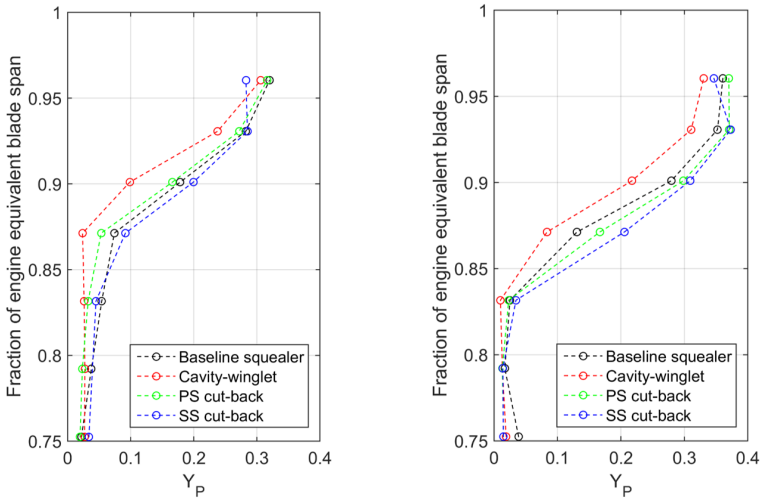
The mass averaged pressure loss coefficients for the small tip gap are shown in Figure 6.9a. This plot enables a comparison of the relative pressure loss coefficients to be drawn between the different tip geometries. The mass averaged losses have been presented without the top 4% of span, since this was only measured for the baseline squealer.

It can be observed that the cavity-winglet tip gives the lowest mass averaged overtip leakage losses of all the designs, supporting the above interpretation of the contour plots. The PS cut-back tip has the second lowest loss, due to the small rim extension on the SS at the LE. The SS cut-back tip shows the largest mass averaged losses, closely followed by the baseline squealer tip, presumably due to the more significant passage vortex seen in Figures 6.8a and 6.5a respectively. The SS cut-back tip, although showing a slightly larger OTL vortex over much of the span height compared to the other tips, actually has the lowest mass averaged loss at the plane measured closest to the casing. The contours of measured loss data indicate that the centre of the OTL vortex for the SS cut-back tip is forming further from the casing wall, and so the measurement area is capturing more of the OTL vortex compared to the other tips, hence the SS cut-back tip performs relatively poorly. From consideration of the likely leakage flow for the SS cut-back tip, it is probable that the flow exiting the cavity rolls into a vortex off the edge of the cavity floor, rather than the top of the squealer rim, hence positioning the OTL vortex further from the casing wall.

Further from the casing, between $0.80 - 0.85$ fractional span, the secondary flows dominate with the passage vortex and blade wake being the predominant loss mechanisms. There is much less difference between the tip geometries in this region, however the winglet tip and PS cut-back display the lowest loss due to the absence of a discernible passage vortex in this region. For fractional spans less than 0.80, in the 2D wake region, there is virtually no difference in mass averaged loss between the geometries, as the effects of the tip geometry are minimal at this location.

6.4.2 Influence of Tip Clearance

The pressure loss coefficients for the 1.15% g/S tip gap are shown in Figures 6.5b, 6.6b, 6.7b and 6.8b. By comparison with the smaller tip gap cases presented in Figures 6.5a - 6.8a, a number of notable differences can be observed, which are uniform for all cases. The effects of increasing tip gap are: an increase in the size and strength of the OTL



(a) g/S = 0.65% **(b) g/S = 1.15%**

Figure 6.9: Experimental mass averaged total pressure loss coefficients at both tip clearances

vortex, as a higher leakage mass flow passes through the tip gap; a reduction in the passage vortex, due to a combination of the OTL vortex interacting with the passage vortex and also a reduction in the boundary layer mass flow responsible for the passage vortex; a reduction in the 2D blade wake, again as a result of the redistribution of mass flow into the OTL vortex; a shifting of the OTL vortex away from the SS of the blade, however there is also a change in the relative pitch-wise positions of the OTL vortices of the different tip designs. From Figure 6.5b it is also observed that the centre of the OTL vortex has moved further from the casing wall, since the edge at which the OTL vortex forms has moved away from the casing.

Due to the absence of the top 4% of data and the reasons already discussed regarding shifting of the OTL vortices away of the casing wall, there is little to be gained quantitatively from comparison of the overall mass-averaged Y_{P0} values at the two tip gaps. However, it is clear from the contour plots that the increased peak loss coefficients and size of the OTL vortices will have produced higher losses at the larger tip gap.

A comparison of the relative performance of the different tip designs at the larger tip gap is displayed in Figure 6.9b, showing mass averaged losses. It is evident that the cavity-winglet tip gives the lowest losses, over the whole of the measured span height. The SS cut-back tip also remains the worst performer; however, there is again evidence

that the centre of the vortex is positioned furthest from the casing, rather than this being the largest OTL vortex of all the geometries. It is interesting to note that, at the larger tip gap, the relative performance of the baseline squealer and PS cut-back tips have switched in the OTL loss region compared to the smaller tip gap results. This behaviour can be attributed to a relatively larger OTL vortex with higher Y_{P0} in the PS cut-back case, which can be seen in Figure 6.7b. This larger OTL vortex can be ascribed to the lessened effectiveness of the small winglet overhang in reducing leakage mass flow over the PS cut-back tip at larger tip clearance. In the secondary flow region, closer to mid-span, the baseline squealer again shows higher losses, due to a wider 2D wake, as shown in Figure 6.5b.

6.5 Summary

This chapter has presented both experimentally measured heat transfer coefficients on the tip surface and aerodynamic losses at a plane 50% downstream of the blade row for four uncooled tip geometries. These geometries were the baseline squealer tip (introduced in Chapter 5), a cavity-winglet tip, a PS cut-back squealer tip and a SS cut-back squealer tip (see Figure 6.1). Measurements were taken at two tip gaps (0.65% and 1.15% g/S) and the relative performance of the tips was compared at the small tip gap, before an investigation into the effects of tip clearance on each of the tips.

The main conclusions drawn for tip heat transfer were:

1. Since all the tip geometries broadly comprise a cavity enclosed by two rims, the OTL flow field on the new tips was very similar to that observed for the baseline squealer tip in each of the three distinct areas; namely the PS rim, SS rim and the cavity floor. Each tip exhibits: a separation over the PS rim; an impingement onto the cavity floor; either a separation and reattachment (near to the LE) or a flow impingement (towards the TE) onto the SS rim. The HTC distribution produced by this generalised flow field depends on the specific details of each tip

geometry, which govern for example, whether the flow reattaches on the PS rim.

2. The data for the tip geometries introduced and investigated in this chapter highlighted the significance a fourth region, namely the cut-back region, which has a large influence on the local flow field and therefore needed to be investigated separately. Comparison of the circumferentially averaged HTCs revealed how the differing trailing edge tip geometries impacted the relative thermal performance of the tips in the local area. The experiments showed that the SS cut-back produced the lowest HTCs over the trailing edge and the PS cut-back tip the highest.

3. It is important to evaluate regions of peak HTC, not just averaged values, which can hide peaks in heat transfer where the blade tip could overheat or require extra cooling. At the small tip gap, peak HTC values were located in different regions of the tips. At high tip gap, the peaks all shifted to the LE of the PS rim and were generally higher than the smaller tip gap data due to increased leakage mass flow.

4. Due to the similarity in flow field between all the tips, the conclusions drawn about the response to a change in tip gap for the baseline squealer (conclusion 2, Chapter 5) can be generalised and applied to these new tips in order to predict the HTC distribution at the higher tip gap. Even though the introduction of cut-back regions alters the local flow field, the HTC distribution is still governed by general flow features and so, once the OTL flow field has been understood, it is possible to identify the influence of increased tip clearance on the HTC distribution in the cut-back and other regions. For this reason, the relative performance of the tip geometries did not change at the higher tip gap.

The following conclusions were drawn for aerodynamic loss:

1. The main loss generating flow features which can be clearly identified for all the tip geometries were the OTL vortex, which contributes most of the loss in the

system and the 2D blade wake, the contribution of which was lower than that of the OTL vortex. All cases except the winglet tip also show evidence of the upper passage vortex.

2. The relative size and position of the main OTL vortex was seen to be governed by the tip geometry. At the small tip gap, the winglet tip showed the smallest OTL vortex (and mass-averaged losses), with the loss core forming furthest from the blade SS. The SS cut-back tip and baseline squealer produced the highest mass-averaged loss due to the prominence of the passage vortex.

3. Since the top 4% of data was missing, a definitive comparison of the overall loss coefficients for each tip could not be performed as the data indicate that the geometry differences, especially the lack of a SS rim in the SS cut-back tip, caused the main loss core to move further away from the casing. This shift meant that a larger proportion of the OTL core was being measured for the SS cut-back compared to the other tips, contributing to the SS cut-back tip showing the highest losses over the measured span.

4. There was little difference in the relative performance of the tips in the 2D wake region.

5. An increase in tip gap increases the size and strength of the OTL vortex but reduces the passage vortex and the 2D wake. The centre of the loss core also moves away from the blade SS and casing wall. This behaviour is common to all the tip geometries.

6. The relative performance of the winglet and SS cut-back tips was maintained at higher tip gap, however the baseline squealer and PS cut-back tips switched. The PS cut-back tip was seen to be more vulnerable to tip leakage at the higher tip gap, with a larger increase in OTL vortex.

Chapter 7

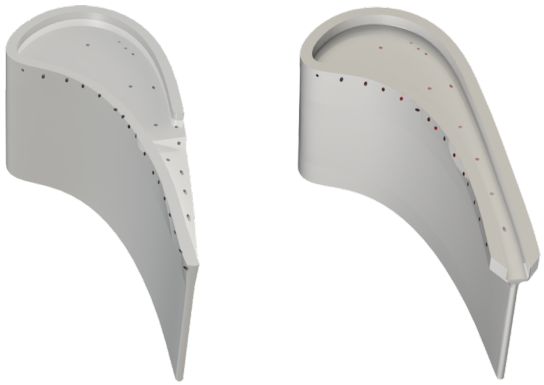
Experimental Comparison of Cooled Tips

7.1 Introduction

This chapter introduces a cooled version of the suction side cut-back squealer tip discussed in Chapter 6 and highlights the differences in cooling arrangement between this tip and the cooled baseline squealer tip introduced in Chapter 5. A detailed comparison of the heat transfer coefficient measurements for the uncooled and cooled suction side cut-back tip is discussed in the first part of this chapter to assess the impact of the addition of cooling. The performance of the cooled SS cut-back tip is then compared to the cooled baseline squealer tip, with the aim of determining which tip engenders the best cooling, i.e. the lowest heat transfer coefficient and highest film cooling effectiveness. The differing effects of changing tip clearance and coolant mass flow are then studied for the two cooled tip designs.

7.2 The Cooled Suction Side Cut-Back Tip

The design of the suction side cut-back cooled tip is shown in Figure 7.1a. The dust hole arrangement in the leading edge region of the cavity is identical to that of the cooled



(a) Suction Side Cut-Back cooled tip geometry

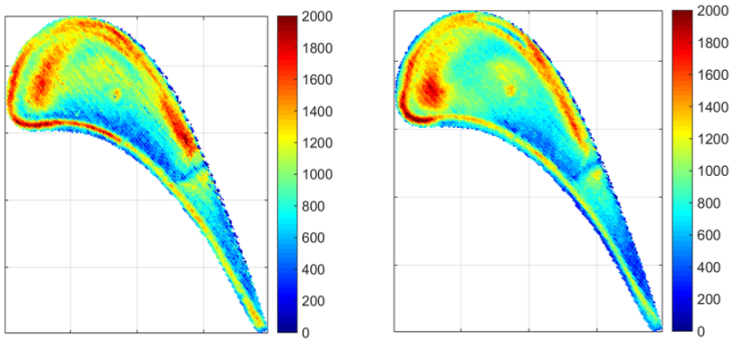
(b) Baseline Squealer cooled tip geometry

Figure 7.1: CAD renderings of the cooled squealer tip geometries

baseline squealer (Figure 7.1b). The cooling arrangements differ between the two designs on the near-rim region of the blade PS and in the cut-back region of the cavity. The dust holes in the cut-back are positioned to provide a film over the trailing edge region of the blade tip. The PS film holes are located in positions and at orientations that are viable under existing manufacturing constraints. Towards the TE, the PS holes are angled more acutely to the blade PS than those found in the baseline squealer tip. Unlike the case of the baseline geometry cooled tip, there are no film holes on the suction surface of the blade tip.

7.3 Comparison of the Uncooled and Cooled Tip

In this section, the addition of cooling to the suction side cut-back tip will be assessed by comparison of the heat transfer coefficients measured on the uncooled and cooled tips at both tip gaps and at the nominal coolant mass flow. For ease of comparison, the HTC for the uncooled tip is shown again in Figure 7.2 at both tip gaps and compared to the cooled tips in Figures 7.3a and 7.8a. As for the baseline squealer tip case, some machining was necessary to the cooled SS cut-back tip during the manufacture process, which created some geometrical disparity between the suction side uncooled and cooled tips. Specifically, the cavity depth of the cooled tip was reduced, and the milling process



(a) 0.65 % g/S **(b) 1.15 % g/S**

Figure 7.2: Experimental uncooled heat transfer coefficients [W/m^2K] for the unmodified suction side cut-back tip

developed a sharp edge to the squealer rims. These changes were reflected in a higher HTC on the cavity floor of the cooled tip and the prominence of the C-shaped LE impingement zone (labelled *A1*) in Figures 7.3a and 7.8a. The PS rim (marked *B1*) also exhibits earlier reattachment for the cooled tip, leading to a large increase in HTC, due to the sharpness of the PS rim.

A comparison of the uncooled and cooled tip HTC data, at 0.65% g/S tip gap with nominal coolant mass flow rate, in Figures 7.2a and 7.3a shows that injection of coolant increases the HTC on the cavity floor in the mid-chord of the tip and at the end of the SS rim (marked *C1*). This increase can be attributed to similar coolant-OTL flow interactions as those described in Chapter 5 and observed by Ma *et al.* (2017). It is further shown in Chapter 9 how the injected coolant can create vortical structure which are capable of blocking the passage of the local OTL flow and directing it to impinge on the cavity floor, raising the HTC as is occurring here. Over the remainder of the SS rim (*D1* in Figure 7.3a), the band of high HTC is set further back from the forward edge of the rim, indicating the high HTC is caused by a flow separation and reattachment, rather than an impingement onto the rim edge. This behaviour was also observed for the uncooled tip in Chapter 6, but it occurs over a larger proportion of the cooled rim. This change in behaviour can be ascribed to the coolant-OTL interactions from the mid-cavity dust holes which prevent direct impingement onto the SS rim, instead causing impingement onto the cavity floor, followed by separation and reattachment over the

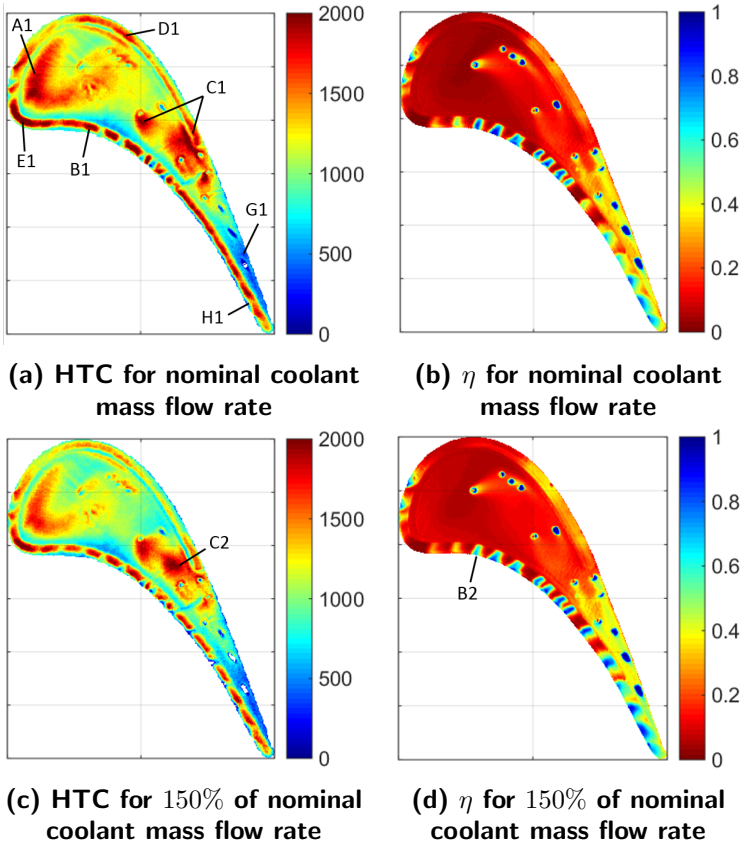
SS rim. Towards the rear of the cooled tip however (at *G1*), the HTC on the angled portion of the cavity is very similar to that seen in the uncooled case, as there is still no reattachment of flow in this region.

The trends in HTC levels with increasing tip gap for the uncooled (Figure 7.2) and cooled tips (Figures 7.3a and 7.8a) show some differences. The observed increase in HTC of the LE impingement region and movement towards the PS rim at higher tip gap is as expected from previous discussion on the baseline squealer. The trend on the PS rim is more complex but essentially the differences are most likely due to the geometry disparity already described. The specific trend with tip clearance for the cooled case will be discussed in Section 7.4.2, during comparison with the baseline squealer. On the SS rim, the cooled tip shows reduced HTC at the higher tip gap, as was the case for the uncooled SS cut-back geometry, except right at the end of the SS rim, which shows an increase in impingement HTC intensity at the higher tip gap (see Figures 7.3a and 7.8a). This enhanced HTC can be attributed to increased interaction between the local injected coolant and the higher mass flow rate of the impingement flow onto the SS rim and leakage flow out of the cut-back.

7.4 Comparison of the Cooled Tip Geometries

In this section, a comparison is drawn between the cooled baseline squealer and suction side cut-back squealer at 0.65 % g/S tip gap with nominal coolant mass flow rate. Figures 5.8a and 7.3a show the tip HTC for the baseline and SS cut-back tips respectively, and the film cooling effectiveness can be found in Figures 5.8b and 7.3b. As mentioned in Chapter 6, the baseline squealer was intended to have a deeper cavity depth (see Table 6.1). The machining of both cooled tips reduced the cavity depths by similar amounts, so the ratio of the cavity depths of the cooled tips to one another are approximately the same as for the uncooled versions of the tips. This enables a worthwhile discussion of the relative performance of the tips to be made.

It can be observed from comparison of Figures 5.8a and 7.3a that the HTC levels



(a) HTC for nominal coolant mass flow rate

(b) η for nominal coolant mass flow rate

(c) HTC for 150% of nominal coolant mass flow rate

(d) η for 150% of nominal coolant mass flow rate

Figure 7.3: Cooled HTC [W/m^2K] (left) and η (right) contours at 0.65% tip gap and two coolant mass flow rates for the suction side cut-back tip

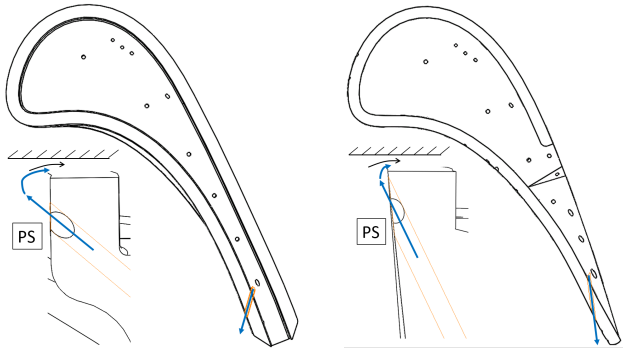
in the impingement region of high HTC on the cavity floor (*A1*) are higher for the SS cut-back tip. Several factors are thought to have contributed to this, most obviously the reduction in cavity depth of the SS cut-back tip compared to the baseline squealer. The same increase in HTC, of approximately 30%, was observed for the uncooled versions of the tips at low tip gap, as discussed in Chapter 6. The earlier discussion also suggested that the formation of a weaker cavity recirculation in the case of the SS cut-back tip offered an explanation for a reduction in blockage of the impingement and associated high level of HTC.

Both cooled geometries show comparably high HTC values along the length of the PS rim, of around 1700-2300 W/m^2K; there is a large range of HTC levels on this rim due to local effects of the coolant injected from the PS film holes. Interestingly, the SS cut-back tip (Figure 7.3a) shows the distinctive striping of high and low HTC around the mid-chord, at low tip gap, due to blockage of the reattaching flow by the

coolant films, whereas the baseline squealer tip does not. From inspection of the film cooling effectiveness (in Figures 5.8b and 7.3b) it can be seen that the SS cut-back tip shows much higher local film effectiveness on the PS rim in this region (effectiveness levels are approximately 0.75-0.85 compared to 0.35-0.45 for the baseline squealer). By examination of the cooling arrangements for both tips in Figure 7.1, it is noted that there are some significant differences in the locations of the PS film holes between the two geometries. The data indicate that positioning the film holes closer to the edge of the rim, or in some cases, breaking through to the top of the rim surface (as is the case for the SS cut-back tip) is advantageous for increased coverage of films installed to cool the rims. However, it is noted that a real turbine blade would have a coating on top of the rim surface, and it is unlikely that cooling holes would be drilled through this. Nonetheless, it remains the case that there is clearly some benefit to be had from careful placement of film cooling holes on the PS of the blade, close to the edge of the rim.

On the cavity floor towards the mid-chord region (*C1*), in Figure 7.3a, the interaction of coolant with the complex flow field around the start of the cut-back region produces peak HTC levels (of approximately 1800-2150 W/m^2K) downstream of the cooling holes which exceed the levels seen in the same region on the baseline squealer in Figure 5.8a (around 1700-1900 W/m^2K).

As with the uncooled cases, a significant difference in tip HTC was measured towards the TE of Figures 5.8a and 7.3a, where the geometries are decidedly different. The cut-back region of the SS cut-back tip shows higher film effectiveness (see Figure 7.3b) than over the rest of the cavity and the baseline squealer tip. The absence of film holes on the SS blade surface has effectively redirected coolant mass flow to the dust holes, resulting in a higher coolant flow ejected from the dust holes and increased film effectiveness for the SS cut-back tip. However, it is proposed that, for the stationary casing conditions studied by the author, this coolant may be wasted as this area of cavity floor displays very low heat transfer even in the uncooled case. Once a moving casing is added (or the real engine case considered), the OTL flow field would be expected to change (see



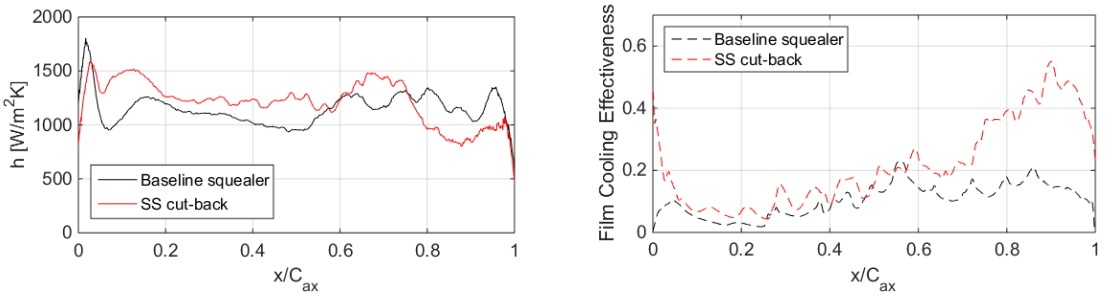
(a) Baseline squealer tip **(b) Suction Side Cut-Back tip**

Figure 7.4: Top view and section view perpendicular to blade pressure surface showing difference in cooling hole angles near tip trailing and suspected coolant flow

Chapter 9); the interaction of the OTL flow with the moving casing could direct the coolant at the rear side of the PS rim to help improve film effectiveness.

At the very trailing edge of the PS rim, there are again very high film effectiveness levels seen in Figure 7.3b. The levels (of up to 0.8) are much higher than those seen on the baseline squealer, where the local film effectiveness is practically zero. The geometrical differences between the two tips, specifically the lack of an overhang PS rim in the SS cut-back tip, allowed for the film holes to be drilled at much shallower angles, i.e. more acute to the blade PS and inclined towards the TE, and also closer to the edge of the rim, as shown in Figure 7.4. The effect of this shallower angle and hole placement allows the coolant to be injected almost directly into the tip gap, rather than out into the passage before being swept into the tip gap; the suggested coolant behaviour is illustrated in Figure 7.4. For this reason the films remained attached to the rim surface much better for the SS cut-back tip, which resulted in delayed reattachment of OTL flow onto the PS rim at the TE (see region *H1* in Figure 7.3a). However, the benefit is not as marked as towards the mid-chord of the tip where total blockage of the reattachment onto the PS rim was observed.

The overall comparison of performance between the two cooled tips was assessed by circumferentially averaging the HTC and film effectiveness along the tip axial chord, with the results shown in Figures 7.5a and 7.5b respectively. From Figure 7.5b it is clear



(a) Heat transfer coefficient [W/m^2K] **(b) Adiabatic film cooling effectiveness**

Figure 7.5: Circumferentially averaged HTC and η of the two cooled blade tips at g/s = 0.65% with nominal coolant mas flow rate

that the SS cut-back tip is a superior cooling design, with much better film effectiveness, especially towards the TE. However, the HTC levels are much closer for the two designs (Figure 7.5a). At a local level, e.g. on the PS rim, the presence of a coolant film can influence the OTL flow field and impact the local HTC, however the trend between the tips is almost identical for the cooled case compared to the uncooled case (see Figure 6.4a), suggesting that the overall HTC distribution is more closely correlated to the tip geometry which in turn determines the overall flow field on the particular tip. As for the uncooled tip, when the tips are cooled, the HTC remains higher for the SS cut-back tip towards the LE and mid-chord, but this geometry exhibits lower HTC towards the TE, mainly due to the angled portion of the cavity floor.

The approximate HTC levels quoted earlier for specific tip regions were used as a secondary measure of relative tip performance. At the smaller tip gap and nominal coolant mass flow rate there is very little difference in the highest HTC levels on the cooled tips, with both tips exhibiting peak HTCs of approximately 2300-2400 W/m^2K, although the location of the peak HTC differs for the two tips. In the case of the baseline squealer the highest HTCs are found at the LE of the PS rim (A), however the peak HTCs shift to the mid-chord region of the PS rim for the SS cut-back tip. This shift suggests a change in location of the most vulnerable part of the tip. However, when considering an engine-realistic case, the part of the tip most at risk of limiting life is likely to extend towards the TE, due to the change in temperature profile of the flow field at the inlet of the blade row; this is when the higher film effectiveness seen in the

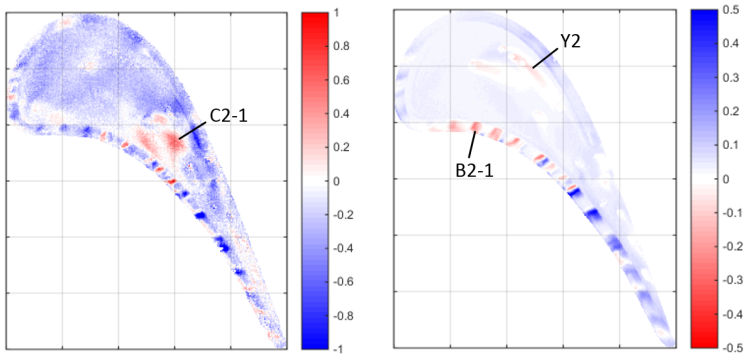
SS cut-back tip will be beneficial.

Due to the geometrical difference on the PS rim between the SS cut-back uncooled and cooled tips, it was not possible to evaluate the net heat flux reduction at engine-realistic temperatures for the SS cut-back tip. However, given the strong correlation between high film effectiveness and a reduction in heat flux seen on the baseline squealer tip in Chapter 5, it is expected that the SS cut-back tip would show a larger reduction in tip heat flux over the TE portion of the tip, compared to the baseline squealer, due to the increased levels of film effectiveness shown.

7.4.1 Influence of Coolant Mass Flow Rate

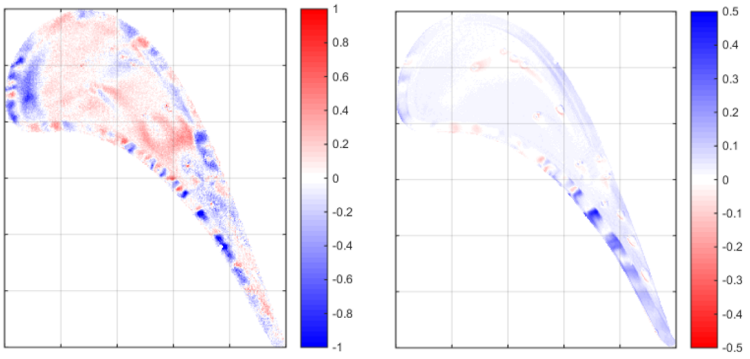
Many of the effects that follow an increase of coolant mass flow rate for the baseline squealer tip were also found to occur on the SS cut-back tip. As for the comparison of Figures 5.8a and 5.8c, the SS cut-back tip in Figures 7.3a and 7.3c shows the following trends when the coolant mass flow is increased: reduced HTC intensity (by approximately 10%) in the LE impingement region due to extra coolant mixing with the cavity recirculation and blocking impingement; the development of a more distinctive striping pattern of high and low HTC over much of the PS rim as the film blocks the reattachment of flow; a reduction in HTC on the SS rim, of around 15%, due to blockage of impinging vortical flow structures by an improved film. It should be noted, however, that the SS cut-back tip exhibits the feature of high local film effectiveness, low HTC along the whole length of the PS rim (including the transonic TE region) as the improved cooling design of this tip maintains patches of high effectiveness in the TE region, unlike for the case of the baseline squealer tip.

Differences occur in the trend with coolant mass flow between the tips in the mid-chord region of the cavity floor (at *C1/C2* in Figures 7.3a and 7.3c). The baseline squealer case showed reduced HTC at the higher coolant mass flow and, although the SS cut-back tip does show this trend adjacent to the SS rim, further from the rim the peak HTC increases as the interaction of coolant and the cavity flow intensifies. This



(a) Change in HTC at 0.65% tip gap

(b) Change in η at 0.65% tip gap



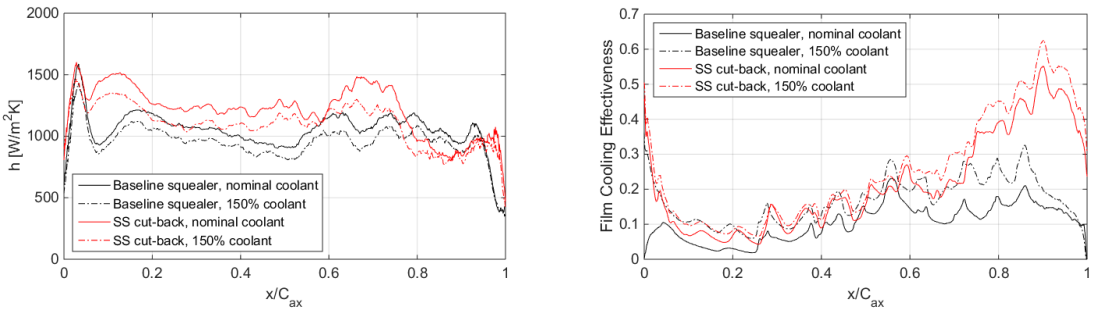
(c) Change in HTC at 1.15% tip gap

(d) Change in η at 1.15% tip gap

Figure 7.6: Change in cooled HTC [W/m^2K] (left) and η (right) with increased coolant mass flow rate at both tip clearance heights (HTC is normalised by maximum change in HTC)

increased HTC is highlighted at *C2-1* in Figure 7.6a, which shows the change in HTC with increased coolant mass flow, and indicates that, when the coolant mass flow is increased, the point of impingement of the OTL flow is altered by the coolant and shifts away from the SS rim edge to the middle of the cavity. It can be seen that the high HTC band on the SS rim adjacent to *C2* in Figure 7.3c is set back from the front edge of the rim, suggesting a separation and reattachment of flow on this portion of the rim as opposed to the direct impingement indicated at *C1* in Figure 7.3a. This change in behaviour means that, for the case of the SS cut-back tip at higher coolant mass flow, there is no longer direct impingement onto any portion of the SS rim.

The expected increase in film effectiveness at higher coolant mass flow (between Figures 7.3b and 7.3d) is observed in Figure 7.6b, showing the change in η, over a majority of the tip. Exceptions to this trend are seen on the PS rim between the LE



(a) Heat transfer coefficient [W/m^2K] **(b) Adiabatic film cooling effectiveness**

Figure 7.7: Circumferentially averaged HTC and FCE comparing relative performance of the two cooled blade tips at two coolant mass flow rates and 0.65% g/S tip gap

and mid-chord (*B2-1*). The films in this location show a slight decrease in effectiveness (from a range of 0.5-0.85 to 0.35-0.75 depending on the individual film), as the higher mass flow coolant penetrates further into the freestream instead of sticking to the rim surface. This is similar to the effect caused by the angle of the film holes discussed in the previous section. The other exception appears around the LE dust holes (marked *Y2*) on the cavity floor due to increased lift off of the films.

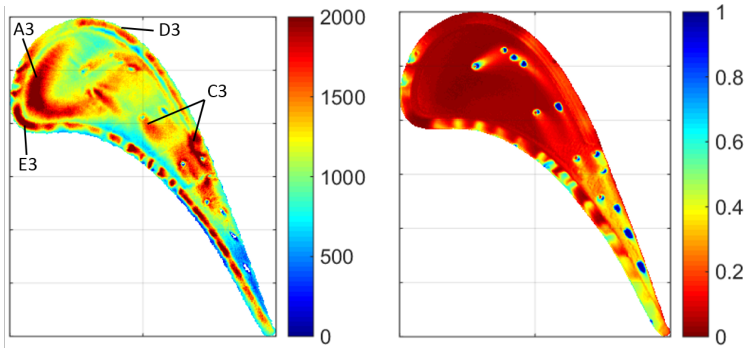
Figures 7.7a and 7.7b show a comparison of the circumferentially averaged HTC and film effectiveness for the baseline squealer and SS cut-back tips for the low tip gap and both coolant mass flow rates. Although these plots reveal that, in general, the HTC decreases at increased coolant mass flow and the film effectiveness is enhanced, the local trends are complex, as discussed, and depend on the individual tip geometry and local OTL flow field. The overall trends with coolant mass flow rate are the same for both tips, and although the baseline squealer tip shows a larger increase in film effectiveness at higher coolant mass flow, the SS cut-back tip still shows a higher effectiveness at both coolant mass flow rates when compared to the baseline squealer. With regards to HTC, the baseline squealer exhibits lower HTC on average at both coolant mass flow rates (apart from the TE region), mainly due to the deeper cavity depth. The SS cut-back tip shows a greater decrease in HTC at higher coolant mass flow, as the improved film coverage on the PS rim is more effective at blocking the reattachment of the OTL flow. It should be noted that the trends described with respect to coolant mass flow for the

low tip clearance are reasonably consistent at the higher tip gap over much of the tip (see Figure 7.6c), apart from towards the end of the SS rim on the SS cut-back tip (region *C4* in Figure 7.8c) where the flow impingement remains at the larger tip clearance (and high coolant mass flow) and in the LE cavity region where a slight increase in HTC is observed at higher tip gap in region of low η, attributed to increased interaction of coolant and a higher OTL mass flow.

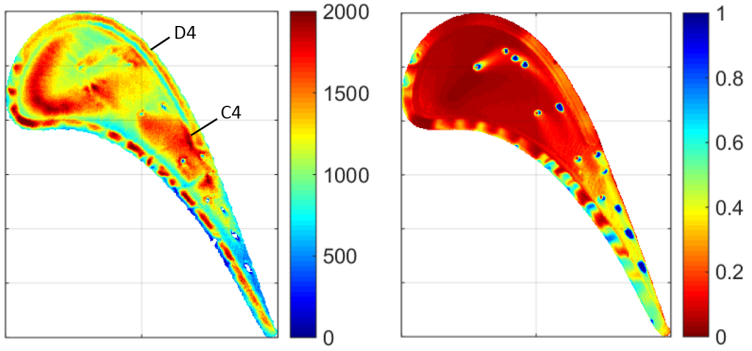
7.4.2 Influence of Tip Clearance

The HTC and film effectiveness for the SS cut-back tip at 1.15% g/S tip gap are shown in Figure 7.8. The change in HTC with increased tip clearance (between Figures 7.3a and 7.8a) at the nominal coolant mass flow is observed in Figure 7.9a and shows some similarity to the baseline squealer on the PS rim and LE cavity impingement region. However, there are differences observed on the SS rim, mid-chord of the cavity and at higher coolant mass flows as will be discussed. At increased tip clearance (and nominal coolant mass flow) both tips show: enhanced HTC at the LE cavity impingement region (*A3/A3-1*), of around 15-25%, due to increased impingement mass flow; a slight increase in HTC on the PS rim at the LE (*E3/E3-1*), of approximately 2-3%, again due to increased leakage mass flow; decreased HTC over a majority of the PS rim, as the reattachment of flow is delayed.

The effect of increased tip gap differs between the baseline squealer and SS cut-back tips on the PS rim at around 0.75 x/C_{ax}. In this region it is observed, from Figures 7.3a and 7.8a, that there is only a small difference in the point of reattachment of the flow, and that at the higher tip gap, the peak level of HTC at reattachment has increased for the SS cut-back tip (from around 2000 to 2300 W/m^2K) as shown at *B3-1* in Figure 7.9a. The regions of increased HTC also coincide with the regions of the PS rim which display the lowest film effectiveness (see Figure 7.8b) and therefore exhibit the least impact on the reattachment of leakage flow. In these areas the coolant is mixing with the OTL flow causing an increase in the turbulence intensity, which together with the higher leakage



(a) HTC for nominal coolant mass flow rate **(b) η for nominal coolant mass flow rate**

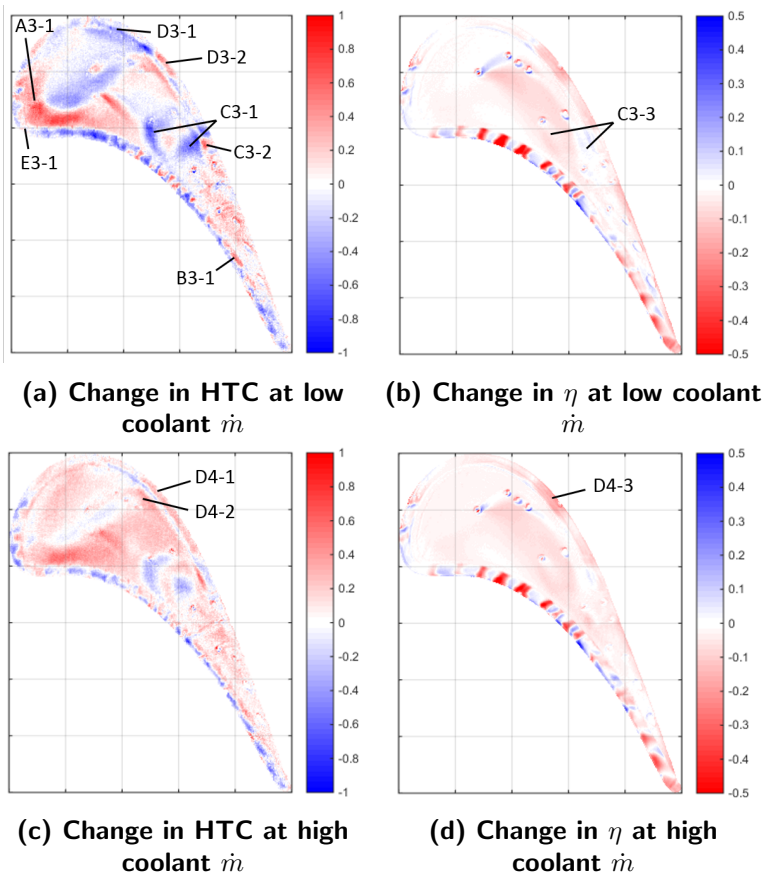


(c) HTC for 150% of nominal coolant mass flow rate **(d) η for 150% of nominal coolant mass flow rate**

Figure 7.8: Cooled HTC [W/m^2K] (left) and η (right) contours at 1.15% tip gap and two coolant mass flow rates for the suction side cut-back tip

mass flow at the higher tip gap, causes increased HTC at reattachment. This behaviour is not seen in the baseline squealer case as the HTC on the rim is dominated by a delay in reattachment at higher tip gap, which reduces the HTC. This delay in reattachment is observed on the PS rim towards the leading and trailing edge for the SS cut-back tip, but less so in the 0.75 x/C_{ax} region.

Both tips show a similar trend on the cavity floor at mid-chord (at *C3*); away from the SS rim (at *C3-1* in Figure 7.9a) there is an observable decrease in peak HTC level at the higher tip gap, contrary to the HTC increase seen just upstream on the LE cavity floor. Whereas for the baseline squealer the data indicated that this decrease (of around 30%) occurred simply due to an enhanced film on the cavity floor (Figures 5.8b and 5.9b), there is less evidence for this when considering the SS cut-back tip (see C3-3 in Figure 7.9b which shows the change in η). For the SS cut-back tip, it can be seen from Figures 7.3b and 7.8b that at the higher tip clearance, the upstream cavity films are



(a) Change in HTC at low coolant $\dot{m}$

(b) Change in η at low coolant $\dot{m}$

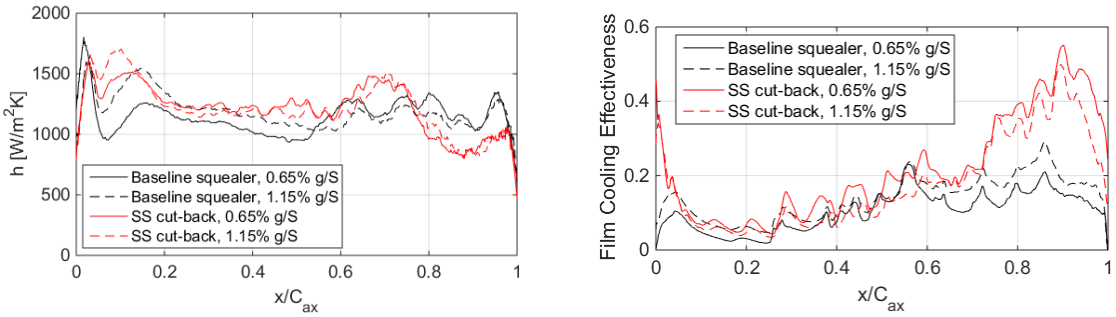
(c) Change in HTC at high coolant $\dot{m}$

(d) Change in η at high coolant $\dot{m}$

Figure 7.9: Change in cooled HTC [W/m^2K] (left) and η (right) with increased tip clearance at both coolant mass flow rates (HTC is normalised by maximum change in HTC)

narrower, indicating less mixing with the cavity vortex and therefore lower HTC (by approximately 10%).

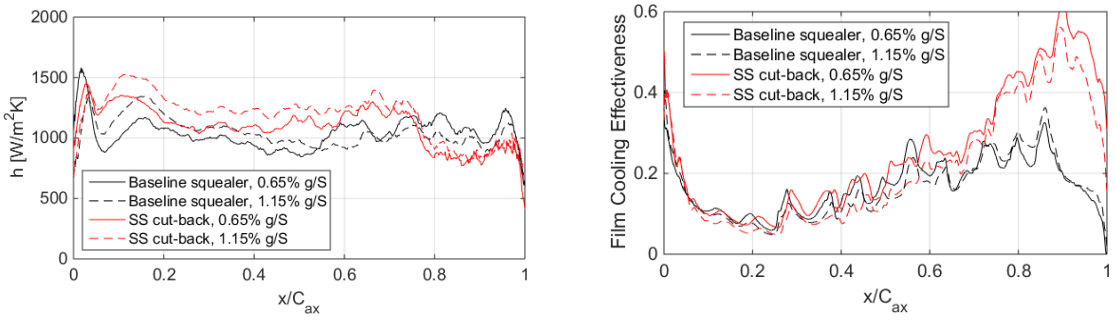
At nominal coolant mass flow, the SS rim of the SS cut-back tip (in Figures 7.3a and 7.8a) can be split into two parts, as discussed previously. Towards the LE (at *D3*), the delayed reattachment of the leakage flow reduces the HTC over the rim at higher tip gap, which is highlighted at *D3-1* in Figure 7.9a. Towards the end of the SS rim however, the HTC is seen to increase at the point of impingement and on the adjacent cavity floor (marked *C3-2* in Figure 7.9a), ascribed to the increased leakage mass flow at the high tip clearance. These two trends are opposite to those observed for the baseline squealer tip, which showed increased HTC towards the LE at higher tip gap due to increased interaction of the coolant and cavity flow, but decreased HTC nearer to the TE due to the effects of an increase in Mach number on the impingement flow.



(a) Heat transfer coefficient [W/m^2K] **(b) Adiabatic film cooling effectiveness**

Figure 7.10: Circumferentially averaged HTC and η for the two cooled blade tips at both tip gaps and the nominal coolant mass flow rate

The trends with increased tip gap on the SS cut-back tip at the higher coolant mass flow are largely similar to those discussed above for the nominal mass flow, other than on the SS rim. Over a majority of the SS rim, where the high HTC is caused by reattachment (*D4*), an increase in HTC is observed at the higher tip gap (see *D4-1* in Figure 7.9c), similar to that measured for both coolant mass flow rates for the baseline squealer tip in the near LE region of the SS rim. This increase in HTC for the SS cut-back tip is caused by two factors. Firstly, from comparison of Figures 7.3d and 7.8d it is clear that the upstream dust holes provide worse coverage of the SS rim in this region at higher tip gap (indicated at *D4-3* in Figure 7.9d), with film effectiveness levels approximately 0.2 as opposed to 0.35; the enhanced cavity recirculation mass flow (at higher tip gap) results in decreased local blowing ratio over these dust holes and reduced lift-off of the coolant film and its passage over the SS rim. The reduced film on the SS rim at higher tip gap causes lessened blockage of the reattachment and therefore increased HTC. Secondly, it is observed in Figures 7.3c and 7.8c that there is increased interaction between coolant and cavity flow at higher tip gap, when the films are better attached to the cavity surface (increased HTC around LE region dust holes observed at *D4-2* in Figure 7.9c). This increased interaction enhances the turbulence in the cavity flow, which leaks over the SS rim producing enhanced HTC at reattachment at higher tip gap. This trend of increasing HTC at higher tip gap is also noted for the low coolant mass flow case at *D3-2* in Figure 7.9a.



(a) Heat transfer coefficient [W/m^2K] **(b) Adiabatic film cooling effectiveness**

Figure 7.11: Circumferentially averaged HTC and η for the two cooled blade tips at both tip gaps and 150% nominal coolant mass flow rate

As has already been alluded to, the SS cut-back tip at the lower tip clearance and higher coolant mass flow is the only case in which the flow behaviour on the end of the SS rim changes from an impingement to a reattachment. This change occurs due to the unique combination of high mass flow of coolant and low cavity recirculation mass flow which enhances the local blowing ratio of the films around the end of the SS rim to a point where the coolant can influence the leakage flow in this region. No such influence is observed at the higher tip gap with high coolant mass flow.

With regards to the trend in film effectiveness with tip gap, the PS rim of the SS cut-back tip shows the same reduction in peak effectiveness and more even dispersion of coolant as noted for the baseline squealer at higher tip gap, which is indicated by bands of increasing and decreasing η in Figures 7.9b and 7.9d. In the cutback region, Figures 7.9b and 7.9d show that the film effectiveness decreases slightly with increasing tip gap, as the higher cavity mass flow exiting from the cut-back disperses the coolant film.

Figures 7.10 and 7.11 show the trends in circumferentially averaged HTC and film effectiveness with tip gap for both tips and at both coolant mass flow rates. These figures highlight important differences between the two tips due to their respective geometries and the impact of tip clearance. Figures 7.10b and 7.11b show that with increasing tip gap, the SS cut-back tip shows a decrease in η at both coolant mass flow rates. This decrease occurs on all sections of the SS cut-back tip due to dispersion of the coolant by the increased leakage mass flow, whereas the baseline tip shows an increase in η at

higher tip gap for the nominal coolant mass flow rate (see Figure 7.10b). This increase is a result of increased cavity recirculation and reduced localised coolant blowing ratio leading to better attached films in the cavity. At the higher coolant mass flow rate, in Figure 7.11b, the η towards the LE of the baseline squealer decreases at higher tip gap, similar to the SS cut-back tip, but an increase is still seen towards the TE as the increase in film effectiveness of the TE dust holes dominates.

There is little change in the average HTC with tip gap on the SS cut-back tip at nominal coolant mass flow (see Figure 7.10a). This is because the increase in HTC in the cavity is offset by a reduction in HTC on the rims. At higher coolant $\dot{m}$ (see Figure 7.11a), there is a clear increase in averaged HTC on the SS cut-back tip as the increase in HTC in the cavity and on the SS rim dominates. The PS rim appears less sensitive to a change in tip gap on this tip, hence the much smaller increase in HTC towards the TE. The baseline squealer shows the same trend at both coolant mass flow rates: an increase in HTC with tip gap towards the LE, as the behaviour is dominated by an increase in the cavity HTC; towards the TE the HTC reduces at higher tip gap as the cavity HTC does not change much and the HTC on the rims reduces dramatically. The baseline squealer shows a much larger variation of rim HTC with changing tip clearance.

7.5 Summary

This chapter has presented a second cooled tip based on the SS cut-back tip. Heat transfer coefficients and adiabatic film cooling effectiveness measurements were taken on this cooled tip at 0.65 % g/S and 1.15 % g/S tip gaps and the nominal and 150 % of nominal coolant mass flow rates. The SS cut-back tip was compared to the uncooled tip (presented in the previous chapter) and similarities drawn between the trends with tip gap with and without coolant. A detailed comparison of the cooled baseline squealer and cooled SS cut-back tip was then undertaken by the author and the effects of tip clearance and coolant mass flow were examined to determine the relative performance of the two cooled tip designs.

The main conclusions drawn were as follows:

1. The geometrical differences between the uncooled and cooled SS cut-back tip had a large impact on the HTC distribution observed with effects similar to those noted for the baseline squealer and this fact somewhat masked the impact of cooling addition. Trends caused by a tip gap increase for the uncooled and cooled tip showed some similarity in regions of the tip where the geometry was not significantly altered.

2. The SS cut-back tip showed higher HTC on the cavity floor in all cases compared to the baseline squealer, due to a shallower cavity depth and lack of recirculating vortex in the SS cut-back tip.

3. Careful placement and angling of PS film cooling holes appears to be very important. When holes are able to be positioned closer to the edge of the PS rim and more tangential to the blade PS, the results showed improved cooling effectiveness and greater blockage of the PS rim OTL flow reattachment in the SS cut-back tip, as the coolant was injected almost directly into the tip gap.

4. Stationary casing tests suggest the high film effectiveness on the cavity floor of the SS cut-back is redundant, as this area displays very low HTC in both uncooled and cooled testing. However, the author notes that experiments in a stationary end wall cascade might not give the whole picture of HTC distribution and film effectiveness. It is likely that the OTL flow field and cooling injection would be altered in the real rotating engine case.

5. The cooled SS cut-back tip was shown to be the superior film cooled design, as it showed improved film effectiveness over the tip, especially towards the trailing edge. However, a beneficial decrease in overall HTC (compared to the baseline squealer) was not observed; the trend between tips seen in the uncooled case was maintained with addition of cooling, suggesting the HTC distribution is more closely correlated to the tip geometry.

6. The trends with coolant mass flow rate are similar for both tip designs, specifically an increase in η and a decrease in HTC at increased coolant mass flow, although some differences were observed locally.

7. At a high localised BR (i.e. low cavity mass flow, high coolant mass flow), there is evidence that the coolant can alter the OTL flow over the SS rim of the SS cut-back tip. At this high BR, the impingement on the end of the SS rim was blocked and replaced with an earlier impingement onto the cavity floor followed by separation and reattachment. This behaviour was not observed at any other combination of tip gap and coolant $\dot{m}$ or on the baseline squealer.

8. Due to the differences in tip geometry, the effect on HTC and η with increased tip clearance are more complex and show some local disparity between the tip designs. The main differences occurred on the SS rim, which can show the opposite effect with increasing tip clearance for the two tip designs, due to the difference in OTL flow pattern caused by the presence of the SS cutback region and the interaction with the coolant.

9. The local blowing ratio of the cavity dust holes determines how much lift-off of the coolant film occurs. At enhanced BR (higher coolant $\dot{m}$ but lower cavity mass flow) the coolant from the cavity dust holes interacts less with the cavity flow but better cools the LE region of the SS rim, affecting the reattachment and lowering the local HTC at low tip clearance.

10. The film effectiveness of the SS cut-back tip was higher than the baseline squealer in all cases. The SS cut-back tip shows a decrease in film effectiveness with increasing tip gap at both coolant mass flow rates. However the baseline squealer showed a variation dependent on the coolant mass flow.

11. The relative thermal performance of the tip designs seen for the uncooled tip was maintained at all tip clearances and coolant mass flows tested. The baseline squealer showed increasing HTC with tip gap towards the LE, where the averaged

value is dominated by the cavity HTC, but lower HTC towards the TE as the rims dominate. The SS cut-back tip shows little difference in HTC with tip gap at the lower mass flow rate, but an increase in HTC with tip gap at the higher coolant $\dot{m}$ as the tip is dominated by the cavity HTC.

12. The PS rim of the baseline squealer was seen to be much more sensitive to a change in tip clearance. Both tip designs show a high HTC on the PS rim at low tip clearance, but the baseline squealer displays a much larger decrease in HTC at the higher tip clearance. Both tips display the characteristic striping of high and low HTC due to blockage by the coolant film; the SS cut-back tip shows this behaviour in all cases considered.

Chapter 8

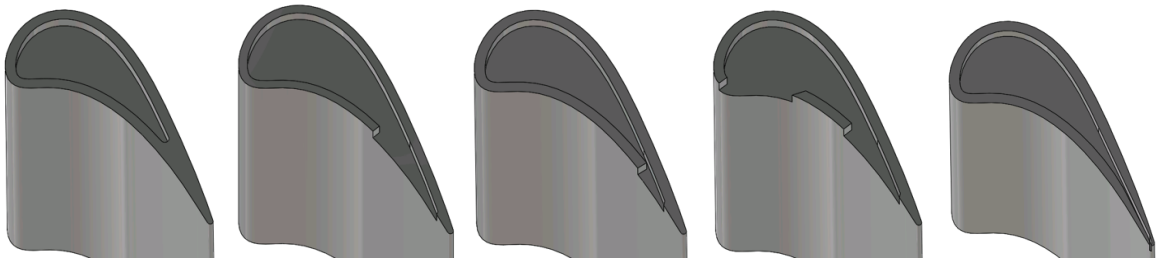
Tip Geometry CFD Study

8.1 Introduction

This chapter examines a series of uncooled tip designs using CFD to evaluate the tip heat transfer coefficients, aerodynamic losses and to attempt to explain some of the more in depth tip flow physics seen in the previous chapters. Validation of the CFD solutions was first done by comparison to HSLC data and Rolls-Royce data. Simulations have been run under stationary conditions at tip gaps of 0.5% g/S and 1.0% g/S, before addition of relative casing motion (at 1.0% g/S only) to give an appreciation of the changes that would occur under a more engine realistic, rotating flow field.

8.2 Tip Models in Study

The design process employed in this study was to use a closed squealer as a starting point and remove portions of the pressure side rim to develop alternative pressure side cut-back designs, which ideally offer improve aerothermal performance. The design philosophy behind this approach was discussed in Chapter 6 (Section 6.2). The geometries developed are shown in Figure 8.1 and described as follows: a closed squealer tip, similar to one examined by Virdi (2015); a first PS cut-back tip with the last 50% of the PS rim removed towards the TE; a second PS cut-back tip with last 25% of the PS rim



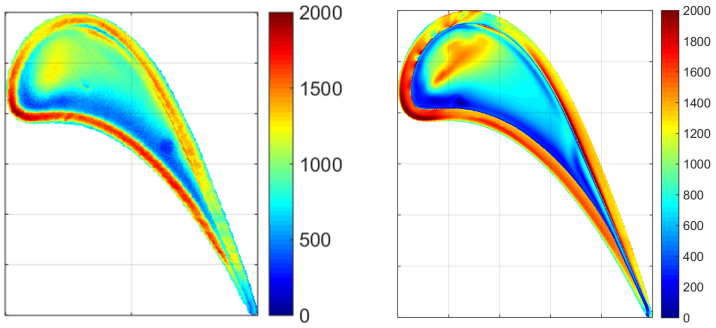
(a) CFD Closed squealer geometry | **(b) CFD PS cut-back geometry 1** | **(c) CFD PS cut-back geometry 2** | **(d) CFD PS cut-back geometry 3** | **(e) CFD Hypothetical geometry**

Figure 8.1: Tip geometries used in the CFD geometry study

removed closer to the TE; a third PS cut-back tip with the first 25% and last 50% of the PS rim removed; a hypothetical tip geometry with a narrow channel running from the tip cavity and TE. The designs were developed iteratively and the thought process behind each design will be discussed in Section 8.3.1 when examining the heat transfer coefficients of each tip geometry. For the main study the cavity depth was kept constant at 3mm and the tip gap at 0.5% and 1% g/S.

8.3 Validation of CFD

Validation of the CFD was done by comparison to experimental results gained in the HSLC. The cavity depths of the CFD models were matched to the physical test blades and the tip clearance set to 0.65% g/S to be consistent with experiment. The primary validation was performed using the CFD hypothetical tip geometry (Figure 8.1e) and assessed using HTC results. A secondary validation of the CFD was carried out using the HTC results and aerodynamic loss data for the CFD PS cut-back geometry 2 (Figure 8.1c), which was very similar in design to the experimental PS cut-back tip tested in Chapter 6. Additional comparison of computational blade loading data to Rolls-Royce data was also performed.



(a) Exp 0.65% **(b) CFD 0.65%**

Figure 8.2: Experimental and computational heat transfer coefficients (W/m^2K) measured on the hypothetical geometry at 0.65% g/S

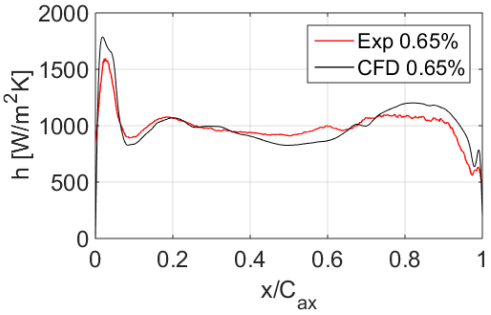


Figure 8.3: Circumferentially averaged heat transfer coefficient (W/m^2K) for the hypothetical tip, both experimental and CFD cases

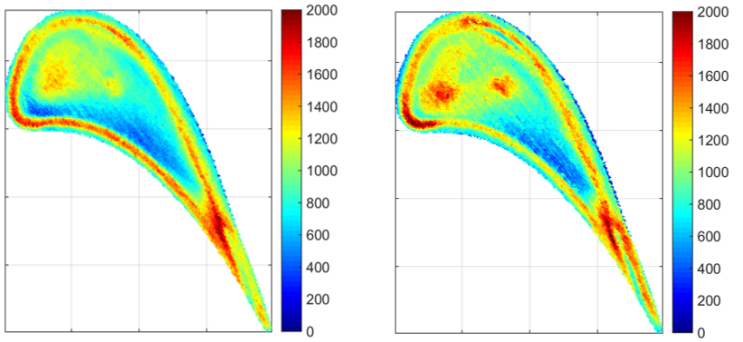
8.3.1 Heat Transfer

Figures 8.2a and 8.2b show the heat transfer coefficients for the experimental and CFD cases for the hypothetical tip geometry at 0.65% g/S. The CFD shows good agreement of the spatial HTC distribution to the HSLC test data, in particular the high HTC on the PS rim, slightly lower HTC on the SS rim, low HTC at the TE and the band of low HTC aft of the PS rim on the cavity floor. However, the cavity LE impingement hotspot is slightly over-predicted by the CFD. Overall heat transfer coefficients and circumferentially averaged HTC for the hypothetical tip geometry can be found in Table 8.1 and Figure 8.3 respectively, showing good agreement between CFD and experiment.

The secondary CFD validation was performed using the PS cut-back geometry 2 CFD model and the experimental PS cut-back tip, at both tip clearances (0.65% and 1.15% g/S). Figures 8.4 and 8.5 show the heat transfer coefficients for this tip. Note that the exact geometry around the cut-back is slightly different between the CFD model and

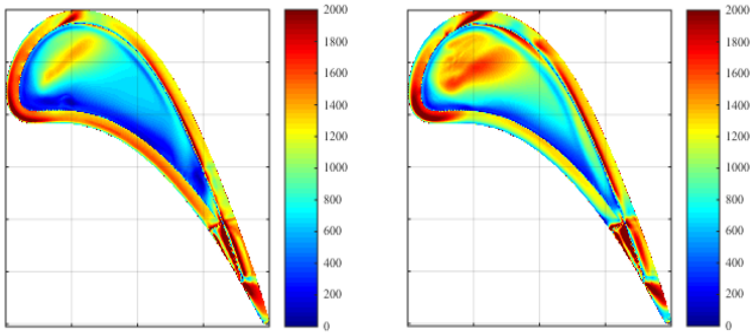
Tip Geometry	Tip Gap (g/S)	HSLC h $[W/m^2K]$	HYDRA h $[W/m^2K]$
Hypothetical tip	0.65%	979.2	1012.3
PS cut-back tip 2	0.65%	1048.2	1057.2
	1.15%	1070.5	1125.8

Table 8.1: Mean tip heat transfer coefficients (W/m^2K)



(a) Exp 0.65% **(b) Exp 1.15%**

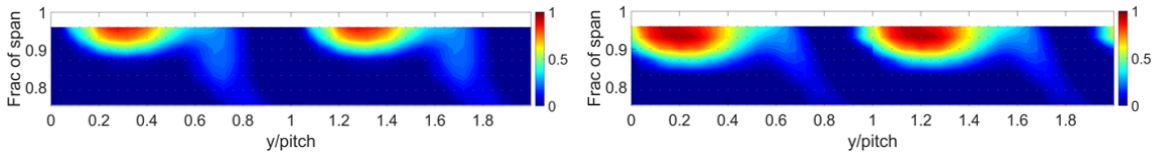
Figure 8.4: Experimental heat transfer coefficients (W/m^2K) measured on the PS cut-back tip at 0.65% and 1.15% g/S (HSLC)



(a) CFD 0.65% **(b) CFD 1.15%**

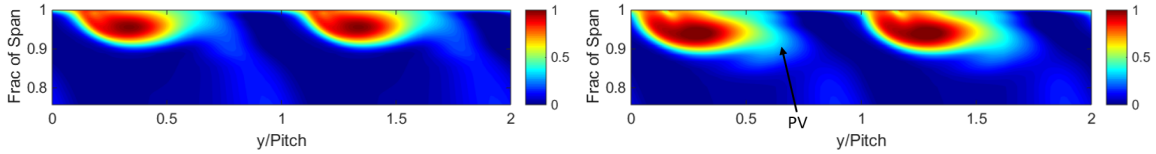
Figure 8.5: Computational heat transfer coefficients (W/m^2K) measured on the hypothetical geometry at 0.65% and 1.15% g/S (HYDRA)

experiment: the PS rim terminates in a blunt end in the CFD and the cut-back opening is slightly narrower. Despite these slight geometrical differences the HTC distribution is well predicted by the CFD, and the trends between tip gap are also in agreement with experiment; in particular the decrease in HTC on the PS rim and increase on the cavity floor at higher tip clearance. At the trailing edge, where the geometry disparity is located, there is evidence in the CFD of the leakage noted over the SS rim in experiment, however the HTC peak at the very TE in the CFD is caused by an angled feature of the



(a) Exp 0.65% **(b) Exp 1.15%**

Figure 8.6: Experimental total pressure loss coefficient Y_{P0} measured on a plane 50% C_{ax} downstream for the PS cut-back tip (variation 2) at 0.65% and 1.15% g/S(HSLC)



(a) CFD 0.65% **(b) CFD 1.15%**

Figure 8.7: Computational total pressure loss coefficient Y_{P0} measured on a plane 50% C_{ax} downstream for the PS cut-back tip (variation 2) at 0.65% and 1.15% g/S (HYDRA)

SS rim which is not present in the printed test tips. Table 8.1 summarises the mean tip HTC, again showing reasonable agreement.

Overall it has been shown that the HYDRA CFD performed in this chapter gave a good representation of the experimental tip HTC in a stationary cascade environment and can therefore be utilised as a tool to investigate tip heat transfer on other tip geometries and in a more realistic flow field with relative casing motion.

8.3.2 Aerodynamic Loss

For validation of computational aerodynamic loss data, the PS cut-back geometry 2 was compared to the experimental PS cut-back geometry. Figures 8.6 and 8.7 show the total pressure loss coefficient Y_{P0} at a plane 50% C_{ax} downstream of the blade row for the experimental and computational cases respectively. Examination of these figures show that the main loss features observed in experiment i.e. the OTL vortex and the 2D blade wake are predicted by the CFD. There is also a small hint of the upper passage vortex, for example at PV in Figure 8.7b. By further comparison of Figures 8.6 and 8.7, it is observed that the CFD predicts many of the same trends as observed in experiment when moving to a higher tip clearance: a shift of the OTL vortex away from the casing and from the blade SS; an increase in the size and strength of the main OTL

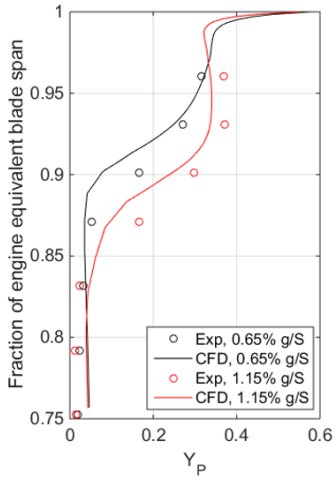


Figure 8.8: Mass averaged total pressure loss coefficient Y_{P0} at the 50% C_{ax} downstream plane for the PS cut-back tip at 0.65% and 1.15% g/S tip gaps (HSLC and HYDRA)

loss vortex; and a weakening of the 2D blade wake. Figure 8.8 shows the mass averaged Y_{P0} at the test plane and highlights the trend in Y_{P0} between tip gaps. There is some disparity in the absolute mass averaged values between CFD and experiment, but the agreement is reasonable and the trends are well predicted, especially considering the small difference in geometry around the cut-back region in the computational model. This gives confidence in the CFD aerodynamic loss results presented in this chapter and has enabled valid discussion of the effects of changing tip geometry and the addition of casing motion.

8.3.3 Blade Loading

Cascade blade loading design data was supplied by Rolls-Royce and compared to the computational blade loading calculated at mid-span by the author; at this location the loading should not vary with differing tip geometry. Blade loading was evaluated by the Isentropic Mach number:

$$M_{isen} = \left[\left(\left(\frac{p_0}{p_s} \right)^{\frac{\gamma-1}{\gamma}} - 1 \right) \left(\frac{2}{\gamma - 1} \right) \right]^{\frac{1}{2}} \tag{8.1}$$

where p_0 inlet total pressure, and p_s is the static pressure on the blade surface.

Figure 8.9 shows the comparison between the Rolls-Royce data and CFD for the

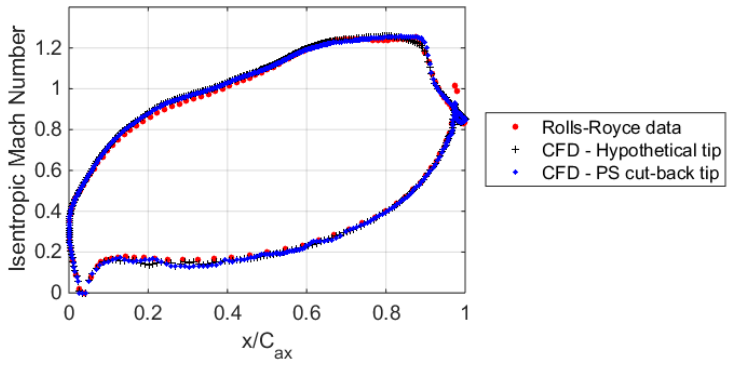


Figure 8.9: Blade mid-span isentropic Mach number

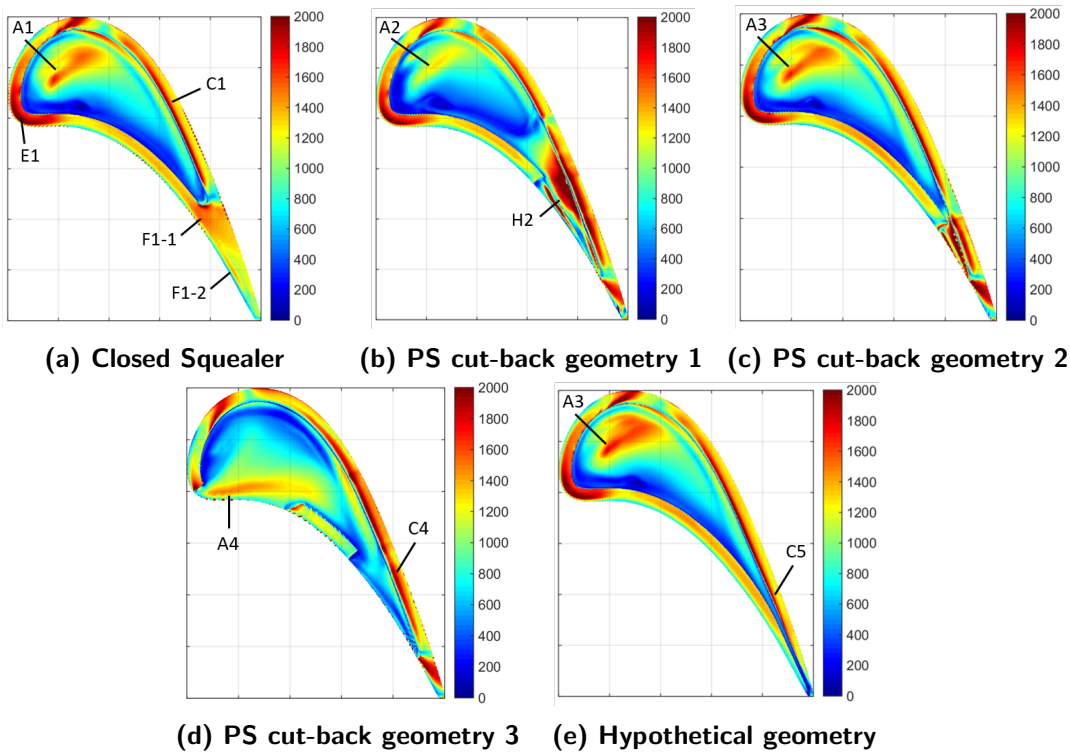
hypothetical blade tip and PS cut-back tip (geometry 2). A reasonably good agreement of blade loading data can be observed, suggesting the boundary conditions applied to the computational model are suitable.

8.4 Stationary Casing

This section examines CFD of the series of tip geometries described in Section 8.2. The heat transfer and aerodynamic loss for each of these tips will first be compared at a tip clearance of 1% g/S, with discussion of the flow physics and design reasons behind each geometry. The influence of tip clearance will then be examined under stationary conditions, by comparison to CFD at a smaller tip gap of 0.5% g/S for the same series of tip geometries.

8.4.1 Heat Transfer

Figure 8.10 shows the heat transfer coefficients for the five CFD tip geometries. The closed squealer tip in Figure 8.10a was the starting point for the geometry study. This tip shows several features, similar to those discussed in previous chapters, which can be related to the OTL flow, observed via streamlines in Figure 8.11. Figure 8.10a shows that the PS squealer rim delays the impingement of flow onto the cavity floor until near the camber line of the tip, creating a band of low HTC inside the PS rim. At the LE, a region of high HTC is seen on the PS rim at the stagnation point (marked *E1*), followed



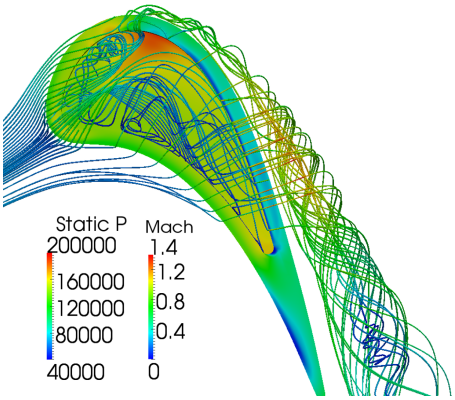
(a) Closed Squealer **(b) PS cut-back geometry 1** **(c) PS cut-back geometry 2**

(d) PS cut-back geometry 3 **(e) Hypothetical geometry**

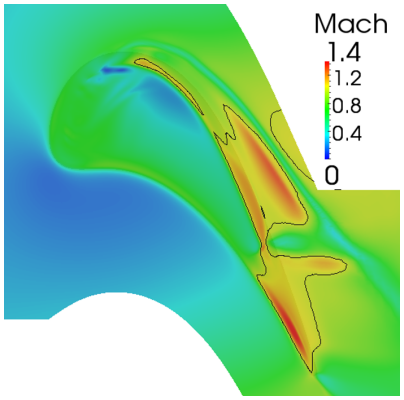
Figure 8.10: Computational tip heat transfer coefficients (W/m^2K) for a range of tip geometries at 1% g/S (HYDRA)

by the characteristic region of high HTC on the cavity floor from the impinging flow (*A1*). The streamlines in Figure 8.11a show that towards the mid-chord, as the tip narrows, the flow does not impinge onto the cavity flow, instead passing over the cavity and impinging on the forward edge of the SS rim at; this manifests in a band of high HTC (*C1*). Over the flat, TE portion of the tip, two differing behaviours are seen. At around 0.80 C_{ax} where $M < 1$ (Figure 8.11b), subsonic reattachment causes high HTC on the wider portion of the tip (marked *F1-1*) in Figure 8.10a. Further towards the TE, Figure 8.11b shows that the Mach number approaches 1.4. Acceleration of flow over the separation bubble at transonic Mach number lowers the turbulent intensity of the reattaching flow, reducing the HTC, and creates stripes of high and low heat transfer (at *F1-2*) due to the interaction of shockwave reflections with the tip boundary layer, as observed by Zhang *et al.* (2011a).

The heat transfer coefficient on the first of the PS cut-back designs is shown in Figure 8.10b. The main impact of the removal of the portion of PS rim is the creation of a large

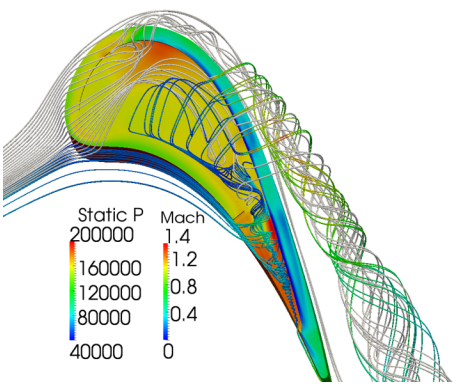


(a) Mach streamlines and static pressure contours

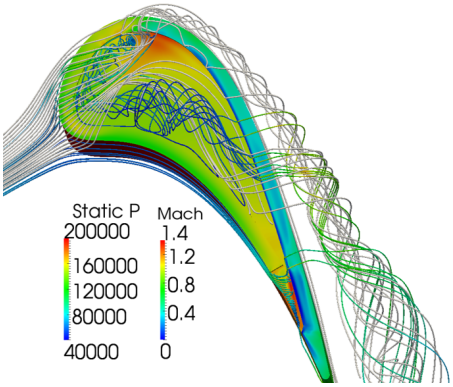


(b) Mach number on a mid tip gap plane with contour at $M = 1$

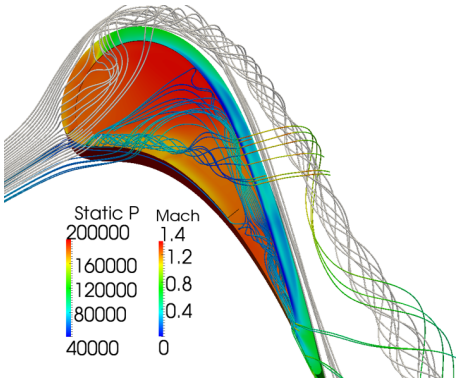
Figure 8.11: OTL flow field for the closed squealer tip (HYDRA)



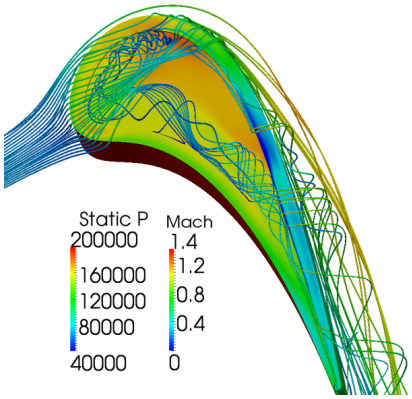
(a) PS cut-back geometry 1



(b) PS cut-back geometry 2



(c) PS cut-back geometry 3



(d) Hypothetical geometry

Figure 8.12: Contours of surface static pressure and Mach streamlines

HTC hotspot in the cutback region (marked *H2*) and the reduction of the HTC levels in the LE impingement region on the cavity floor. These changes can be explained with reference to Figure 8.12a which shows the tip surface static pressure contours and Mach streamlines of the OTL flow for the PS cut-back geometry 1. On entering the cut-back

region, the OTL flow impinges directly onto the inside vertical face of the SS rim and rolls up into a small diameter vortex which scrapes on the cavity floor. The creation of this vortex produces high levels of turbulence in the cut-back region and the scraping of the energetic vortex on the cavity floor produces the high HTC levels (of approximately 2200-2700 W/m^2K) predicted in Figure 8.10b. The HTC near to the LE reduces as the pressure gradient inside the tip cavity forces flow in through the cut-back (seen in Figure 8.12a). This flow enhances the cavity recirculation and blocks the impingement of the OTL flow over the PS rim onto the cavity floor, reducing the intensity of the impingement HTC at *A2*.

PS cut-back geometry 2 was iterated from geometry 1 by moving the location of the PS cut-back closer to the TE. This was done in order to reduce the HTC levels in the cut-back region, which forms a vulnerable area of the tip. Comparison of Figures 8.10b and 8.10c shows that this strategy was partially successful, by reducing the size of the high HTC area, with a corresponding reduction in the cut-back vortex observed in Figure 8.12b. However, Figure 8.13, which shows a circumferentially averaged comparison of HTC on each of the tip designs, suggests that the region of peak HTC has simply been shifted further downstream, without much of a reduction in peak HTC magnitude (approximate HTC levels are predicted to remain at 2200-2700 W/m^2K).

In the upstream cavity and rims, the HTC distribution on the cut-back geometry 2 is almost identical to the closed squealer (see Figures 8.10c and 8.10a); the blockage created at the narrow entrance to the cut-back region prevents the inflow from the cut-back into the upstream cavity (see Figure 8.12b) and the cavity flow pattern for the PS cut-back geometry 2 has reverted to a pattern similar to that seen in the closed squealer in Figure 8.11a. This observation indicates that if this gap is narrow, the upstream cavity is insensitive to the TE cut-back geometry, in agreement with the findings of Bunker & Bailey (2001) for low speed flows. Compared to the cut-back geometry 1, the absence of the in-flow through the cut-back (of the PS cut-back geometry 2 tip) is reflected by increased HTC in the LE cavity (*A3*), observed in Figure 8.10c.

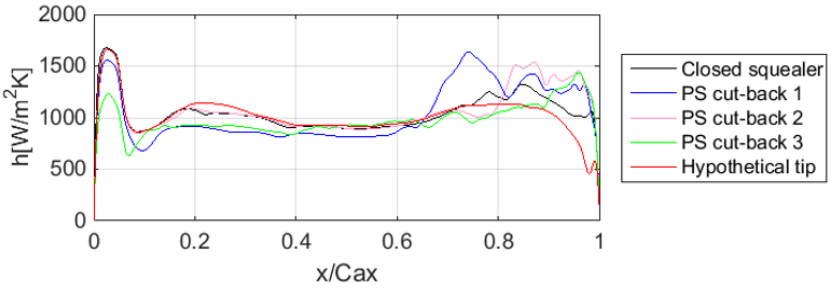


Figure 8.13: Circumferentially averaged heat transfer coefficients (W/m^2K) for the CFD tip geometries at 1.0% g/S tip gap (HYDRA)

The original aim of implementing a cut-back was to provide an exit route for entrained cavity flow and eventually coolant, to aid with cooling of the TE. Due to the inherent pressure field around the blade, the surface static pressure in the cut-back is very high whereas that in the upstream cavity is much lower (see Figures 8.12a and 8.12b), due to the loss in pressure head as the OTL flow passes over the PS rim. This adverse pressure gradient was preventing any flow from exiting through the cut-back as intended and allowing the creation of the narrow cut-back vortex.

To even out the pressure field in the tip cavity and cut-back, a portion of the PS rim was removed at the LE to prevent the loss of pressure head in the flow into the cavity. Figure 8.12c shows that this change has altered the OTL flow in several ways: firstly, the creation of a tightly wound vortex in the LE cut-back region; secondly, the direction of flow is now from the upstream cavity towards the TE; and lastly, the reattachment and small diameter vortex in the TE cut-back region has been removed, as the flow into this downstream cut-back from the blade passage is swept up by the TE bound cavity flow. The effect on the tip HTC of this change in flow field is quite marked. It is observed in Figure 8.10d that the LE vortex manifests in a strip of increased HTC, although the previous impingement hotspot is removed ($A4$). There is no longer any region of high HTC in the TE cut-back region, however the HTC on the SS rim remains high when compared to the PS cutback geometry 1 (Figure 8.10b), as the reattachment of flow onto this rim (at $C4$) is not largely altered by the addition of the upstream PS rim cut-back.

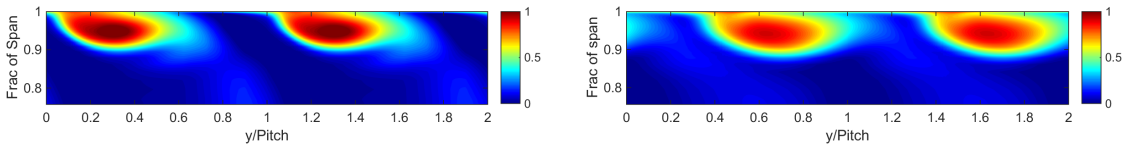
The hypothetical tip geometry in Figure 8.10e performs reasonably well compared

to the other tips discussed, keeping peaks of HTC to a minimum. Compared to the closed squealer, on average there is reduced HTC towards the trailing edge as a result of the narrow channel breaking up the flat rear portion of the tip. However the presence of this channel does increase the length of the impingement region onto the SS rim (towards region *C5*). Nonetheless, the hypothetical tip does show the lowest HTC at the TE (see Figure 8.13) and on the SS rim of all the CFD designs. It is expected that without the slight 'blunt end' geometry anomaly of the cut-back tips 1-3 that the HTC at TE of these tips would be reduced, but the experimental data in Section 8.3.1 indicate that the hypothetical geometry would still give lower HTC at the TE. Away from the trailing edge the HTC distribution on the hypothetical tip is much the same as the closed squealer, but with an increased area of high HTC in the LE cavity, at *A5* (approximate HTC levels are 1600-1750 compared with 1550-1700 W/m^2K). This is due to a slight reduction in cavity recirculation as a result of opening up the TE of the tip, seen by comparison of Mach streamlines in Figures 8.11a and 8.12d.

8.4.2 Aerodynamic Loss

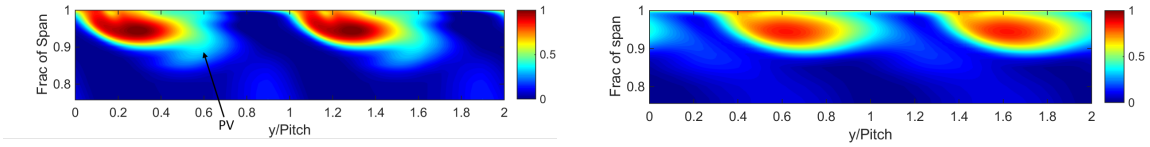
Figures 8.14 - 8.18 show the total pressure loss contours Y_{P0} for each of the tip geometries at both 50% C_{ax} and 100% C_{ax} downstream planes. The manner in which the loss cores develop as they move downstream can be observed. In all cases there is a reduction in peak Y_{P0} of the main OTL vortex from the 50% to 100% C_{ax} planes as the loss vortices mix out, but at the same time an elongation of the OTL vortex in the pitchwise direction occurs. It can also be observed that as the OTL vortex moves downstream, it shifts further away from both the SS of the blade and the casing.

There are some clear differences noted in the loss contours of the CFD geometries at 50% C_{ax}. All but the PS cut-back geometry 3 in Figure 8.17a show a large OTL vortex and a hint of the upper passage vortex (for example at *PV*) which has been mostly overwhelmed by the OTL vortex. This behaviour can be examined using flow streamlines in Figure 8.19a, using the example of the closed squealer tip. However,



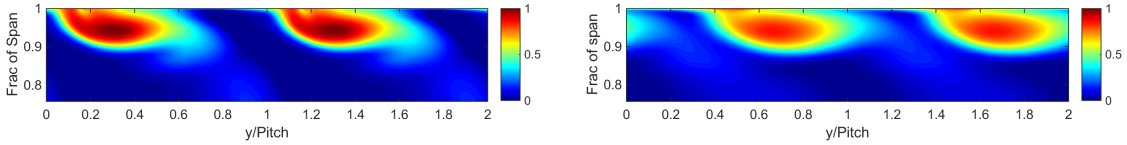
(a) 50% C_{ax} downstream **(b) 100% C_{ax} downstream**

Figure 8.14: Computational total pressure loss coefficient Y_{P0} measured at 50% and 100% C_{ax} downstream for the closed squealer tip at 1% g/S (HYDRA)



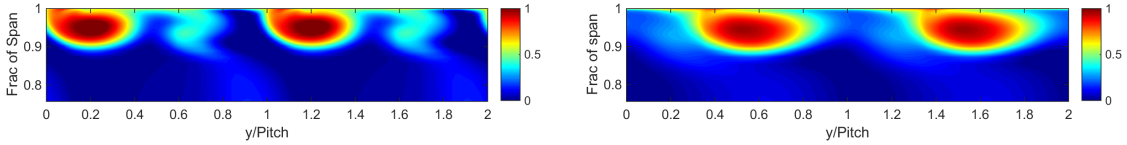
(a) 50% C_{ax} downstream **(b) 100% C_{ax} downstream**

Figure 8.15: Computational total pressure loss coefficient Y_{P0} measured at 50% and 100% C_{ax} downstream for the PS cut-back geometry 1 at 1% g/S (HYDRA)



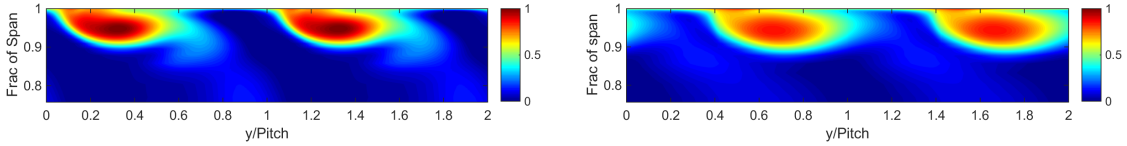
(a) 50% C_{ax} downstream **(b) 100% C_{ax} downstream**

Figure 8.16: Computational total pressure loss coefficient Y_{P0} measured at 50% and 100% C_{ax} downstream for PS cut-back geometry 2 at 1% g/S (HYDRA)



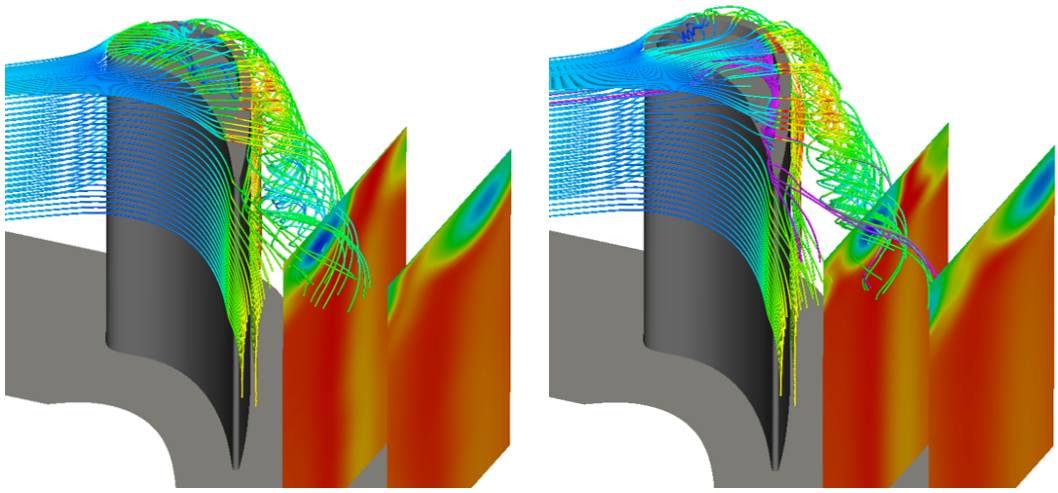
(a) 50% C_{ax} downstream **(b) 100% C_{ax} downstream**

Figure 8.17: Computational total pressure loss coefficient Y_{P0} measured at 50% and 100% C_{ax} downstream for PS cut-back geometry 3 at 1% g/S (HYDRA)



(a) 50% C_{ax} downstream **(b) 100% C_{ax} downstream**

Figure 8.18: Computational total pressure loss coefficient Y_{P0} measured at 50% and 100% C_{ax} downstream for the hypothetical geometry at 1% g/S (HYDRA)



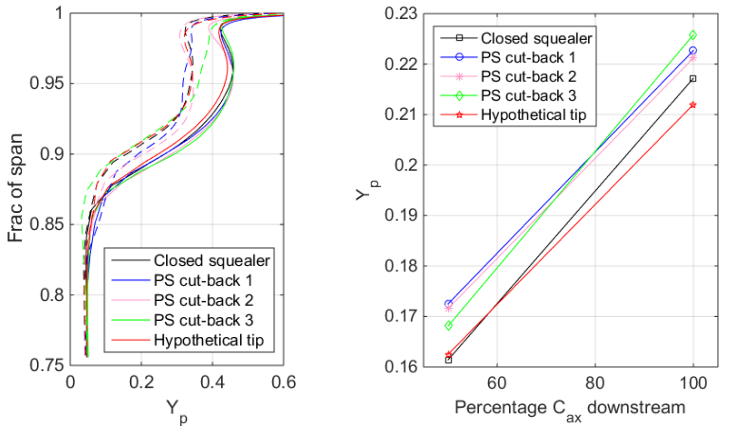
(a) Closed squealer

(b) PS cut-back geometry 3. Purple streamlines are exiting from the TE cut-back.

Figure 8.19: Streamlines of Mach number (range $M = 0 - 1.4$) showing source of loss features at 50% and 100% axial planes. Plane shows total pressure (HYDRA)

the PS cut-back geometry 3 shows very distinct separation of the OTL and upper passage vortices (in Figure 8.17a). This separation is reflected in Figure 8.19b, where the underlying cause can be evaluated. It is evident that the Mach number over the SS rim is higher for the PS cut-back geometry 3; this coupled with the lack of pressure loss of the flow into the tip gap (as shown in Figure 8.12c) results in a higher mass flow over the SS rim, which reaches further into the passage, hence the OTL vortex forms further from the blade SS. It is far enough from the SS that the OTL vortex does not consume the upper passage vortex at the 50% axial plane, and the upper passage vortex is further enhanced by flow exiting the TE cut-back on the blade PS, as shown in purple in Figure 8.19b (note that some of this flow does still join the main OTL vortex). As the only tip geometry with the LE rim opening, the PS cutback tip 3 is the only one displaying this behaviour. However, the geometry variations in the other tips do cause a shift in position of the OTL vortex, observed by comparison of the Y_{P0} contours in Figures 8.14 - 8.18.

The diverging nature of the OTL vortex and other secondary flow features is much more pronounced at the 100% C_{ax} downstream plane. Whereas, at 50% C_{ax} the OTL vortex and 2D wake form roughly $y/P = 0.6$ apart, by the 100% axial plane, the two



(a) Pitch-wise mass-averaged **(b) Overall mass averaged Y_{P0}**

Figure 8.20: Mass averaged total pressure loss coefficient Y_{P0} at 50% and 100% C_{ax} downstream for the CFD tip geometries (HYDRA). In (a) the dotted lines represent 50% C_{ax} and solid lines 100% C_{ax}

features are separated by almost a whole blade pitch in the y-direction. This was already mentioned in Chapter 3 when discussing periodicity in the HSLC, and means that when measuring over one exit plane the OTL vortex and 2D wake originate from different blades in the row. This can be observed for example when isolating a single pitch in Figure 8.14. With this principle in mind, examination of Figure 8.17 reveals that the upper passage vortex which was clearly observed at the 50% axial plane for the PS cut-back geometry 3, has been consumed by the OTL vortex originating from the next blade in the row at 100% C_{ax} downstream and all but disappeared.

Comparison of the mass averaged Y_{P0} in Figure 8.20a shows that there is little difference in the loss caused by the 2D wake from the CFD designs. While the experimental study described in Chapter 6 found larger differences, this CFD study considers more modest changes to the tip design. Closer to the casing (in Figure 8.20a), there is a larger difference caused by the relative size and strength of the OTL vortices. It is observed in Figure 8.20b that in all cases higher losses are present at the 100% Cax plane (largely due to mixing) but that the relative performance of the tips changes between the two exit planes. The influence of the LE cut-back and additional loss from the TE are evident in Figure 8.20a, where the PS cut-back geometry 3 tip shows the highest losses

close to the casing at 50% C_{ax} and the highest losses overall at 100% C_{ax}. Overall, with a stationary casing the hypothetical tip geometry produced the lowest mass averaged losses at 100% axial plane and almost the lowest at the 50% plane. The worst performer at both exit planes were the PS cut-back designs. This result suggests that the PS rim plays an essential part in sealing the tip gap and that removal, or erosion, of this rim would result in higher losses, as the single constriction of the SS rim is not sufficient to prevent a higher leakage mass flow from passing through the tip gap.

8.4.3 Tip Clearance

As the influence of tip clearance has already been examined in previous chapters, this section will focus on averaged trends and relative performance between tips when moving from a 1.0% g/S tip gap to a more engine realistic 0.5% g/S tip gap, rather than detailed analysis of each CFD design.

8.4.3.1 Heat Transfer

The trends in tip heat transfer coefficient were examined by taking circumferentially averaged HTCs at both 0.5% g/S and 1.0% g/S and are shown in Figure 8.23. For reference, the tip HTC maps at 0.5 g/S tip gap are shown in Figure 8.22. Figure 8.23 reveals a common trend for all the CFD designs when increasing tip gap: a small decrease in HTC at the LE; increased HTC through the mid portion of the tip; decreased HTC at the trailing edge. Similar behaviour was found by both Zhang *et al.* (2011b) and Virdi (2015) for a variety of tip designs.

If these trends are examined further, either by comparison of the HTC maps (Figures 8.22 and 8.10) or by use of area averaged HTCs in Figure 8.21, it can be determined that the squealer cavity shows a increase in HTC, but the rims a decrease in HTC at higher tip gap. This is consistent with findings in earlier chapters, where these behaviour were explained in detail with relation to the overtip flow field. Significantly, this can be used to offer an alternative explanation to what Virdi (2015) dubbed a

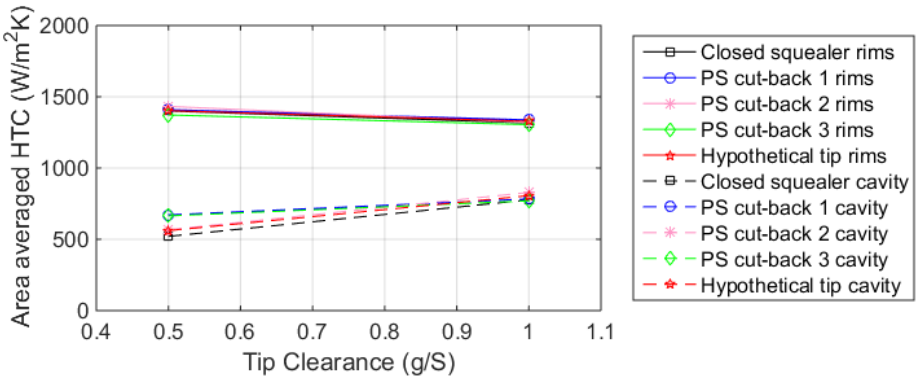
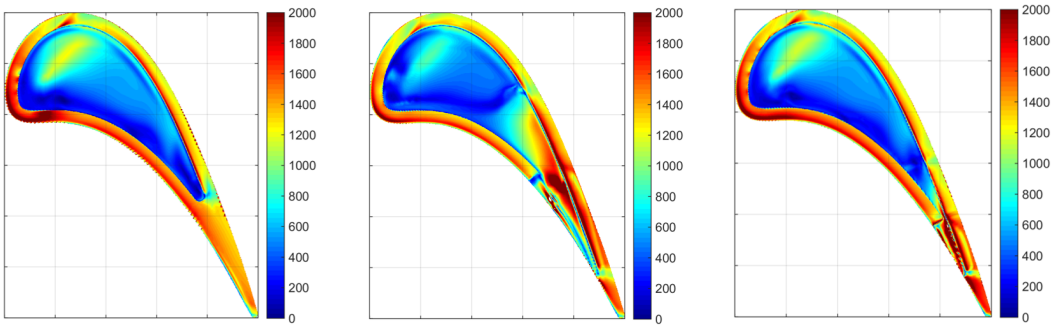
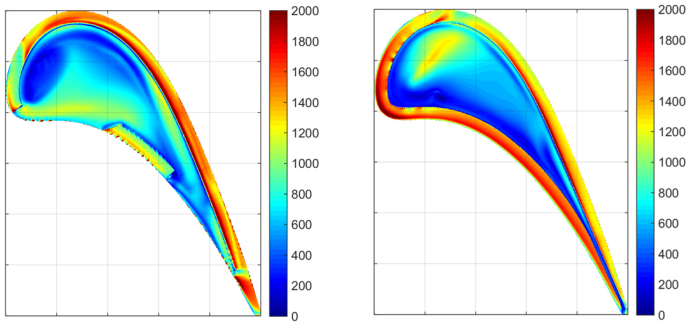


Figure 8.21: Area averaged heat transfer coefficient on the upper surfaces of the squealer rims and cavity for all CFD tip designs (HYDRA)

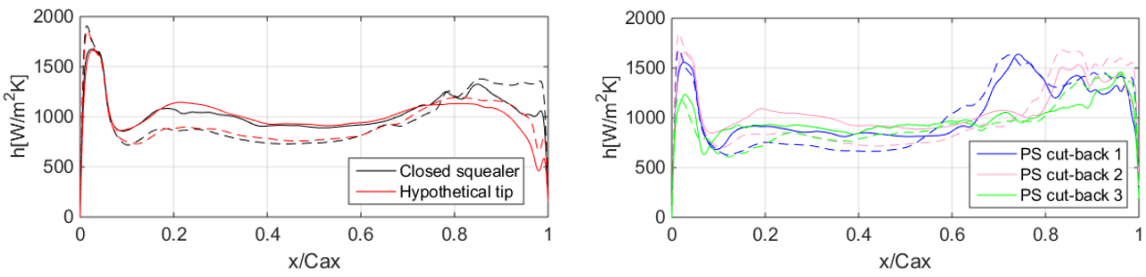


(a) Closed Squealer **(b) PS cut-back geometry 1** **(c) PS cut-back geometry 2**



(d) PS cut-back geometry 3 **(e) Hypothetical geometry**

Figure 8.22: Computational tip heat transfer coefficients (W/m^2K) for a range of tip geometries at 0.5% g/S (HYDRA)



(a) Closed squealer and hypothetical tip **(b) PS cut-back geometries**

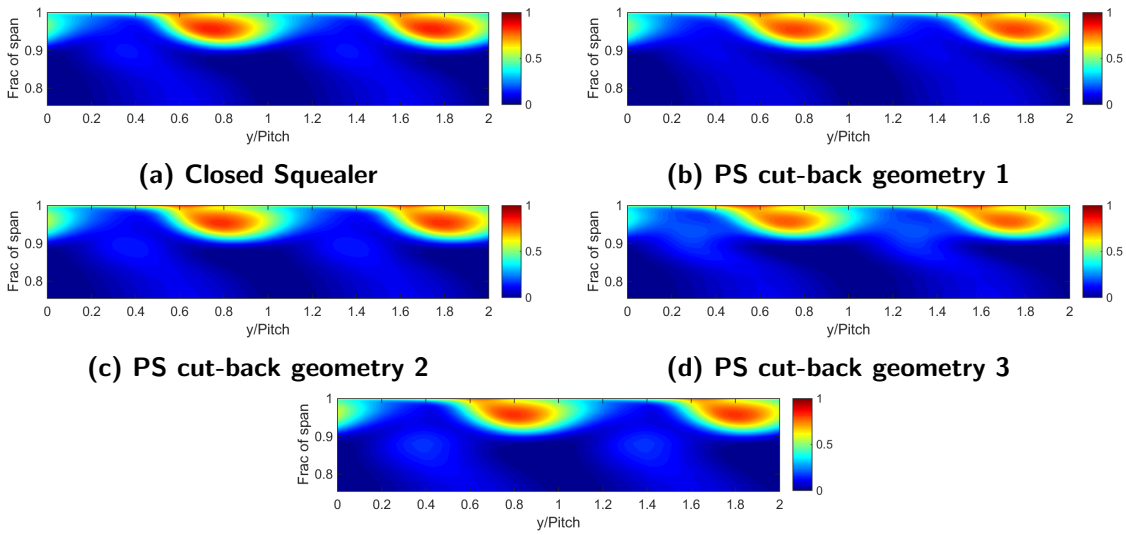
Figure 8.23: Circumferentially averaged heat transfer coefficients (W/m^2K) for each tip designs at 0.5% (dotted lines) and 1.0% g/S (solid lines) tip gaps.

crossover behaviour, whereby the trend with tip gap switches towards the tip TE. Virdi (2015) claimed this was due to a change in local flow regime from transonic to subsonic at reduced tip gap, which should result in increased HTC. The author ascribes this *crossover behaviour* simply to whether the cavity or squealer rims dominate the local circumferentially averaged HTC. In the mid-chord region, the tip area is dominated by the cavity and so the circumferentially averaged HTC is shown to increase with increasing tip clearance due to enhanced OTL mass flow. However, in the pitchwise direction, the LE and TE of the tip are comprised almost exclusively of squealer rim, which has been shown in previous chapters to decrease in HTC with increasing tip clearance. Therefore, the trend in circumferentially averaged HTC with tip gap switches as the location on the tip moves in the axial direction.

From examination of Figures 8.23a and 8.23b it is observed that at the 0.5% g/S tip gap the hypothetical tip still gives comparable HTC over most of the tip surface and the lowest HTC at the trailing edge. Figure 8.22e shows that the narrow channel is effective in splitting up the flat rear portion of the blade, and this results in lower HTC over the SS rim as a result of flow impingement onto the forwards edge of this rim at the TE. The other CFD designs display higher HTC over the full width of the SS rim, caused by a separation and reattachment of flow in the cut-back area or flat tip area of those tips (seen by comparison of other HTC maps in Figure 8.22).

8.4.3.2 Aerodynamic Loss

The influence of tip clearance on the aerodynamic loss will be discussed at the 100% C_{ax} downstream plane only. Figure 8.24 shows contours of total pressure loss coefficient Y_{P0} for the CFD designs with a 0.5% tip clearance. Comparison of this figure with the 1% g/S tip gap cases in Figures 8.14b - 8.18b reveals several trends which are consistent for all the tip designs and also agree with experimental observations in Chapter 6. These trends with increasing tip gap are: a slight shift of the OTL vortex away from the blade SS and away from the casing; an increase in the size and strength of the OTL vortex.



(a) Closed Squealer

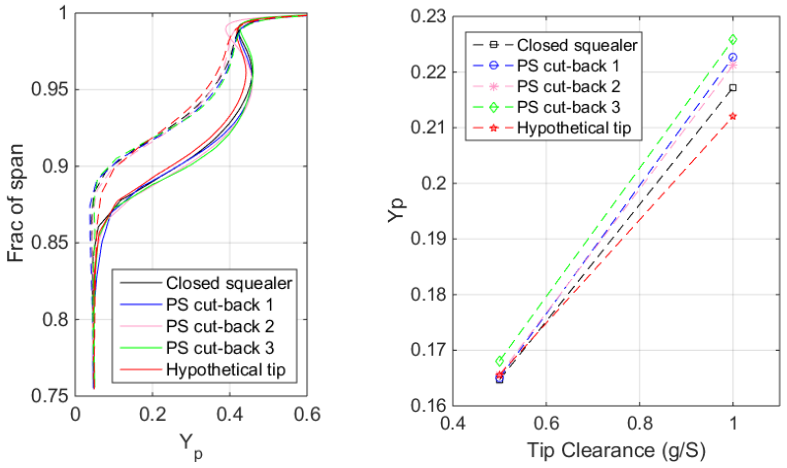
(b) PS cut-back geometry 1

(c) PS cut-back geometry 2

(d) PS cut-back geometry 3

(e) Hypothetical geometry

Figure 8.24: Computational total pressure loss coefficient Y_{P0} measured at 0.5% g/S tip gap and 100% C_{ax} downstream plane (HYDRA)



(a) Pitch-wise mass-averaged

(b) Overall mass averaged Y_{P0}

Figure 8.25: Mass averaged total pressure loss coefficient Y_{P0} at 0.5% g/S and 1.0% g/S tip gaps and 100% C_{ax} downstream for the CFD tip geometries (HYDRA). In (a) the dotted lines represent 0.5% g/S and solid lines 1.0% g/S

The relative performance of these CFD designs is more easily observed by use of the mass averaged Y_{P0} in Figure 8.25. The pitch-wise mass-averaged plot (Figure 8.25a) shows that the hypothetical tip has the smallest OTL vortex at both tip gaps, but at the small tip gap, between 0.85-0.9 fractional span, shows higher losses due to a slightly wider 2D wake. Further from the casing, the 2D wakes are comparable for all tips at both tip gaps, as expected from previous chapters. The overall mass averaged losses are

given in Figure 8.25b and it is observed that there is much less difference in the mass averaged loss at 0.5% g/S compared to 1.0% g/S. All of the CFD designs, other than the PS cut-back geometry 3 (with removed LE rim portion), have comparable losses; the PS cut-back 3 was the worst performer. This indicates that when the tip gap is small, the PS rim close to the trailing edge is less significant and that the SS rim does a good job at sealing the tip gap even when the PS rim is removed. However the loss of the PS rim at the LE still has an adverse impact on the tip losses.

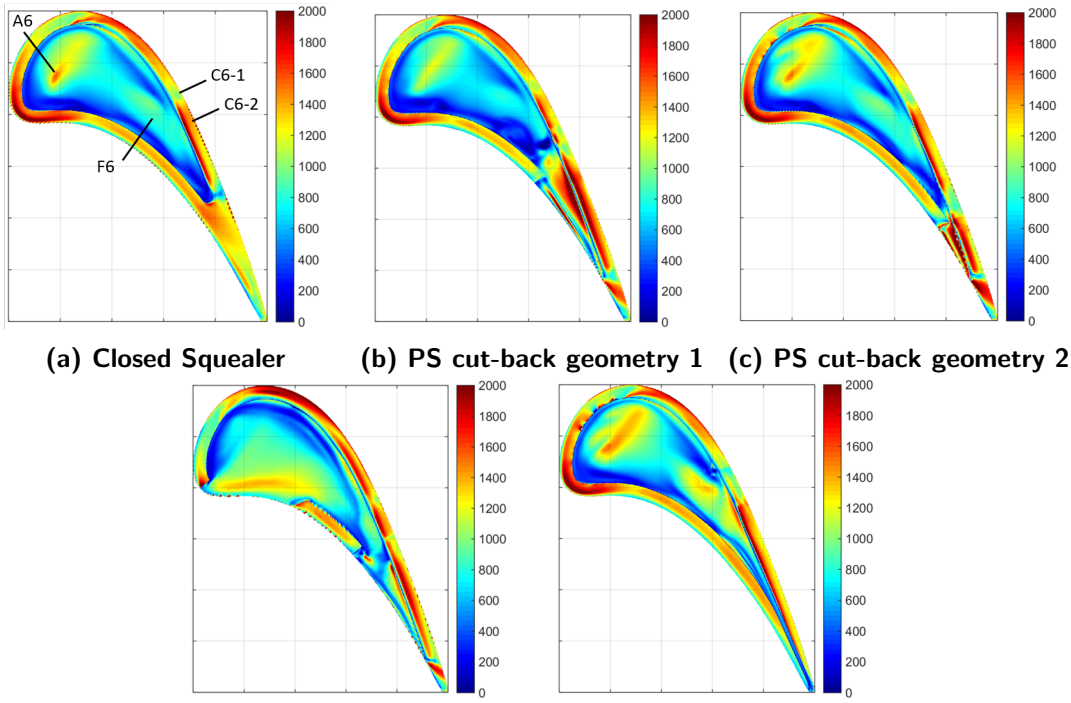
8.5 Moving Casing

Until now this chapter has focussed on investigations of the OTL flow field under stationary conditions, as would be found in a linear cascade rig such as the HSLC. However, a real engine would be rotating and many previous studies, such as those discussed in the literature review (Chapter 2), describe how a rotating flow field differs from a stationary one. It was therefore important to gain an understanding of these differences applied to the CFD designs and examine whether their relative performance would change with relative motion of the casing.

This investigation will focus on the larger 1.0% g/S tip gap only, and will compare the aero-thermal performance of the tips under stationary conditions to that when casing motion is applied, as well an examination of the relative performance under moving casing conditions. Casing motion was simulated in HYDRA by applying a tangential velocity to the casing wall boundary, in a direction from the blade SS to the PS. The casing velocity was chosen to be representative of a typical HP turbine blade. All other boundary conditions remain identical to those described in Chapter 4.

8.5.1 Heat Transfer

There are several notable trends from the addition of casing motion which are applicable to a majority of the tip designs (all except the PS cut-back geometry 3). Compared to



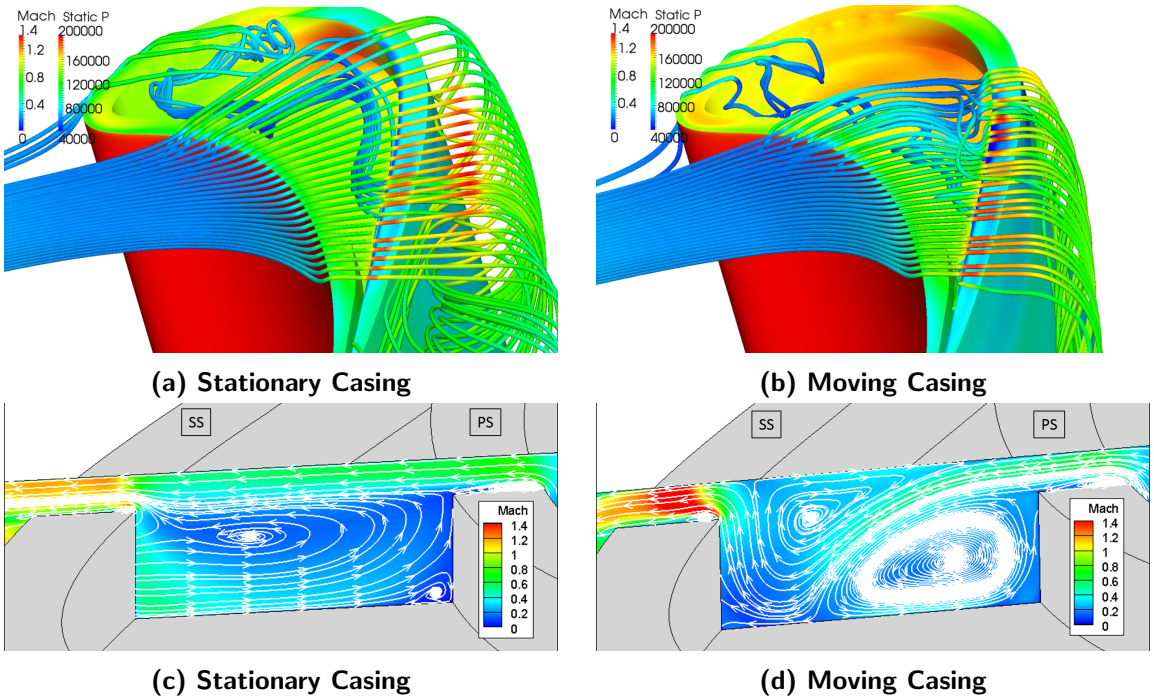
(a) Closed Squealer **(b) PS cut-back geometry 1** **(c) PS cut-back geometry 2**

(d) PS cut-back geometry 3 **(e) Hypothetical geometry**

Figure 8.26: Computational tip heat transfer coefficients (W/m^2K) for a range of tip geometries at 1.0% g/S with relative casing motion (HYDRA)

the tips with stationary casing in Figure 8.10, the HTC on the PS rim in Figure 8.26 is almost identical with the moving casing, suggesting a very similar flow reattachment onto this rim. The main differences in tip HTC distribution between stationary (Figure 8.10) and moving casing (Figure 8.26) are observed on the cavity floor and SS rim. In the LE cavity impingement region (*A6*), casing motion reduces the HTC levels (by around 5%) indicating reduced OTL mass flow, whereas in the mid-cavity (at *F6*) a new area of impingement is formed. Adjacent to this mid-cavity impingement, is an area of reduced HTC on the SS rim (at *C6-1*), followed further towards the TE by high HTC (at *C6-2*). These trends, both the similarity in HTC on the PS rim and the differences observed elsewhere are in-line with observations made on the tip geometry studied in Chapter 5. The trends will be examined in more detail below.

Using the hypothetical tip as an example, Figure 8.27 shows OTL streamlines with and without casing motion. It can be observed that with a stationary casing (Figure 8.27a), the indicated streamlines pass directly over the tip cavity and impinge on the



(a) Stationary Casing

(b) Moving Casing

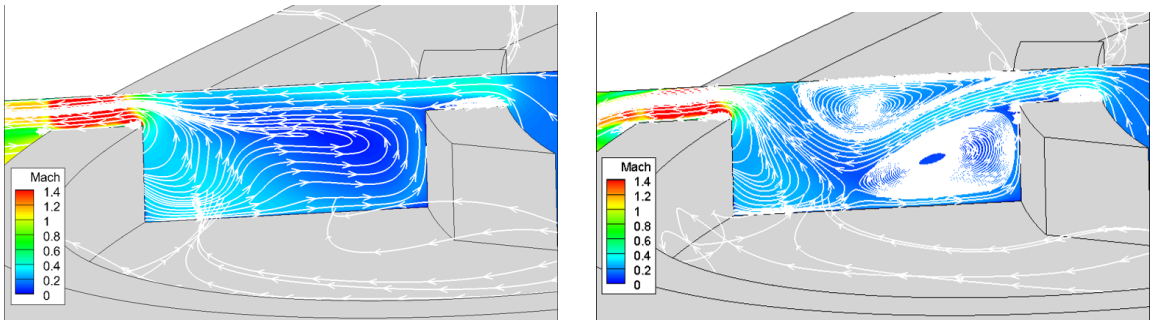
(c) Stationary Casing

(d) Moving Casing

Figure 8.27: Overtip leakage flow for the hypothetical tip with and without casing motion. (a), (b) streamlines of Mach number and contours of static pressure, (c), (d) velocity streamlines and Mach number contours (Note: orientation flipped) (HYDRA)

SS rim. The cavity in this case is dominated by a recirculation of flow, shown in Figure 8.27c. However, the flow field with casing motion changes significantly. The moving casing promotes separation of the OTL flow from the casing, tending to make the flow impinge onto the cavity floor, as seen in Figure 8.27b. In the cavity, it is observed in Figure 8.27d that a pair of counter-rotating vortices are formed: one adjacent to the PS rim, rotating in the same direction as the cavity recirculation; the other vortex rotates in the opposite direction, under influence from the moving casing and is commonly referred to as the cavity vortex. The counter-rotation of these two vortices forces the OTL flow down into the cavity, where it impinges on the cavity floor and results in the region of increased HTC observed (in region *F6*) throughout Figure 8.26. As the tip narrows, towards the TE, the cavity vortex leaks out of the cavity over the SS rim creating the region of high HTC on this rim. This region coincides with a known region of deterioration in a real engine, described by Bunker (2004).

The only exception to these observed patterns is on the PS cut-back 3 tip (see Figure 8.26d). The PS rim shows an increase in HTC with casing motion which is not observed

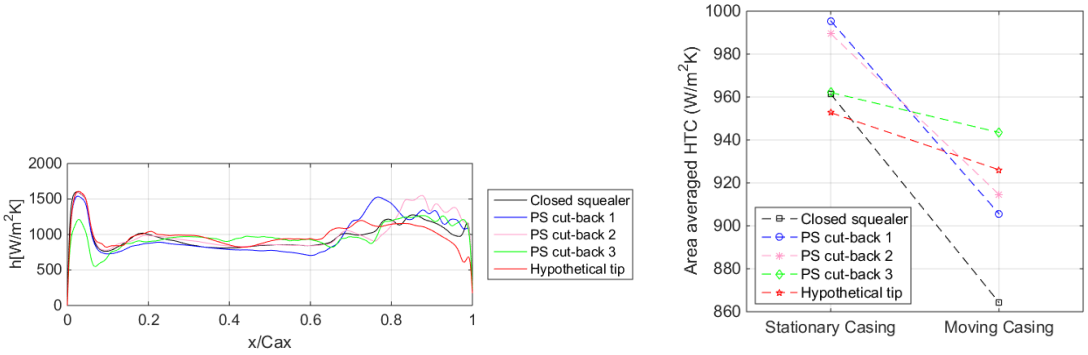


(a) Stationary Casing **(b) Moving Casing**

Figure 8.28: Overtip leakage flow for the PS cut-back geometry 3 with and without casing motion showing velocity streamlines and Mach number contours (HYDRA)

on the other tips. This increase can be explained by the earlier reattachment observed in the streamlines for this tip in Figure 8.28. Notably the impingement of the flow in the mid-cavity and reduction of HTC towards the LE is less noticeable in Figure 8.26d. It has been discussed previously in this chapter how the absence of the PS rim at the LE creates a very different flow pattern on the tip. With a stationary casing, the flow between the LE and TE cut-backs forms a large cavity recirculation and the OTL flow over the PS rim passes directly over the SS rim (Figure 8.28a). With casing motion, a network of counter-rotating flow is observed in Figure 8.28b. The cavity recirculation splits into two distinct regions rotating in the same direction, one adjacent to the PS rim and the other to the SS rim. A cavity vortex is again formed under the influence of the moving casing, counter-rotating to the cavity recirculation, and forces the OTL flow towards the cavity floor. However, in this tip design Figure 8.28b shows that the secondary cavity recirculation, adjacent to the SS rim, blocks the impingement of the over-rim flow onto the cavity floor, diverting it upwards toward the casing, so little change in HTC is seen in the mid-cavity in Figure 8.26d.

Figure 8.29 shows averaged HTC for all tip designs at 1.0% g/S tip gap. With casing motion, the area averaged HTCs decrease for all designs, driven mainly by the decrease of HTC at the LE cavity hotspot, however some change in relative performance is noted in Figure 8.29b. The hypothetical tip and PS cut-back geometry 3 show less reduction in HTC with casing motion than the other tips. For the hypothetical tip the mid-cavity



(a) Circumferentially averaged HTC with casing motion

(b) Area averaged HTC with stationary and moving casing

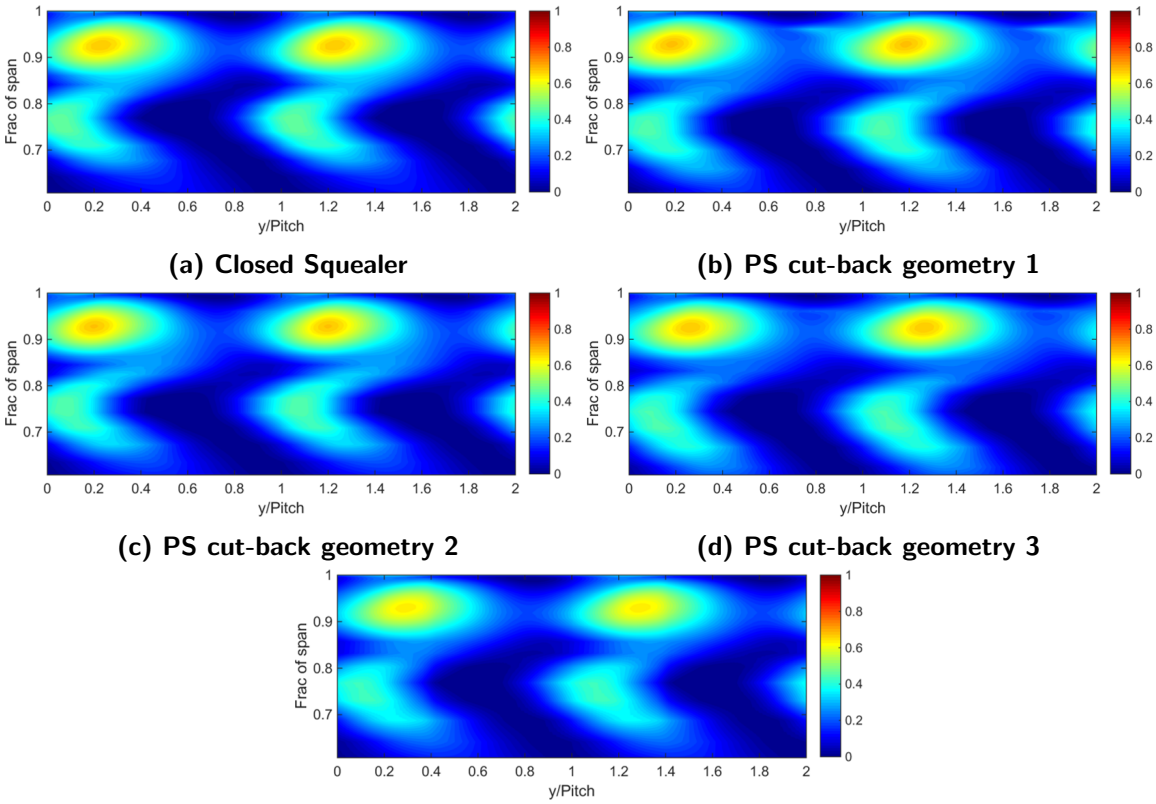
Figure 8.29: Averaged heat transfer coefficients (W/m^2K) for all tip designs at 1.0% g/S (HYDRA)

impingement caused by casing motion is the highest of all the designs. Whereas, the flow pattern observed in Figure 8.28 for the PS cut-back 3 tip limits the change in HTC with casing motion. Overall, the closed squealer design shows the lowest HTC with casing motion. This change in relative performance is not clearly observable by comparison of circumferentially averaged heat transfer coefficients between Figure 8.29a and 8.13, however it can be seen that the hypothetical tip still shows the lowest HTC at the TE with casing motion.

8.5.2 Aerodynamic Loss

Contours of Y_{P0} for 1.0% g/S tip gap with moving casing are presented in Figure 8.30 and show striking differences from the comparable tip gap with stationary casing (in Figures 8.14b - 8.18b). With casing motion: the OTL vortex reduces in intensity and shifts away from the casing and towards the blade SS; the upper passage vortex is greatly enhanced. Similar trends were observed by Palafox *et al.* (2007) and Virdi (2015).

The cause of these trends was examined using Mach streamlines in Figure 8.31. It has already been described how, with a stationary casing, the OTL vortex overwhelms the upper passage vortex. Figure 8.31a shows that, under stationary conditions, the OTL flow rolls up into the OTL vortex along the full length of the tip. However, with a moving casing, Figure 8.31b shows that the OTL flow is diverted away from the casing



(a) Closed Squealer

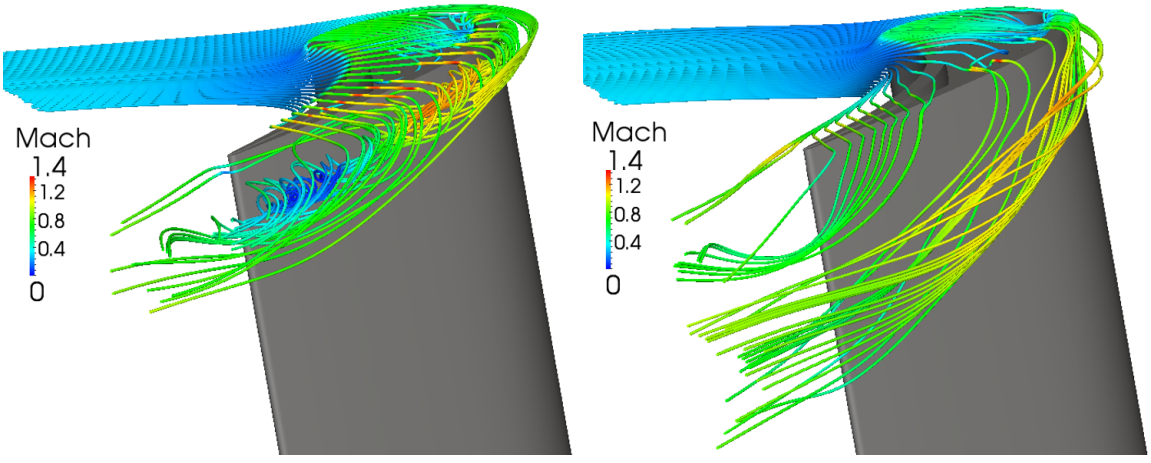
(b) PS cut-back geometry 1

(c) PS cut-back geometry 2

(d) PS cut-back geometry 3

(e) Hypothetical geometry

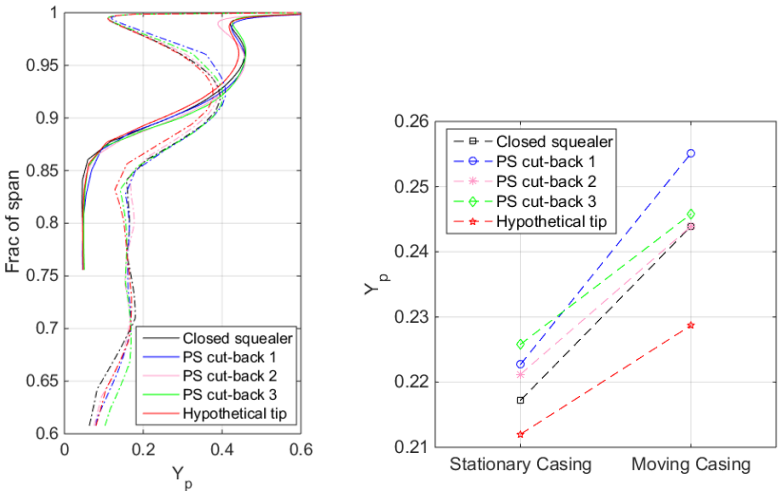
Figure 8.30: Computational total pressure loss coefficient Y_{P0} measured at 1.0% g/S tip gap and 100% C_{ax} downstream plane with casing motion(HYDRA)



(a) Stationary Casing

(b) Moving Casing

Figure 8.31: Mach number streamlines showing source of loss features for the hypothetical tip with a stationary and moving casing (HYDRA)



(a) Pitch-wise averaged **(b) Overall mass averaged Y_{P0} (top 25% of span)**

Figure 8.32: Mass averaged total pressure loss coefficient Y_{P0} at 1.0% g/S tip gap and 100% C_{ax} downstream for the CFD tip geometries with stationary and moving casing (HYDRA). In (a) the solid lines represent a stationary casing and dot-dash lines a moving casing

and towards the blade SS by the casing motion. Towards the LE of the tip, this leakage flow becomes entrained in the passage vortex, emphasising that loss feature. Only the leakage flow towards the TE is seen to wrap up into the OTL vortex, closer to the casing, reducing it's intensity compared to the stationary case, as a smaller proportion of the total OTL flow forms this feature.

Pitch-wise mass-averaged loss coefficient Y_{P0} are presented in Figure 8.32a for the stationary and moving casing. The influence of the reduced OTL vortex, shift away from the casing and enhanced passage vortex are evident. With casing motion, the hypothetical tip geometry is seen to give the smallest OTL vortex, due to the double constriction of the geometry near the TE. There is some change in the overall relative performance of the tips with moving casing (see Figure 8.32). The increased relative loss of the PS cut-back 1 geometry can be ascribed to the large portion of single squealer rim towards the TE, resulting in the largest OTL vortex for that tip (8.32a). This result indicates that with a moving casing, a single squealer constriction is not sufficient to effectively seal the tip gap. The hypothetical tip geometry still produces the lowest losses with a moving casing, mainly due to it's reduced OTL vortex; this shows the benefit the double flow constriction over the rims near the TE.

8.6 Summary and Conclusions

The aerothermal performance of a series of uncooled squealer tip geometries has been numerically investigated with examination of some of the in-depth tip flow physics. Validation of the HYDRA CFD solver to experiment showed good agreement. CFD was used to evaluate the relative performance of the tip designs for a range of tip gaps and with a stationary and moving casing. The main conclusions drawn are summarised as follows:

1. The aerothermal performance is very sensitive to tip geometry. Changes in tip geometry due to deterioration of the design intended geometry would radically alter the OTL flow and resulting aerothermal performance of the tip.

2. The removal of the PS squealer rim towards the TE creates high HTC in the cut-back region and in some cases allows inflow through the downstream cut-back into the tip cavity, altering the upstream heat transfer.

3. Removing the PS rim near the LE (in addition to the TE) radically alters the cavity flow pattern and resulting HTC distribution by removing the adverse pressure gradient in the TE cut-back region.

4. The presence of the squealer cavity at the TE proved beneficial for reduced HTC in the TE region as a result of altered flow behaviour due to the splitting of the TE rims.

5. Development of losses downstream showed a reduction in intensity but an increase in the size of the OTL vortex and a shift away from the casing and blade SS.

6. The removal of the PS rim at the LE resulted in the formation of distinctly separate OTL and upper passage vortices at the 50% C_{ax} downstream plane, but at the 100% exit plane the passage vortex is overwhelmed by the OTL vortex originating from the next blade in the row.

7. The PS rim plays an essential part in sealing of the tip gap at a clearance of 1% g/S; the designs without a PS rim cut-back produced the lowest losses. At reduced tip gap, the PS rim close to the TE is less significant and deterioration of this rim would cause little impact to loss performance. However, loss of the PS rim at the LE would still adversely affect the aero performance of the tip.

8. With increasing tip gap, the tip cavity shows increased HTC but the squealer rims decrease in HTC due to differing flow behaviours. The domination of the tip area by either cavity or rims explains the crossover behaviour in circumferentially averaged HTC observed by previous authors.

9. A reduction in tip clearance reduces overall losses, corroborating previous findings.

10. Addition of casing motion creates the cavity vortex which counter-rotates to the existing cavity recirculation and forces the OTL flow to separate from the casing and impinge on the cavity floor, resulting in enhanced HTC in the mid-cavity.

11. In the majority of designs, casing motion does not alter the flow reattachment and HTC on the PS rim.

12. The tip with PS rim removed at TE and LE responds differently to casing motion that the other designs. Three distinct regions of rotating cavity flow were observed along with an earlier flow reattachment onto the remaining PS rim, which resulted in contrasting changes in HTC.

13. Casing motion causes a split of the OTL and upper passage vortices. The OTL vortex is seen to form from flow over the tip TE, whereas the leakage flow at the LE merges with the upper passage vortex. This strengthens the passage vortex but weakens the OTL vortex. Overall, casing motion increases tip losses.

14. Throughout this chapter the design of the narrow channel at the TE of the hypothetical tip has been beneficial for decreased HTC over the TE and improved loss performance.

Chapter 9

Influence of Tip Cooling CFD Study

9.1 Introduction

Dust holes are primarily used as a means to remove particles from the flow within internal cooling passages, but can be simultaneously used to cool the blade tip. This chapter presents a CFD investigation into film cooling injection using both source term modelling and high fidelity, fully resolved cooling, as described in Section 4.6. The cooled CFD is first compared to experimental results. Following discussion of the CFD validation, the bulk of the cooling study focusses on the effects of altering the cooling hole size, coolant mass flow and hole location of a single dust hole on the aerothermal behaviour and film cooling effectiveness of the tip with an engine-realistic coolant to mainstream temperature ratio (CTR; T_{0c}/T_{01}). The final part of the chapter considers the use of an alternative turbulence model to predict film cooling effectiveness.

9.2 The Cooled CFD Tip Geometry

The tip geometry chosen for this cooling study was the hypothetical tip geometry which was investigated in Chapter 8. This tip showed reduced HTC over the trailing edge and comparable aerodynamic performance when compared to a standard closed squealer tip. Two variations of this tip were used. Due to the necessity to match the geometry

Case	Cavity Depth (mm)	Tip Clearance (g/S)
Exp and CFD validation	2.40	0.65%
Main CFD	3.00	0.50%

Table 9.1: Cooled tip geometry parameters

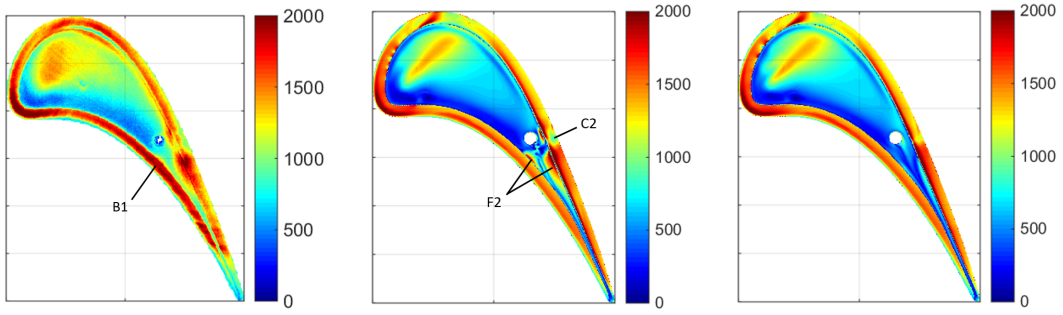
exactly to experiment, the tip model used in the validation study had a smaller cavity depth and was tested at 0.65% g/S tip clearance. For the remainder of the cooling study, the tip model has increased cavity depth and a smaller tip clearance of 0.5% g/S. These differences are summarised in Table 9.1. A single dust hole was added to this tip, as shown in Figure 4.6a. The initial dust hole location and coolant injection direction were determined in an attempt to reduce coolant-OTL interactions which can lead to increased HTC (Ma *et al.* (2017)). As shown in Chapter 8, the OTL flow over the downstream, mid-chord portion of the uncooled tip does not impinge onto the cavity floor. Furthermore, the coolant was injected in the same direction as the movement of the bulk cavity flow, towards the TE.

9.3 Validation of Cooled CFD

For the CFD validation, the single dust hole was fully meshed, with the final mesh containing 8 million cells (see Section 4.6.2). The CAD model used for the meshing of this tip was 3D printed (in epoxy and metal) to enable experimental testing for validation purposes. Testing was completed in the HSLC at 0.65% g/S tip gap for heat transfer coefficients and film effectiveness data and is compared to the fully resolved CFD, which uses the Spalart-Allmaras (SA) turbulence model below.

9.3.1 Heat Transfer

The inlet boundary conditions (uniform inlet) and those for the coolant inlet (temperature and coolant mass flow) match those measured in the HSLC. Figures 9.1a and 9.1b shows the comparison of experimental and computational HTC for the cooled hypothetical tip (Figure 9.1c presents CFD predictions with a more engine-realistic temperature



(a) Experiment (HSLC) **(b) CFD, $T_{cool} = 298K$ (HYDRA)** **(c) CFD, $T_{cool} = 147K$ (HYDRA)**

Figure 9.1: Experimental and computational heat transfer coefficients (W/m^2K) measured on the cooled hypothetical tip geometry at 0.65% g/S

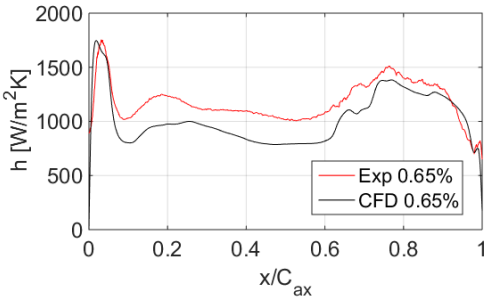


Figure 9.2: Circumferentially averaged heat transfer coefficient (W/m^2K) for the cooled hypothetical tip, both experimental and CFD cases ($T_{cool} = 298K$)

ratio and will be discussed below). Good agreement of the spatial HTC distribution is observed, with the CFD predicting many of the main features: the high HTC on the PS rim; impingement at the LE cavity; the high HTC downstream of the cooling hole (at *F2*) and the reduced HTC on the SS rim (at *C2*), both as a result of coolant-OTL interactions. Such coolant-OTL interactions were discussed in Chapter 5 and will be investigated further in this chapter. There is however, some quantitative disagreement between the experiment and CFD, with the CFD under-predicting the HTC on the PS rim adjacent to the cooling hole (marked *B1*) and on the cavity floor. Comparison to the uncooled hypothetical tip validation in Chapter 8 (Figure 8.2) suggests that this quantitative difference can be attributed to some blockage of the OTL flow by the coolant which the cooled CFD is missing. This discrepancy is more noticeable in Figure 9.2 which shows the circumferentially averaged HTC comparison of the two methods. Towards LE and TE, away from the cooling hole, the experiment and CFD show better

agreement. Despite the differences in quantitative HTC, the CFD using SA turbulence model shows satisfactory performance when predicting HTC on a cooled tip as a result of coolant-OTL interactions, as has been seen previously, for example by Ma *et al.* (2017). This gives some faith in the following CFD investigations regarding tip HTC and the changes to the OTL flow field due to coolant injection presented in this chapter.

9.3.2 Adiabatic Film Cooling Effectiveness

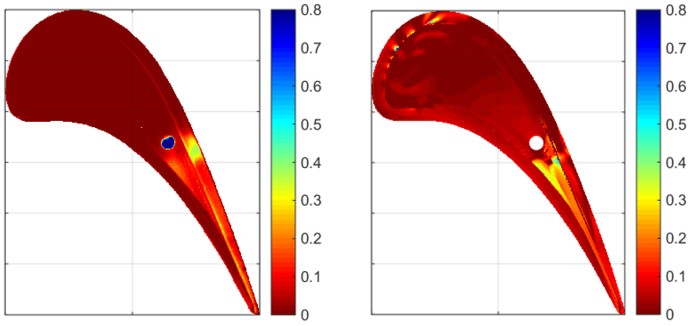
The use of CFD and the SA turbulence model to predict film cooling effectiveness has been shown in the past to produce satisfactory qualitative agreement of the effectiveness distribution compared to experiment on a blade tip, for example Ma *et al.* (2016). However, quantitatively their results showed a large over-prediction of the film effectiveness downstream of the cooling holes.

In the following validation, film cooling effectiveness will be presented for CFD cases using several coolant temperatures. Since the HSLC used ambient temperature coolant, the temperature based CFD method described in Chapter 4 is not really suitable for quantitatively predicting the film cooling effectiveness, as matching to rig conditions gives very similar coolant and mainstream temperatures. However, the case with matched coolant temperature should give the most realistic prediction of the coolant-OTL interactions present in the HSLC. To achieve a more sensible quantitative answer, a temperature difference between the coolant and freestream temperatures must be maintained. It was found that a coolant to mainstream temperature ratio (CTR) of around 0.8 was sufficient. However, lowering the coolant temperature increases the density of the coolant and so the characteristics of the coolant jet and resulting film effectiveness are likely to change, as will be demonstrated below.

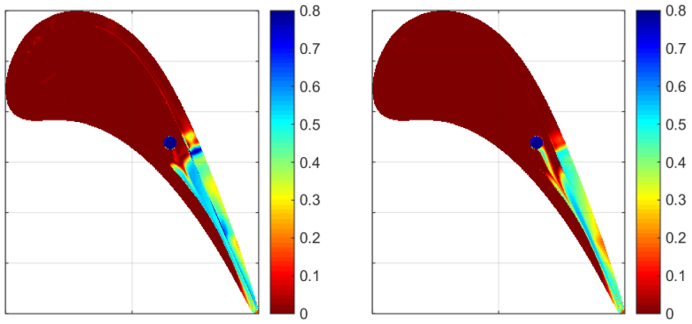
Table 9.2 summarises the coolant parameters measured in the HSLC and for three CFD cases which matched the coolant mass flow present in the HSLC but with differing coolant temperatures. It should be noted that the parameters for the HSLC are measured inside the coolant plenum, whereas the CFD parameters are evaluated at the

	$\dot{m}$ (g/s)	BR	T_{cool} (K)	CTR	ρ_{cool} (kgm^{-3})	ρ_{rat}	U_{cool} (ms^{-1})
Exp[1]	1.46	1.21	298.2	1.01	2.60	1.083	114.1
CFD 1	1.45	1.21	298.9	1.02	1.94	0.808	152.8
CFD 2	1.47	1.23	243.2	0.84	2.35	0.967	128.4
CFD 3	1.43	1.20	147.1	0.51	3.81	1.568	77.4

Table 9.2: Coolant parameters for experimental and CFD validation cases



(a) Experiment (HSLC) **(b) CFD 1, $T_{cool} = 298K$ (HYDRA)**



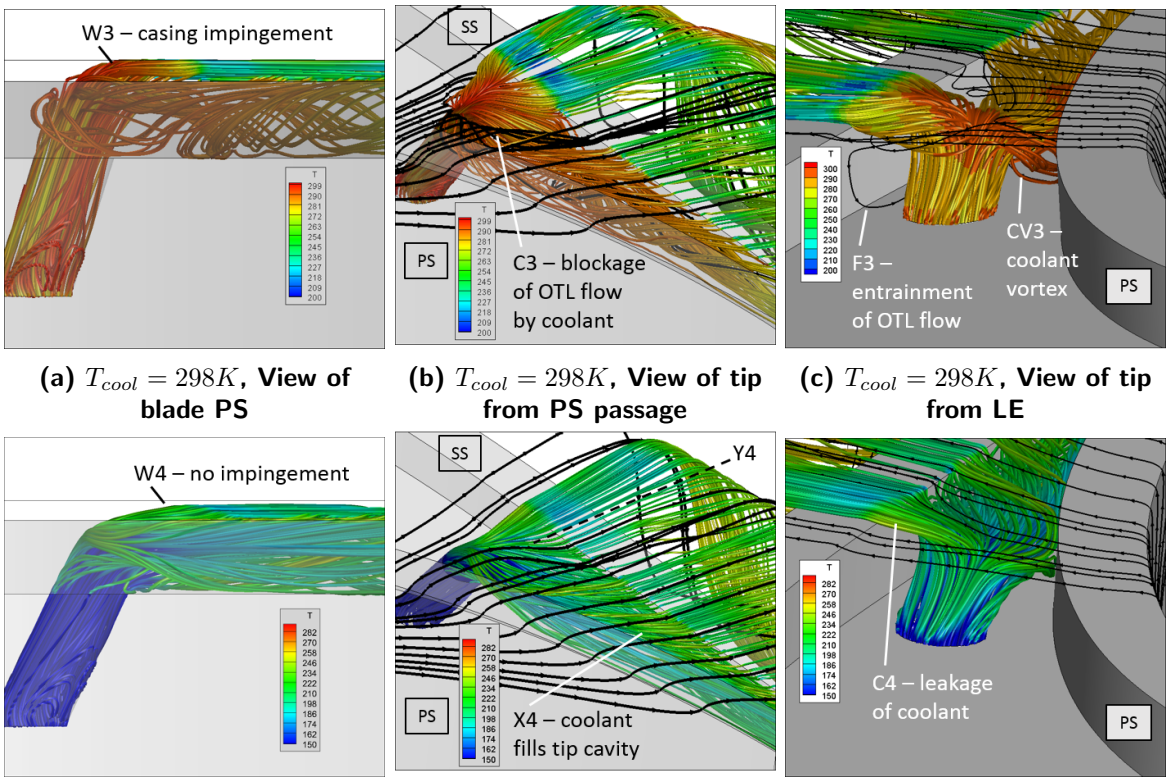
(c) CFD 2, $T_{cool} = 240K$ (HYDRA) **(d) CFD 3, $T_{cool} = 147K$ (HYDRA)**

Figure 9.3: Experimental and computational film cooling effectiveness measured on the cooled hypothetical tip geometry at 0.65% g/S

cooling hole exit. Pressure loss within the cooling hole would drive the coolant density down and by conservation of mass, the coolant velocity would increase compared to the quoted values for the experimental case in Table 9.2

The film effectiveness for the cases is shown in Figure 9.3. It can be seen that the CFD case using HSLC matched coolant temperature (Figure 9.3b) shows the most similar film effectiveness distribution, however little can be gained from the quantitative comparison, partly due to the very small coolant to mainstream temperature ratio and secondly because the 'coolant' temperature is higher than inlet. Comparing to the other

[1]Experimental parameters measured in coolant plenum; CFD parameters measured at hole exit



(a) $T_{cool} = 298K$**, View of blade PS** **(b)** $T_{cool} = 298K$**, View of tip from PS passage** **(c)** $T_{cool} = 298K$**, View of tip from LE**

(d) $T_{cool} = 147K$**, View of blade PS** **(e)** $T_{cool} = 147K$**, View of tip from PS passage** **(f)** $T_{cool} = 147K$**, View of tip from LE**

Figure 9.4: Predicted coolant-OTL interactions for the hypothetical tip at low coolant temperature (147K) and experimental coolant temperature (298K) (HYDRA)

CFD cases, using lower coolant temperature, there is a small qualitative difference seen to CFD case 2 (CTR = 0.8) and a much larger difference to CFD case 3, which uses a more engine-realistic CTR of 0.5. In this low temperature case, a distinct trail of higher effectiveness can be seen emanating from the coolant hole, indicating the presence of an attached film. For both case 2 and case 3, the film effectiveness levels are significantly in excess of the experimental results, either indicating that the film is far better attached when the coolant density is higher (and velocity lower) or that the CFD over-predicts the film cooling effectiveness.

To examine the coolant-OTL interactions responsible for the film effectiveness distributions in Figure 9.3, flow streamlines of the two extremes in coolant temperature are presented in Figure 9.4. From Figures 9.4d - 9.4f it is observed that with an engine-realistic temperature ratio, when the coolant temperature is low and therefore density is high, the coolant does not reach the casing (at *W4*). The coolant emerges from the

dust hole at low speed (see Table 9.2) and fills the tip cavity (at *X4*), with a small proportion leaking directly over the SS rim adjacent to the cooling hole (at *C4*). There is a small disturbance of the OTL flow, which is diverted around the path of coolant over the SS rim (marked *Y4*), with no observed OTL flow being entrained into the cavity. However, Figures 9.4a - 9.4c show that at rig conditions the higher velocity injected coolant penetrates the OTL flow and impinges on the casing (at *W3*), where it splits into several distinct flow paths, with the creation of vortices within the coolant flow (at *CV3*). A portion of the coolant flow leaks over the SS rim and the path of the OTL flow across the tip is completely blocked (at *C3*), being diverted either side of the coolant flow. This behaviour creates the pattern of low and high HTC observed on the SS rim in Figure 9.1b (marked *C2*). In Figure 9.4c it is also observed that some of the OTL flow is entrained into the cavity (at *F3*), where it forms a series of cavity vortices which impinge on the cavity floor adjacent to the SS and PS rims. These newly formed vortices were not present in the uncooled case presented in the previous chapter (see Figure 8.27c) and are the cause of the increased HTC on the cavity floor around the cooling hole observed in Figure 9.1a and 9.1b. In contrast, Figure 9.1c shows that with lower coolant temperature, the lack of coolant-OTL interactions around the cooling hole produce little in the way of increased cavity HTC, however the reduced HTC on the SS rim is still present due to the slight blockage of the OTL flow.

Overall, the CFD has shown fair qualitative agreement to experiment and is capable of predicting differences in coolant-OTL interactions, stemming from differing coolant temperatures, which may occur when comparing experiment to a case using an engine realistic temperature ratio. Quantitatively, the data indicate that the CFD still over-predicts the film effectiveness, however an exact match to experiment was not possible due to the ambient temperature coolant used in the HSLC.

CPR	Coolant $\dot{m}$ (g/s)	BR
0.8	0.12	0.76
0.9	0.20	1.24
1.0	0.25	1.56
1.1	0.29	1.83
1.8	0.52	3.29

Table 9.3: Coolant parameters for CFD cases at a range of pressure ratios with a 0.9 mm diameter dust hole, measured at hole exit

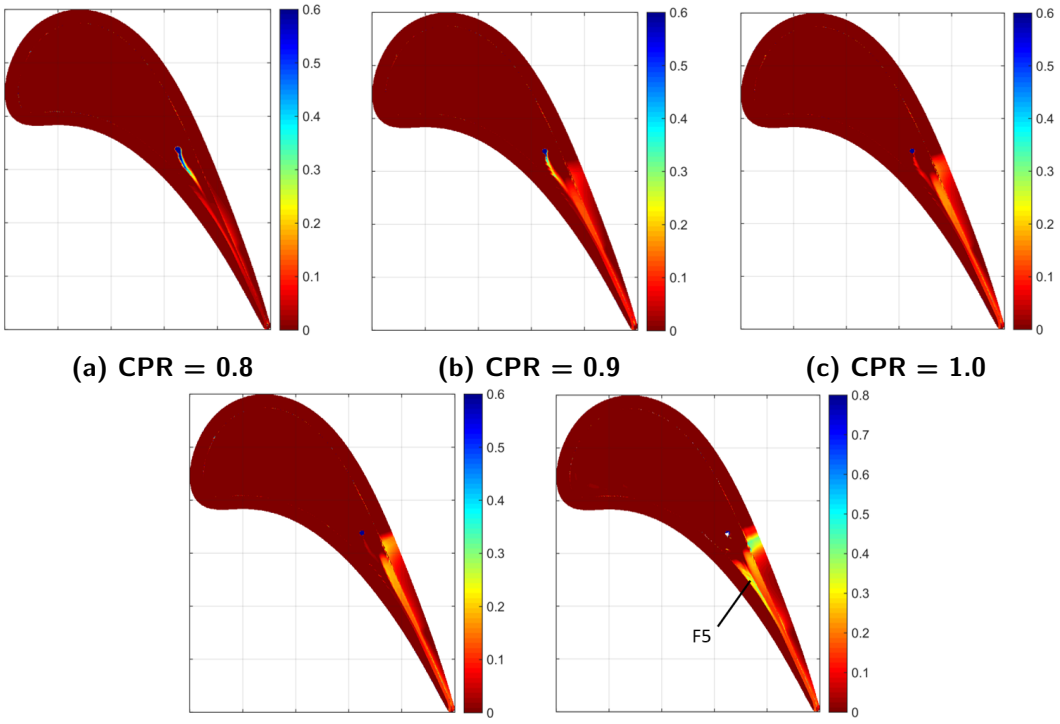
9.4 Coolant Mass Flow

This section investigates the effects of altering the coolant mass flow on the film effectiveness, by means of adjusting the coolant to mainstream pressure ratio (CPR; P_{0c}/P_{01}), for a dust hole of 0.9 mm in diameter. This dust hole size is typical for the scaled up rig geometry. The CTR is set to approximately 0.5, to be representative of the real engine case.

9.4.1 Film Cooling Effectiveness

Figure 9.5 presents the film cooling effectiveness for a range of CPR from 0.8 to 1.1 and a higher mass flow case with CPR 1.8. The coolant mass flows and BR for each these cases is given in Table 9.3. It is observed in Figure 9.5 that as the coolant mass flow increases, from a CPR of 0.8 - 1.1, the film effectiveness reduces immediately downstream of the coolant hole, as the BR has increased and lift-off occurs. Further downstream of the dust hole, increasing coolant mass flow increases the film effectiveness on the cavity and rims at the trailing edge. The film effectiveness on the SS rim, adjacent to the cooling hole also increases, indicating that more coolant is leaking directly over the SS rim.

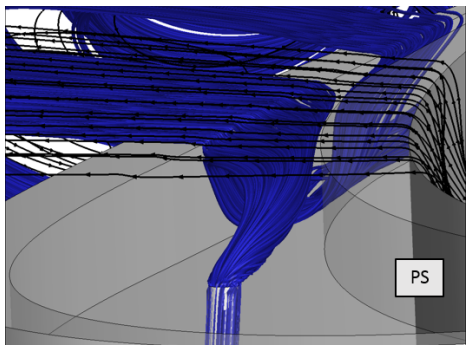
Increasing the CPR to 1.8 further enhances the film effectiveness, however the distribution also changes, with a new patch of higher film effectiveness adjacent to the PS rim (at *F5*). The cause of this can be attributed to a change in behaviour of the coolant jet and is observed in Figure 9.6. At low mass flow, the CFD predicts that the coolant remains as a jet (see Figures 9.6a and 9.6b). This jet does not penetrate through



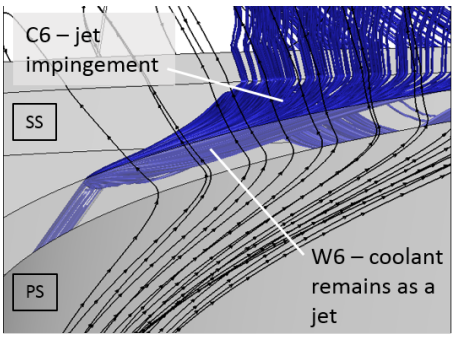
(a) CPR = 0.8 (b) CPR = 0.9 (c) CPR = 1.0

(d) CPR = 1.1 (e) CPR = 1.8

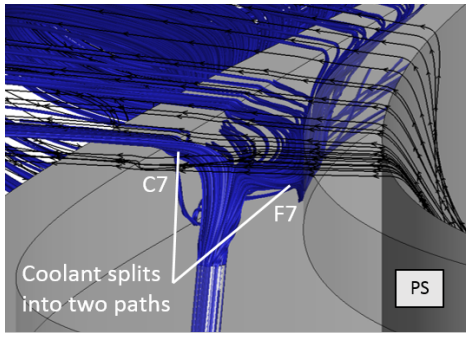
Figure 9.5: Predicted η on the cooled hypothetical tip geometry for a range of coolant to mainstream pressure ratios at 0.5% g/S tip gap. Dust hole size = 0.9 mm, CTR = 0.5 (HYDRA)



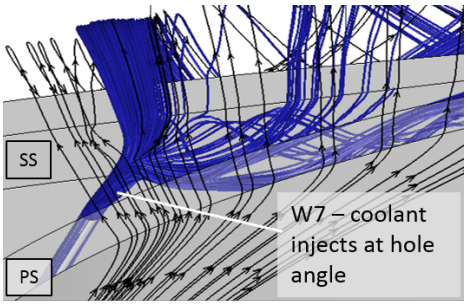
(a) 0.9 mm hole, CPR 0.9, View of tip from LE



(b) 0.9 mm hole, CPR 0.9, View of tip from PS passage



(c) 0.9 mm hole, CPR 1.8, View of tip from LE



(d) 0.9 mm hole, CPR 1.8, View of tip from PS passage

Figure 9.6: Streamlines of coolant and OTL flow for 0.9 mm cooling hole diameter and two CPRs. CTR = 0.5 (HYDRA)

the OTL flow to the casing, instead proceeding downstream under the influence of the cavity flow where it impinges on the inside vertical wall of the SS rim (at *C6*) before leaking over rim. The coolant remains in a defined jet until it reaches the TE of the tip. However, at high mass flow, the coolant jet injects directly at the coolant hole angle. Figures 9.6c and 9.6d predict that interaction of the coolant and OTL flow splits the coolant jet into two defined paths; one which leaks over the SS rim as before (at *C7*), and the other which migrates towards the PS rim (at *F7*), causing the new area of high film effectiveness in Figure 9.5e at *F5*. Note that this injected coolant does not impinge directly on the casing, but remains below the OTL flow path until it leaks over the SS rim. It is therefore not impingement on the casing which causes the split of the coolant jet in this case (as was seen by Ma *et al.* (2017)), but interaction of the coolant jet and OTL flow.

9.5 Cooling Hole Size

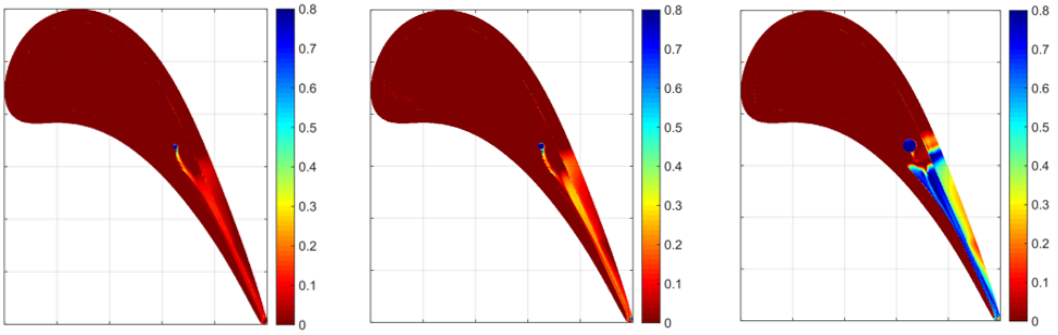
This section investigates the effects of altering the cooling hole diameter, using both the fully resolved and source term cooling methods described in Chapter 4. Again the CTR is set to 0.5 and CPR = 0.9 throughout. Although the same CPR and coolant temperature was set at the cooling hole inlet, greater pressure loss and heat pick-up occurs in the smaller diameter holes, meaning that the injected coolant jet is of a lower density and higher velocity than that of the largest dust hole. The coolant conditions at the hole exit are shown in Table 9.4. The constant CPR gives an almost constant BR of the coolant, but increased coolant mass flow with larger hole diameter.

9.5.1 Film Cooling Effectiveness and Coolant-OTL Flow Interactions

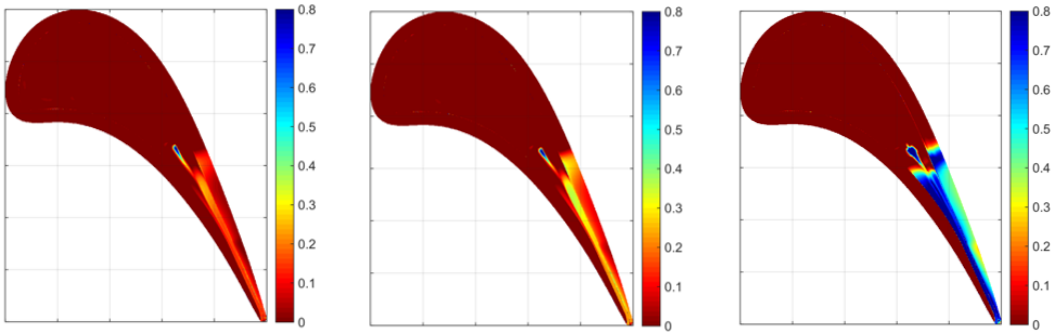
Film cooling effectiveness is presented for the range of cooling hole sizes in Figure 9.7. For the source term cooling approach, the coolant mass flow and density was matched to

Hole Diameter (mm)	Coolant $\dot{m}$ (kg/s)	Coolant $\dot{m}_c/\dot{m}_\infty$	Velocity (m/s)	Density (kg/m^3)	BR
0.9	1.96×10^{-4}	0.0245	107.0	2.9	1.26
1.2	3.54×10^{-4}	0.04425	104.4	3.0	1.28
2.5	1.46×10^{-3}	0.1825	89.4	3.3	1.21

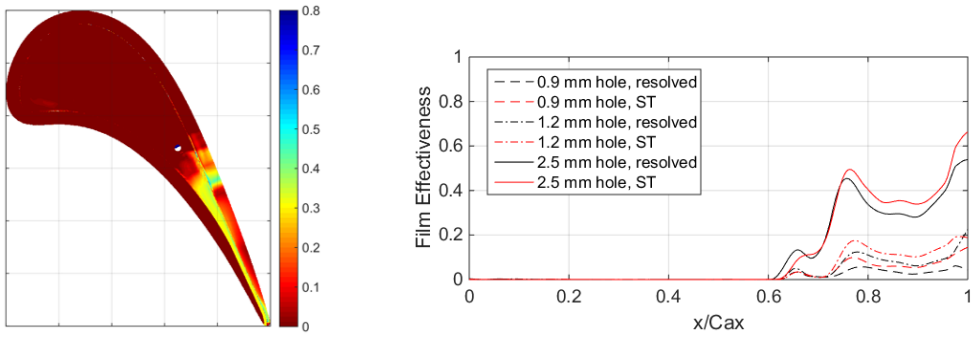
Table 9.4: Coolant parameters for CFD cases at a range of cooling hole diameters, measured at hole exit



(a) 0.9 mm hole, fully resolved **(b) 1.2 mm hole, fully resolved** **(c) 2.5 mm hole, fully resolved**



(d) 0.9 mm hole, source term **(e) 1.2 mm hole, source term** **(f) 2.5 mm hole, source term**



(g) 1.2 mm hole, CPR = 2.25 **(h) Circumferentially averaged film cooling effectiveness**

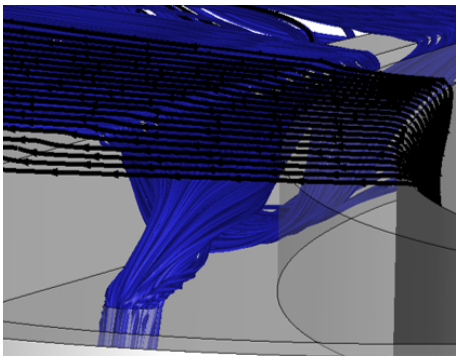
Figure 9.7: Predicted film cooling effectiveness on the cooled hypothetical tip geometry for a range of coolant hole diameters at constant CPR and 0.5% g/S tip gap (HYDRA)

the evaluated parameters at hole exit of the fully resolved case. It is observed that as the hole area increases, the film cooling effectiveness over the tip trailing edge is enhanced. In part, this increase is simply due to the increased coolant mass flow allowed by the larger cooing hole, which was seen in the previous section to increase film effectiveness. However, the film effectiveness distribution is also affected by the coolant hole size. The source term method is shown to accurately predict the film effectiveness distribution, but quantitatively a slight over-prediction is observed in Figure 9.7h.

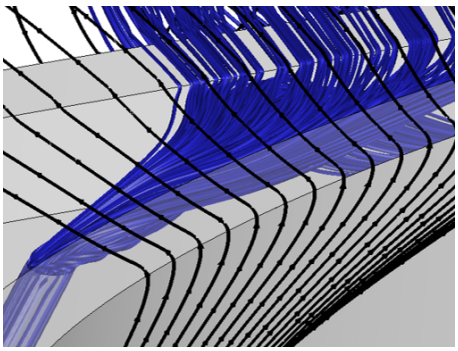
Streamlines of the coolant flow are shown in Figure 9.8 for the 1.2 mm and 2.5 mm hole sizes. The coolant injected from the 1.2 mm hole (see Figures 9.8a and 9.8b) behaves almost identically to that from the 0.9 mm hole (at $CPR = 0.9$) presented in the previous section (see Figures 9.6a and 9.6b). However, when the coolant hole is larger (Figures 9.8c and 9.8d), a higher allowable mass flow of coolant can be injected at the same CPR and the coolant flow pattern is very similar to that seen previously in the low temperature coolant case in Figure 9.4 and the higher mass flow case with 0.9 mm hole diameter (see Figures 9.6c and 9.6d).

Considering the difference between the two predicted coolant flow patterns for the 1.2 mm and 2.5 mm hole diameters, the higher level of cooling effectiveness produced by the larger hole can be ascribed to two factors: firstly, the higher allowable coolant mass flow which fills the downstream tip cavity (at $X8$); secondly, the streamlines indicate a higher level of mixing of the coolant jet when the cooling hole is large, whereby the jet quickly diffuses into a mass of coolant rather than a defined narrow jet, providing wider coverage of the coolant film.

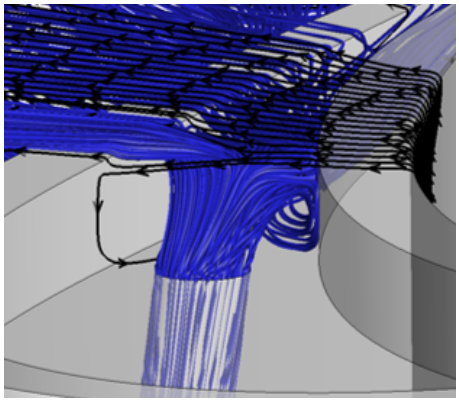
Since the total coolant mass flow rate constraints are critical in a real engine it is prudent to investigate whether the increase in film effectiveness seen at larger hole diameter is simply due to increased allowable coolant mass flow. To achieve this, the mass flow of coolant from the 1.2 mm diameter hole was increased. However, it is pointed out that since the dust hole area limits the coolant mass flow at a given CPR, the CPR required at the coolant hole inlet (CPR = 2.25) for the example case became



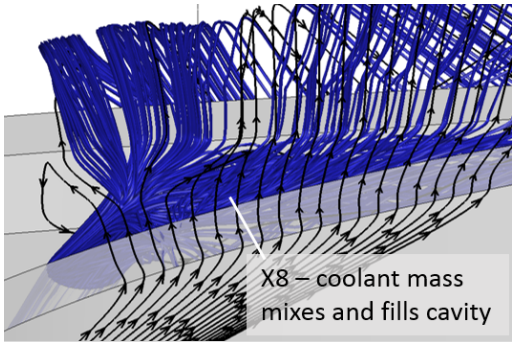
(a) 1.2 mm hole, View of tip from LE



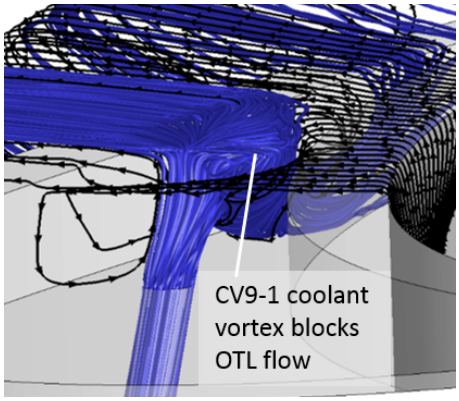
(b) 1.2 mm hole, View of tip from PS passage



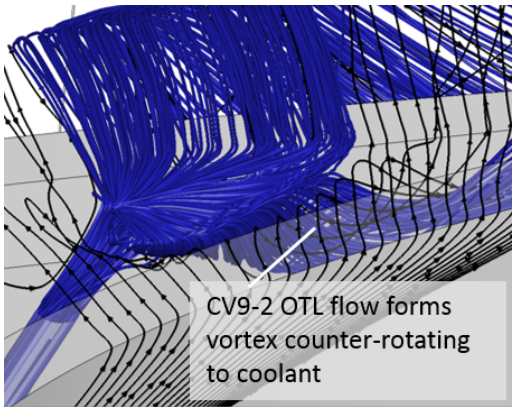
(c) 2.5 mm hole, View of tip from LE



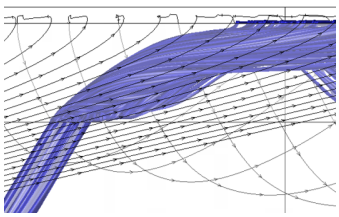
(d) 2.5 mm hole, View of tip from PS passage



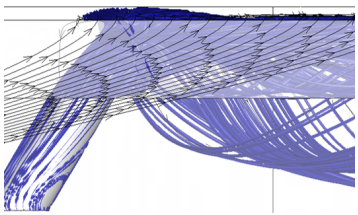
(e) 1.2 mm hole, CPR = 2.25, View of tip from LE



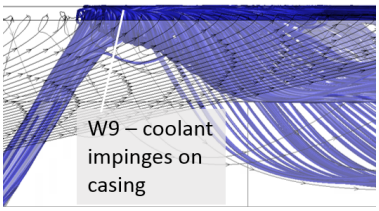
(f) 1.2 mm hole, CPR = 2.25, View of tip from PS passage



(g) 1.2 mm hole, View of blade PS



(h) 2.5 mm hole, View of blade PS



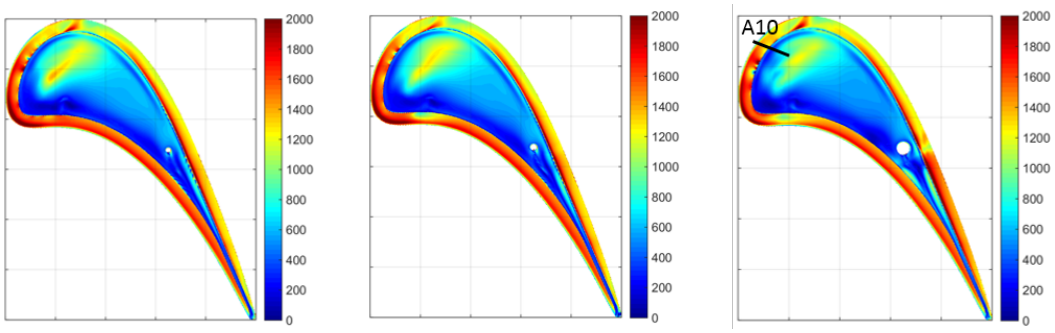
(i) 1.2 mm hole, CPR = 2.25, View of blade PS

Figure 9.8: Streamlines of coolant and OTL flow for 1.2mm and 2.5mm cooling hole sizes (HYDRA)

unrealistically high and would not be used in a real engine. The resultant coolant mass flow ratio ($\dot{m}_c/\dot{m}_\infty$) at this CPR from a 1.2 mm dust hole was 0.146, which was slightly lower than that ejected from the 2.5 mm hole earlier in this section.

The film cooling effectiveness for the high CPR case is shown in Figure 9.7g. It is observed that the increased coolant mass flow has reduced the effectiveness close to the hole but increased it downstream, as seen in Section 9.4.1. However, the levels of effectiveness remain well below those seen for the larger cooling hole size, indicating the benefit of increased dust hole area. The effectiveness distribution has also changed, which is examined by flow streamlines in Figures 9.8e - 9.8i. At higher CPR, the blowing ratio of the coolant has increased and the coolant jet impinges directly on the casing (at *W9*). The impinging coolant rolls up into a large vortex which takes up most of the tip cavity and blocks the passage of the OTL flow (marked *CV9-1*). The coolant vortex directs the OTL flow beneath this vortex, away from the casing. Further downstream, adjacent to the PS rim and coolant mass, the diverted OTL flow rolls up into a counter-rotating vortex, as shown at *CV9-2* in Figure 9.8f. There is evidence in Figures 9.8b and 9.8f that the coolant from the 1.2 mm hole stays as a jet, even when the coolant mass flow is increased, which tends to produce less coverage of the film compared to the larger hole case.

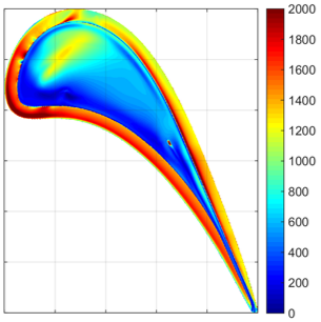
It is clear that the injection of coolant can alter the OTL flow, if the coolant mass flow is high enough and the jet penetrates the OTL flow. Even more radical is the influence of the coolant if the jet impacts on the casing, whereby vortical flow structures are produced similar to those reported by Ma *et al.* (2017). From a film effectiveness perspective the findings indicate that the larger hole size is beneficial for cooling, as it allows a larger mass flow of coolant to be injected at a realistic CPR, which fills the downstream cavity with coolant. The resultant heat transfer coefficients and overall effect of the cooling strategies will be inspected in the next section.



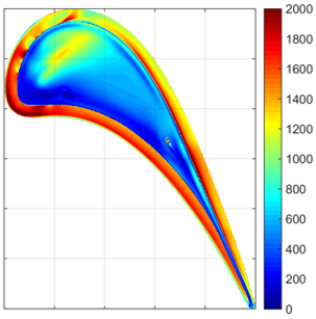
(a) 0.9 mm hole, fully resolved

(b) 1.2 mm hole, fully resolved

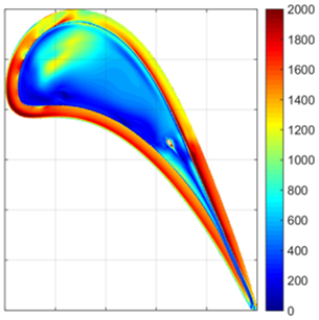
(c) 2.5 mm hole, fully resolved



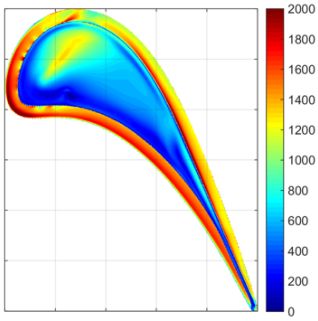
(d) 0.9 mm hole, source term



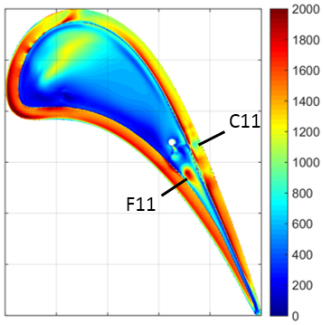
(e) 1.2 mm hole, source term



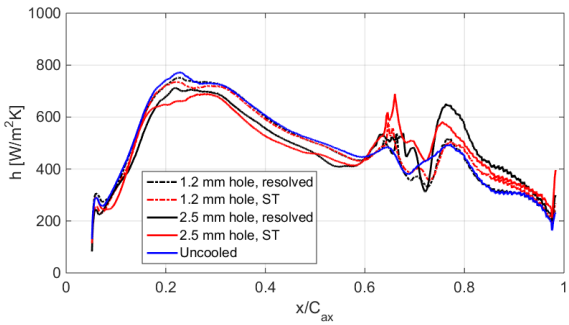
(f) 2.5 mm hole, source term



(g) Uncooled

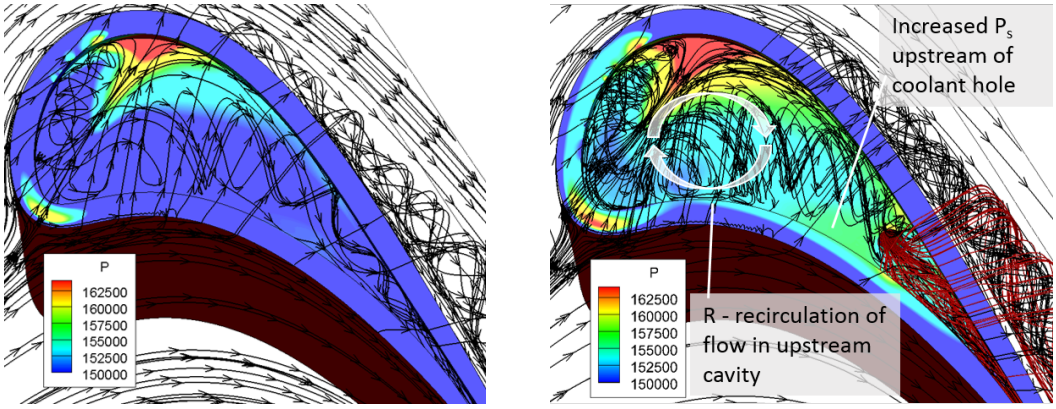


(h) 1.2 mm hole, CPR 2.25



(i) Circumferentially averaged HTC on the tip cavity floor

Figure 9.9: Predicted HTC $[W/m^2K]$ on the cooled hypothetical tip geometry for a range of coolant hole diameters at constant CPR, CTR = 0.5 and 0.5% g/S tip gap (HYDRA)



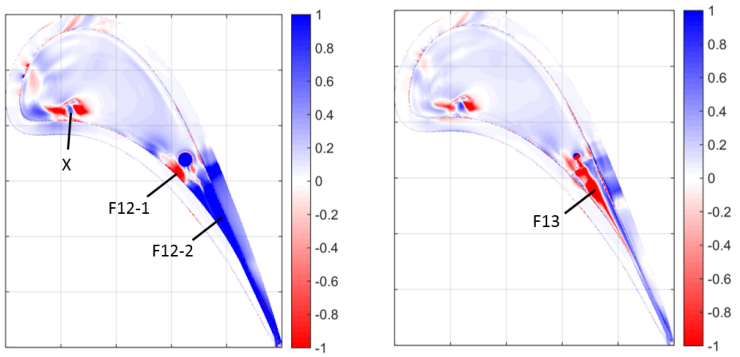
(a) Uncooled tip **(b) Cooled tip, 2.5 mm dust hole**

Figure 9.10: Streamlines of uncooled and cooled tip with 2.5 mm dust hole diameter, contours of tip surface static pressure (HYDRA)

9.5.2 Heat Transfer Coefficient

Heat transfer coefficients for the three cooling hole sizes are presented in Figure 9.9, along with the HTC for the uncooled tip. It is observed that, compared to the uncooled case in Figure 9.9g, the addition of coolant from the 0.9 mm hole does not appear to the change the tip HTC. There is still limited change observed in the 1.2 mm hole case, which is highlighted in the circumferentially averaged plot in Figure 9.9i. However, the 2.5 mm hole case shows more significant change. The HTC downstream of the cooling hole increases slightly, due to impingement of the coolant mass onto the cavity floor (but no entrainment of the OTL flow). More notable is the decrease in HTC upstream of the coolant hole in an area unaffected by the coolant film (see region *A10* in Figure 9.7c), which was also reported by Ma *et al.* (2017). This decrease (of approximately 5%) can be attributed to aerodynamic changes due to the influence of the injected coolant which will be investigated further.

Figure 9.10 shows flow streamlines for the uncooled and cooled hypothetical tip (cooled case with the 2.5 mm hole diameter). It is observed that the injection of coolant downstream increases the tip surface static pressure in the vicinity of and upstream of the cooling hole. The influence of the downstream coolant can be seen to promote recirculation of flow in the upstream cavity (marked *R*), which slightly blocks impingement of the flow onto the cavity floor from over the PS rim. This blockage reduces the



(a) Cooled tip, 2.5 mm dust hole **(b) Cooled tip, 1.2 mm dust hole at CPR 2.25**

Figure 9.11: Net Heat Flux Reduction for cooled cases with a 2.5 mm dust hole and a 1.2 mm dust hole at increased mass flow (HYDRA)

impingement HTC compared to the uncooled tip, as seen by comparison of Figures 9.9c and 9.9g.

The HTC distribution is shown in Figure 9.9h for the 1.2 mm hole with higher CPR from the previous section. The influence of the additional coolant mass flow has several effects: a reduction of the upstream HTC at the LE cavity impingement region, compared to the lower mass flow case in Figure 9.9b; a reduction in HTC on the SS rim adjacent to the cooling hole (*C11*). Both of these findings are similar to those seen for the 2.5mm hole case in Figure 9.9c. Downstream of the coolant hole there is a new region of high HTC (*F11*), either due to impingement of the OTL flow which is driven beneath the coolant jet, or from impingement of the coolant jet itself. Evaluation of the Net Heat Flux Reduction (NHFR, as defined in Chapter 5) allows the source of this high HTC to be determined.

Figure 9.11 shows the NHFR for the 2.5 mm dust hole case and the 1.2 mm hole case at $CPR = 2.25$, corresponding to Figures 9.9c and 9.9h respectively. Both figures show a slight reduction in heat flux upstream of the cooling hole due to the influence of the injected coolant. Note that close to the PS rim at the LE (marked X), a region of high heat flux appears to be caused by a patch of instability in the CFD solution, which had no significant impact on the earlier results. Around the cooling hole, it can be seen that the 2.5 mm dust hole (Figure 9.11a) produces an area of heat flux increase

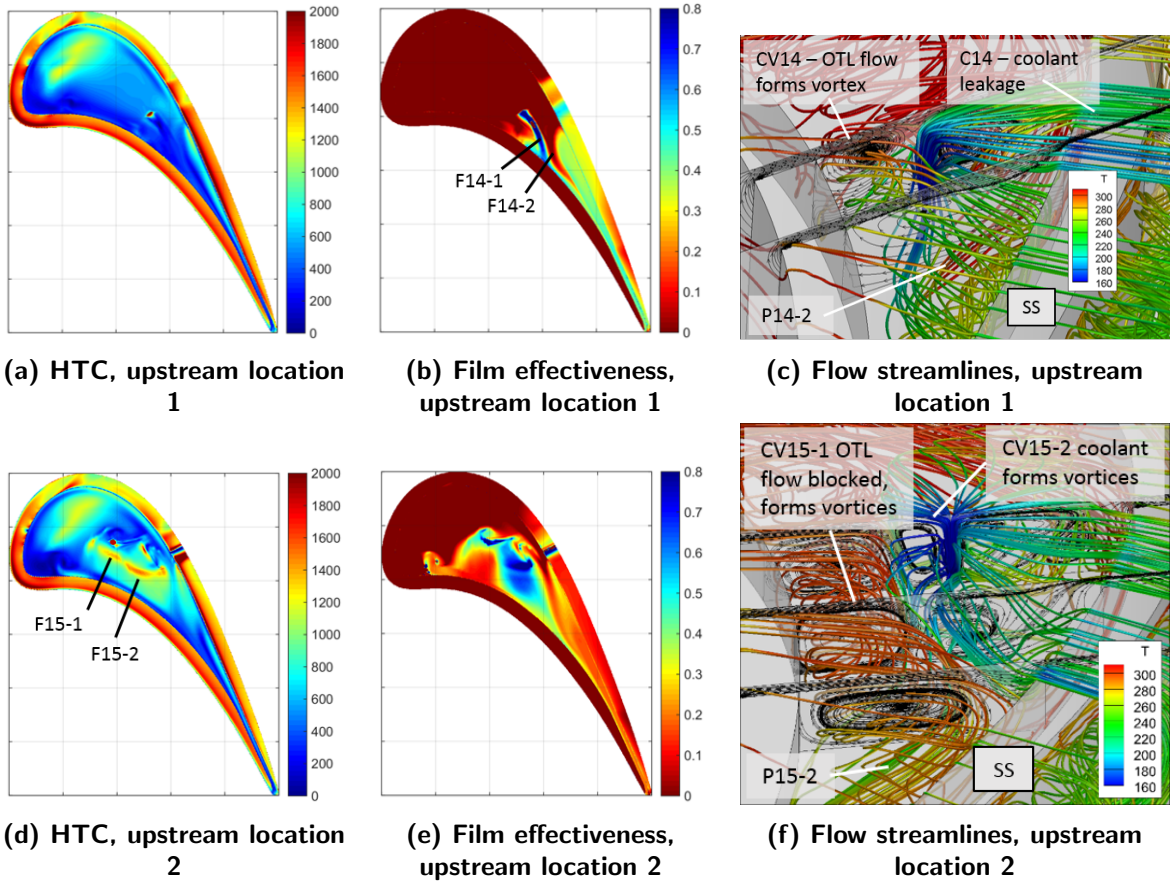
adjacent to the PS rim (marked *F12-1*) which is caused by an increase in HTC and can be ascribed to the interactions between the coolant and cavity flow, as the cavity flow is forced around the coolant mass. Further downstream from the cooling hole, in region *F12-2*, a reduction in heat flux is observed coinciding with the region of high film effectiveness in Figure 9.7c; this reduction is slightly lessened on the SS rim where the effectiveness is lower. Comparison of Figures 9.11a and 9.11b shows that when the cooling hole is smaller, the strong interactions between the coolant jet and OTL flow cause an increase in heat flux downstream of the cooling hole at *F13*. Thus the increase in HTC downstream of the dust hole (at *F11*) noted in Figure 9.9h is caused by an impingement of the hot OTL flow which was forced towards the cavity floor by the vortical nature of the coolant jet.

9.6 Cooling Hole Location

This section examines the effect of altering the location of a 2.5 mm dust hole, implemented by both fully resolved and source term cooling. The starting point for the dust hole was the downstream location presented earlier in this chapter. The dust hole was traversed upstream by small increments until the interactions of the coolant and OTL flow changed dramatically; the coolant was modelled via source terms to save on meshing time. The coolant hole was then moved to a location near to the LE and simulated using both fully resolved and source term methods. Heat transfer coefficients and film effectiveness are presented, along with flow streamlines showing the relevant coolant - OTL interactions.

9.6.1 Heat Transfer and Film Cooling Effectiveness

Figure 9.12 presents the HTC, film effectiveness and flow streamlines for two cases in which the dust hole has be shifted upstream compared to the original starting position. The source term cooling method was used to apply the coolant film in both cases. The



(a) HTC, upstream location 1 **(b) Film effectiveness, upstream location 1** **(c) Flow streamlines, upstream location 1**

(d) HTC, upstream location 2 **(e) Film effectiveness, upstream location 2** **(f) Flow streamlines, upstream location 2**

Figure 9.12: Predicted HTC [W/m^2K] , film effectiveness and flow streamlines (coloured by temperature) on the cooled hypothetical tip geometry with various upstream dust hole locations at $\dot{m}_{cool} = 1.46 \times 10^{-3} kg/s$ and CTR = 0.5. Source term cooled (HYDRA)

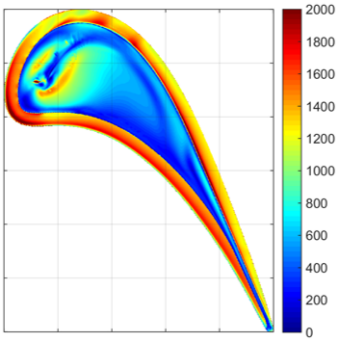
dust hole at upstream location 1 (see Figures 9.12a - 9.12c) has caused little impact on the tip HTC compared to the original dust hole location in Figure 9.9f, other than the removal of the strip of slightly higher HTC adjacent to the PS rim and a reduction in the band of lower HTC on the SS rim, corresponding to the movement of the dust hole. In contrast, there has been a much larger change in film effectiveness, observed by comparison of Figures 9.12b and 9.7f. Moving the dust hole upstream has reduced the film effectiveness downstream of the coolant hole. The narrow band of high effectiveness (marked *F14-1*) emanating from the dust hole indicates that some of the coolant remains attached, however, it is observed in Figure 9.12c that a large proportion impacts on the casing and leaks directly over the SS rim (at *C14*). Adjacent to the SS rim, it is also seen in Figure 9.12c that some of the cavity flow passes beneath the coolant path (marked *P14-2*), creating the region of zero effectiveness between the coolant hole and SS rim at

F14-2 in Figure 9.12b. Figure 9.12c also shows that a vortex is predicted to form close to the casing (at *CV14*) as the OTL flow over the PS rim is blocked by the coolant jet.

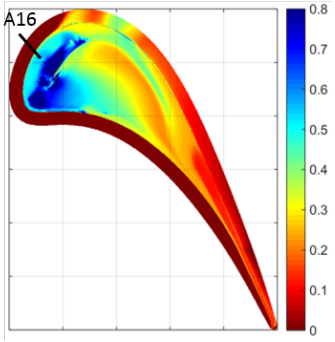
Moving the dust hole further upstream, to a location in the centre of the cavity, radically changes the OTL flow pattern and cavity flow, as can be observed via the flow streamlines in Figure 9.12f. Again the coolant impinges directly on the casing, but this time splits in all directions, rolling up into vortical structures (marked *CV15-2*). These vortices block the OTL flow over a large portion of the mid-chord of the tip and direct the flow towards the cavity floor where it rolls up into a counter-rotating vortex (at *CV15-1*). Adjacent to the cooling injection point, where the blockage effect is stronger, the counter-rotating cavity vortex impinges on the cavity floor, creating the area of increased HTC observed at *F15-1* in Figure 9.12d. Further downstream, the blockage is predicted to be weaker and the cavity vortex takes up a majority of the cavity width. In this region, Figure 9.12e predicts good film coverage and it is seen in Figure 9.12f that the coolant passes beneath the cavity vortex. This indicates that the increased HTC in this region (at *F15-2* in Figure 9.12d) is caused by impingement of the coolant vortex, not the cavity vortex, so would result in a reduction in tip heat flux.

The dust hole is now moved to a location near to the LE of the tip. Figures 9.13a - 9.13c relate to case with source terms used to model the coolant, whereas Figures 9.13d - 9.13f show the result for the fully resolved method. It is worth noting that at the LE a lower CPR is required to produce the same coolant mass flow as from the downstream cooling hole (original location). Comparison of the HTC plots for both cooling methods show good agreement, with the source term method predicting slightly higher HTC around the cooling hole. The predicted film effectiveness (see Figures 9.13b and 9.13h) also shows reasonable agreement, both qualitatively and quantitatively, apart from directly around the dust hole and towards the LE rim.

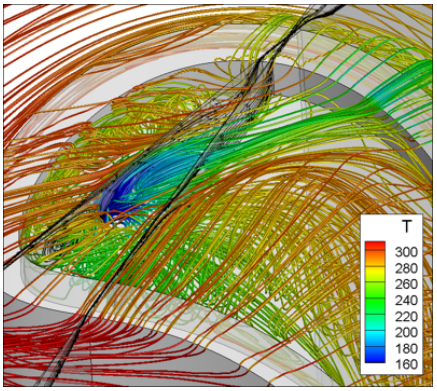
By comparison of the flow streamlines in Figures 9.13c and 9.13f it is observed that the coolant jets predicted by the source term and fully resolved methods have a very similar flow pattern and both jets leak over the SS rim at a similar location. The



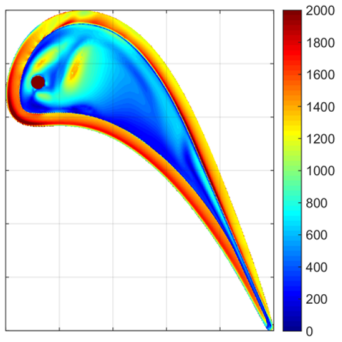
(a) HTC, LE location, source term



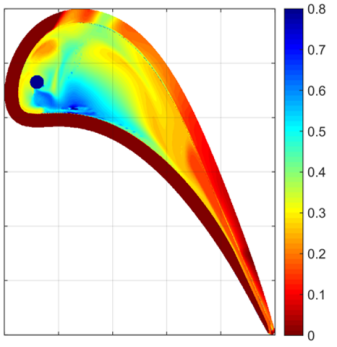
(b) Film effectiveness, LE location, source term



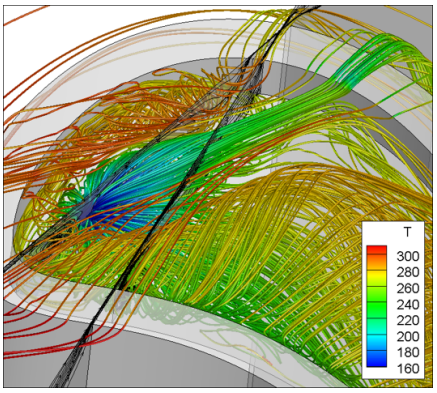
(c) Flow streamlines, LE location, source term



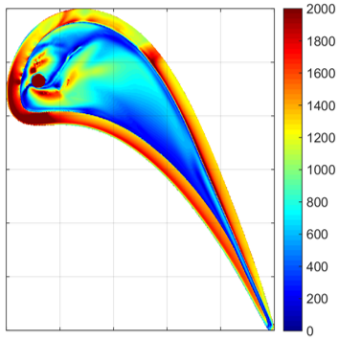
(d) HTC, LE location, fully resolved



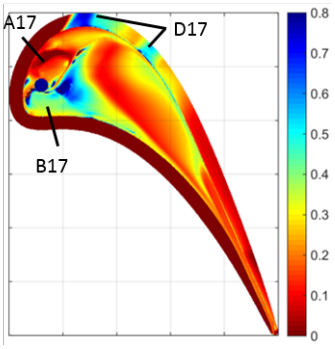
(e) Film effectiveness, LE location, fully resolved



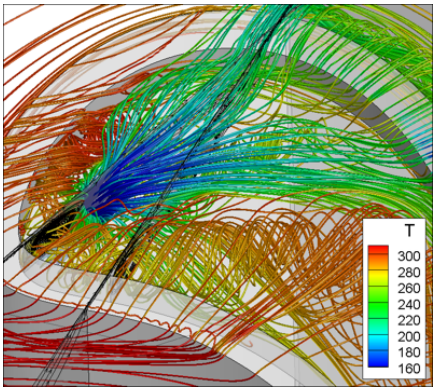
(f) Flow streamlines, LE location, fully resolved



(g) HTC, LE location, fully resolved, high coolant $\dot{m}$



(h) Film effectiveness, LE location, fully resolved, high coolant $\dot{m}$



(i) Flow streamlines, LE location, fully resolved, high coolant $\dot{m}$

Figure 9.13: Predicted HTC [W/m^2K], film effectiveness and flow streamlines (coloured by temperature) on the cooled hypothetical tip geometry with a LE dust hole, source term and fully resolved methods (HYDRA)

difference in film effectiveness between the two methods arises from an accumulation of coolant inside the LE rim predicted by the source term method and indicates the presence of a better attached film immediately downstream of the coolant hole (seen at *A16* in Figure 9.13b). The fully resolved method however predicts lift-off and the OTL flow to dominate the inside of the LE rim, mixing with the coolant and dispersing it. This difference in behaviour of the coolant jets can be ascribed to the differing ways in which the coolant is injected and how that coolant interacts with the OTL flow when the coolant jet is modelled by source terms compared to when the coolant hole is fully meshed and resolved. However, given the rudimentary nature of the source term approach, the method is considered to perform well.

Increasing the coolant mass flow drastically alters the coolant flow pattern. The fully resolved method (see Figures 9.13g - 9.13i) predicts that the coolant spreads out over the LE portion of the cavity, towards the SS rim. This produces higher film effectiveness over a wider portion of the SS rim (at *D17*) compared to the lower coolant mass flow case, with two patches of high effectiveness. One other key difference in the behaviour of the injected coolant is the absence of the accumulation of coolant beneath the OTL flow inside the LE rim and PS rims which was predicted by both the source term and fully resolved methods at lower coolant mass flow. The wider coolant jet predicted at higher $\dot{m}$ forces the OTL flow to impinge closer to the rim which mixes with the coolant and reduces the effectiveness in this near rim region (*A17* and *B17*).

From this analysis, the HYDRA source term method appears to be satisfactory when predicting the tip HTC and film effectiveness which arises from coolant-OTL interactions. This makes the source term method a useful tool for optimisation processes, for having a 'quick look' at the impact of cooling designs on the tip and in the understanding of the interactions between coolant and OTL flow.

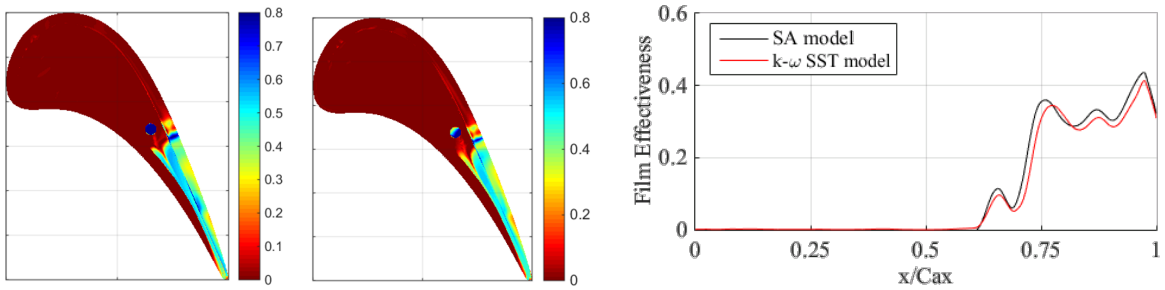
9.7 Effect of Alternative Turbulence Models

Although previous literature, for example Virdi (2015), has explored the sensitivity of tip heat transfer results to the choice of turbulence model, the turbulence model used is often evaluated by HTC results alone (for example Huang *et al.* (2013) and Ma *et al.* (2016)), with the model showing best agreement to experimental HTC data being used to predict cooling performance without further validation. However, Yang *et al.* (2009) shows an example of a study in which the validation of predicted tip film effectiveness to experimental data was performed using different turbulence models. This showed the success of models such as the $k-\epsilon$, $k-\omega$ and $k-\omega$ SST in predicting averaged film effectiveness, albeit at low Reynolds number. Moving away from the tip, Ornano & Povey (2017) showed that the $k-\omega$ SST model shows some success when predicting film effectiveness on a high pressure nozzle guide vane. The qualitative prediction was shown to agree well, however an over-prediction by the CFD of approximately 15% (of full scale) was reported due to an under-prediction of mixing between the coolant and mainstream flow.

Given the sub-optimal nature of the film effectiveness validation described in Section 9.3.2, it is worth exploring whether the predicted film effectiveness is sensitive to other turbulence models. This section focusses on the use of the $k-\omega$ SST model to predict film effectiveness, which is available in the Rolls-Royce HYDRA suite. Taking into account that there is still the disparity in coolant density between the CFD and experimental cases, the predicted film effectiveness using the $k-\omega$ SST model will be compared to the similar case using the SA model, to see if any difference arises due to the choice of turbulence model.

9.7.1 Theory of the $k-\omega$ SST Model

The $k-\omega$ SST model is a two-equation eddy-viscosity model, as described by Menter (1994), which uses the standard $k-\omega$ model (Wilcox (1994)) near to the wall but switches to a $k-\omega$ formulation derived from the $k-\epsilon$ model in the outer boundary



(a) SA model **(b) $k-\omega$ SST model** **(c) Circumferentially averaged film effectiveness**

Figure 9.14: Film cooling effectiveness predicted using SA and $k-\omega$ SST turbulence models (HYDRA)

layer and free shear flows which takes advantage of the $k-\epsilon$ model's independence from the freestream turbulence properties.

The $k-\omega$ model solves additional transport equations for the turbulent kinetic energy, k, and the specific dissipation rate, ω, which were calculated at inlet as follows:

$$k = \frac{3}{2}(UI)^2 \tag{9.1}$$

$$\omega = \frac{k^{\frac{1}{2}}}{C_{\mu}^{\frac{1}{4}} l} \tag{9.2}$$

where, U is the inlet freestream velocity, I is the turbulence intensity, C_{μ} is a constant and l is the turbulence length scale.

The SST (shear-stress transport) variant of the $k-\omega$ model redefines the eddy viscosity to account for the effects of the transport of the principal turbulent shear stress, τ, as in the full Reynolds-stress model, which improves the performance of the model in predicting adverse pressure gradient flows.

9.7.2 Film Cooling Effectiveness

Figure 9.14 shows the comparison of film effectiveness predicted with the SA and $k-\omega$ SST turbulence models. It is observed that both turbulence models predict good qualitative agreement of the film effectiveness distribution, suggesting that the predicted coolant flow interactions are very similar. The quantitative difference between the two

is also very small. Figure 9.14c shows that the SA model predicts slightly higher film effectiveness than the $k-\omega$ SST model which can be ascribed to slightly higher levels of mixing predicted between the coolant and OTL flow by the $k-\omega$ SST model. However, given the extra solution time required for the two-equation model and the fact that a definitive validation to experiment could not be performed, this difference is not considered significant enough to warrant a change from the SA model.

9.8 Summary and Conclusions

This chapter has presented a CFD study into film cooling using a single dust hole on a hypothetical geometry tip which was evaluated in Chapter 8. A validation of the CFD was first performed on the predicted HTC and film effectiveness using experimental data from the HSLC. The bulk of the cooling study focussed on the effects of altering the mass flow of coolant, dust hole size and dust hole location on the tip HTC, coolant-OTL interactions and film cooling effectiveness.

The main conclusions drawn were as follows:

1. The CFD with SA turbulence model shows reasonable agreement to experimental HTC data over a majority of the tip.

2. At rig conditions, the CFD shows fair qualitative agreement to experimental film effectiveness data. Quantitatively, the CFD over-predicts the film effectiveness, which could in part be due to the difference in coolant temperature between experiment and CFD. It is not possible in HYDRA to exactly match rig conditions and produce sensible results from CFD.

3. Increasing the coolant mass flow (therefore BR) reduces the film effectiveness close to the coolant hole but increases it downstream. At high coolant mass flow, interactions of the coolant and OTL flow are observed, altering the film effectiveness distribution.

4. Increasing the cooling hole diameter allows for a larger mass flow of coolant to be injected at an engine-realistic coolant-to-mainstream pressure ratio, increasing the film effectiveness.

5. The larger coolant hole alters the nature of the injected coolant jet and enhances the film effectiveness.

6. If a high mass flow of coolant is injected from a small cooling hole, the high velocity jet impinges on the casing, producing vortical flow structures which block the OTL flow and induce a counter-rotating cavity vortex. Resulting impingement of the OTL flow on the cavity floor increases the tip HTC and heat flux.

7. Injection of a high coolant mass flow downstream reduces the HTC and tip heat flux in the upstream cavity, due to additional cavity recirculation which blocks the impingement of flow onto the cavity floor near the LE.

8. Shifting the location of the dust hole to mid-cavity produces a system of counter-rotating vortices of coolant and OTL flow, as the coolant impacts on the casing. This blocks the OTL flow and causes it to impinge on the cavity floor, increasing HTC near the cooling hole. Downstream, the HTC also increases due to impingement of the coolant flow.

9. Source term cooling gives reasonably good agreement to the fully resolved method when predicting tip HTC, film effectiveness and coolant-OTL interactions. Small differences arise due to the differing representation of the modelled and resolved coolant jet, especially around the coolant hole.

10. Consideration of the $k-\omega$ SST model showed minimal change in film effectiveness levels and qualitative distribution compared to the SA model and did not warrant a change in turbulence model.

Chapter 10

Summary, Conclusions and Recommendations

10.1 Introduction

A review of open literature revealed that a majority of research on blade tips has been performed at low speed, often utilising cascades which allow for ease of testing and accessibility to the blade tip for spatially resolved measurements. Findings at low speed, often performed under stationary conditions, have therefore formed a bulk of the understanding of tip flow physics, but more recently it has been revealed that low speed tests fail to capture certain flow features which occur at transonic speeds in engine-realistic conditions. Ideally, all research into blade tips would take place in rotating rigs which are more able to reproduce the tip flows in a real engine. However, rotating rigs are very complex and tend to be prohibitively expensive as well as restricting access to the blade tip for data capture purposes. High speed cascade rigs offer an excellent alternative to rotating rigs as they are able to produce engine-representative aerodynamic flow conditions at a fraction of the cost, while maintaining accessibility to the tip. For this reason, high speed cascade rigs have become an important and yet still under-utilised research tool in recent years.

The Oxford University High Speed Linear Cascade (HSLC) was developed to allow

investigation of tip heat transfer coefficients and aerodynamic loss at engine-representative aerodynamic conditions, in order to improve the understanding of transonic tip flows. Over the last decade the HSLC has helped to challenge the conventional wisdoms established from low speed testing, highlighting the necessity for high speed rigs.

It is appreciated that the HSLC does not incorporate some engine-realistic effects such as rotation or a realistic inlet temperature profile. However, CFD validated to HSLC test data has been successfully used to give an appreciation of the changes in tip flow physics which would occur under rotating conditions and how that alters the tip aero-thermal performance.

Recent literature has examined a variety of tip designs under high speed flows, including the flat tip, winglet tip and more recently the squealer tip. The winglet tip and squealer tip have both shown aerodynamic benefits over the flat tip, although the winglet tip can be susceptible to high heat load. However, comparatively there is still a lack of research in open literature investigating these tip designs at transonic conditions. Furthermore, to the author's knowledge, certain novel tip designs incorporating cut-back squealer rims, which have shown benefit at low speed conditions, have not been investigated under transonic conditions. There are even fewer examples in open literature of tip cooling on transonic squealer tips and as a result this aspect is not well understood. To the author's knowledge there is no experimental research available in open literature examining the effects of tip clearance and coolant mass flow rate on a cooled transonic squealer tip. The above aspects have been the focus of the current research.

10.2 Uncooled Tip Heat Transfer

Infrared thermography using a transient technique was implemented to measure the tip heat transfer coefficient on a variety of tip designs. The HSLC was upgraded with a new IR camera which gave higher quality data and lower measurement uncertainty. Results revealed a strong dependence of the tip HTC distribution on the local overtip

leakage flow, which is similar on each tip tested, as all the tips broadly comprise a cavity enclosed by two rims. This overtip leakage flow exhibits a pattern of: separation (and possible reattachment) on the PS rim; impingement on the cavity floor; on the SS rim, a separation and reattachment near to the leading edge or a direct impingement towards the trailing edge. The HTC distribution produced by this generalised OTL flow field differs locally due to the specific tip geometry and warrants separate investigation in the region of rim cut-backs. Also found to be significant was the sharpness of the PS rim edge radius at low tip clearance; a sharp rim promotes reattachment and enhanced HTC on the PS rim. Rim edge radius must be carefully considered when discussing consistency of experimental data and comparison to CFD.

The experimental tip geometries were found to vary in thermal performance towards the trailing edge where the difference in tip geometry and therefore OTL flow field was significant. The squealer tip with suction side cut-back produced the lowest HTC at the trailing edge, with the PS cut-back tip giving the highest. As the tip clearance increases, the local behaviour of the OTL flow causes the following trends in distinct regions of the tip: the squealer rims show reduced HTC due to delayed reattachment, whereas the cavity floor HTC levels increase as a result of higher OTL mass flow. Although the presence of a cut-back changes the local OTL flow field, the same general flow features govern the HTC distribution of all the tip designs, including in the cut-back regions, and so the influence of increased tip clearance does not change the relative performance of the tips.

After validation to experimental data, which showed good agreement, CFD was used to expand the tip geometry study and examine the influence of relative casing motion on the overtip leakage flow and tip heat transfer. A variety of squealer tips with a cut-back PS rim were investigated. The study confirmed that removal of sections of the PS rim, perhaps from thermal deterioration, radically alters the local OTL flow and thermal performance of the tip, especially if the PS rim at the LE were to be lost. The best thermal performance was found to come from a hypothetical tip geometry with a

narrow cavity running to the trailing edge which splits the rear portion of the tip and reduces the HTC on the separate SS rim. With reduced tip clearance, the increase in HTC on the rims dominates the averaged HTC towards the TE, explaining the observed cross-over in the trend with tip gap towards the TE.

The addition of casing motion did not alter the flow reattachment and HTC on the PS rim in a majority of cases. The designs with downstream PS rim cut-backs showed the formation of a cavity vortex which counter-rotates to the existing cavity recirculation and forces the OTL flow to impinge on the cavity floor, increasing HTC in the mid-chord of the tip. When the PS rim cut-back at the LE is introduced, the effect of casing motion forms a network of cavity vortices and promotes earlier reattachment of flow onto the PS rim.

10.3 Tip Film Cooling

A significant upgrade to the HSLC was implemented to incorporate the use of the pressure sensitive paint (PSP) technique to measure adiabatic film cooling effectiveness. A new coolant system was installed, which uses mass flow controllers to deliver a specified mass flow of coolant (either air or Oxygen Free Nitrogen gas) to each of three plena inside the three adjustable tip gap blade tips. This system allows the mass flow of coolant to the LE, central or TE regions of the tip to be adjusted individually, to allow a high level of control over the tip coolant distribution.

The PSP method relies on the mass transfer analogy, so is devoid of conduction related issues which occur in thermal measurement techniques in areas of high thermal gradient, such as thin sections of the tip or around coolant holes, where 2D conduction effects become significant. There remains a temperature sensitivity of the PSP, which was accounted for using a simple temperature correction; this improved the repeatability of film effectiveness results.

The baseline squealer and SS cut-back squealer tips were tested with film cooling. The combined HTC and film effectiveness results for the baseline squealer tip have been

published. To the author's knowledge this is the first time experimental data focussing on the significance of tip gap and coolant mass flow rate has been presented for a cooled transonic squealer tip. It is further believed to be the first time the PSP technique has been applied for this purpose.

Results revealed that the injection of coolant can have a strong influence on the OTL flow field and resultant HTC distribution. Areas of high film effectiveness on the PS rim are strongly correlated to reduced heat flux at engine temperatures and to low HTC, due to blockage by the coolant film. Both tips show increased film effectiveness and reduced HTC at higher coolant mass flow rate, although locally some differences were observed. Trends in HTC with tip clearance were broadly similar to those observed on the uncooled tips but showed some local disparity due to exact tip geometry and differing interactions of the OTL flow and coolant. General trends with respect to film effectiveness were an increase in the cavity but a reduction on the rims at increased tip clearance due to the enhanced OTL mass flow.

The relative performance in HTC of the uncooled tips was maintained by the cooled tips, indicating that the HTC distribution is more closely correlated to the tip geometry. Compared to the SS cut-back tip, the HTC on the PS rim of the baseline squealer was much more sensitive to a change in tip clearance. The SS cut-back tip showed much higher levels of film effectiveness over much of the PS rim and towards the trailing edge due to a combination of improved hole placement and injection angle.

CFD was used to examine coolant - OTL interactions in detail. Validation to experiment showed reasonable agreement of tip HTC and fair qualitative agreement of film effectiveness, but also highlighted the importance of matching the CFD coolant temperature to experiment. Results showed that injected coolant can significantly alter the OTL flow. Advantages were shown from the use of a larger dust hole diameter: firstly, more coolant mass flow can be injected at an engine-representative coolant-to-mainstream pressure ratio without the coolant interacting with the OTL flow; secondly, the lower velocity coolant mixes out more, filling the cavity, compared to a similar

coolant mass flow injected from a smaller dust hole. These two factors increased the film effectiveness when a larger cooling hole was used. If the coolant interacts with the OTL flow or impinges on the casing, vortical structures are produced which block the OTL flow and induce counter-rotating cavity vortices. These vortices can entrain the OTL flow, resulting in impingement on the cavity floor and increased HTC and heat flux in the local area of the dust hole. Interestingly, the injection of a high coolant mass flow downstream was seen to reduce the upstream cavity HTC due to an increase in effective blockage from enhanced cavity recirculation, where there is zero film effectiveness.

The rudimentary source term cooling method gave good agreement to the fully resolved method when predicting tip HTC, film effectiveness and coolant-OTL interactions, suggesting the suitably of the source term method for coolant optimisation processes.

10.4 Aerodynamic Loss

Aerodynamic loss measurements were taken at a plane 50% of axial chord downstream of the blade row using a three hole probe which was traversed along a full blade pitch and the top 4-25% of blade span. The 50% axial chord downstream plane showed much improved periodicity over the 100% downstream plane due to the diverging flow paths of the blade wake and overtip leakage vortices. The uncooled blade tips were tested at two different tip clearance heights.

Evidence was seen of the OTL vortex, 2D blade wake and in most cases a hint of the upper passage vortex, with the OTL vortex being the largest contribution to the overall losses. The relative size and position of the OTL vortex is governed by the tip geometry. The winglet tip showed the lowest OTL vortex loss at both tip gaps, with the SS cut-back tip showing the highest. However, it was not possible to do a definitive comparison of the overall losses due to the missing top 4% of data and the fact that the differing tip geometries caused a shift in the position of the OTL vortex relative to the casing.

At increased tip clearance the OTL vortex was enhanced and moved away from the blade SS and casing wall, whereas the secondary flows and blade wake were reduced. The PS cut-back produced higher than expected loss at increased tip gap due to the reduced effectiveness of the small suction side overhang near the LE.

CFD was validated to experiment, showing good agreement, and was used to examine the development of losses downstream and the effects of a moving casing. The OTL vortex was seen to grow downstream but reduce in peak intensity. The OTL flow pattern caused by the removal of the PS rim at the LE resulted in distinctly separate OTL and upper passage vortices at the 50% downstream plane but at the 100% plane the passage vortex is overwhelmed by the OTL vortex from the next blade tip in the row. The PS cut-back rim at the TE was found to be less significant at low tip gap, suggesting deterioration of the rim in this region would have little impact on loss performance, however loss of the rim at the LE would still impact the aerodynamic performance of the tip.

With casing motion the OTL vortex is seen to originate exclusively from the trailing edge portion of the tip, whereas the OTL flow at the LE edge merges with the upper passage vortex; this promotes the passage vortex and weakens the OTL vortex. Overall, the addition of casing motion increases the losses at exit.

10.5 Recommendations for Future Work

This section details the recommendations by the author for future work based on the research presented in this thesis.

Regarding experimental work, measurements of the inlet boundary layer profile of the HSLC are recommended. These had been taken previously (O'Dowd *et al.* (2010b)) but reinforcement of the inlet turbulence grid and failure of the grid since the end of the current research necessitates new measurement of the inlet boundary layer profile. This could then be used for the inlet boundary condition profile in future CFD, although it is pointed out that the uniform boundary has given good agreement to experimental data

throughout this thesis.

On the aerodynamics side, the use of the 4 hole probe (which was calibrated during the current work but not presented) is strongly advised for future aerodynamic loss measurements. This will enable simple measurement of the top 4% of the blade span, without the vast amount of set-up time associated with switching probes and manually adjusting the 1-hole probe angle. This saved time will allow for a higher resolution of measurements in the area traverse, especially close to the casing.

For thermal measurements, it is recommended to consider redesigning the heater mesh unit into a double heater mesh setup. The switch to a new grade of mesh has improved the reliability of the mesh and manufacturing spare meshes will mitigate the time lost in future due to a mesh failure. However, the use of two meshes in series would further reduce the load on each mesh and the chance of failure. This set-up would also give the option of using a higher step-change in mainstream temperature, which would further reduce the HTC measurement uncertainty. An alternative to this approach would be to reduce the size of the inlet boundary layer bleeds, as currently an estimated $2/5^{th}$ of the mass flow through the mesh is bled off. This would mean that the same mass flow at inlet could be produced with a lower mass flow through the heater mesh, which would reduce the mechanical load on the mesh and produce a higher temperature step-change in the mainstream flow. Either approach would require redesign of certain sections of the rig's pipework and is a significant undertaking.

To improve the capabilities of the HSLC, it is suggested to install a transparent rotating disc above the blade row to enable the experimental measurement of moving casing data. This would be an ambitious but highly useful task as it would remove one of the drawbacks of testing in a stationary linear cascade and would furthermore allow direct validation of CFD result with casing motion. There are examples in literature of moving belts simulating the casing wall in low speed cascades, but to the author's knowledge the implementation of a moving casing wall in a high speed linear cascade has never been attempted and would be an exciting prospect.

On the PSP side, it is important to finish the portable calibration rig, so as to further reduce the uncertainty in PSP measurements taken in the HSLC. Although the tip temperature distribution is small and has limited impact on the presented film effectiveness results and the simple temperature correction used was successful, it is desirable to eliminate the temperature sensitivity of PSP. It is therefore recommended to further upgrade the PSP capabilities of the HSLC by implementation of binary PSP (as detailed by Le Sant & Merienne (2005)). This PSP has a second, pressure-insensitive luminophore which emits light of a different wavelength in response to a change in temperature. The separate signals can be measured independently using red and green filters and the temperature sensitivity of PSP significantly reduced by taking a ratio of ratios of the red and green light intensities.

The last recommendation made is to consider using an alternative foreign gas in place of Nitrogen, for example CO_2, which would give a more engine representative coolant-to-mainstream density ratio and make the cooled tip results more engine-realistic. It would also solve the issues around validating CFD film effectiveness results to the HSLC, as the coolant density could be matched whilst maintaining a larger temperature gradient between coolant and mainstream. However, from a review of other rigs in the lab, the author is aware that the expansion of CO_2 gas from a gas bottle can produce a large enough drop in coolant temperature to cause some of the tip coolant holes to ice over and become blocked. The use of binary PSP would reduce the problem associated with temperature gradient between the coolant and mainstream, however any blockage of coolant holes would be problematic and require a solution to reheat the coolant before it enters the tips.

Bibliography

Acharya, S., & Moreaux, L. 2013. Numerical Study of the Flow Past a Turbine Blade Tip: Effect of Relative Motion Between Blade and Shroud. *J. Turbomach*, **136**(3), 031015–031015–9.

Acharya, S., Yang, H., Ekkad, S. V., Prakash, C., & Bunker, R. 2002 (Jan.). Numerical Simulation of Film Cooling on the Tip of a Gas Turbine Blade. ASME Paper No. GT2002-30553.

Acharya, S., Yang, H., Prakash, C., & Bunker, R. 2003 (Jan.). Numerical Study of Flow and Heat Transfer on a Blade Tip With Different Leakage Reduction Strategies. ASME Paper No. GT2003-38617.

Acharya, S, Kramer, G, Moreaux, L, & Nakamata, C. 2010 (Oct.). Squealer Tip Heat Transfer With Film Cooling. ASME Paper No. GT2010-23688.

Ahn, J., Mhetras, S., & Han, J-C. 2005. Film-Cooling Effectiveness on a Gas Turbine Blade Tip Using Pressure-Sensitive Paint. *J. Heat Transfer*, **127**(5), 521–530.

Ahn, J., Schobeiri, M. T., Han, J-C., & Moon, H-K. 2006. Film Cooling Effectiveness on the Leading Edge Region of a Rotating Turbine Blade With Two Rows of Film Cooling Holes Using Pressure Sensitive Paint. *J. Heat Transfer*, **128**(9), 879–888.

Ahn, J., Schobeiri, M. T., Han, J-C., & Moon, H-K. 2007. Effect of rotation on leading edge region film cooling of a gas turbine blade with three rows of film cooling holes. *International Journal of Heat and Mass Transfer*, **50**(1), 15–25.

Ainsworth, R. W., & Batt, J. J. M. 1993 (Sept.). The Development of a 3D Fast Response Aerodynamic Probe. *Pages 27.1–27.9 of: International Congress on Instrumentation in Aerospace Simulation Facilities,*.

Ainsworth, R. W., Schultz, D. L., Davies, M. R. D., Forth, C. J. P., Hilditch, M. A., Oldfield, M. L. G., & Sheard, A. G. 1988 (June). A Transient Flow Facility for the Study of the Thermofluid-Dynamics of a Full Stage Turbine Under Engine Representative Conditions. ASME Paper No. 88-GT-144.

Ameri, A. A., & Bunker, R. S. 1999. Heat Transfer and Flow on the First-Stage Blade Tip of a Power Generation Gas Turbine: Part 2Simulation Results. *J. Turbomach*, **122**(2), 272–277.

Ameri, A. A., Steinthorsson, E., & Rigby, D. L. 1998. Effect of Squealer Tip on Rotor Heat Transfer and Efficiency. *J. Turbomach*, **120**(4), 753–759.

Anto, K., Xue, S., Ng, W. F., Zhang, L. J., & Moon, H. K. 2013 (June). Effects of Tip Clearance Gap and Exit Mach Number on Turbine Blade Tip and Near-Tip Heat Transfer. ASME Paper No. GT2013-94345.

Arisi, A., Phillips, J., Ng, W. F., Xue, S., Moon, H. K., & Zhang, L. 2016. An Experimental and Numerical Study on the Aerothermal Characteristics of a Ribbed Transonic Squealer-Tip Turbine Blade With Purge Flow. *J. Turbomach*, **138**(10), 101007–101007–11.

Azad, G. S., Han, J-C., Teng, S., & Boyle, R. J. 2000. Heat Transfer and Pressure Distributions on a Gas Turbine Blade Tip. *J. Turbomach*, **122**(4), 717–724.

Azad, G. S., Han, J-C., Bunker, R. S., & Lee, C. P. 2002. Effect of Squealer Geometry Arrangement on a Gas Turbine Blade Tip Heat Transfer. *J. Heat Transfer*, **124**(3), 452–459.

Bindon, J. P. 1987. Pressure Distributions in the Tip Clearance Region of an Unshrouded Axial Turbine as Affecting the Problem of Tip Burnout. *In: Proceedings of the ASME Gas Turbine Conference and Exhibition*, vol. 87-GT-230.

Bindon, J. P. 1989. The Measurement and Formation of Tip Clearance Loss. *J. Turbomach*, **111**(3), 257–263.

Bindon, J. P., & Morphis, G. 1992. The Development of Axial Turbine Leakage Loss for Two Profiled Tip Geometries Using Linear Cascade Data. *J. Turbomach*, **114**(1), 198–203.

Brunner, M. H., Rose, M. G., Mhlbauer, K., & Abhari, R. S. 2007. In-engine turbine heat transfer measurement. *Proceedings of the Institution of Mechanical Engineers, Part A: Journal of Power and Energy*, **221**(5), 727–734.

Bunker, R. S. 2001. A Review of Turbine Blade Tip Heat Transfer. *Annals of the New York Academy of Sciences*, **934**(June), 64–79.

Bunker, R. S. 2004. Blade Tip Heat Transfer and Cooling Techniques. VKI Lecture Series, Paper no. 2004-02.

Bunker, R. S., & Bailey, J. C. 2001. Effect of Squealer Cavity Depth and Oxidation on Turbine Blade Tip Heat Transfer. ASME Paper No. 2001-GT-0155. American Society of Mechanical Engineers.

Bunker, R. S., Bailey, J. C., & Ameri, A. A. 1999. Heat Transfer and Flow on the First-Stage Blade Tip of a Power Generation Gas Turbine: Part 1 - Experimental Results. *J. Turbomach*, **122**(2), 263–271.

Camci, C., Dey, D., & Kavurmacioglu, L. 2005. Aerodynamics of Tip Leakage Flows Near Partial Squealer Rims in an Axial Flow Turbine Stage. *J. Turbomach*, **127**(1), 14–24.

Chana, K. S., & Jones, T. V. 2003. An Investigation on Turbine Tip and Shroud Heat Transfer. *J. Turbomach*, **125**(3), 513–520.

Cho, H. H., & Goldstein, R. J. 1995. Heat (Mass) Transfer and Film Cooling Effectiveness With Injection Through Discrete Holes: Part IWithin Holes and on the Back Surface. *J. Turbomach*, **117**(3), 440–450.

Christophel, J. R., Thole, K. A., & Cunha, F. J. 2005. Cooling the Tip of a Turbine Blade Using Pressure Side Holes - Part II: Heat Transfer Measurements. *J. Turbomach*, **127**(2), 278–286.

Collins, M., Chana, K., & Povey, T. 2015. New technique for the fabrication of miniature thin film heat flux gauges. *Meas. Sci. Technol.*, **26**(2), 025303.

Coull, J. D., & Atkins, N. R. 2015. The Influence of Boundary Conditions on Tip Leakage Flow. *J. Turbomach*, **137**(6), 061005–061005–10.

Coull, J. D., Atkins, N. R., & Hodson, H. P. 2014a (June). High Efficiency Cavity Winglets for High Pressure Turbines. ASME Paper No. GT2014-25261.

Coull, J. D., Atkins, N. R., & Hodson, H. P. 2014b. Winglets for Improved Aerothermal Performance of High Pressure Turbines. *J. Turbomach*, **136**(9), 091007–091007–11.

Denton, J. D. 1993. Loss Mechanisms in Turbomachines. *J. Turbomach*, **115**(4), 621–656.

Dey, D., & Camci, C. 2001 (June). Aerodynamic Tip Desensitization of an Axial Turbine Rotor Using Tip Platform Extensions. ASME Paper No. 2001-GT-0484.

Dishart, P. T., & Moore, J. 1990. Tip Leakage Losses in a Linear Turbine Cascade. *J. Turbomach*, **112**(4), 599–608.

Dominy, R. G., & Hodson, H. P. 1992 (June). An Investigation of Factors Influencing the Calibration of 5-Hole Probes for 3-D Flow Measurements. ASME Paper No. 92-GT-216.

Dring, R. P., Blair, M. F., & Joslyn, H. D. 1980. An Experimental Investigation of Film Cooling on a Turbine Rotor Blade. *J. Eng. Power*, **102**(1), 81–87.

Dunn, M. G., & Haldeman, C. W. 2000. Time-Averaged Heat Flux for a Recessed Tip, Lip, and Platform of a Transonic Turbine Blade. *J. Turbomach*, **122**(4), 692–698.

Dunn, M. G., Rae, W. J., & Holt, J. L. 1984a. Measurement and Analyses of Heat Flux Data in a Turbine Stage: Part IDescription of Experimental Apparatus and Data Analysis. *J. Eng. Gas Turbines Power*, **106**(1), 229–233.

Dunn, M. G., Rae, W. J., & Holt, J. L. 1984b. Measurement and Analyses of Heat Flux Data in a Turbine Stage: Part IIDiscussion of Results and Comparison With Predictions. *J. Eng. Gas Turbines Power*, **106**(1), 234–240.

El-Ghandour, M., Ibrahim, M. K., Doi, K., & Nakamura, Y. 2010. Effects of Tip Cavity Depth, Width, and Location on the Leakage Flow in an Axial Turbine Cascade. *JFST*, **5**(3), 558–573.

El-Ghandour, M., Shatat, M. M. E., & Nakamura, Y. 2012 (June). On the Physics of Vortex Formation at the Tip of a Turbine Blade. ASME Paper No. GT2012-70128.

Gao, Z., Narzary, D., Mhetras, S., & Han, J-C. 2009. Effect of Inlet Flow Angle on Gas Turbine Blade Tip Film Cooling. *J. Turbomach*, **131**(3), 031005–031005–12.

Gillespie, D. R. H. 1996. *Intricate Internal Cooling Systems for Gas Turbine Blading.* DPhil Thesis, University of Oxford.

Goldstein, R. J., & Cho, H. H. 1995. A review of mass transfer measurements using naphthalene sublimation. *Experimental Thermal and Fluid Science*, **10**(4), 416–434.

Graham, J. A. H. 1986. Investigation of a Tip Clearance Cascade in a Water Analogy Rig. *J. Eng. Gas Turbines Power*, **108**(1), 38–46.

Han, J-C., & Rallabandi, A. 2010. Turbine Blade Film Cooling Using PSP Technique. *Frontiers in Heat and Mass Transfer (FHMT)*, **1**(1).

Harvey, N. W., & Ramsden, K. 2000. A Computational Study of a Novel Turbine Rotor Partial Shroud. *J. Turbomach*, **123**(3), 534–543.

Heyes, F. J. G., Hodson, H. P., & Dailey, G. M. 1992. The Effect of Blade Tip Geometry on the Tip Leakage Flow in Axial Turbine Cascades. *J. Turbomach*, **114**(3), 643–651.

Hofer, T., & Arts, T. 2009 (Jan.). Aerodynamic Investigation of the Tip Leakage Flow for Blades With Different Tip Squealer Geometries at Transonic Conditions. ASME Paper No. GT2009-59909.

Huang, Q., Wang, J., He, L., & Xu, Q. 2013 (Sept.). Numerical Study of Heat Transfer and Cooling Effectiveness on a Flat-Tip Turbine Blade. ASME Paper No. TBTS2013-2053.

Ireland, P. T., & Jones, T. V. 2000. Liquid crystal measurements of heat transfer and surface shear stress. *Meas. Sci. Technol.*, **11**(7), 969.

Ireland, P. T., Neely, A. J., Gillespie, D. R. H., & Robertson, A. J. 1999. Turbulent heat transfer measurements using liquid crystals. *International Journal of Heat and Fluid Flow*, **20**(4), 355–367.

Jackson, A. J., Wheeler, A. P. S., & Ainsworth, R. W. 2015. An experimental and computational study of tip clearance effects on a transonic turbine stage. *International Journal of Heat and Fluid Flow*, **56**(Dec.), 335–343.

Jones, T. V. 1999. Theory for the use of foreign gas in simulating film cooling. *International Journal of Heat and Fluid Flow*, **20**(3), 349–354.

Kays, W, Crawford, M, & Weigand, B. 2005. *Convective Heat and Mass Transfer.* McGraw-Hill.

Kegalj, M., Schmid, G., Wartzek, F., Schiffer, H-P., & Willer, Lars. 2012 (June). Experimental and Numerical Investigation of Tip Leakage Flow in a 1 1/2 Stage Turbine Rig Comparing Flat and Cavity-Squealer Tip Geometries. ASME Paper No. GT2012-69568.

Key, N. L., & Arts, T. 2004. Comparison of Turbine Tip Leakage Flow for Flat Tip and Squealer Tip Geometries at High-Speed Conditions. *J. Turbomach*, **128**(2), 213–220.

Kline, S. J., & McClintock, F. A. 1953. Describing Uncertainties in Single-Sample Experiments. *Mechnical Engineering (ASME)*, **75**(1), 3–8.

Krishnababu, S. K., Hodson, H. P., Booth, G. D., Lock, G. D., & Dawes, W. N. 2008a (Jan.). Aero-Thermal Investigation of Tip Leakage Flow in a Film Cooled Industrial Turbine Rotor. ASME Paper No. GT2008-50222.

Krishnababu, S. K., Newton, P. J., Dawes, W. N., Lock, G. D., Hodson, H. P., Hannis, J., & Whitney, C. 2008b. Aerothermal Investigations of Tip Leakage Flow in Axial Flow TurbinesPart I: Effect of Tip Geometry and Tip Clearance Gap. *J. Turbomach*, **131**(1), 011006–011006–14.

Krishnababu, S. K., Dawes, W. N., Hodson, H. P., Lock, G. D., Hannis, J., & Whitney, C. 2008c. Aerothermal Investigations of Tip Leakage Flow in Axial Flow TurbinesPart II: Effect of Relative Casing Motion. *J. Turbomach*, **131**(1), 011007–011007–10.

Kwak, J. S., & Han, J-C. 2003. Heat Transfer Coefficients and Film Cooling Effectiveness on the Squealer Tip of a Gas Turbine Blade. *J. Turbomach*, **125**(4), 648–657.

Kwak, J. S., Ahn, J., Han, J-C., Lee, C. P., Bunker, R. S., Boyle, R., & Gaugler, R. 2003. Heat Transfer Coefficients on the Squealer Tip and Near-Tip Regions of a Gas Turbine Blade With Single or Double Squealer. *J. Turbomach*, **125**(4), 778–787.

Le Sant, Y., & Merienne, M. C. 2005. Surface pressure measurements by using pressure-sensitive paints. *Aerospace Science and Technology*, **9**(4), 285–299.

Ledezma, G. A., Allen, J., & Bunker, R. S. 2013 (Sept.). An Experimental and Numerical Investigation Into the Effects of Squealer Blade Tip Modifications on Aerodynamic Performance. ASME Paper No. TBTS2013-2004.

Lee, S. W., & Chae, B. J. 2008. Effects of squealer rim height on aerodynamic losses downstream of a high-turning turbine rotor blade. *Experimental Thermal and Fluid Science*, **32**(8), 1440–1447.

Liu, T., Guille, M., & Sullivan, J. P. 2001. Accuracy of Pressure-Sensitive Paint. *AIAA Journal*, **39**(1), 103–112.

Lomakin, N., Granovskiy, A., Belkanov, V., & Szwedowicz, J. 2013 (Sept.). Effect of Common Blade Tip Squealer Designs in Terms of Tip Clearance Loss Control. ASME Paper No. TBTS2013-2040.

Lu, K., Schobeiri, M. T., & Han, J. C. 2013 (June). Numerical Simulation of Film Cooling on Rotating Blade Tips Within a High-Pressure Turbine. ASME Paper No. GT2013-94806.

Ma, H., Zhang, Q., He, L., Wang, Z., & Wang, L. 2016 (June). Cooling Injection Effect on a Transonic Squealer Tip: Part 1 Experimental Heat Transfer Results and CFD Validation. ASME Paper No. GT2016-57579.

Ma, H., Zhang, Q., He, L., Wang, Z., & Wang, L. 2017. Cooling Injection Effect on a Transonic Squealer TipPart II: Analysis of Aerothermal Interaction Physics. *J. Eng. Gas Turbines Power*, **139**(5), 052507–052507–9.

Main, A. D. J. 1994. *Annular Turbine Cascade Aerodynamics*. DPhil Thesis, University of Oxford.

Main, A. J., Day, C. R. B., Lock, G. D., & Oldfield, M. L. G. 1996. Calibration of a four-hole pyramid probe and area traverse measurements in a short-duration transonic turbine cascade tunnel. *Experiments in Fluids*, **21**(4), 302–311.

McCarter, A. A., Xiao, X., & Lakshminarayana, B. 2000. Tip Clearance Effects in a Turbine Rotor: Part IIVelocity Field and Flow Physics. *J. Turbomach*, **123**(2), 305–313.

McGreehan, W. F., & Schotsch, M. J. 1988. Flow Characteristics of Long Orifices With Rotation and Corner Radiusing. *J. Turbomach*, **110**(2), 213–217.

McLachlan, B. G., & Bell, J. H. 1995. Pressure-sensitive paint in aerodynamic testing. *Experimental Thermal and Fluid Science*, **10**(4), 470–485.

Menter, F. R. 1994. Two-Equation Eddy-Viscosity Turbulence Models for Engineering Applications. *AIAA Journal*, **32**(8), 1598–1605.

Metzger, D., Rued, K., & Chyu, M. 1989a. Influence of clearance leakage on turbine heat transfer at and near blade tips - Summary of recent results. *In: 27th Aerospace Sciences Meeting*. AIAA Paper No. AIAA-89-0327. American Institute of Aeronautics and Astronautics.

Metzger, D. E., & Rued, K. 1989. The Influence of Turbine Clearance Gap Leakage on Passage Velocity and Heat Transfer Near Blade Tips: Part ISink Flow Effects on Blade Pressure Side. *J. Turbomach*, **111**(3), 284–292.

Metzger, D. E., Bunker, R. S., & Chyu, M. K. 1989b. Cavity Heat Transfer on a Transverse Grooved Wall in a Narrow Flow Channel. *J. Heat Transfer*, **111**(1), 73–79.

Mhetras, S., Narzary, D., Gao, Z., & Han, J-C. 2008. Effect of a Cutback Squealer and Cavity Depth on Film-Cooling Effectiveness on a Gas Turbine Blade Tip. *J. Turbomach*, **130**(2), 021002–021002–13.

Mischo, B., Behr, T., & Abhari, R. S. 2008. Flow Physics and Profiling of Recessed Blade Tips: Impact on Performance and Heat Load. *J. Turbomach*, **130**(2), 021008–021008–8.

Mitsuo, K., Kurita, M., Nakakita, K., & Watanabe, S. 2005. Temperature Correction of PSP Measurement for Low-Speed Flow Using Infrared Camera. *Pages 214–220 of: ICIASF 2005 Record International Congress on Instrumentation in Aerospace Simulation Facilities*.

Moffat, R. J. 1988. Describing the uncertainties in experimental results. *Experimental Thermal and Fluid Science*, **1**(1), 3–17.

Moinier, P., & Giles, M. 1998. Preconditioned Euler and Navier-Stokes Calculations on Unstructured Meshes. 6th ICFD Conference on Numerical Methods for Fluid Dynamics.

Moore, J., & Elward, K. M. 1993. Shock Formation in Overexpanded Tip Leakage Flow. *Journal of Turbomachinery*, **115**, 392 – 399.

Moore, J., & Tilton, J. S. 1988. Tip Leakage Flow in a Linear Turbine Cascade. *J. Turbomach*, **110**(1), 18–26.

Moore, J., Moore, J. G., Henry, G. S., & Chaudhry, U. 1989. Flow and Heat Transfer in Turbine Tip Gaps. *J. Turbomach*, **111**(3), 301–309.

Naik, S., Georgakis, C., Hofer, T., & Lengani, D. 2011. Heat Transfer and Film Cooling of Blade Tips and Endwalls. *J. Turbomach*, **134**(4), 041004–041004–11.

Narzary, D., Liu, K., Han, J-C., Mhetras, S., & Landis, K. 2014 (June). Turbine Blade Tip Film-Cooling and Heat Transfer Measurements at High Blowing Ratios. ASME Paper No. GT2014-25793.

Newton, P. J., Lock, G. D., Krishnababu, S. K., Hodson, H. P., Dawes, W. N., Hannis, J., & Whitney, C. 2004. Heat Transfer and Aerodynamics of Turbine Blade Tips in a Linear Cascade. *J. Turbomach*, **128**(2), 300–309.

Newton, P. J., Lock, G. D., Krishnababu, S. K., Hodson, H. P., Dawes, W. N., Hannis, J., & Whitney, C. 2008. Aerothermal Investigations of Tip Leakage Flow in Axial Flow TurbinesPart III: TIP Cooling. *J. Turbomach*, **131**(1), 011008–011008–12.

O'Dowd, D. O. 2010. *Aero-Thermal Performance of Transonic High-Pressure Turbine Blade Tips*. DPhil Thesis, University of Oxford.

O'Dowd, D. O., Zhang, Q., He, L., Ligrani, P. M., & Friedrichs, S. 2010a. Comparison of Heat Transfer Measurement Techniques on a Transonic Turbine Blade Tip. *J. Turbomach*, **133**(2), 021028–021028–10.

O'Dowd, D. O., Zhang, Q., Usandizaga, I., He, L., & Ligrani, P. M. 2010b (Oct.). Transonic Turbine Blade Tip Aero-Thermal Performance With Different Tip Gaps: Part II - Tip Aerodynamic Loss. ASME Paper No. GT2010-22780.

O'Dowd, D. O., Zhang, Q., He, L., Cheong, B. C. Y., & Tibbott, I. 2012. Aerothermal Performance of a Cooled Winglet at Engine Representative Mach and Reynolds Numbers. *J. Turbomach*, **135**(1), 011041–011041–10.

Oldfield, M. L. 2008. Impulse Response Processing of Transient Heat Transfer Gauge Signals. *J. Turbomach*, **130**(2), 021023–021023–9.

Oldfield, M. L. G., Jones, T. V., & Schultz, D. L. 1978. On-Line Computer for Transient Turbine Cascade Instrumentation. *IEEE Transactions on Aerospace and Electronic Systems*, **AES-14**(5), 738–749.

Ornano, F., & Povey, T. 2017. Experimental and Computational Study of the Effect of Momentum-Flux Ratio on High-Pressure Nozzle Guide Vane Endwall Cooling Systems. *J. Turbomach*, **139**(12), 121002–121002–14.

Palafox, P., Oldfield, M. L. G., LaGraff, J. E., & Jones, T. V. 2007. PIV Maps of Tip Leakage and Secondary Flow Fields on a Low-Speed Turbine Blade Cascade With Moving End Wall. *J. Turbomach*, **130**(1), 011001–011001–9.

Palafox, P., Oldfield, M. L. G., Ireland, P. T., Jones, T. V., & LaGraff, J. E. 2011. Blade Tip Heat Transfer and Aerodynamics in a Large Scale Turbine Cascade With Moving Endwall. *J. Turbomach*, **134**(2), 021020–021020–11.

Papa, M., Goldstein, R. J., & Gori, F. 2003. Effects of Tip Geometry and Tip Clearance on the Mass/Heat Transfer From a Large-Scale Gas Turbine Blade. *J. Turbomach*, **125**(1), 90–96.

Park, J. S., Lee, S. H., Kwak, J. S., Lee, W. S., & Chung, J. T. 2013 (Sept.). Measurement of Blade Tip Heat Transfer and Leakage Flow in a Turbine Cascade With a Multi-Cavity Squealer Tip. ASME Paper No. TBTS2013-2072.

Park, J. S., Lee, D. H., Rhee, D-H., Kang, S. H., & Cho, H. H. 2014. Heat transfer and film cooling effectiveness on the squealer tip of a turbine blade. *Energy*, **72**(Supplement C), 331–343.

Payne, S. J., Ainsworth, R. W., Miller, R. J., Moss, R. W., & Harvey, N. W. 2003. Unsteady loss in a high pressure turbine stage. *International Journal of Heat and Fluid Flow*, **24**(5), 698–708.

Povey, T., Oldfield, M. L. G., & Haselbach, F. 2008. Transonic turbine vane tests in a new miniature cascade facility. *Proceedings of The Institution of Mechanical Engineers Part A - Journal of Power and Energy*, **222**(5), 529–539.

Quinn, Mark Kenneth, Gongora-Orozco, Nalleli, Kontis, Konstantinos, & Ireland, Peter. 2013. Application of pressure-sensitive paint to low-speed flow around a U-bend of strong curvature. *Experimental Thermal and Fluid Science*, **48**(Supplement C), 58–66.

Rains, D. A. 1954. *Tip Clearance Flows in Axial Compressors and Pumps*. Ph.D. Thesis, California Institute of Technology.

Rao, N. M., & Camci, C. 2005 (Jan.). Visualization of Rotor Endwall, Tip Gap, and Outer Casing Surface Flows in a Rotating Axial Turbine Rig. ASME Paper No. GT2005-68264.

Rezasoltani, M., Lu, K., Schobeiri, M. T., & Han, J-C. 2015. A Combined Experimental and Numerical Study of the Turbine Blade Tip Film Cooling Effectiveness Under Rotation Condition. *J. Turbomach*, **137**(5), 051009–051009–12.

Rolls-Royce. 2005. *The Jet Engine*. Rolls-Royce plc.

Rued, K., & Metzger, D. E. 1989. The Influence of Turbine Clearance Gap Leakage on Passage Velocity and Heat Transfer Near Blade Tips: Part IISource Flow Effects on Blade Suction Sides. *J. Turbomach*, **111**(3), 293–300.

Saxena, V., Nasir, H., & Ekkad, S. V. 2004. Effect of Blade Tip Geometry on Tip Flow and Heat Transfer for a Blade in a Low-Speed Cascade. *J. Turbomach*, **126**(1), 130–138.

Schabowski, Z, & Hodson, H. 2013. The Reduction of Over Tip Leakage Loss in Unshrouded Axial Turbines Using Winglets and Squealers. *J. Turbomach*, **136**(4), 041001–041001–11.

Schabowski, Z, Hodson, H, Giacche, D, Power, B, & Stokes, M. R. 2014. Aeromechanical Optimization of a Winglet-Squealer Tip for an Axial Turbine. *J. Turbomach*, **136**(7), 071004–071004–12.

Schneider, P. J. 1955. *Conduction heat transfer*. Addison-Wesley series in mechanical engineering. Cambridge, Mass: Addison-Wesley.

Sjolander, S. A., & Amrud, K. K. 1987. Effects of Tip Clearance on Blade Loading in a Planar Cascade of Turbine Blades. *J. Turbomach*, **109**(2), 237–244.

Spalart, P. R., & Allmaras, S. R. 1992. A One-Equation Turbulence Model for Aerodynamic Flows. *AIAA*, **439**(Jan.), 5–21.

Takeishi, K., Aoki, S., Sato, T., & Tsukagoshi, K. 1992. Film Cooling on a Gas Turbine Rotor Blade. *J. Turbomach*, **114**(4), 828–834.

Teager, M. 2015. *Drake DC Power Supply Operating Instructions*.

Thorpe, S. J., Yoshino, S., Ainsworth, R. W., & Harvey, N. W. 2004a. Improved fast-response heat transfer instrumentation for short-duration wind tunnels. *Meas. Sci. Technol.*, **15**(9), 1897.

Thorpe, S. J., Yoshino, S., Ainsworth, R. W., & Harvey, N. W. 2004b. An investigation of the heat transfer and static pressure on the over-tip casing wall of an axial turbine operating at engine representative flow conditions. (I). Time-mean results. *International Journal of Heat and Fluid Flow*, **25**(6), 933–944.

Thorpe, S. J., Yoshino, S., Ainsworth, R. W., & Harvey, N. W. 2004c. An investigation of the heat transfer and static pressure on the over-tip casing wall of an axial turbine operating at engine representative flow conditions. (II). Time-resolved results. *International Journal of Heat and Fluid Flow*, **25**(6), 945–960.

Thorpe, S. J., Yoshino, S., Thomas, G. A., Ainsworth, R. W., & Harvey, N. W. 2005. Blade-tip heat transfer in a transonic turbine. *Proceedings of the Institution of Mechanical Engineers, Part A: Journal of Power and Energy*, **219**(6), 421–430.

Tu, J., Yeoh, G-H., & Liu, C. 2012. *Computational Fluid Dynamics: A Practical Approach*. Elsevier Science & Technology.

Versteeg, H. K., & Malalasekera, W. 1995. *An Introduction to Computational Fluid Dynamics: The Finite Volume Approach*. Longman Scientific & Technical.

Virdi, A. S. 2015. *Aero-Thermal Performance and Enhanced Internal Cooling of Unshrouded Turbine Blade Tips*. DPhil Thesis, University of Oxford.

Virdi, A. S., Zhang, Q., He, L., Li, H. D., & Hunsley, R. 2013 (Sept.). Aerothermal Performance of Shroudless Turbine Blade Tips With Effects of Relative Casing Motion. *In: ASME 2013 Turbine Blade Tip Symposium*. ASME Paper No. TBTS2013-2021.

Vogel, J. C., & Eaton, J. K. 1985. Combined Heat Transfer and Fluid Dynamic Measurements Downstream of a Backward-Facing Step. *J. Heat Transfer*, **107**(4), 922–929.

Wang, J., Liu, Y., Wang, X., Du, Z., & Yang, S. 2010 (Oct.). Characteristics of Tip Leakage Flow of the Turbine Blade With Cutback Squealer and Coolant Injection. ASME Paper No. GT2010-22566.

Wang, Z., Zhang, Q., Liu, Y., & He, L. 2015. Impact of Cooling Injection on the Transonic Over-Tip Leakage Flow and Squealer Aerothermal Design Optimization. *J. Eng. Gas Turbines Power*, **137**(6), 062603–062603–7.

Wheeler, A. P. S., & Saleh, Z. 2013. Effect of Cooling Injection on Transonic Tip Flows. *Journal of Propulsion and Power*, **29**(6), 1374–1381.

Wheeler, A. P. S., Atkins, N. R., & He, L. 2011. Turbine Blade Tip Heat Transfer in Low Speed and High Speed Flows. *J. Turbomach*, **133**(4), 041025–041025–9.

Wilcox, D. C. 1994. Simulation of Transition with a Two-Equation Turbulence Model. *AIAA Journal*, **32**(2), 247–255.

Wong, T. H., Ireland, P. T., & Self, K. P. 2016. Film Cooling Effectiveness Downstream of Trailing Edge Slots Including Cutback Surface Protuberances. *International Journal of Turbomachinery, Propulsion and Power*, **1**(1), 4.

Wright, L. M., Gao, Z., Varvel, T. A., & Han, J-C. 2005 (Jan.). Assessment of Steady State PSP, TSP, and IR Measurement Techniques for Flat Plate Film Cooling. ASME Paper No. HT2005-72363.

Xiao, X., McCarter, A. A., & Lakshminarayana, B. 2000. Tip Clearance Effects in a Turbine Rotor: Part IPressure Field and Loss. *J. Turbomach*, **123**(2), 296–304.

Yamamoto, A. 1988. Interaction Mechanisms Between Tip Leakage Flow and the Passage Vortex in a Linear Turbine Rotor Cascade. *J. Turbomach*, **110**(3), 329–338.

Yamamoto, A. 1989. Endwall Flow/Loss Mechanisms in a Linear Turbine Cascade With Blade Tip Clearance. *J. Turbomach*, **111**(3), 264–275.

Yang, D., Feng, Z., & Yu, X. 2009 (Jan.). Investigation of Film Cooling Effectiveness on Squealer Tip of a Gas Turbine Blade. ASME Paper No. GT2009-60280.

Yaras, M., Zhu, Y., & Sjolander, S. A. 1989. Flow Field in the Tip Gap of a Planar Cascade of Turbine Blades. *J. Turbomach*, **111**(3), 276–283.

Yaras, M. I., & Sjolander, S. A. 1991. Measurements of the effects of winglets on tip-leakage losses in a linear turbine cascade. *Pages 127–135 of: 10th International Symposium on Air Breathing Engines, Nottingham, England.*

Yaras, M. I., & Sjolander, S. A. 1992. Effects of Simulated Rotation on Tip Leakage in a Planar Cascade of Turbine Blades: Part I - Tip Gap Flow. *J. Turbomach*, **114**(3), 652–659.

Yaras, M. I., Sjolander, S. A., & Kind, R. J. 1992. Effects of Simulated Rotation on Tip Leakage in a Planar Cascade of Turbine Blades: Part II - Downstream Flow Field and Blade Loading. *J. Turbomach*, **114**(3), 660–667.

Zhang, Q. 2007a. *Drawings of HSLC*. Tech. rept. University of Oxford, Department of Engineering Science.

Zhang, Q. 2007b. *Thermal Property Transient Measurement*. Tech. rept. Department of Engineering Science, University of Oxford.

Zhang, Q., & He, L. 2011. Overtip Choking and Its Implications on Turbine Blade-Tip Aerodynamic Performance. *Journal of Propulsion and Power*, **27**(5), 1008–1014.

Zhang, Q., & He, L. 2013. Tip-Shaping for HP Turbine Blade Aerothermal Performance Management. *J. Turbomach*, **135**(5), 051025–051025–7.

Zhang, Q., ODowd, D. O., He, L., Wheeler, A. P. S., Ligrani, P. M., & Cheong, B. C. Y. 2011a. Overtip Shock Wave Structure and Its Impact on Turbine Blade Tip Heat Transfer. *J. Turbomach*, **133**(4), 041001–041001–8.

Zhang, Q., ODowd, D. O., He, L., Oldfield, M. L. G., & Ligrani, P. M. 2011b. Transonic Turbine Blade Tip Aerothermal Performance With Different Tip Gaps - Part I: Tip Heat Transfer. *J. Turbomach*, **133**(4), 041027–041027–9.

Zhang, Q., He, L., & Rawlinson, A. 2014. Effects of Inlet Turbulence and End-Wall Boundary Layer on Aerothermal Performance of a Transonic Turbine Blade Tip. *J. Eng. Gas Turbines Power*, **136**(5), 052603–052603–7.

Zhong, F., Zhou, C., Ma, H., & Zhang, Q. 2016. Heat Transfer of Winglet Tips in a Transonic Turbine Cascade. *J. Eng. Gas Turbines Power*, **139**(1), 012605–012605–11.

Zhou, C., & Hodson, H. 2011. The Tip Leakage Flow of an Unshrouded High Pressure Turbine Blade With Tip Cooling. *J. Turbomach*, **133**(4), 041028–041028–12.

Zhou, C., & Zhong, F. 2016 (June). A Novel Suction Side Winglet Design Method for High Pressure Turbine Rotor Tips. ASME Paper No. GT2016-56218.

Zhou, C., Hodson, H., Tibbott, I., & Stokes, M. 2013. Effects of Winglet Geometry on the Aerodynamic Performance of Tip Leakage Flow in a Turbine Cascade. *J. Turbomach*, **135**(5), 051009–051009–10.